

20030225022

E 2. 157

2

AD-A256 672



PL-TR-92-2108

**PHYSICAL CONSTRAINTS ON SEISMIC WAVES
FROM CHEMICAL AND NUCLEAR EXPLOSIONS**

Brian Stump
Robert Reinke
Ken Olsen

Lane Johnson
Sharon Reamer
Klaus-G. Hinzen

Southern Methodist University
Department of Geological Sciences
Dallas, TX 75275-0395

S DTIC ELECTE D
AUG 20 1992
A

22 April 1992

Final Report
17 February 1989-31 April 1992

APPROVED FOR PUBLIC RELEASE; DISTRIBUTION UNLIMITED



PHILLIPS LABORATORY
AIR FORCE SYSTEMS COMMAND
HANSCOM AIR FORCE BASE, MASSACHUSETTS 01731-5000

92 8 19 59

92-23124



SPONSORED BY
Defense Advanced Research Projects Agency
Nuclear Monitoring Research Office
ARPA ORDER NO. 5307

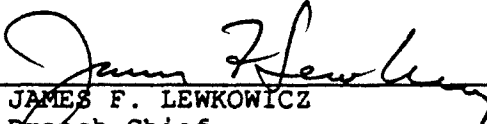
MONITORED BY
Phillips Laboratory
Contract No. F19628-89-K-0025

The views and conclusions contained in this document are those of the authors and should not be interpreted as representing the official policies, either expressed or implied, of the Defense Advanced Research Projects Agency or the U.S. Government.

This technical report has been reviewed and is approved for publication.



JAMES F. LEWKOWICZ
Contract Manager
Solid Earth Geophysics Branch
Earth Sciences Division



JAMES F. LEWKOWICZ
Branch Chief
Solid Earth Geophysics Branch
Earth Sciences Division



DONALD H. ECKHARDT, Director
Earth Sciences Division

This report has been reviewed by the ESD Public Affairs Office (PA) and is releasable to the National Technical Information Service (NTIS).

Qualified requestors may obtain additional copies from the Defense Technical Information Center. All others should apply to the National Technical Information Service.

If your address has changed, or if you wish to be removed from the mailing list, or if the addressee is no longer employed by your organization, please notify PL/IMA, Hanscom AFB, MA 01731-5000. This will assist us in maintaining a current mailing list.

Do not return copies of this report unless contractual obligations or notices on a specific document requires that it be returned.

REPORT DOCUMENTATION PAGE

Form Approved
OMB No. 0704-0188

Public reporting burden for this collection of information is estimated to average 1 hour per response, including the time for reviewing instructions, searching existing data sources, gathering and maintaining the data needed, and completing and reviewing the collection of information. Send comments regarding this burden estimate or any other aspect of this collection of information, including suggestions for reducing this burden, to Washington Headquarters Services, Directorate for Information Operations and Reports, 1215 Jefferson Davis Highway, Suite 1204, Arlington, VA 22202-4302, and to the Office of Management and Budget, Paperwork Reduction Project (0704-0188), Washington, DC 20503.

1. AGENCY USE ONLY (Leave blank)		2. REPORT DATE 22 April 1992	3. REPORT TYPE AND DATES COVERED Final (17 Feb 1989-31 Apr 1992)	
4. TITLE AND SUBTITLE Physical Constraints on Seismic Waves From Chemical and Nuclear Explosions			5. FUNDING NUMBERS PE: 61101E PR 9A10 TA DA WU AQ Contract F19628-89-K-0025	
6. AUTHOR(S) Brian Stump Robert Reinke Ken Olsen Lane Johnson Sharon Reamer Klaus-G. Hinzen				
7. PERFORMING ORGANIZATION NAME(S) AND ADDRESS(ES) Southern Methodist University Department of Geological Sciences Dallas, TX 75275-0395			8. PERFORMING ORGANIZATION REPORT NUMBER	
9. SPONSORING/MONITORING AGENCY NAME(S) AND ADDRESS(ES) Phillips Laboratory Hanscom AFB, MA 01731-5000 Contract Manager: James Lewkowicz/GPEH			10. SPONSORING/MONITORING AGENCY REPORT NUMBER PL-TR-92-2108	
11. SUPPLEMENTARY NOTES				
12a. DISTRIBUTION/AVAILABILITY STATEMENT Approved for public release; Distribution unlimited			12b. DISTRIBUTION CODE	
13. ABSTRACT (Maximum 200 words) Quantification of physical processes near an explosion that contribute to the radiated seismic wavefield was the goal of this work. Characterization of both nuclear and chemical explosions using near-source observations was conducted. This report is divided into six sections. The first is a review research in nuclear seismology, Nuclear Explosion Seismology: Verification, Source Theory, Wave Propagation and Politics. The second contributino reviews the types of free-field and free surface data recorded around nuclear explosions, Free-Field and Free-Surface Ground Motions from Nuclear Explosions, Their Spatial Variations and the Constraint of Physical Source Mechanisms. The third paper is a numerical study designed to investigate the scatter observed in near-source observations, Variability of Near-Source Waveforms from Contained				
14. SUBJECT TERMS Nuclear explosion, chemical explosion, quarry blast, free-field and free surface ground motion, seismology, verification, moment tensors, superposition.			15. NUMBER OF PAGES 190	
			15. PRICE CODE	
17. SECURITY CLASSIFICATION OF REPORT Unclassified	18. SECURITY CLASSIFICATION OF THIS PAGE Unclassified	19. SECURITY CLASSIFICATION OF ABSTRACT Unclassified	20. LIMITATION OF ABSTRACT SAR	

Explosions - Pahute Mesa, A Case Example. The fourth section describes the source characterization of a moderate size explosion in Yucca Flats. Both the isotropic and deviatoric source contributions are characterized, Isotropic and Deviatoric Characterization of the Coalora Nuclear Explosion in Yucca Flats. The fifth paper reports on the characterization of chemical explosions in a cylindrical geometry, Near-Source Characterization of the Seismic Wavefield Radiated from Quarry Blasts. The final contribution, Physical Models of Spall Zone Ground Motions and the Determination of Spatial Decay Rates, is presented only in abstract form. This work was cooperative with the Source Region Program at Los Alamos National Laboratory and has been published under LAUR-92-451.

Nuclear Explosion Seismology: Verification, Source Theory, Wave Propagation and Politics

Brian W. Stump

DTIC QUALITY INSPECTED 8

Accession For	
NTIS CRA&I	<input checked="" type="checkbox"/>
DTIC TAB	<input type="checkbox"/>
Unannounced	<input type="checkbox"/>
Justification	
By	
Distribution /	
Availability Codes	
Dist	Avail and/or Special
A-1	

Reprinted from U.S. National Report to
International Union of Geodesy and
Geophysics 1987-1990

Published by American Geophysical Union

NUCLEAR EXPLOSION SEISMOLOGY: Verification, Source Theory, Wave Propagation and Politics

BRIAN W. STUMP

Department of Geological Sciences, Southern Methodist University

Introduction

Nuclear explosion seismology, as a result of the international consequences of nuclear testing, has a strong political component. The time period 1987-1990 was marked by increased political interest in this subject as well as rapid scientific developments. Joint Verification Experiments (JVE's) between the Soviet Union and the United States provided new opportunities for joint testing of seismic instrumentation and capabilities. A new set of protocols were exchanged between the U.S. and the Soviet Union concerning the enforcement of the 1974 Threshold Test Ban Treaty (TTBT) and 1976 Peaceful Nuclear Explosion Treaty (PNET). These and other political/scientific developments are discussed in the first main section of this review.

Research has continued on verification issues including detection, location, discrimination and yield determination. These issues are addressed in the second section. Much emphasis was placed on the utilization of arrays in detection and location problems. Yield determination research has focused upon the L_g phase as a stable indicator of yield as well as ways to combine multiple yield estimates from a single explosion.

Explosion source theory is the third area of research that is reported. Work has been divided primarily between teleseismic and regional studies although a small amount of research has continued with close-in data extending into the hydrodynamic regime. A number of researchers have begun to quantify the secondary source process, spall (tensile failure of near surface layers above the explosion) as to its contribution to regional seismograms. As identified in the Office of Technology Assessment (OTA) Report on Seismic Verification (1988), discrimination difficulties may develop for low-yield test ban treaties with large chemical explosions detonated for mining purposes. Following the work in the early 60's in this area, a number of researchers have returned to study the source signatures from chemical explosions at regional distances.

Wave propagation problems continue to play a dominant role in many of the explosion studies. This subject comprises the fourth section. Regional waveforms have been studied with renewed intensity in response to the increased political interest in treaty verification. The development of a physical understanding of the propagation of the various regional phases, including P_n , P_g , mantle P , S_n , L_g , and R_g , has been the focus of many papers.

Issues of attenuation at teleseismic distances and thus bias in yield estimation remain of interest although the JVEs provided an independent assessment of these effects at Shagan River. The physical description of transverse motions from explosions continues to be explored in terms of tectonic strain release although new results characterizing wave propagation in anisotropic materials offer an alternate explanation for these observations.

Political/Scientific Developments

The political aspects of nuclear seismology are no better portrayed than in the Reagan Administrations claim that the Soviet Union had "likely violations" of the Threshold Test Ban Treaty [Arms Control Today, July/August 1990]. In an attempt to address questions associated with seismic measurements from underground nuclear tests, the Office of Technology Assessment (OTA) in 1988 published SEISMIC VERIFICATION of Nuclear Testing Treaties. This document culminated a national review of seismic capabilities by government, private, and academic geophysicists, seismologists, geologists, statisticians, and physicists. The report identified the tasks in monitoring underground nuclear explosions including detection, identification, evasion, and yield determination.

It discussed Soviet compliance and the ability to verify the TTBT and PNET. The report concluded that all yield estimates of U.S. and Soviet tests are within the 90 percent confidence level for yields of 150 kt or less. A number of authors in the past four years have looked closely at the yield estimation question and come to similar conclusions [Evernden and Marsh, 1987; Sykes and Davis, 1987]. The report recommended a phased approach to further treaties restricting or eliminating the testing of nuclear weapons. It was concluded that a threshold between 5 and 10 kt could be reliably monitored seismically with lower levels possible. Restricted testing practices that limit detonations to below the water table, avoid decoupling scenarios, and provide special handling for large chemical explosions would make even lower threshold limits possible with existing seismic instrumentation. As noted by Richards (1990) not all government officials agreed with the conclusions of the OTA Report. Robert Barker a spokesman for the Department of Defense stated "(the OTA Report) has homogenized fact with fiction." Richards and Lindh (1987) have argued for the low-yield threshold test ban treaty while Hamm (1987) has presented arguments against such a testing change. A further debate of testing issues can be found in the discussions of Miller et al. (1987) and Feiveson et al. (1987).

As noted in the OTA Report, the Federal Government has continued to request independent estimates of yields to assess uncertainties in seismic yield estimates. CORRTEx (Continuous Reflectometry for Radius versus Time) is a non-

Copyright 1991 by the American Geophysical Union.

Paper number 91RG00735.
8755-1209/91/91RG00735 \$15.00

STUMP: NUCLEAR EXPLOSION SEISMOLOGY

seismic method suggested to fit this verification requirement. This hydrodynamic methodology requires on-site measurements and deduces the yield of the explosion from the velocity of the shock wave and the properties of the surrounding media. In a recent interview [Arms Control Today, July/August 1990] Ambassador C. Paul Robinson claims that the U. S. experience with CORRTEX gives an error in yield of 12% which in a new geological environment may become as large as 30%. Lamb (1988) suggests that under certain circumstances that these errors may be larger. Robinson attributes the seismic yield error factors to be in the range of 1.7 to 1.75. He goes on to remark that prior to the 1 June 1990 testing protocols exchanged between the Soviet Union and the United States that the U. S. could not be certain if the Soviets had tested over 400 to 500 kilotons. These statements about seismic and CORRTEX yield estimates were criticized by Richards and Lamb in Arms Control Today, September 1990.

A set of Joint Verification Experiments with U. S. and Soviet cooperation were conducted in 1988 [Robinson, 1989]. Hydrodynamic measurements were made by both countries at the Nevada Test Site (NTS) [Anderson and Manning, 1988] and the Soviet test site [Manning and Anderson, 1988] at Shagan River in Eastern Kazakhstan. Seismic measurements of these explosions in both the U.S. and the Soviet Union [Priestley et al., 1990] indicate that hydrodynamic yields determined from these explosions are in good agreement with seismic yield estimates [Sykes and Ekstrom, 1989].

Seismic experiments involving the Soviet Union and the United States have included installation of seismic stations within the borders of both nations [Science, 25 August 1989]. This instrumentation program began in 1987 as a cooperative enterprise between the Natural Resources Defense Council (NRDC) and the Soviet Union [von Hippel, 1989]. It has since expanded to include the Incorporated Research Institutions for Seismology (IRIS) and the Federal government [Science, 25 August 1989]. The IRIS sponsored instrumentation has been entitled the Eurasian Seismic Studies Program (ESSP). The program is designed to provide data for constraining the seismic properties of the crust and continental lithosphere, seismic propagation characteristics, noise properties, and differences in seismic sources. Six broadband Global Seismic Network (GSN) stations have been installed with a target of twenty stations. Two regional networks are planned for Caucasus and Kirghizia with an additional small aperture (2 km) array at Kirghizia [IRIS Proposal, 1991-1995]. The coming years will see much activity in the study of crust and upper mantle structure [Priestley et al., 1988], seismic noise [Berger et al., 1988], seismicity [Thurber et al., 1989] and regional wave propagation in the Soviet Union.

A set of protocols was signed at the summit meeting between the Soviet Union and the United States on June 1, 1990. These led to consent by the Senate of the TTBT (1974) and PNET (1976) in October of 1990. The Treaties came into force on December 11, 1990. The protocols establish on-site inspections of tests as well as the use of in-country seismic stations for monitoring certain underground tests [Chemical and Engineering News, October 8, 1990]. These protocols were discussed with Ambassador C. Paul Robinson in an interview in Arms Control Today (July/August 1990). The responsibility for seismic in-country monitoring went to the On-Site Inspection Agency. For explosions with anticipated yields above 35 kilotons the U. S. has the right for on-site inspection of the test

location. For explosions that are planned to exceed 50 kilotons, CORRTEX measurements are possible. In addition, in-country seismic measurements are allowed for these larger explosions.

Under the United Nations sponsored Conference on Disarmament (CD), the Group of Scientific Experts (GSE) has undertaken a series of experiments to investigate the exchange and interpretation of seismograms on an international scale [Lamb, 1988 and Tirman, 1988]. These experiments are designed to investigate, develop and deploy tools necessary for electronic data transfer and management and provide experience that might be necessary in an international effort to monitor underground nuclear testing. DARPA has taken the US lead in this effort with the establishment of an Experimental International Data Center in Washington, DC. Seismic stations that will be participating in the program are Blacksburg, VA; Lajitas, TX; North Pole, AK; Pinon Flat Observatory, CA; Pinedale, WY; and Berkeley, CA.

Verification

The initial task of signal detection in any verification process was well reviewed in the OTA report. Quantification of background noise in Eastern Kazakhstan [Berger et al., 1988] and the United States [Rodgers et al., 1987] continue in an effort to improve the detection capabilities of new systems. Given (1990) reports on noise levels at the four IRIS installations in the Soviet Union. Renewed interest in high frequency signal propagation has resulted in broadband noise characterization and consideration of instruments buried at great depths [Barstow et al., 1990]. As noted by Sereno (1990) detection capabilities are dependent on signal attenuation as well as noise levels. Detection capabilities of existing networks were concluded to be adequate for well coupled explosions with yields of a few kilotons or less in USSR [OTA Report]. Small aperture regional arrays have also been investigated as to their detection capabilities as exemplified by the study at NORESS [Sereno and Bratt, 1989]. Problems with detection of decoupled explosions [OTA Report; Glenn and Rial, 1987] which would require more extensive in-country networks for monitoring to the lowest yield levels were identified.

The second task in any verification operation is event location. Work in this area has extended to the utilization of single station three-component data for both event detection and location [Magotra et al., 1987]. Similar analysis was conducted using a sparse array of single three-component stations in Eastern Kazakhstan [Thurber et al., 1989]. These studies indicate the strength of polarization analysis [Nakanishi and Jarpe, 1988] along with multiple phase identification in conducting earthquake and explosion locations. Increased reliance on small arrays in verification has resulted in the investigation of arrays as location tools. Bratt and Bache (1988) discuss back-azimuth and arrival time determination using the NORESS and FINISS arrays. Bame et al. (1990) report on azimuth estimation using the NORESS regional array. Harris (1990) and Suteau-Henson (1990) compare direction estimation from high frequency arrays and three-component stations and find that the single station estimates are more susceptible to errors introduced by low signal to noise ratios. Recent work has been reported that attempts to take explicit consideration of the two- and three-dimensional nature of the earth in producing locations [Traill and Johnson, 1987; Nelson and Vidale, 1990].

Discrimination studies during the past four years have focused primarily on events from the Western U. S. and the Soviet Union. Utilizing the four broadband stations operated around NTS by Lawrence Livermore National Laboratory (LLNL), Taylor et al. (1988) investigated low (1-2 Hz) and high (6-8 Hz) frequency contributions to P_n , P_g , and L_g as possible earthquake/explosion discriminants. The earthquakes were found to be richer in high frequencies than the explosions although overburied explosions were enriched in high frequencies and often misclassified. The authors note that it is difficult to separate the effects of a depth dependent Q model resulting in stronger attenuation in the shallower explosions from a true difference between explosion and earthquake sources. Chael (1988) also reports enriched high frequencies from Western U.S. earthquakes compared to explosions above 10 Hz, in contradiction to the claims of Evernden et al. (1986). Denny et al. (1987) investigated the M_S/m_b discriminant in the Western U. S. and found its success was dependent on the equation used for determining magnitude. A comprehensive discrimination study, again with data from the LLNL array, was reported by Taylor et al. (1989). All discriminants suggested by Pomeroy et al. (1982) were tested in a systematic way against a data set consisting of 233 NTS explosions and 130 Western U.S. earthquakes. The explosions were recorded at ranges of 200-400 km while the earthquakes were observed at ranges of 175-1300 km. Multi-station discrimination led to misclassification of up to 2% of the explosions and 4% of the earthquakes, with most problems occurring for events below m_b 4.0. Suteau-Henson and Bache (1988) report on a discrimination study using P_n and L_g recorded at NORESS. They find that spectral ratios can sometimes separate explosions from earthquakes but that in general the spectral ratios vary as much within a class of events as they do between classes. Baumgardt and Young (1990) report on a discrimination study using the NORESS array and small sources (magnitude 2-3) in the 300-500 km distance range. In contrast to studies in the Western United States they find the best discriminants to consist of ratios between compressional and shear energy (P_n/S_n). At the lowest yields (1 kt), the discrimination of nuclear explosions from quarry explosions may become a problem. A number of researchers have begun to study these sources (see source theory discussion). Baumgardt and Ziegler (1988), Smith (1989) and Hedlin et al. (1989, 1990) have suggested that spectral scalloping may be a useful discriminant for ripple-fired quarry explosions.

Yield determination has been one of the most active areas of research in the past four years, with focus on application to regional observations in both the U. S. and the U.S.S.R. This emphasis is a natural result of the newly deployed stations and data that have been exchanged between the two countries. In the case of regional observations, primary focus has been placed upon the utilization of L_g amplitudes as a stable measure of explosion yield. Nuttli pioneered the L_g yield work and reported on yield estimates for explosions in E. Kazakhstan [Nuttli, 1987] and Novaya Zemlya [Nuttli, 1988]. The L_g method of yield estimation has been scrutinized by a number of other researchers. Patton (1988) reported on a comprehensive study of U. S. explosions from the NTS recorded at the LLNL broadband array around the test site. He also notes small scatter in these L_g yield estimates. Hansen et al. (1990) report on the stability of \log RMS L_g to 0.03 units for IRIS, CDSN, and NORSAR data from Shagan River explosions. Refinement of yield estimates using m_b measurements has included the assessment of data sensing, clipping, and noise contamination [McLaughlin et al., 1989; Jih and Shumway, 1989]. A number

of authors have made maximum likelihood magnitude estimates [McLaughlin, 1988]. Scatter in m_b measurements, resulting from either near-source or near-receiver structure, have been analyzed and modeled [McLaughlin and Jih, 1988]. Specific attention has been applied to understanding the variation of magnitudes for explosions detonated in Yucca Flats at NTS where the systematic variations in magnitude can be linked to the basin structure [Ferguson, 1988; McLaughlin et al., 1987]. These studies indicate a growing modeling capability for two- and three-dimensional wave propagation and an application of these tools to yield determination questions. Work continues in other areas of yield determination as exemplified by the utilization of hydrophone records to make yield estimates [McCreery, 1987].

Source Theory

Although not strictly a seismic wave propagation problem, one of the biggest source measurement developments in the past four years has been the utilization of time of arrival measurements in the hydrodynamic region around explosions to determine yield [OTA Report]. CORRTX measurements played an important role during the JVEs in 1988. King et al., 1989 report on a detailed equation of state analysis that describes the coupling of energy in the hydrodynamic region. The study focuses upon the claim that enhanced coupling can result from small cavities, $1-3.5 \text{ m/kt}^{1/3}$. Their numerical results suggest that there is no enhanced coupling predicted when radiation transport of energy is included in the calculations. These types of studies can be seen as an initial step in accounting for energy transport from explosions. Such data, linked to intermediate stress observations, offer opportunity to study development of the seismic source function from nuclear explosions. Denny and Goodman (1990) report a re-analysis of the Salmon and Sterling data. They argue that the intermediate stress regime data show a two-wave system that yields a f^{-3} high frequency reduced velocity potential decay. They also find the Salmon-Sterling decoupling value to be 72.

In attempts to further utilize teleseismic measurements, Murphy et al. (1989) and Murphy (1989) have focused upon network averaged teleseismic spectra for recovery of source information, such as yield and burial depth. They suggest that the network averaging process, which includes frequency dependent station corrections, reduces the variances of spectra and emphasizes source properties. The above analysis has allowed the determination of scaling relations and source depth effects. Der et al. (1987) report a multi-channel deconvolution technique which factors teleseismic spectra into source and receiver effects, again attempting to separate these contributions to isolate the source. At regional arrays Der et al. (1990) suggest the application of coherent processing techniques to identify interevent differences separate from intersite effects. Walter et al. (1988) investigated regional P waves at frequencies as high as 30 Hz to identify explosion and earthquake source differences. They report an increase in spectral amplitude with moment from earthquakes that is consistent with an f^{-2} source model. The explosion data they investigated showed greater scatter than earthquake data but indicated a spectral decay that was in excess of f^{-2} . As noted by Chael (1988), this effect could be a result of either source or attenuation processes.

Inversion techniques designed to characterize the explosion source in terms of moment tensors continue to be investigated with emphasis on isolating isotropic and deviatoric components.

STUMP: NUCLEAR EXPLOSION SEISMOLOGY

Patton (1988b) describes an inversion of regional fundamental and higher mode surface waves to determine the moment tensor. He finds that a spall correction is necessary. Johnson (1988) reported on second order moment tensor inversions of near-source data (1-11 km) from two Pahute Mesa nuclear explosions. The source was dominated by the isotropic moment tensor although a secondary, long-period contribution (0.3-0.4 Hz) was identified in the vertical dipole. This secondary source might be attributed to near surface spallation. Stump (1987) found a similar secondary source contribution in the vertical dipole of the moment tensor when inverting data from chemical explosions. In this case, acceleration measurements within the spall zone were able to corroborate the spall interpretation. In an attempt to investigate the robustness of isotropic source estimates, Vasco and Johnson (1989) conducted an investigation of extremal solutions. Their results indicate that an isotropic contribution of 10% or more is necessary for unique identification in data with 10% random noise or 2% lateral heterogeneity. In a search for other basis functions for the seismic source representation, Vasco has suggested decomposing the source into orthogonal source time functions (1989). He [Vasco, 1990] also suggests an orthogonal decomposition of the moment density tensor which might be applicable to sources with finite dimensions.

As noted in the verification discussion, one future discrimination task under a Reduced Threshold Test Ban Treaty is the discrimination of waveforms generated by large chemical explosions and small nuclear explosions. This motivation and the more basic desire to use chemical explosions as small scale analogs of nuclear explosions has led to a moderate amount of work in characterizing chemical explosions as sources of seismic waves. Stump and Reinke (1987) discuss the design and implementation of relatively low-cost contained chemical explosions for source studies. They [Stump and Reinke, 1988] go on to use multiple chemical explosions to experimentally test linear superposition. Baumgardt and Ziegler (1988) report on regional observations from ripple-fired quarry explosions that suggest that spectral scalloping can be used as a discriminant [Smith, 1989] for such blasts. Hedlin et al. (1989) report that seismograms from suspected quarry explosions have energy organized in discrete, time-independent frequency bands while a single explosion calibration event shows no such modulation.

Tectonic release is another secondary source accompanying explosions which may contaminate observations [Cohee and Lay, 1988]. The phase reversal of some Rayleigh waves generated by underground explosions from E. Kazakhstan has been used as evidence for tectonic release. Day et al. (1987) replicate these observed phase reversals coupled with time delays on the order of a few seconds. Their two-dimensional models include tectonic prestress which is released during the explosion process. Pre-stress greater than 100 bars was required to generate synthetics that matched observations.

The secondary source process known as spall, which results from the tensile failure of near surface materials above the explosion, has continued to be investigated as a source of intermediate frequency (0.1-5 Hz) regional waves. Taylor and Randall's (1989) modeling of waveforms suggest that the spall source may have important regional contributions. Patton (1990), in an attempt to put better constraints on the size of the secondary spall source, has begun the investigation of data from within the spall zone using it to develop scaling relations for spall mass and momentum.

Wave Propagation and Structure

Waves from underground explosions are observed at near-source, regional, and teleseismic distances. Regional and teleseismic observations have application to verification issues while near-source observations provide the opportunity to resolve questions about explosion source characterization and possibly unique separation of propagation and source contributions. We review wave propagation studies that have developed for all three observation ranges from explosions. The regional and, to a lesser extent, the teleseismic observations have received the most attention by the research community. These studies are motivated by a desire to produce physical models that describe the generation and propagation of seismic energy from the explosion to the receiver. Such a physical basis must be developed for waves that are used in verification tasks of discrimination and yield determination.

The scarcity of near-source research reflects the fact that such observations have not been seen to play a verification role and further, that most such data is recorded and analyzed by persons responsible for underground testing. Murphy and Shah (1988) studied near-field Rayleigh waves generated by atmospheric explosions. They found that these waves were strongly affected by the shallow shear wave structure near the explosion. Leonard and Johnson (1987), in an attempt to refine the velocity structure at Pahute Mesa, conducted one-dimensional travel time inversions for P and S structure utilizing near-source observations. Their philosophy was to begin the development of simple one-dimensional models that could be revised as two- and three-dimensional structural information becomes available. The effect of random structure in the near-source region and quantification of scattering effects was discussed by Stump and Reinke (1988). They argue that to quantify source models with near-source data it is necessary first to separate stochastic and deterministic wave propagation effects.

Regional wave propagation studies have resulted from: (1) the desire to monitor explosions of all sizes throughout the world; (2) the development of regional arrays which are providing abundant regional data [Serenio et al., 1987]; (3) the apparent stability of the L_g phase as a measure of yield [Patton, 1988; Hansen et al., 1990]; and (4) the recent establishment of new regional stations in the Soviet Union [Priestley et al., 1990]. The primary regional phases that have been studied include P_g , P_n , S_n , L_g , and R_g . Characterization of regional propagation effects in the Western U.S. is one area where there has been much work since NTS provides an abundant set of artificial sources [Hough et al., 1989].

Chael (1988) reports on P_g observations at Nelson, NV of NTS explosions and nearby earthquakes. As mentioned in the discrimination discussion, he uses these observations to illustrate that the earthquakes have more energy above 10 Hz than explosions. Walter et al. (1988) also report on regional P wave observations from NTS. Serenio and Given (1990) describe numerical models intended to replicate P_n attenuation in the crust and uppermost mantle to frequencies as high as 15 Hz. They find that a frequency independent P_n spreading is a bad assumption for data reduction. Serenio et al. (1988) have used P_n and L_g observations at NORESS to invert for both attenuation and source moment. Their approach allows for a quantification of regional wave propagation effects. Vogtfjord and Langston (1990) use f-k analysis of regional seismograms (50-300 km) recorded at NORESS to identify coherent phases.

Composite seismograms are then constructed by piecing together stacked records at the phase velocities for which coherent energy is identified. Wave propagation in the oceanic lithosphere was investigated by Sereno and Orcutt (1987) with focus on P_n and S_n phases. They find that the coda associated with these ocean phases can be explained in terms of a leaky organ-pipe mode in the sediment layer/oceanic water column.

One of the most interesting but least understood regional phases is L_g . The primary motivation for a physical understanding of the phase comes from its utilization as an estimator of yield [Nuttli, 1987 and 1988; Patton, 1988]. Work continues in an attempt to quantify this phase [Frankel et al., 1990] and, in particular, understand its attenuation characteristics [Mitchell and Hwang, 1987; Xie and Mitchell, 1990]. A major outstanding problem in understanding L_g is the insufficient excitation of the phase in one dimensional velocity models. Baumgardt (1990) has reported on observational data supporting the blockage and scattering of the phase further indicating the importance of two and three dimensional structures on this phase. Dainty and Toksöz (1990) also investigate the scattered energy in L_g as well as P phases.

Shallow explosions and earthquakes in the Eastern U. S. have been found to generate relatively high frequency (0.4-2.5 Hz) fundamental mode Rayleigh waves [Kafka and Reiter, 1987]. Kafka (1990) has suggested that these waves may be a good depth discriminant in areas where they are observed.

Analysis and modeling of teleseismic observations from nuclear explosions has explored the effect of multipathing and scattering on these waveforms. Lay (1987 a and b), Lay and Wele (1987), and Lynnes and Lay (1989) have investigated teleseismic P waves and early coda for evidence of near-source scattering. Gupta and Blandford (1987) suggest that spectral ratios between P and P coda can be used to characterize near-source material properties. Gupta et al., (1990a) through a broadband f-k analysis at the EKA array of U.S. and Soviet explosions, quantify the effects of near-receiver scattering. This same group of workers [Gupta et al., 1990b] suggest that both near-receiver and near-source information can be recovered from the scattered waveforms. Cormier (1987), in a modeling study, attempted to determine the effects a three-dimensional velocity model beneath NTS with scale lengths of 20-100 km and a few percent velocity fluctuation would have on teleseismic m_b . He finds that such variations lead to as much as a factor of three variation in amplitudes and if considered could reduce the m_b variances by 25%. He also suggests that P coda may be a more stable measure if scattering in the crust and upper mantle is important. McLaughlin and Jih (1988) and McLaughlin et al. (1987) investigated the effect of near-source scattering on teleseismic m_b through a series of two-dimensional linear-elastic, finite-difference calculations. For explosions at the French Sahara Test Site the maximum effect is $\pm 0.15 m_b$ units. At Yucca Flats variations as large as $\pm 0.30 m_b$ units were modelled. These variations can be reduced by averaging over a network of observations. Determination of teleseismic receiver functions, using multiple component data, continues in an attempt to further quantify receiver effects. Broadband receiver functions for seismic stations in E. Kazakhstan were reported by Priestley et al., (1988).

One of the newest developments in wave propagation has been a number of papers beginning to quantify effects of anisotropic media on seismic waves observed from explosions.

This work has developed out of an emphasis on anisotropic effects in the seismic exploration industry. A series of papers by Ben-Menahem (1990) and Ben-Menahem and Sena (1990) report Green's functions for anisotropic media with special consideration of SH waves. Other studies of explosions in anisotropic media have been reported by Mandal and Toksöz (1990). They indicate that, with a moderate amount of anisotropy around the explosion, SH waves might be generated.

Future Issues

The progress in a field over a time period such as the last four years is motivated by important issues that are confronting a particular area. In an attempt to provide a glimpse into the future of nuclear seismology, five outstanding areas of research are identified. These include the development of a physical basis for regional wave propagation, the investigation of the seismic source characterization of small nuclear explosions, quantification of explosion phenomenology, the exploration of quarry and engineering explosions as seismic sources, and utilization of automated signal processing tools.

Physical Basis for Regional Wave Propagation

This topic is particularly important as small yield explosions will most likely be monitored at regional distances. A physical understanding of the processes is needed if techniques developed in one geographical area are to be transported to a new area. Much of the work that has been completed to date on regional waves has been primarily experimental. This work must be extended to the development of physical models which can be tested. This testing may involve extensive instrumentation, not unlike that suggested by Pascal, in order to resolve important aspects of the regional wave propagation. Some key questions to be addressed include: (1) How is energy distributed among the phases P_n , P_g , S_n , L_g ?; (2) How homogeneous or inhomogeneous is the crust and upper mantle (1D,2D,3D)?; (3) How do we characterize this homogeneity/inhomogeneity experimentally?; (4) What are the source depth effects on each of these phases?; (5) How does the regional energy compare to that observed locally and teleseismically?

Small Source Physics

The seismological community has spent a good deal of its efforts and time characterizing large (>100 kt) nuclear explosions. This focus has resulted from the 150 kt TTBT and PNET and the good signal to noise ratios resulting from such events. These sources are often deeply buried ($122m/kt^{1/3}$). A number of techniques exist for separating these events from the earthquake population as well as determining yield from the wave amplitudes ($m_b - \log(\text{Yield})$ relations). Little work has been completed in characterizing small yield nuclear explosions including careful resolution of such basic questions as the appropriate slope for a $m_b - \log(\text{Yield})$ relation and the effect material properties have on such relations. As a result of their shallow depth, these sources can be detonated in highly porous, dry materials as well as in cavities offering an opportunity for decoupling. The seismological community has spent little time studying such events either experimentally or theoretically. No consideration has been given to how one might characterize an explosive site before a test so that some of these effects might be anticipated and mitigated. Some of the questions that arise are: (1) What are earthquake/explosion source

STUMP: NUCLEAR EXPLOSION SEISMOLOGY

functions at small magnitude?; (2) What coupling variations can be expected in shallow, weathered, dry materials?; (3) How effective is decoupling in cavities or previously explosively disturbed materials?; (4) What are the effects of source region inhomogeneity?; (5) How do we complete geophysical/geological site characterization to constrain explosion coupling?

Explosion Phenomenology

Physical processes by which chemical and nuclear explosions couple energy into the earth are not well quantified from first principles. As one might expect, these processes are highly dependent upon the material properties of the media of interest. In many cases the complete data sets for resolving these coupling processes are not available. Source related research might include: (1) Quantification of chemical/nuclear source differences; (2) Determination of the importance of tensile failure of near-surface layers (spall); (3) Development of a physical model for spall; (4) Determination of energy balance in the three spatial dimensions; (5) A quantification of energy coupling from the hydrodynamic to the linear regimes.

Quarry/Engineering Explosions

Many industrial explosions are detonated each year for purposes ranging from excavation for construction to the recovery of subsurface resources. Each of these sources generate seismic waves and must be separated from the population of nu-

clear explosions. Little work has been completed in describing these sources as generators of regional seismic energy. Some key questions that must be addressed: (1) What are the different types of industrial explosions?; (2) How does each type generate seismic waves (P and S waves)?; (3) Do the individual explosions interact linearly or nonlinearly?; (4) Can multiple explosions be discriminated from a single explosion?

Array Processing/Automatic Data Analysis

Increasingly rigorous verification requirements may require increased data processing and analysis capabilities [Bache et al., 1990; Bratt et al., 1990]. Automation of these tasks is and will remain an important area of research [Anderson, 1990; Dysart and Pulli, 1990].

Much work has been completed in the past four years thanks to continuing support for basic research in nuclear seismology. Many questions still remain, particularly those associated with the physical processes of energy coupling and wave propagation. As new requirements are imposed under future treaty scenarios, an understanding of these processes will be necessary for developing refined yield determination, discrimination and detection tools.

Acknowledgements. Work on this review paper was supported under DARPA/GL contract F19628-89-K-0025 at Southern Methodist University. Constructive reviews by Paul G. Richards and Fred Followill are gratefully noted.

REFERENCES

- AFGL/DARPA, Papers Presented at the 9th Annual AFGL/DARPA Seismic Research Symposium, Air Force Geophysics Laboratory, Hanscom AFB, Mass, 15-18 June 1987.
- AFGL/DARPA, Papers Presented at the 10th Annual DARPA/AFGL Seismic Research Symposium, Air Force Geophysics Laboratory, Hanscom AFB, Mass, 2-4 May 1988.
- AFGL/DARPA, Papers presented at the 11th Annual DARPA/AFGL Seismic Research Symposium, Air Force Geophysics Laboratory, Hanscom AFB, Mass, 2-4 May 1989.
- Alexeev, R. W., III, H. L. Gray, G. D. McCarter, and G. L. Withers, Seismic monitoring of a threshold test bed treaty (TTBT) following calibration of the test site with CORTEX experiments, Air Force Geophysics Laboratory Technical Report, AFGL-TR-88-0055, 92 pp., 1988.
- Anderson, A. and M. Manning, US-Soviet joint monitoring of nuclear explosions in Nevada, *Nature*, **334**, 641, August 25 1988.
- Anderson, C. G., US-Soviet summit: Seismic monitoring in favour, *Nature*, **345**, 463, June 7 1990.
- Anderson, K. R., Programming as a geophysical inverse problem, *Bull. Seismol. Soc. Am.*, **80B**, 1893-1909, 1990.
- Bacon, T. C., S. R. Bratt, J. Wang, R. M. Fung, C. Kobryn and J. W. Given, The intelligent monitoring system, *Bull. Seismol. Soc. Am.*, **80B**, 1833-1851, 1990.
- Bacon, D. A., M. C. Walck, K. L. Hiebert-Dodd, Azimuth estimation capabilities of the NORESS regional seismic array, *Bull. Seismol. Soc. Am.*, **80B**, 1999-2015, 1990.
- Barstow, N., J. A. Carter, P. W. Pottery, G. H. Sutton, E. P. Chael, and P. J. Leahy, High frequency (1-100 Hz) noise and signal recorded at different depths in a mine, Northwest Adirondacks, NY, *Geophys. Res. Lett.*, **11**, 681-684.
- Bausgard, D. R. and K. A. Ziegler, Spectral evidence for source multiplicity in explosions: Apparent to regional discrimination of earthquakes and explosions, *Bull. Seismol. Soc. Am.*, **78**, 1773-1795, 1988.
- Bausgard, D. R., and G. B. Young, Regional seismic waveform discrimination and case-based event identification using regional arrays, *Bull. Seismol. Soc. Am.*, **80B**, 1874-1892, 1990.
- Bausgard, D. R., Investigation of teleseismic L_g blooms and scattering using regional arrays, *Bull. Seismol. Soc. Am.*, **80B**, 2261-2281, 1990.
- Bratt, S. R., F. J. Sengeler, R. J. Sneed, F. Ryan and T. C. Ziegler, Initial results from the intelligent monitoring system, *Bull. Seismol. Soc. Am.*, **80B**, 1852-1873, 1990.
- Ben-Menahem, A. and A. G. Seng, Seismic source theory in stratified anisotropic media, *J. Geophys. Res.*, **95**, 15399-15427, 1990.
- Ben-Menahem, A. and A. G. Seng, The elastodynamic Green's tensor in an anisotropic half-space, *Geophys. J. Int.*, **102**, 421-443, 1990.
- Ben-Menahem, A., editor, *Vincent Verjovs: A Portrait of the Life and Work of Norman Abramov Hainst*, 1905-1970, American Geophysical Union, 2000 Florida Avenue, NW, Washington, DC 20009, 1990.
- Ben-Menahem, A., SH waves from point sources in anisotropic inhomogeneous media, *Geophysics*, **55**, 488-491, 1990.
- Berger, J., H. K. Eissler, F. L. Vernon, L. L. Nerisov, M. B. Goldberg, O. A. Stolyrov, and M. T. Terakov, Studies of high-frequency seismic noise in Eastern Kazakhstan, *Bull. Seismol. Soc. Am.*, **78**, 1744-1758, 1988.
- Bollinger, G. A., Microearthquake activity associated with underground coal-mining in Buchanan County, Virginia, USA, *Paraglyph*, **128**, 407-421, 1989.
- Bratt, S. R. and T. C. Bache, Locating events with a sparse network of regional arrays, *Bull. Seismol. Soc. Am.*, **78**, 780-798, 1988.
- Bratt, S. R., T. C. Bache, and D. J. Williams, Seismic monitoring capability in the Soviet Union using hypothetical regional networks, Air Force Geophysics Laboratory Technical Report, AFGL-TR-87-0244, 86 pp., 1987.
- Brune, J. N. and K. Priestley, Recent developments in the study of seismic techniques for monitoring a nuclear test ban, *Physics Today*, **42**, 548-549, 1989.
- Burger, R. W., T. Lay, and L. J. Burdick, Average Q and yield estimates from the Pahute Mesa Test Site, *Bull. Seismol. Soc. Am.*, **77**, 1274-1294, 1987.
- Chael, E. P. and R. P. Kroeger, Hi- β frequency spectral scaling of a main shock/aftershock sequence near the Norwegian coast, *Bull. Seismol. Soc. Am.*, **78**, 561-570, 1988.
- Chael, E. P., Spectral discrimination of NTS explosions and earthquakes in the Southwestern United States using high-frequency regional data, *Geophys. Res. Lett.*, **15**, 625-628, 1988.
- Cobac, B. P. and T. Lay, Modeling teleseismic SV waves from underground explosions with tectonic resonator: Results for Southern Nevada Zephyr, *Bull. Seismol. Soc. Am.*, **78**, 1158-1178, 1988.
- Comser, V. F., Focusing and defocusing of teleseismic P waves by unknowns three-dimensional structure beneath Pahute Mesa, Nevada Test Site, *Bull. Seismol. Soc. Am.*, **77**, 1688-1703, 1987.
- Coyner, K. B. and R. J. Martin III, Frequency dependent attenuation in rocks, Geophysics Laboratory Technical Report, GL-TR-90-0012, 44 pp., 1990.
- Denny, A. M. and M. N. Toksich, Array analysis of seismic scattering, *Bull. Seismol. Soc. Am.*, **80B**, 2242-2260, 1990.
- Dun, C. and S. Connor, Seismic tomography successfully measures nuclear blast, *New Scientist*, **119**, 30, Sept 15 1988.
- Dey, S. M., J. T. Cherry, N. Rumer, and J. L. Stevens, Nonlinear model of tectonic release from underground explosions, *Bull. Seismol. Soc. Am.*, **77**, 996-1016, 1987.
- Denny, M. D. and D. M. Goodman, A case study of the seismic source function: Salmon and Sterling reevaluation, *J. Geophys. Res.*, **95**, 19705-19723, 1990.
- Denny, M. D., S. R. Taylor, and E. S. Vergara, Investigation of m_p and M_s formulas for the Western United States and their impact on the M_w discriminant, *Bull. Seismol. Soc. Am.*, **77**, 987-995, 1987.
- Der, Z. A., P. H. Staunway, A. C. Lees, Frequency domain coherent processing of regional seismic signals at small arrays, *Bull. Seismol. Soc. Am.*, **78**, 326-338, 1988.
- Der, Z. A., R. H. Staunway, A. C. Lees, Multi-channel deconvolution of P waves at seismic arrays, *Bull. Seismol. Soc. Am.*, **77**, 195-211, 1987.
- Der, Z. A., M. R. Hiram and R. H. Staunway, Coherent processing of regional signals at small arrays, *Bull. Seismol. Soc. Am.*, **80B**, 2161-2176, 1990.
- Dowle, F. U., S. R. Taylor, and R. W. Anderson, Seismic discrimination with artificial neural networks: Preliminary results with regional spectral data, *Bull. Seismol. Soc. Am.*, **80**, 1346-1373, 1990.
- Duan, L. A., *Arms Control Verification and the New Role of On-Site Inspection*, Lexington Books, 1988.
- Dysart, P. S. and J. J. Pulli, Regional seismic event discrimination at the NORESS Array: Seismological measurements and the use of trained neural networks, *Bull. Seismol. Soc. Am.*, **80B**, 1910-1933, 1990.
- Evered, J. F. and G. E. Marsh, Yields of U. S. and Soviet nuclear tests, *Physics Today*, **37-44**, August 1987.
- Evered, J. F., C. B. Archambeau and E. Crawford, An evaluation of seismic decoupling and underground nuclear test monitoring using high frequency seismic data, *Rev. Geophys.*, **24**, 143-215, 1986.
- Evered, J. F., Lies that stopped a test ban, *Bull. Atomic Sci.*, **44**, 33-44.
- Feverson, H. A., C. E. Phares, and F. Von Hippel, A low-threshold test ban is feasible, *Science*, **238**, 455-458, October 23, 1987.
- Ferguson, J. F., Body-wave magnitude variations at Yucca Flat, Nevada, *Bull. Seismol. Soc. Am.*, **78**, 863-872, 1988.
- Fetter, S., *Towards a Comprehensive Test Ban*, Balingier Publishing Company, 1988.
- Findlay, T., *Nuclear Deterrence: The Peaceful Nuclear Explosion Fiasco*, Brassey's Australia, Portmange Press, 1990.
- Fisk, M. D. and G. D. McCarter, The plane-wave method for seismic wave and seismic discrimination, Geophysics Laboratory Technical Report, GL-TR-89-0330, 63 pp., 1989.
- Frankel, A., A. McGarr, J. Bicknell, J. Mori, L. Sceder, and E.

Crosswell, R. F., Attenuation of high-frequency shear waves in the crust: Measurements from New York State, South Africa, and Southern California, *J. Geophys. Res.*, **95**, 17441-17457, 1990.

Probst, C. M., A. Radicati, and K. D. Apperloo, Note concerning possible mechanisms for non-double-couple earthquake sources, *Geophys. Res. Lett.*, **16**, 523-524, 1989.

Probst, C., Note concerning non-double-couple source components from the long surface of revolution, *J. Geophys. Res.*, **95**, 6861-6864, 1990.

Reay, R. R., Nevada Test Site's dirty little secret, *Bull. Atomic Sci.*, **45**, 35-38, 1989.

Reay, R. R., Variations in broadband seismic noise at RUSTDA stations in the USSR with implications for event detection, *Bull. Seismol. Soc. Am.*, **80B**, 2072-2088, 1990.

GLDARPA, Papers Presented at the 12th Annual DARPA/AGL Seismic Research Symposium, Geophysics Laboratory, Hanscom AFB, MASS, 18-20 Sept 1990.

Reiss, L. A. and J. A. Rial, Blast wave effects on decoupling by asymmetric cavities, *Geophys. J. Int.*, **91**, 229-239, 1987.

Roberts, J. and D. Cox, *Nuclear Weapons Test: Prohibition or Limitation?*, Oxford University Press, 1988.

Supin, I. N. and K. L. McLaughlin, Stress and frequency-dependent attenuation in salt based on Salomon and Sterling near-field recordings, *Bull. Seismol. Soc. Am.*, **79**, 1111-1121, 1989.

Supin, I. N. and R. R. Bradford, A study of P waves from Nevada Test Site explosions: Near-source information from teleseismic observations, *Bull. Seismol. Soc. Am.*, **77**, 1041-1054, 1987.

Supin, I. N., C. S. Lysons, and R. A. Wagner, Broadband f-t analysis of array data to identify sources of local scattering, *Geophys. Res. Lett.*, **17**, 183-186, 1990.

Supin, I. N., C. S. Lysons, T. W. McElfresh and R. A. Wagner, F-t analysis of NORESS array and near-source data to identify sources of near-receiver and near-source scattering, *Bull. Seismol. Soc. Am.*, **80B**, 2227-2241, 1990.

Haas, M. R., The case against a quietest test ban, *Issues in Science and Technology*, Vol. VII, Spring 1987, 95-100.

Hauser, R. A., H. Bungum, and A. Abakar, Three months after large earthquakes offshore Norway, *Terra Nova*, **3**, 284, 1990.

Hansen, R. A., F. Ringdal and P. G. Richards, The stability of RMS L_2 measurements and their potential for accurate estimation of the yields of Soviet underground nuclear explosions, *Bull. Seismol. Soc. Am.*, **80B**, 2106-2126, 1990.

Harris, D. B., Comparison of direct estimation performance of high-frequency seismic arrays and three-component stations, *Bull. Seismol. Soc. Am.*, **80B**, 1951-1968, 1990.

Harvey, D. J., A spectral method for computing complete synthetic seismograms, Air Force Geophysics Laboratory Technical Report, AFGL-TR-87-0238, 304 pp., 1987.

Hewler, P. G., R. C. Hansen, D. A. Thurman, and W. L. Nicholson, Application of general linear models to event yield estimation, Pacific Northwest Laboratories Report, PNL-CC-1801 171, 1988.

Hedra, M. A., H. J. B. Minister, and J. A. Orcutt, The time-frequency characteristics of quarry blasts and calibration explosions recorded in Kazakhstan, USSR, *Geophys. J. Int.*, **92**, 109-121, 1989.

Hedra, M. A., H. J. B. Minister, and J. A. Orcutt, An automatic method to discriminate between earthquakes and quarry blasts, *Bull. Seismol. Soc. Am.*, **80B**, 2143-2160, 1990.

Hough, S. E., J. G. Anderson and H. J. Patton, Attenuation in Western Nevada: Preliminary results from earthquake and explosion sources, *Geophys. Res. Lett.*, **16**, 207-210, 1989.

Jib, R. S., and R. H. Shumway, Iterative network magnitude estimation and uncertainty assessment with noisy and clipped data, *Bull. Seismol. Soc. Am.*, **79**, 1122-1141, 1989.

Johnson, L. R., Source characteristics of two underground nuclear explosions, *Geophys. J.*, **95**, 15-30, 1988.

Kafra, A. L. and E. C. Reber, Dispersion of R_2 waves in the southeastern Mass: Evidence for lateral anisotropy in the shallow crust, *Bull. Seismol. Soc. Am.*, **77**, 925-931, 1987.

Kafra, A. L., R_2 as a depth discriminator for earthquakes and explosions: A case study in New England, *Bull. Seismol. Soc. Am.*, **80**, 373-394, 1990.

King, D. S., B. E. Freeman, D. D. Ebers, and J. D. Johnson, The effective yield of a nuclear explosion in a small cavity in geologic material: Enhanced coupling revealed, *J. Geophys. Res.*, **94**, 12375-12383, 1989.

Lamb, F. K., Monitoring yields of underground tests using hydrodynamic methods, in *Nuclear Arms Technologies in the 1990's*, AIP Conf. Proc., **73**, D. Schroeder and D. Halpernstein, Eds. New York: Amer. Inst. Phys., 1988, 109-148.

Lemo, J., Software routines for nuclear tests, *New Scientist*, **119**, 35, August 23 1988.

Lay, T. and J. L. Wele, Analysis of near-source contributions to early P-wave coda for underground explosions. I. Waveform complexity, *Bull. Seismol. Soc. Am.*, **77**, 1017-1040, 1987.

Lay, T., Analysis of near-source contributions to early P-wave coda for underground explosions II. Frequency dependence, *Bull. Seismol. Soc. Am.*, **77**, 1252-1273, 1987.

Lay, T., Analysis of near-source contributions to early P-wave coda for underground explosions. III. Inversion for isotropic scatterers, *Bull. Seismol. Soc. Am.*, **77**, 1767-1783, 1987.

Leonard, M. A. and L. R. Johnson, Velocity structure of Silet Canyon Caldera, Nevada Test Site, *Bull. Seismol. Soc. Am.*, **77**, 597-613, 1987.

Lewis, J. W. and X. Liu, *China Builds the Bomb*, Stanford University Press, 1988.

Lawrence, J. F. and J. M. McPheeters, Proceedings of the Twelfth Annual DARPA/AGL Seismic Research Symposium, Geophysics Laboratory, GL-TR-90-0210, Special Reports, No. 21, 390 pp., 1990.

Lysons, C. S. and T. Lay, Effects of lateral velocity heterogeneity under the Nevada Test Site on short-period P wave spectra, data and travel times, *Phys. Earth Planet. Inter.*, **112**, 245-257, 1990.

Lysons, C. S. and T. Lay, Inversion of P coda for isotropic scatterers at the Yucca Flat Test Site, *Bull. Seismol. Soc. Am.*, **79**, 790-804, 1989.

Lysons, C. S. and T. Lay, Observations of teleseismic P wave coda for underground explosions, *Phys. Earth Planet. Inter.*, **123**, 231-249, 1988.

Margolis, N. H., Ahmad, and E. Chast, Seismic event detection and source location using single-station (three-component) data, *Bull. Seismol. Soc. Am.*, **77**, 958-971, 1987.

Maoddi, B. and M. N. Toksoz, Computation of complete waveforms in general anisotropic media-results from an explosion source in a 78 anisotropic medium, *Geophys. J. Int.*, **93**, 33-45, 1990.

Maozoug, M. and A. Anderson, Soviets put on impressive show, *Nature*, **335**, 291, Sept 22 1988.

McCreery, C. S., Yield estimation from spectral amplitudes of direct P and P coda recorded by the wide area deep ocean hydrophone array, *Bull. Seismol. Soc. Am.*, **77**, 1748-1766, 1987.

McGarr, A., J. Bicknell, E. Senguba and R. W. E. Green, Analysis of exceptionally large tremors in a two gold mining districts of South Africa, *Phys. Earth Planet. Inter.*, **128**, 295-307, 1989.

McLaughlin, K. L. and R. S. Jib, Scattering from near-source topography: Teleseismic observations and numerical simulations, *Bull. Seismol. Soc. Am.*, **73**, 1399-1414, 1983.

McLaughlin, K. L., A. C. Lewis, Z. A. Dor, and M. E. Marshall, Teleseismic spectral and Temporal M_0 and T_0 estimates for four French explosions at the Souleuvre Sabart, *Bull. Seismol. Soc. Am.*, **78**, 1580-1596, 1988.

McLaughlin, K. L., I. M. Anderson, and A. C. Lewis, Effects of local geologic structure on Yucca Flat, Nevada Test Site, Explosion Waveforms: Two-dimensional linear time-difference simulations, *Bull. Seismol. Soc. Am.*, **77**, 1211-1222, 1987.

McLaughlin, K. L., Maximum-likelihood event magnitude estimation with bootstrapping for uncertainty estimation, *Bull. Seismol. Soc. Am.*, **80B**, 855-862, 1988.

McLaughlin, K. L., R. H. Shumway, and T. W. McElfresh, Determination of event magnitudes with corrected data and censoring: A maximum likelihood approach, *Geophys. J.*, **95**, 37-44, 1988.

McLaughlin, K. L., T. G. Barber, S. M. Day, B. Shuster, and J. L. Stevens, Effects of depth of burial and isotropic strain release on regional and teleseismic explosion waveforms, Air Force Geophysics Laboratory Technical Report, AFGL-TR-88-0314, 116 pp., 1988.

Miller, G. H., P. S. Brown and M. D. Novotny, Facing nuclear reality, *Science*, **233**, 455, October 23 1987.

Miller, S. A. and A. L. Flores, Laboratory particle velocity experiments on rock from a USSR underground nuclear test site, Geophysics Laboratory Technical Report, GL-TR-90-0053, 31 pp., 1990.

Mitchell, B. J. and H. J. H. Hing, Effect of low Q sediments and crustal Q on L_2 attenuation in the United States, *Bull. Seismol. Soc. Am.*, **77**, 1197-1210, 1987.

Moss, W. C., A method to estimate the yield of an underground nuclear explosion, *J. of App. Phys.*, **63**, 4771-4773, 1988.

Murphy, J. R. and H. K. Shah, An analysis of the effects of site geology on the characteristics of near-field Rayleigh waves, *Bull. Seismol. Soc. Am.*, **78**, 64-82, 1988.

Murphy, J. R., B. W. Barber, and A. O'Donnell, Network-averaged teleseismic P wave spectra for underground explosions, Part I. Definitions and examples, *Bull. Seismol. Soc. Am.*, **79**, 141-155, 1989.

Murphy, J. R., J. L. Stevens, and N. Riser, High frequency seismic source characteristics of cavity decoupled underground nuclear explosions, Air Force Geophysics Laboratory Technical Report, AFGL-TR-88-0130, 51 pp., 1987.

Murphy, J. R., Network-averaged teleseismic P-wave spectra for underground explosions, Part II. Source characteristics of Pabusa Mesa explosions, *Bull. Seismol. Soc. Am.*, **79**, 156-171, 1989.

Nakazawa, K. K. and S. P. Jee, Summary of corrections needed for accurate backscattered maximum using regional seismic test network data, *Bull. Seismol. Soc. Am.*, **78**, 1830-1833, 1988.

Nelson, G. D. and J. E. Vidale, Earthquake locations by 3-D finite difference travel times, *Bull. Seismol. Soc. Am.*, **80**, 395-410, 1990.

News, O. W., L_2 magnitudes of Deyles, East Kazakhstan underground explosions, *Bull. Seismol. Soc. Am.*, **77**, 679-681, 1987.

News, O. W., Magnitudes and yield estimates for underground Norway Zvezda nuclear explosions, *Bull. Seismol. Soc. Am.*, **73**, 873-884, 1983.

Patton, H. J. and S. R. Taylor, editors, Proceedings of the DOE/LLNL Symposium on Explosion-Source Phenomenology, CONF-900398, Lawrence Livermore National Laboratory, 12 May 1989.

Patton, H. J., Application of Nishi's method to estimate yield of Nevada Test Site explosions recorded on Lawrence Livermore National Laboratory's Digital Seismic System, *Bull. Seismol. Soc. Am.*, **79**, 1739-1774, 1989.

Patton, H. J., Application of Nishi's method to explosions from regional wave field observations: 3000 and higher mode surface waves, *Phys. Earth Planet. Inter.*, **113**, 1133-1157, 1988.

Patton, H. J., Near-source L_2 and L_3 observed strong ground motion at Pabusa Mesa, *Bull. Seismol. Soc. Am.*, **80**, 1326-1345, 1990.

Porfirov, P. W., W. J. Bin, and T. G. Egan, Test buoyancy verification with regional seismic review, *Bull. Seismol. Soc. Am.*, **77**, Part 1, 10-32.

Prokhorov, K. F., G. Zamboni, and A. L. Chumak, Crustal structure in Eastern Kazakhstan from teleseismic receiver functions, *Geophys. Res. Lett.*, **15**, 613-616, 1988.

Presley, K. F., W. R. Asper, T. Marinov, Regional seismic recordings of the Soviet Union explosion of the Joint Verification Experiment, *Geophys. Res. Lett.*, **13**, 179-187, 1986.

Regan, J. and D. G. Harbater, Numerical modeling of SH L_2 waves in and near circumaxial margins, *Geophys. Res. Lett.*, **16**, 107-130, 1989.

Regan, J. and D. G. Harbater, Seismic reproduction (inverted coupling) Synthetic SH mode wave seismograms for non-homogeneous media, *Geophys. Res. Lett.*, **15**, 429-444, 1988.

Reinke, R. E. and B. W. Smith, Stochastic seismic effects on near-field ground motion at altitudes, *Bull. Seismol. Soc. Am.*, **78**, 1037-1058, 1988.

Richards, P. G. and A. Lamb, Toward a new test ban regime, *Issues in Science and Technology*, Vol. III, Spring 1987, 101-106.

Richards, P. G. and J. Mc, Weapons testing and nuclear weapons proliferation: Prospects for the future, in *Science and Security: The Future of Arms Control*, Colloquium Proceedings, December 4-5, 1986, 189-218, AAAS Publication No. 87-17, 1987.

Richards, Paul G., Steps toward a new test ban, chapter 4 in *Verification and Compliance: A Problem-Solving Approach*, edited by M. Krepon and M. Underger, Macmillan (U.K.) and Ballinger (U.S.A.), 73-91, 1988.

Richards, P. G., Seismic constraints for verifying test ban treaties, in *Nuclear Arms Technologies in the 1990's*, AIP Conf. Proc., **73**, D. Schroeder and D. Halpernstein, Eds. New York: Amer. Inst. Phys., 1988, 54-108.

Richards, P. G., Seismic monitoring of nuclear explosions, in *Encyclopedia of Geophysics*, ed. D. E. James, 1071-1089, Van Nostrand Reinhold, 1989.

Richards, P. G. and J. Zeman, Seismic determination of nuclear explosions, *Ann. Rev. Earth Planet. Sci.*, **18**, 1990, 257-286.

Richards, P. G., Progress in seismic verification of test ban treaties, *IEEE Technology and Society Magazine*, **3**, 44-52, Dec 90.

Robinson, C. Paul, The past verification experiments: A unique approach to detecting verification agreements, *Disarmament*, **12**, 92-98, 1989.

Rodgers, P. W., S. R. Taylor, E. K. Nakazawa, System and test case in the regional seismic test network from 0.1 to 20 Hz, *Bull. Seismol. Soc. Am.*, **77**, 663-678, 1987.

Sanzos, C. G., Seismic pulse broadening associated with fracture damage caused by explosions in crystalline rock, Geophysics Laboratory Technical Report, GL-TR-89-0161, 85 pp., 1989.

Sarason, T. J., Jr., J. W. Green, P_0 attenuation for a spherically symmetric earth model, *Geophys. Res. Lett.*, **17**, 1141-1144, 1990.

Sarason, T. J., Jr. and J. A. Orcutt, Synthetic P_0 and S_0 phases and frequency dependence of Q of constant topography, *J. Geophys. Res.*, **92**, 3541-3548, 1987.

Sarason, T. J., Jr., and S. R. Brant, Seismic detection capability at NORESS and implications for the detection threshold of a hypothetical network in the Soviet Union, *J. Geophys. Res.*, **94**, 10397-10414, 1989.

Sarason, T. J., Jr., S. R. Brant, and T. C. Probst, Simultaneous inversion of regional wave spectra for attenuation and seismic moment in Kazakhstan, *J. Geophys. Res.*, **93**, 2019-2035, 1988.

Sarason, T. J., Jr., Frequency-dependent attenuation in Eastern Kazakhstan and implications for seismic detection thresholds in the Soviet Union, *Bull. Seismol. Soc. Am.*, **80B**, 2089-2105, 1990.

Shamber, P. M. and J. A. Orcutt, Surface and near-surface effects on seismic waves: Theory and borehole accelerometer results, *Bull. Seismol. Soc. Am.*, **77**, 1168-1196, 1987.

Smith, A. T., High-frequency seismic observations and models of chemical explosion mechanisms for the oceanographic of ripple-lined mining sites, *Bull. Seismol. Soc. Am.*, **79**, 1089-1110, 1989.

Smith, A. T., Seismic air witness at high frequencies: A case study, Lawrence Livermore National Laboratory Report, UCID-21047, 160 pp., 1987.

Smith, R. J., U.S. Soviets share seismic points, *Science*, **215**, 807-808, 25 August 1988.

Stevens, J. L., J. R. Murphy, and N. Riser, Nonlinear time difference simulations of cavity decoupled explosions in salt and ruff, Geophysics Laboratory Technical Report, GL-TR-89-0192, 49 pp., 1989.

Strump, B. W. and R. E. Reine, 1987, Experimental seismol-

STUMP: NUCLEAR EXPLOSION SEISMOLOGY

- ogy: In situ source experiments. *Bull. Seismol. Soc. Am.* **77**, 1295-1311, 1987.
- Stump, B. W. and R. E. Rabin, Experimental confirmation of source parameters from small-scale explosions. *Bull. Seismol. Soc. Am.* **73**, 1059-1073, 1983.
- Stump, B. W., Mathematical representations and physical interpretation of a combined chemical explosion at alluvium. *Bull. Seismol. Soc. Am.* **77**, 1312-1325, 1987.
- Suzuki-Hirota, A., and T. C. Becht, Spectral characteristics of regional phases recorded at NORESS. *Bull. Seismol. Soc. Am.* **73**, 708-725, 1983.
- Suzuki-Hirota, A., Estimating azimuth and slowness from three-component and array stations. *Bull. Seismol. Soc. Am.* **80B**, 1987-1998, 1990.
- Sweet, W., U.S. - Soviet research in arms control. *Physics Today*, **42**, 31.
- Swath, H. S. and J. B. Walsh, The theory and prototype development of a stress-monitoring system. *Bull. Seismol. Soc. Am.* **80**, 197-208, 1990.
- Sykes, L. R. and D. M. Davis, The yields of Soviet strategic weapons. *Scientific American*, **246**, 39-37, 1987.
- Sykes, L. R. and G. Ekstrom, Comparison of seismic and hydrodynamic yield determinations for the Soviet joint ventilation experiments of 1986. *Proc. Natl. Acad. Sci.* **86**, 3456-3460, May 1990.
- Taylor, S. R. and G. E. Randall, The effects of spill on regional seismograms. *Geophys. Res. Lett.* **16**, 211-214, 1989.
- Taylor, S. R. and J. T. Ramon, Near-source effects on regional seismograms: An analysis of the NTS explosions PERA and QUESO. Lawrence Livermore National Laboratory Report, UCRL-101704, 32 pp., 1989.
- Taylor, S. R. and M. D. Deary, An analysis of spectral differences between NTS and Shagan River nuclear explosions. Lawrence Livermore National Laboratory Report, UCRL-102276, 29 pp., 1990.
- Taylor, S. R., M. D. Deary, E. S. Vergoo, and R. E. Glasser, Regional discrimination between NTS explosions and Western U. S. earthquakes. *Bull. Seismol. Soc. Am.* **79**, 1142-1174, 1989.
- Taylor, S. R., M. W. Sherman, and M. D. Deary, Spectral discrimination between NTS explosions and Western United States earthquakes at regional distances. *Bull. Seismol. Soc. Am.* **73**, 1543-1579, 1983.
- Thurber, C. H. Green, and J. Berger, Regional seismic event location with a sparse network: Application to Eastern Kazakhstan, USSR. *J. Geophys. Res.* **94**, 17767-17780, 1989.
- Truman, J., International monitoring for Peace. *Issues in Science and Technology* Vol. IV, Summer 1988, 53-54.
- Trull, D. M. and L. R. Johnson, Epicentral confidence regions of nuclear test events at teleseismic distances. *Bull. Seismol. Soc. Am.* **77**, 2212-2217, 1987.
- Vasco, D. W. and L. R. Johnson, Inversion of waveforms for extreme source models with an application to the isotropic moment tensor component. *Geophys. J.* **97**, 1-18, 1989.
- Vasco, D. W., Deriving source-time functions using principal component analysis. *Bull. Seismol. Soc. Am.* **79**, 711-730, 1989.
- Vasco, D. W., Moment-tensor invariants searching for non-double couple earthquakes. *Bull. Seismol. Soc. Am.* **80**, 354-371, 1990.
- Vasco, D. W., Seismic source representation in orthogonal functions. *Geophys. J. Int.* **102**, 531-535.
- Vergoo, E. S. and R. W. Messing, Yield estimation using regional $m_b(P_n)$. *Bull. Seismol. Soc. Am.* **80**, 656-674.
- Vogfjord, K. S. and C. A. Langston, Analysis of regional events recorded at NORESS. *Bull. Seismol. Soc. Am.* **80B**, 2016-2031, 1990.
- von Hippel, F., Arms control physics: The new Soviet connection. *Physics Today*, **42**, 39-46.
- Walck, M. C., P-wave path attenuation from Siberia to Norway. *Bull. Seismol. Soc. Am.* **79**, 910-913, 1989.
- Walck, M. C., Spectral estimates of teleseismic P-wave attenuation to 15 Hz. *Bull. Seismol. Soc. Am.* **73**, 726-740, 1983.
- Walton, T. C., The effects of structure and source complexity on waveforms: Crustal structure of Tibet and the recovery of complex seismic sources. Geophysics Laboratory Technical Report, GL-TR-89-0259, 181 pp., 1989.
- Walter, W. R., J. Bruce, R. F. Priestley, J. Fletcher, Observations of high-frequency P wave earthquake and explosion spectra compared with m_b and M_s source models. *J. Geophys. Res.* **93**, 6318-6324, 1988.
- Williams, D. J. and W. J. Arabasz, Mining-related and tectonic seismicity in the coal mountain area Wasatch Plateau, Utah, USA. *Phys. Earth Planet. Inter.* **123**, 344-368, 1989.
- Wong, I. G., J. R. Humphrey, J. A. Adams and W. J. Silva, Observations of mine seismicity in the Eastern Wasatch Plateau, Utah, USA: A possible case of implosion failure. *Phys. Earth Planet. Inter.* **123**, 369-405, 1989.
- Xie, J. and B. J. Mitchell, Attenuation of multiple α surface waves in the Basin and Range province, part I: L_3 and L_4 coda. *Geophys. J. Int.* **102**, 121-137, 1990.
- Zeng, Y., T. Teng, and K. Aki, Surface wave ray tracing and M_s Yield determination in a laterally heterogeneous earth. Air Force Geophysics Laboratory Technical Report, AFGL-TR-89-0063, 62 pp., 1989.

Brian W. Stump, Southern Methodist University, Department of Geological Sciences, Dallas, Texas, 75275-0395.

(Received December 20, 1990;
revised February 27, 1990;
accepted March 1, 1991.)

FREE-FIELD AND FREE SURFACE GROUND MOTIONS FROM NUCLEAR EXPLOSIONS, THEIR SPATIAL VARIATIONS,
AND THE CONSTRAINT OF PHYSICAL SOURCE MECHANISMS

Brian W. Stump

Department of Geological Sciences, Southern Methodist University, Dallas, Texas 75275

Robert E. Reinke

Geodynamics Section, Phillips Laboratory, Kirtland Air Force Base, Albuquerque, New Mexico 87117-6008

Abstract. Near-source waveforms from explosions detonated at the Nevada Test Site (NTS) are reviewed. Data are separated into four types: free-field strong (FFS), representative of the region where material strength dominates; free-field weak (FFV), the region where weakly nonlinear properties and transition from plastic to elastic response are important; free surface spall (FSS), where material tensile strength is important; and free surface elastic (FSE), where most seismic observations begin. Data from Pahute Mesa (FSS & FSE), Rainier Mesa (FFW & FSE), and Yucca Flats (FSS & FSE) are specifically considered. Each of the data types is explored as to its resolution of important physical processes in the source region and resultant seismic radiation. Specific attention is paid to the variability of these motions. Single and scaled multiple explosion peak accelerations from Pahute Mesa and Yucca Flats show as much as a factor of 6-8 scatter with range. Large scatter in single explosion data suggests a propagation path effect while large amplitudes for a scaled explosion from below the water table supports a coupling difference between explosions. Data scatter decreases at long periods as exemplified by long period moments which have a multiplicative error of 1.49 for Pahute Mesa. Numerical models of body and surface wave propagation in realistic one-dimensional Pahute Mesa models indicate strong effects of velocity structure near the shot point for body waves traveling to the free surface at short offset (<2 depths of burial). Synthetic waveform difference between a site specific model and an average model decrease with increasing source-receiver offset or increasing period where near-source surface waves are emphasized. Comparison of free-field and free surface data from the same explosion at Rainier Mesa supports significantly reduced scatter in free-field data. Removal of the weathered layer as a dominant effect in the free-field data can explain the reduced scatter. Analysis of data spanning the transition from FSS to FSE regions indicates that explosion geometry plays a strong role in the decay of free surface data. These data and extended reflectivity calculations appropriate for Pahute Mesa predict that strong spall zone motions come from a region out to a free surface range just beyond one depth of burial for explosions with standard scaled depths of burial.

Introduction

A physically based understanding of the nuclear explosion source function is necessary for improving discrimination between earthquakes and explosions as well as refining yield estimates for explosions. The

physical model allows prediction and extrapolation to new environments where experimental data may not exist (Murphy, 1977). It provides correlation between data observed at different ranges such as near-source, regional, and teleseismic (Taylor and Rambo, 1990). An empirical approach to problems of discrimination and yield determination may be adequate for limited conditions, but is not acceptable for the wide range of environments and distances that exist on the earth. The focus of this study is near-source data sets and their utility in physical source model resolution (Stump and Johnson, 1984; Johnson, 1988). Emphasis will be placed on the successes and failures in separating source and propagation path effects. Near-source is loosely defined for this study as source-receiver separations of hundreds of meters to tens of kilometers.

Explosions, unlike natural events, can be controlled. Time of occurrence and location are determined by the experimenter, which allows for design of ground motion experiments whose expressed purpose is the characterization of seismic source properties (Stump and Reinke, 1987). Not only can the elastic field be determined, but development of this field from the near-source region where the material is nonlinear can be documented. Quantification of the motion field in this environment allows the linkage of seismic observations to measurements of pressure, stress, and shock front propagation in the hydrodynamic, strongly nonlinear, and weakly nonlinear regions. Each motion environment is related to the yield of the explosion and material in which the explosion is detonated. Comparison of yield estimates made from data within each region is dependent upon a physical understanding of appropriate cumulative physical processes.

Seismic discrimination and yield determination studies rely upon regional and teleseismic data since most monitoring scenarios are limited to such data (Bache, 1982; Pomeroy et al., 1982; U.S. Congress, 1988). Physical source constraints provided by near-source data can be used as consistency checks against models developed from regional and teleseismic data where propagation path effects may be more severe (Taylor and Rambo, 1990).

Near-source data sets discussed in this paper are from the Nevada Test Site (NTS) where materials such as loosely consolidated alluvium, volcanic tuffs and rhyolites, granites, and other sedimentary rocks can be found. Particular attention will be paid to the documentation of free surface and subsurface ground motions recorded from a variety of explosions at NTS. These motions will be used to constrain the equivalent elastic source function and size of the explosion. Special attention will be paid to the spatial variability of such motions and resulting errors in source strength estimates.

This paper begins with a division of the near-source motion fields around the explosion followed by a review of previous work. Observational data sets from Pahute Mesa, Yucca Flats, and Rainier Mesa are introduced and explored. Wavefield modeling and source inversion are

Explosion Source Phenomenology
Geophysical Monograph 65
Copyright 1991 American Geophysical Union

The U.S. Government is authorized to reproduce and sell this report. Permission for further reproduction by others must be obtained from the copyright owner.



FREE-FIELD AND FREE SURFACE GROUND MOTIONS

presented as the observational data are used to constrain physical processes around the explosion. Implications and conclusions are given as developed from data analysis.

Near-Source Waves

Ground motion around nuclear explosions can be observed at the free surface where instrumentation is relatively inexpensive or at depth (free-field) where the effects of the free surface are a minimum. Both free-field (FF) and free surface (FS) data will be discussed in this paper.

For the purposes of our discussion the motion field around the explosion is divided into five regions (Rodean, 1971, 1981). The strongest motions from contained explosions are found in the free-field hydrodynamic (FFH) region where shock waves propagate. The velocity of this shock front is used to make yield estimates utilizing the CORRTEX methodology (King et al., 1989). Moving farther from the explosion one encounters a region of strongly nonlinear motions where material strength dominates the response. This region is given the nomenclature FFS (free-field strong). Pressure and stress measurements are typically used to characterize this region. A weakly nonlinear region is encountered as the motion field decays further. More subtle material properties such as the transition from plastic to elastic response become important. For free-field data we designate this region as FFW with the W for weak.

As the motion field interacts with the free surface, tensile failure of near-surface layers can result in ballistic motions or spall. This motion environment is designated as FSS (free surface spall). The spall process extends to depth as the reflected tensile wave propagates back into the material. The cost of fielding subsurface gauges is often prohibitive, so most spall data has been taken at the free surface (Patton, 1990). As waves propagate further, they transition to purely elastic/anelastic motions which are designated as free-surface elastic (FSE).

This paper will document motions within the FFW, FSS, and FSE regions from NTS explosions. Each of the motion fields will be illustrated with specific examples from Pahute Mesa (FSS & FSE), Rainier Mesa (FFW & FSE), and Yucca Flats (FSS & FSE).

Previous Work

Free-field and free surface ground motions and stresses have been measured since the inception of underground testing. Free-field motions (FFS & FFW) have been used to assess the importance of material properties on strong ground motions. Such assessments are particularly important when large engineering structures are placed close to the explosion. The tunnel shots in Rainier Mesa are an example of this type of test. Measurements are often associated with these structures which might bias free-field motions. Some of the earliest estimates of free-field decay rates in alluvium, tuff, granite, and salt were summarized by Wheeler and Preston (1968). Perret and Bass (1975) extended the data sets to include nuclear detonations in dry alluvium, dry tuff, wet tuff, and hard rock (granite, salt, dolomite, and other sedimentary rocks). These studies focused upon attenuation of waveforms with slant range scaled by the cube root of explosive yield. Germain (1986) has reworked the Perret and Bass analysis including more recent data.

Application of free-field data to calculation of seismic source functions in the form of reduced displacement potentials for a number of materials was made by Werth and Herbst (1963) followed by the analytic modeling of Haskell (1967). Murphy and Bennett (1979) review free-field seismic data for alluvium, tuff, dolomite, sandstone-shale, and interbedded lava flows.

Near-source, free surface ground motion gauges have typically been placed at ranges within 2 depths of burial (DOB) where recording equipment is located. The primary purpose of these gages is in assessing equipment survivability. These gages are usually within the spall zone

(Patton, 1990) and are useful in characterizing motions designated as FSS. Free-field decay rates are not strictly applicable since these motions involve interaction with the free surface. Bernreuter et al. (1970) developed a set of decay curves for free surface data. Patton (1990) has discussed the utilization of these spall waveforms and their decay rates in constraining the secondary seismic source from spall.

A second set of common free surface data involves measurements designed to quantify effects on populated areas surrounding NTS (Hays, 1974; O'Brien and Lahoud, 1982). These observations and models involve propagation distances of tens to hundreds of kilometers. A final, small data set exists for free surface ground motion from just outside the spall zone to tens of kilometers (Stump and Johnson, 1984; Johnson, 1988). These data sets have been used to constrain the equivalent seismic source (Helmberger and Hadley, 1981). Such measurements are less expensive and easier to field than free-field measurements.

This work is designed to compare and contrast the FFW, FSS, and FFE data sets for purposes of constraining different parts of the explosive source function. Data sets, which have been separately studied in the past, are investigated as an integrated set. Each contains different information; for example FSS is dominated by interaction of the upgoing stress wave with the free surface. An important part of this discussion is the identification of the variability of each data set. The goal is to quantify how each different type of near-source data constrains the seismic source function.

Observational Data

Data from three areas of NTS are reviewed including Pahute Mesa, Yucca Flats, and Rainier Mesa. In an attempt to emphasize the different physical processes leading to these motions the data is divided into that represented by weakly nonlinear motions in the free-field (FFW), spall motions at the free surface (FSS) and elastic motions from the free surface (FSE).

Pahute Mesa (FSS & FSE)

Los Alamos National Laboratory (LANL) routinely makes three-component, free surface digital acceleration measurements within the spall zone of contained nuclear explosions. A typical array of accelerometers for the AMARILLO explosion with accompanying acceleration records is given in Figure 1. Spall zone accelerograms are characterized by an initial compressive wave (positive acceleration), $-1 g$ dwell during free-fall (ballistic motion) following tensile failure, and a large spall closure signal (positive acceleration). Dwell times for multiple kiloton explosions are near 1 s as illustrated by the AMARILLO ground zero (GZ) record with a dwell time of 0.65 s. The spatial effects of spall are illustrated in Figure 1 where acceleration records at free surface ranges of 15 m, 258 m, and 640 m are reproduced. Spall initiation time, identified by the start of $-1 g$ dwell, increases with range while spall rejoin, designated by the impulsive rejoin signal, decreases with range. Dwell time decreases from 0.65 to 0.25 s over the observational range. As a result of the temporal and spatial finiteness of the spall secondary source, its equivalent source function is peaked in the frequency domain (Day et al., 1983; Stump, 1985).

Free surface, peak velocity measurements from FSS are summarized in Figure 2 where they are plotted against scaled free surface range ($r = R/kt^{1/3}$). The data are derived through numerical integration from the original accelerograms. Six nuclear explosions (Table 1) from Pahute Mesa are represented in the plot. Data such as that displayed in Figure 2 can be plotted against free surface range as done in the figure or slant range as suggested by Perret and Bass (1975) or Patton (1990). If propagation path effects dominate the motion field, then slant range is the more appropriate variable. If free surface interaction is more important, then free surface range may be more appropriate. As source-receiver range

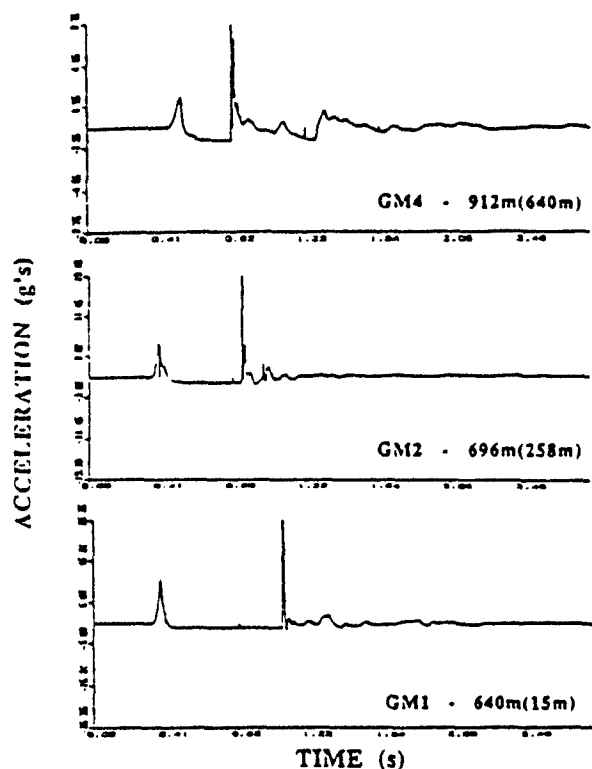


Fig. 1. Three, free-surface vertical acceleration records from the nuclear explosion AMARILLO. The slant ranges (GM4-912m, GM2-696m, GM1-640m) and free surface ranges from ground zero (GM4-15m, GM2-258m, GM6-640m) are given. The horizontal time scale is 2.87 s. The initial compressive wave reaches each successive station at greater time while spall rejoin, indicated by the impulsive secondary signal, occurs at earlier times for the farther stations. The surface geometry of the accelerometer array is given at the bottom of the figure.

increases relative to source depth, the two distance measures converge. The data are displayed as a function of *free surface range* in this case since this form emphasizes the spall zone which commonly extends to 2-3 DOB range ($244-366 \text{ m/kt}^{1/3}$) on the scaled plot. This representation

Table 1. Event Characteristics

Event name	Date	NEIS m/s
BACKBEACH	780411	5.5
SHEEPSHEAD	790926	5.6
NEBBIOLO	820624	5.6
CHANCELLOR	830901	5.4
CYBAR	860717	5.7
AMARILLO	890627	4.9

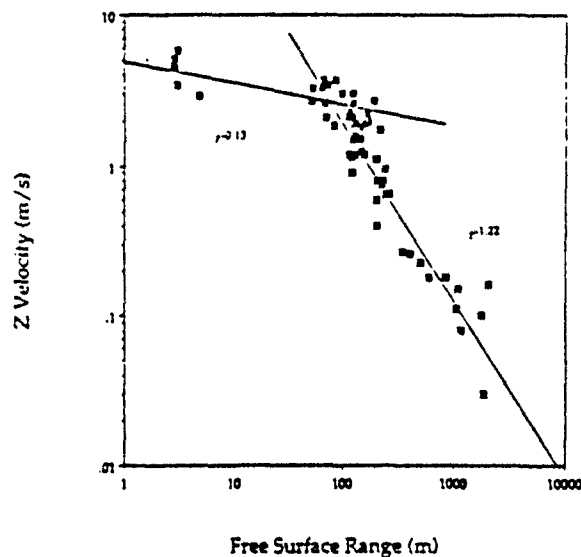


Fig. 2. Peak vertical velocity from the Pahute Mesa spall zone data (Table 1) is plotted against scaled free surface range. The free surface range is scaled by the cube root of the explosion yield while the peak velocity values are unscaled. Power law models were fit to the data for ranges less than and greater than $100 \text{ m/kt}^{1/3}$. This free surface range corresponds to approximately one scaled depth of burial, $122 \text{ m/kt}^{1/3}$, for NTS explosions.

emphasizes the strong impact geometry has on spall zone data. From GZ to a *free surface range* of approximately 1 DOB, velocity (acceleration and displacement also) decays little ($r = -0.13$ for velocity data) followed by a faster decay at farther ranges ($r = -1.22$). This central region with little spatial decay indicates that out to a *free surface range* equal to one DOB there is little change in *slant range*. The implication of such decay patterns is that the central portion of the spall zone will have nearly constant escape velocities or momentum contribution to a *free surface range* equal to 1 DOB. Beyond this range to the edge of the spall zone, motions decay rapidly, thus reducing the spall contribution from this area. A second implication of this decay pattern is that strong variations or asymmetries in the edge of the spall zone found from overhead photography of the process may not be as important in the central region where motions decay little [Walker, 1982]. This velocity data shows scatter of between a factor of 3 and 5 for the explosions represented.

Moving outside the spall zone, a typical FSE array for characterizing a nuclear explosion is given in Figure 3a. The dimension of the array is on the order of 10 km. Careful attention is paid to coverage in both range and azimuth. Most gages are accelerometers although velocity transducers are sometimes used at more distant ranges. Peak vertical accelerations from a single explosion observed at a number of azimuths and ranges are

FREE-FIELD AND FREE SURFACE GROUND MOTIONS

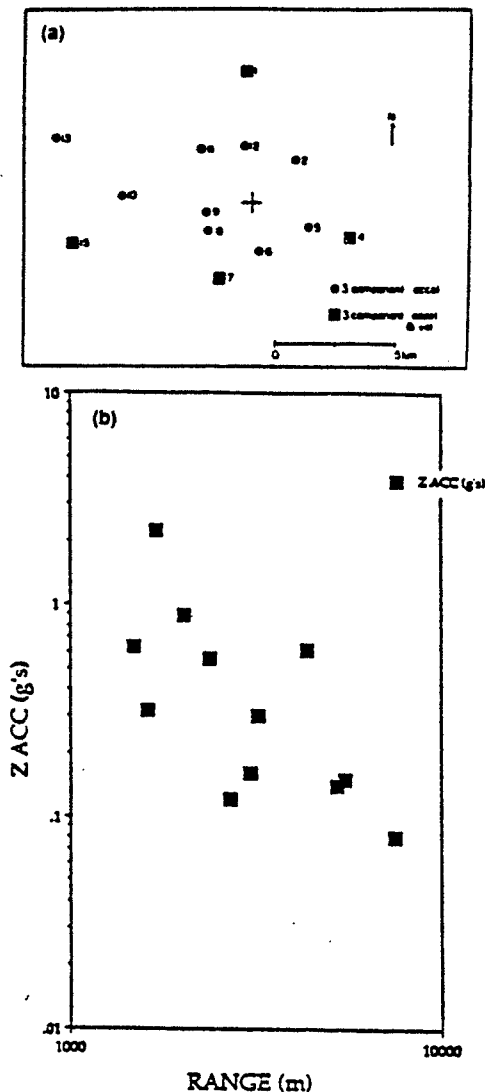


Fig. 3. (a) A typical free surface instrument array for characterization of the explosion source function. The accelerometers are all outside the spill zone (FSE region) and designed to give good azimuthal coverage of the source. (b) Peak vertical accelerations are plotted against free surface range (unscaled) for a single nuclear explosion. The large scatter (6-8) in these observations with range is evident.

given in Figure 3b. Accelerations span over an order of magnitude in amplitude and slightly less than an order of magnitude in range. A distinct amplitude decay with range is observed although it is obscured by a factor of 6-8 scatter in peak accelerations.

The single explosion data can be compared to scaled peak accelerations (FSE) from a number of Pahute Mesa explosions, one of which was detonated below the water table (Figure 4). The same characteristics observed in the single explosion data are replicated in the multiple explosion data set. There is an approximate order of magnitude scatter in peak acceleration data with the shot from below the water table exhibiting

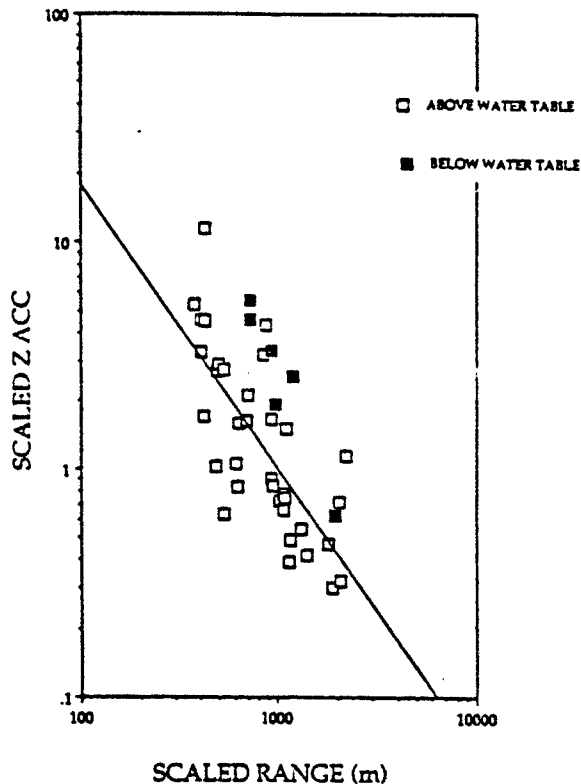


Fig. 4. Peak accelerations from a number of Pahute Mesa explosions are scaled by the cube root of yield and plotted against scaled free surface range. All data is from outside the spill zone (FSE region). A large amount of scatter (6-8) is observed in this data. There is some indication of a coupling effect as the data from an explosion detonated below the water table (solid squares) plots at the upper bounds of the data.

the highest accelerations. The physical mechanism for the scatter in these data could either be different wave propagation effects (depth of burial, proximity to interfaces, different source-receiver structures) or source coupling effects. Large amplitudes for the source below the water table support a coupling effect. On the other hand, large scatter in the single explosion data (Figure 3b) suggests propagation path effects.

Scatter in observational data is frequency dependent. The accelerograms used for the peak amplitude study (Figure 3b) are Fourier transformed and long period spectral estimates are made and converted to moment:

$$M_l = 4\pi\rho R\alpha^2\Omega_0 \quad (1)$$

where ρ is density, R is slant range, α is compressional velocity, and Ω_0 is the long period displacement spectral level. Since the data is from the free surface, a simple factor of two is introduced into the Ω_0 estimate. Problems with this simple interpretation of the free surface data include the inability to separate body and surface waves in these data sets. Isotropic moments interpreted from vertical (Z), radial (R), and transverse (T) data are given in Figure 5 (strictly speaking only Z and R should be used). The scatter in moments from this single explosion is a factor of 2-3, reduced from variations in peak acceleration. The fact that Z, R, and T moments all follow the same spatial pattern argues that the variation

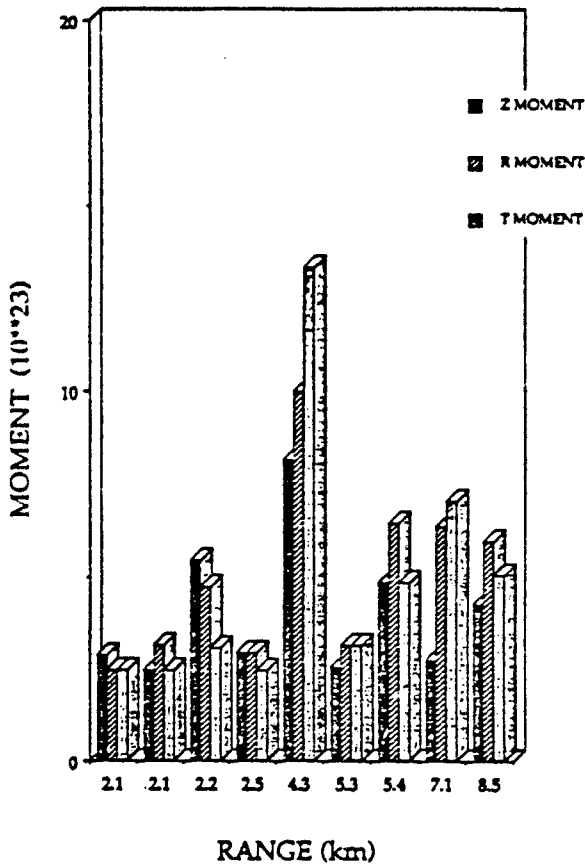


Fig. 5. Seismic moments from the Pahute Mesa nuclear explosion (Fig. 3) were determined from observations at ranges between 2.1 to 8.5 km. Moments were calculated from vertical (Z), radial (R) and transverse (T) observations. The scatter in the moment estimates is a factor of 2-3, reduced from the scatter in peak accelerations given in Figs. 3b and 4.

may be a propagation effect. Similar variations are found for moments estimated from near-source earthquake data (Archuleta et al., 1982; Fletcher et al., 1984). Following the methodology of Archuleta, average log moments and their standard deviations are computed according to:

$$\log(M_c) = \left[\frac{1}{ns} \sum_{i=1}^{ns} \log(M_{oi}) \right] \quad (2)$$

$$\text{std dev}(\log(M_o)) = \left[\left(\frac{1}{ns-1} \sum_{i=1}^{ns} (\log M_{oi} - \log(M_o))^2 \right)^{1/2} \right] \quad (3)$$

The multiplicative error is defined according to:

$$EM_e = \text{antilog}[\text{std dev}(\log(M_o))] \quad (4)$$

The average moment for the vertical data in Figure 6 is 3.8×10^{23} dyne-cm with a multiplicative error of 1.49.

Changes in frequency content with propagation distance for data summarized in Figure 3 are characterized by picking corner frequencies from raw accelerograms. Acceleration spectra are interpreted in terms of a long period rise that is used in the moment estimate, an intermediate frequency band in which acceleration spectra are flat, followed by high-frequency decay (Figure 6). A first corner frequency is chosen at the point of transition from long period rise to the constant level at intermediate frequencies. A second corner frequency is identified at the high-frequency point where the acceleration spectra begin to decay. These two corner frequencies are plotted against source-receiver offset for a single explosion in Figure 6. The first corner frequency changes little with range and is estimated to be 1 Hz. This spectral characteristic is taken to be the source corner frequency which is related to the source elastic radius. The second corner shows a systematic decrease with range indicative of a propagation path effects. Simple frequency independent attenuation operators:

$$e^{-\pi r/Qa} \quad (5)$$

suggest that a Q between 20-30 replicates this decay with range.

These frequency domain measures show less variation than the amplitude information for this particular explosion. The flat acceleration spectrum between the two corner frequencies (Figure 6) argues for a f^{-2} high-frequency source model for this explosion. As source-receiver offset increases, this intermediate high-frequency decay becomes obscured by attenuation effects.

Yucca Flats (FSS & FSE)

Yucca Flats is a valley filled with alluvium at shallow depths underlain by dry and wet tuffs. The basement consists of Paleozoic rocks. A set of FSS data from the COALORA experiment is reproduced in Figure 7. The depth and range of the spall phenomena is constrained with this data. Spall extends in this case to a free surface range of 1 DOB while the depth of the spall zone is estimated to be 1/2 DOB. Spall dwell time increases near GZ as noted for Pahute Mesa data. Spall zone accelerations are used to estimate escape velocities (after integration) of the spalled mass. Spall volume is delineated by the spatial distribution of accelerograms. These data combined with the equivalent body force spall model of Day et al. (1983) are used to estimate an equivalent body force time history for the secondary source. The model predicts a peak force of 1.1×10^{16} dynes and a time duration of 0.6 s.

Peak acceleration data from this explosion which mark the transition from FSS to FSE are plotted against free surface range in Figure 8. As found for Pahute Mesa data, explosion geometry controls the gradual decay of the data close to GZ followed by more rapid decays. Radial and vertical peak motions merge. Scatter in the peak motions is between a factor of 3-5 for the Yucca Flats single explosion data. This variation is less than the single shot Pahute Mesa acceleration scatter.

Differences in wave shapes and spectra from COALORA are documented with observational displacements at the 549 m range displayed in Figure 9. Peak radial and vertical displacements vary by 30% about the mean. Radial and vertical wave shapes are very similar at the three azimuths. These characteristics argue for cylindrical or spherical symmetry in the source function. Transverse components in comparison are much shorter in duration, delayed in time, and exhibit significant fluctuations with azimuth including changes in first motion. Displacement spectra are estimated from these records (Figure 9). Envelope functions are fit to each spectrum which include a long period level, corner frequency, and high-frequency decay (Table 2). These data show little variation in radial and vertical long period levels and a factor of two increase in corner frequency for the transverse component accompanied by reduced long period levels. Source spectral interpretation of the above data supplemented by additional near-source gauges gives an isotropic moment (R, Z) of 1.95×10^{21} dyne-cm (multiplicative error of

FREE-FIELD AND FREE SURFACE GROUND MOTIONS

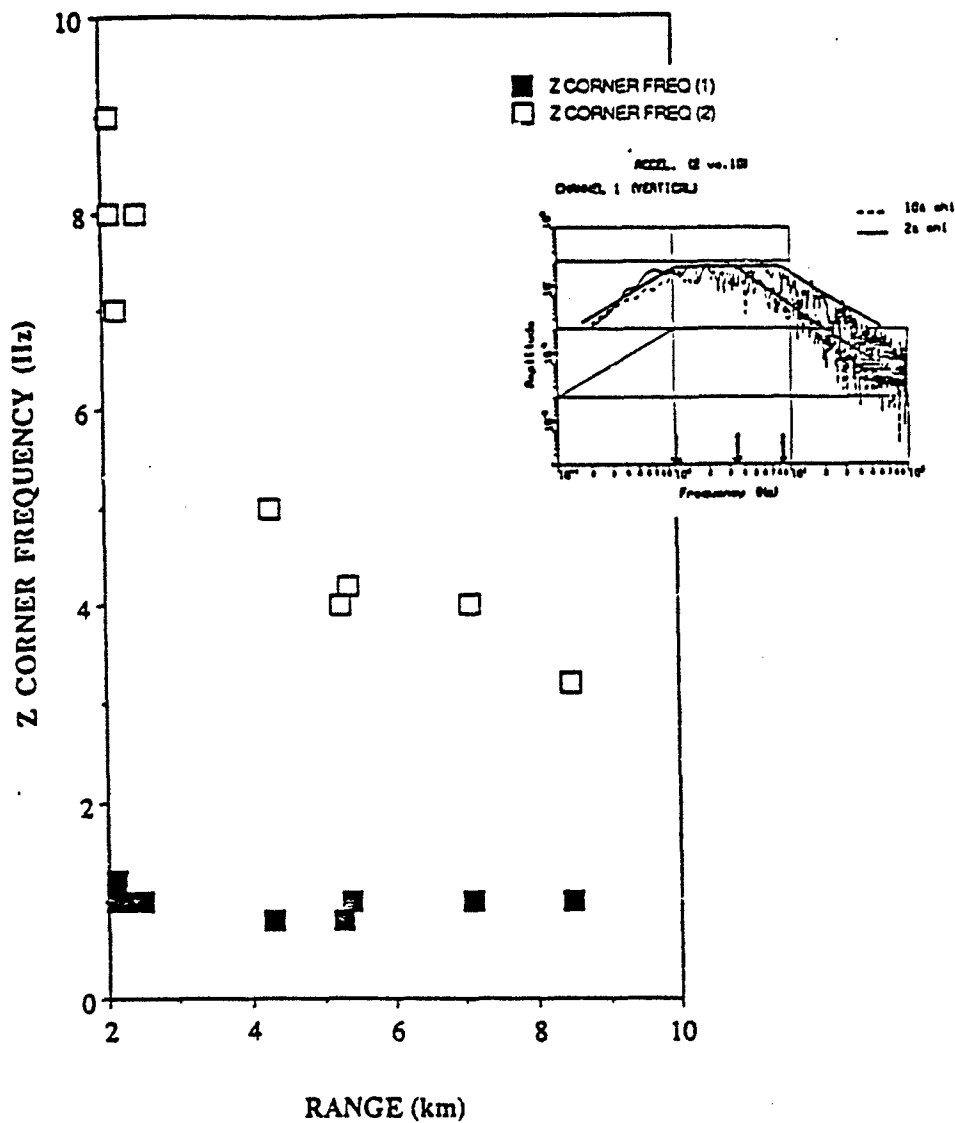


Fig. 6. Corner frequency interpretation from acceleration spectra of the same data used in Fig. 5. As shown in the inset, two corner frequencies were measured. The first represents the transition from the rise in acceleration spectra at low frequency to the flattening at intermediate frequencies. The second corner frequency marks the transition from the flat, intermediate frequency region to the decay at high frequencies. The first corner frequency (1 Hz) which is attributed to the source is insensitive to range while the second corner decreases with range from 9 to 3 Hz. The flat spectra between the two corners supports a f^{-2} source model. The second corner frequency is attributed to attenuation.

1.36) and a deviatoric moment (T) of 3.97×10^{20} dynes-cm (multiplicative error of 1.44). The accompanying corner frequency estimates are 1.82 for the isotropic spectra (1.12 multiplicative error) and 3.28 for the deviatoric spectra (1.13 multiplicative error). As found for Pahute Mesa spectral data, corner frequencies show less variation than moments.

The isotropic corner frequency lies between a Mueller-Murphy model prediction of 2.5 Hz for 1 kt and 1.7 Hz for 10 kt which is in agreement

with the announced yield of less than 20 kt. The high frequencies decay as f^{-2} , like the Pahute Mesa data and the Mueller-Murphy source model.

A simple Brune's model is used for comparative purposes to interpret the transverse spectra in terms of stress drop and source dimension. These estimates are applicable only for earthquake sources and may not be strictly applied to tectonically driven motions triggered by the explosion. The parameters predicted by this model are given for comparison. The mean source radius is 124 m with a stress drop of 89 bars and an average

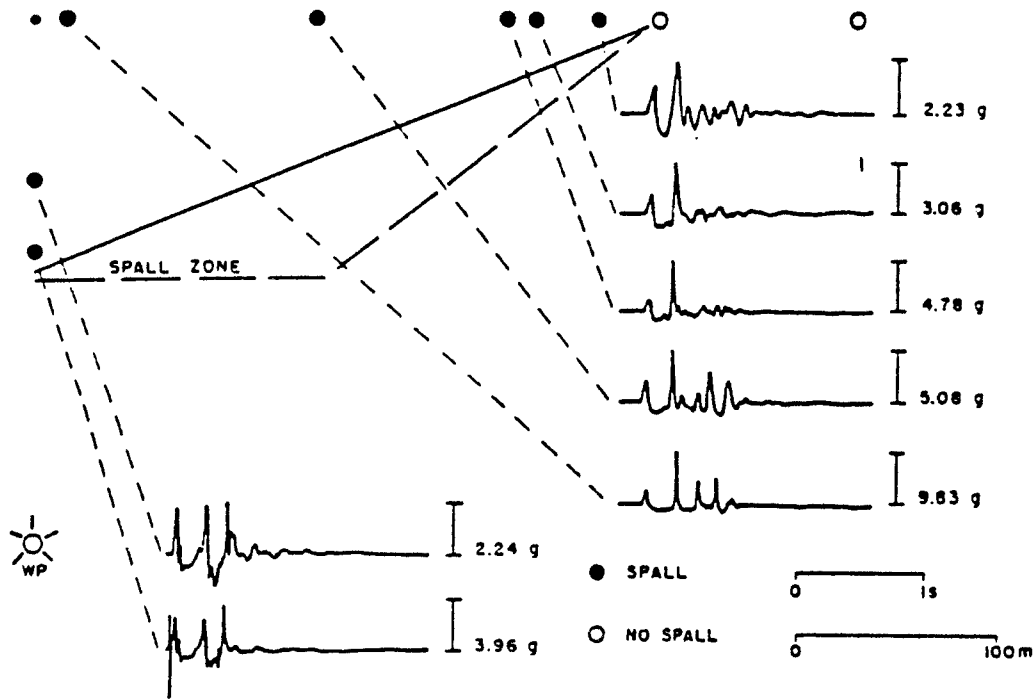


Fig. 7. Vertical cross-section displaying accelerograms from downhole and surface gauges within a range equal to two depths of burial which constrains the spall zone. Solid circles represent vertical accelerometer records that show characteristic $-1g$ dwell indicative of spall. Solid and long dashed lines are two dimensional bounds on the spall zone.

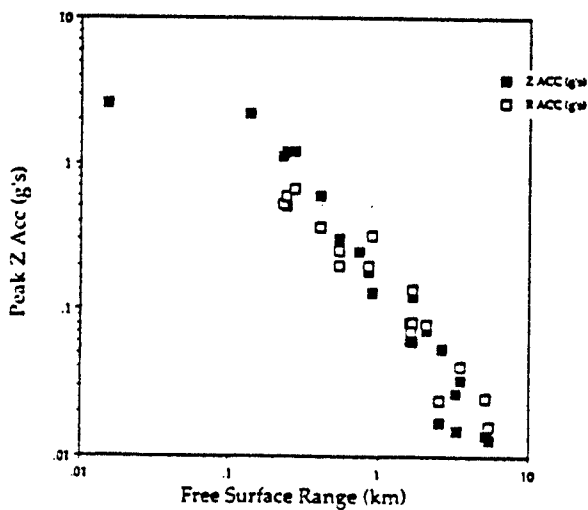


Fig. 8. Peak vertical (solid squares) and radial (open squares) acceleration plotted against free surface range (unscaled) for the COALORA explosion at Yucca Flats. This data like that for Pahute Mesa in Fig. 2 spans the transition from the free surface spall (FSS) to the free surface elastic (FSE) regions.

displacement of 33 cm. These displacements calculated from the radiated wavefield are similar in size to displacements observed on faults and bedding planes found upon re-entering tunnels surrounding nuclear explosions at Rainier Mesa (Kennedy, 1984). The equivalent elastic radii for 1 and 10 kt explosions are predicted to be between 133 and 202 m. The deviatoric source radius falls near the lower bound of the equivalent elastic source radius.

As seismic waves propagate within Yucca Flat valley, differences between radial, vertical, and transverse waveforms and spectra disappear. Displacement records and spectra at the 5.16 km distance are given in Figure 10. The duration of ground motion has grown from 1-2 s at 549 m to nearly 20 s at 5.16 km. The transverse motion is the largest of the three components and comparable in frequency to the other two components. Spectral differences found at the closest ranges and attributed to deviatoric/isotropic source processes have disappeared at this distance.

Rainier Mesa (FFW & FSE)

Data from the free-field can be used to constrain coupling of explosive energy into the linear regime. It is used in the calculation of the representative seismic source function known as the reduced displacement potential (Murphy and Bennett, 1979). As noted by Murphy (1989), existing free-field data is often complicated by complex geological models between explosion and receiver. Much of the existing free-field ground motion data base is also associated with underground structures. Instruments are primarily fielded to document survivability levels for these structures and not free-field motions necessary for seismic source characterization.

An experiment was designed to quantify the seismic source of a

FREE-FIELD AND FREE SURFACE GROUND MOTIONS

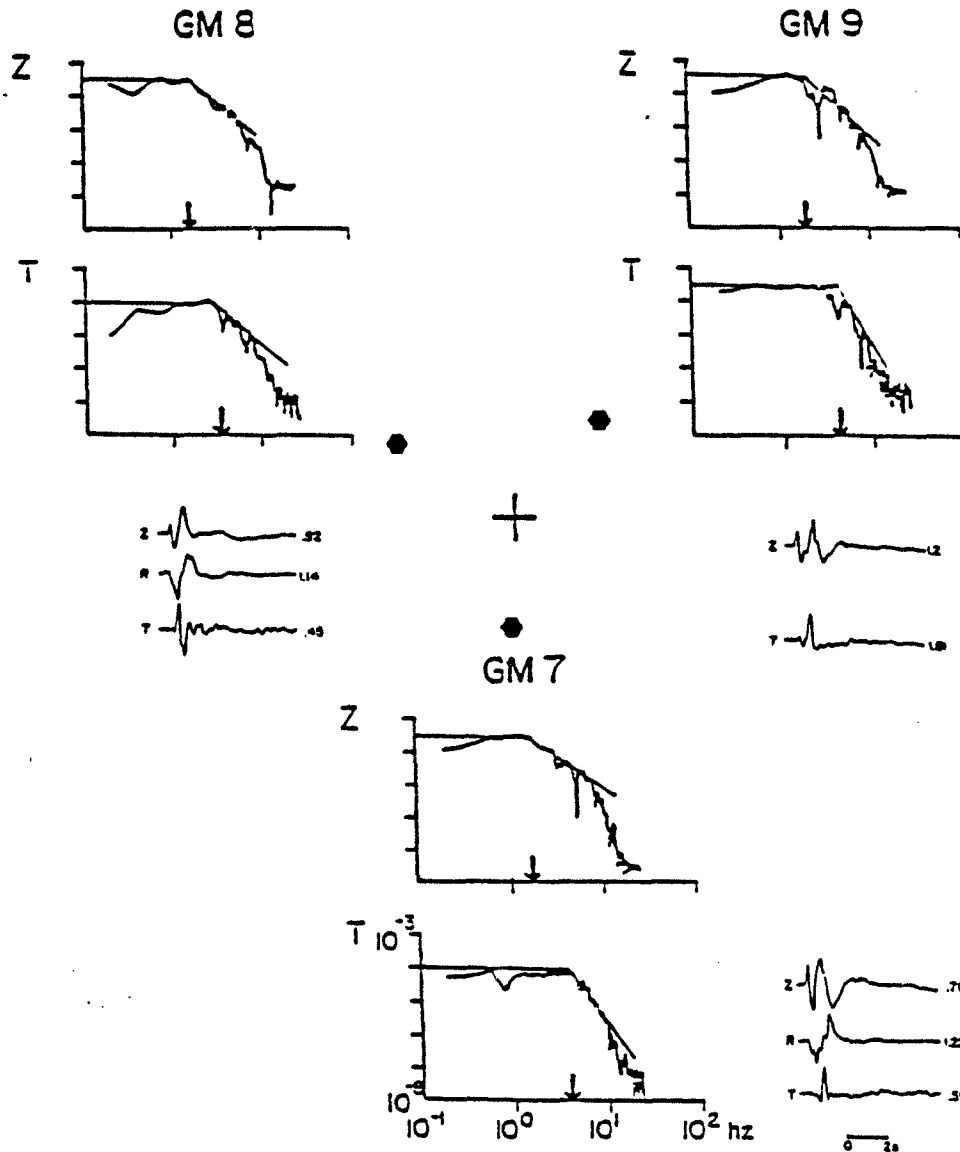


Fig. 9. Vertical (Z) and transverse (T) displacements spectra along with the displacement waveforms from the COALORA explosion. The three stations (GM7, GM8, GM9) are all at a free surface range of 549 m. Peak displacements for each waveform are given in cm. A simple spectral model consisting of a constant long period level, high frequency decay (f^{-n}), and a corner frequency (f_c) is fit to the spectral data.

Rainier Mesa explosion using free-field (FFW) and free surface (FSS & FSE) gauges (Figure 11a). Free-field measurements were made with three-component accelerometers located to minimize geological effects as well as document the transition of the motion field into the elastic regime. Free-surface gauges were fielded so that comparisons between the two data sets could be made. The radial, free-field data is reproduced in Figure 11c with absolute amplitudes compared to the free-surface data in Figure 11b. Amplitude data indicates a smoothly decaying acceleration and velocity field which follows model predictions by Perret and Bass

[1975] for wet tuff, $R^{-2.43}$ (acceleration). Waveforms show an azimuthal effect in wave shape with two accelerometers to the NE having longer durations than gauges to the NW. Duration of motion also increases with range as noted by Murphy [1989]. Another measure of propagation complexity is the ratio of radial to vertical peak acceleration (free-field) which is 5.1 for the closest gauge (193 m) and decreases to 1.8 for the farthest gauge (887 m).

Comparison of free-field, radial, peak acceleration (open square) and free-surface, peak acceleration (solid square) indicates increased scatter for

Table 2. COALORA Spectral Interpretation

Station	Range (m)	DC (cm-s)	f_c (Hz)	Slope
GM7Z	612	0.30	1.8	2
GM7R	612	0.36	2.1	2+
GM7T	612	0.09	4.0	4
GM8Z	614	0.30	1.6	2
GM8R	614	0.36	1.8	2
GM8T	614	0.10	3.5	2+
GM9Z	612	0.34	1.8	2+
GM9T	612	0.30	3.5	3+

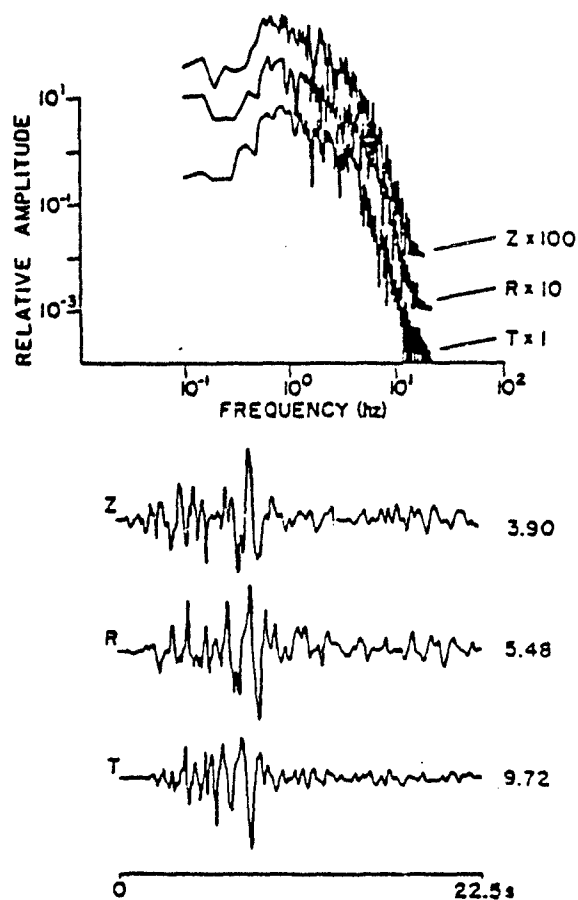


Fig. 10. Vertical (Z), radial (R) and transverse (T) displacements and displacement spectra at the 5.16 km source-receiver range for COALORA are displayed. The Z and R spectra are arbitrarily scaled by factors of 100 and 10 so that all three can be compared. Where the Z and T spectra showed significantly different spectral levels ($\Omega_Z > \Omega_T$) and corner frequency ($f_{CT} > f_{CZ}$) at 549 m (Fig. 9), at 6.16 km both spectral levels and corner frequencies for all components are identical.

free-surface data. The single source scatter in free-surface data is similar to that from Pahute Mesa. Free-field scatter is much reduced which might be a reflection of the fact that receivers have been moved away from the weathered zone. At approximately 800-900 m, free-field and free-surface data merge with no factor of two amplification at the free-surface. This observation is only an apparent discrepancy since free surface data displayed in Figure 11b are gauges from outside the spall zone (triangles in Figure 13a) and as such represent oblique rather than normal free surface incident angles.

Wavefield Modeling and Inversion

FSS to FSE transition

The transition from FSS to FSE is identified by a region of gradual peak amplitude decay to a range near $100 \text{ m/kt}^{1/3}$ followed by more rapid decay at greater ranges for both Pahute Mesa (Figure 2) and Yucca Flats (Figure 8). These data argue that explosion geometry has a dominant effect on ground motions. An elastic numerical modeling exercise is undertaken for this transition region at NTS in an attempt to quantify wave propagation effects and develop an understanding of free-surface motion decay rates. The velocity model, HOLE, used in this exercise is given in Figure 12a and is developed from emplacement hole data at Pahute Mesa (Table 3). A second average velocity model developed by Leonard and Jonsson (1987), LJ, is given in the figure for comparison. The explosion source is placed at a depth of 616 m just above a poorly welded tuff that shows reduced P wave velocity.

Full wave synthetics using the modified reflectivity methodology (Müller, 1985) are computed. Vertical and radial velocity waveforms between 0.1 and 3.0 km are reproduced in Figure 12b. Waveforms are multiplied by r^1 to balance amplitudes for viewing. Figure 13 displays the peak synthetic velocities plotted as a function of scaled range where the explosion yield is taken to be 150 kt for the source depth of 616 m. Vertical waveforms show little decay to approximately 100 m (scaled range) with increased decay beyond this free surface range. Least squares fit to amplitude data result in a spatial decay of $r^{-0.15}$ to a scaled range of $100 \text{ m/kt}^{1/3}$ while the decay rate at greater ranges is $r^{-1.30}$. These theoretical results compare to Pahute Mesa observations (Figure 2) that decay as $r^{-0.13}$ and $r^{-1.22}$ and indicate that elastic wave propagation effects which include attenuation match the observation transition. Data and models imply that spall momentum contributions from the region inside of $100 \text{ m/kt}^{1/3}$ range may be dominant due to increased spatial decay at greater ranges.

Spall Ballistic Model

Velocities and displacements are derived from acceleration observations within FSS region for the Pahute Mesa data. These measurements as well as spall dwell time are interrelated for a gravity controlled process. A gravity driven or ballistic model of the spall process predicts the following relation will hold between peak velocity at failure and peak displacement:

$$D = \frac{v^2}{2g} \tag{6}$$

Peak displacement is plotted against velocity at failure (spall initiation) in Figure 14. The relationship predicted by equation 6 is designated by open squares. Observational data follow the slope of predictions but displacements are as much as a factor of two bigger than predictions throughout the data set.

Although large displacements may be a result of bias introduced in the integration procedure in deriving these values, the consistency of large

FREE-FIELD AND FREE SURFACE GROUND MOTIONS

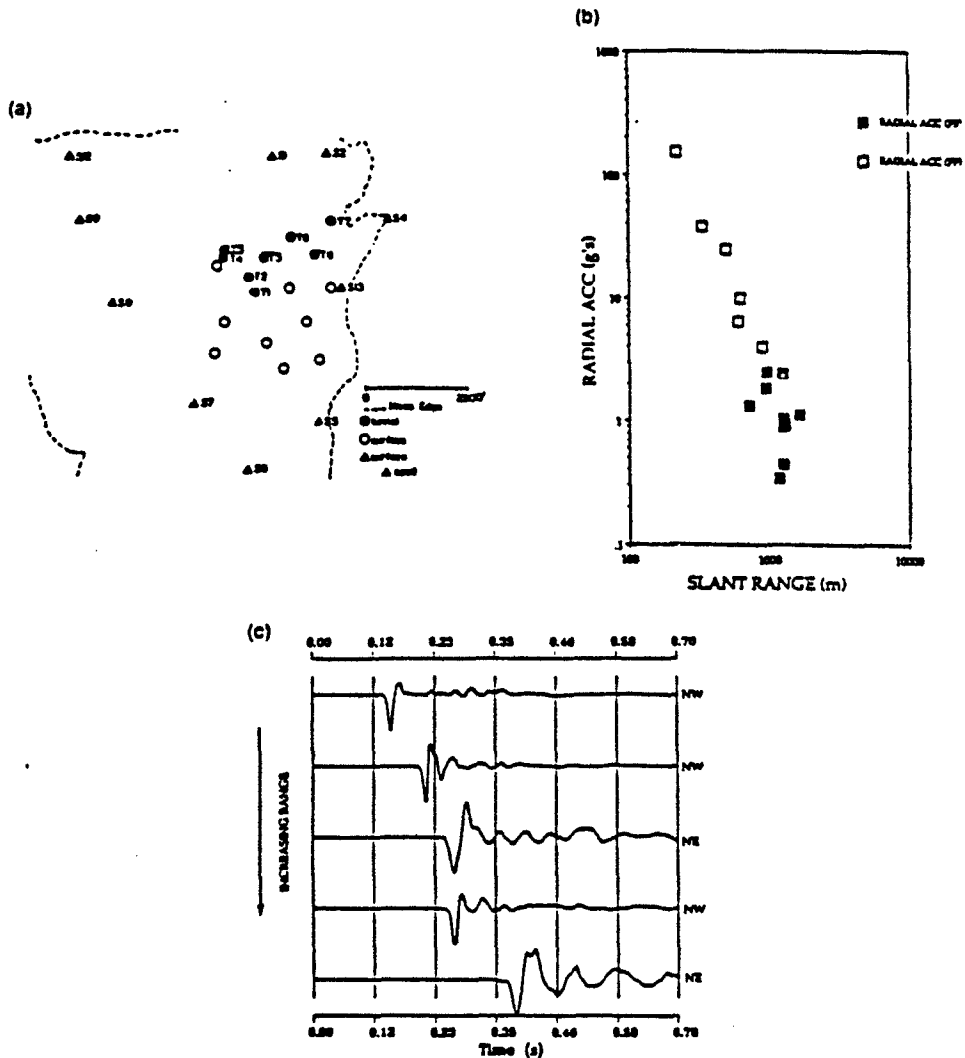


Fig. 11. (a) Plan view of the instrument array for a combined free-field (solid circles) and free surface (open circles and all triangles) ground motion experiment at Rainier Mesa, NTS. (b) Comparison of the peak radial accelerations in the free-field (open squares) and at the free surface (solid squares). A marked increase in data scatter is noted for the free surface data. (c) Normalized free-field radial velocity waveforms from the experiment.

displacements for a number of shots at a variety of motion levels argues against this interpretation. Alternatively, departure from a purely gravitational spall model may be explained by viewing spall as a continuous rather than a simple, discontinuous process. Even though peak velocity indicates failure, spalled material may still receive long period input from material below thus boosting displacements over those predicted by a simple ballistic model. More data supplemented with numerical modeling is needed to investigate this point.

Velocity Model Effects/Data Scatter

Scaled acceleration and velocity data from Pahute Mesa (Figure 5) show considerable scatter. A number of authors have argued that such

scatter in the near-source region is a result of lateral variations in the geological structure at NTS. There are strong vertical variations in velocity in addition to lateral variations. Figure 12a displays the velocity log developed from an emplacement hole at Pahute Mesa (HOLE) and contrasts it with an average model developed by Leonard and Johnson [1987] from inversion of near-source travel-time data (LJ). The site specific velocity model shows strong low velocity zones (LVZ) representative of poorly welded tuff units. Differences in synthetics developed from the average and site specific velocity models are investigated to determine how much detail must be included in the velocity model. A set of numerical trials will be discussed using the site specific velocity model with sources just above, in, and below a LVZ such as that which exists below 616 m (HOLE) in Figure 12a. This

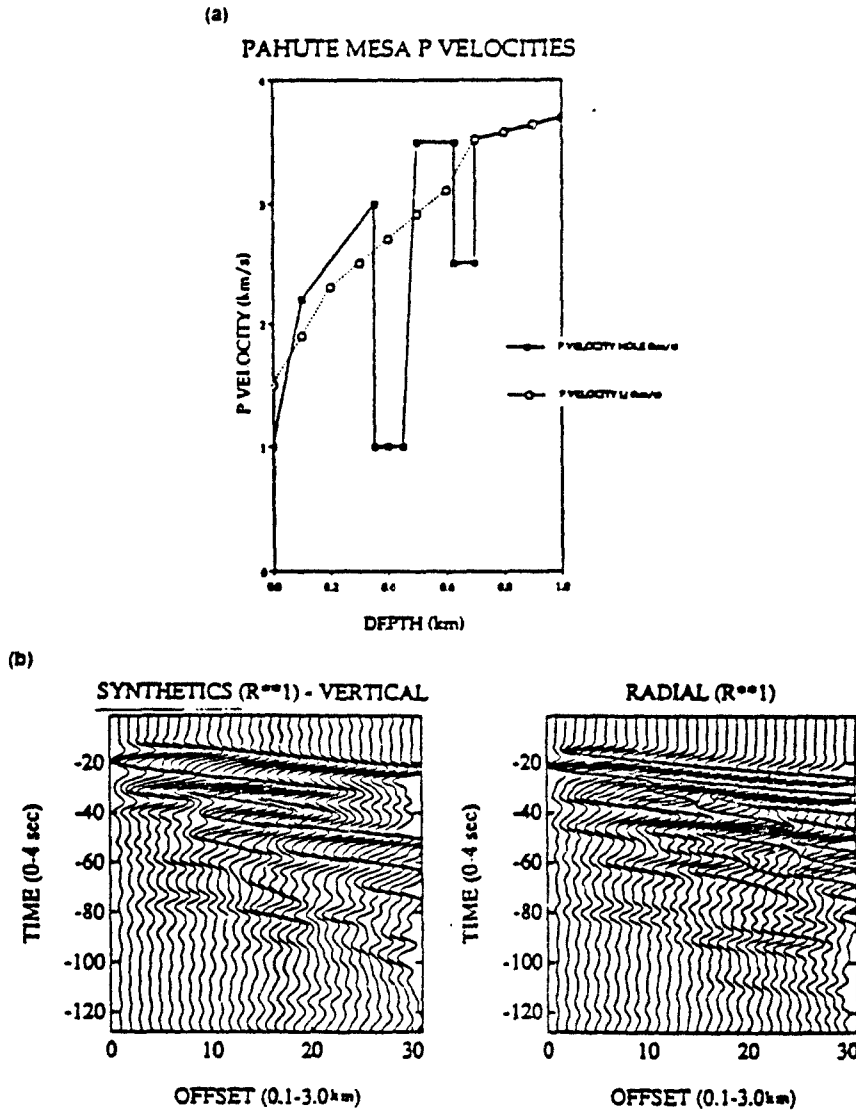


Fig. 12. (a) The P wave velocity model interpreted from emplacement hole data at Pahute Mesa (solid squares, Table 3) contrasted against an average Pahute Mesa velocity model (open circles) developed by Leonard and Johnson (1987). (b) Vertical and radial synthetic velocity records developed from the site specific velocity model using the extended reflectivity modeling technique. The synthetics calculated for the free surface ranges of 0.1 to 3.0 km have all been scaled by free surface range (r^1) to balance amplitudes for display.

numerical experiment will help determine the effect of material properties around the explosion on near-source wavefields.

A number of researchers [Vidale and Heimberger, 1987; Johnson, 1988; Stump and Johnson, 1984] have noted the importance of both body and surface waves in near-source waveforms. Although distances over which observations are made in this study are relatively short (0-10 km), the shallow source depths (200-1000 m) lead to these effects. The modified reflectivity method [Muller, 1985] is employed in seismogram synthesis to include both body and surface wave contributions. Sources

in these calculations have a constant moment with a source time function appropriate for a 150-kt explosion. A simple separation of dominant body and surface wave contributions is found by low-pass filtering the data at 1 Hz to emphasize surface waves and high-pass filtering the data at 1 Hz to focus on body waves. Peak velocities are picked from synthetics for comparison between the various models.

The site specific velocity model (HOLE) is first investigated with sources above the LVZ (616 m), in the LVZ (665 m), and below the LVZ (750 m) (Figure 12a). The body wave data (Figure 15) shows strong

FREE-FIELD AND FREE SURFACE GROUND MOTIONS

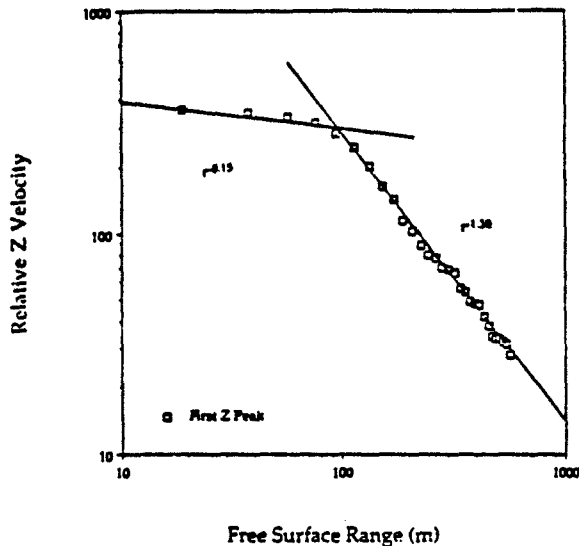


Fig. 13. Peak vertical velocities from Fig. 12b plotted against scaled free surface range. Source depth for the synthetics in Fig. 12b was appropriate for an explosion of 150 kt and so the free surface ranges were scaled by this yield. As done for the Pahute Mesa data displayed in Fig. 2, power law decay models were fit to the synthetic amplitudes for ranges less than and greater than $100 \text{ m/kt}^{1/3}$.

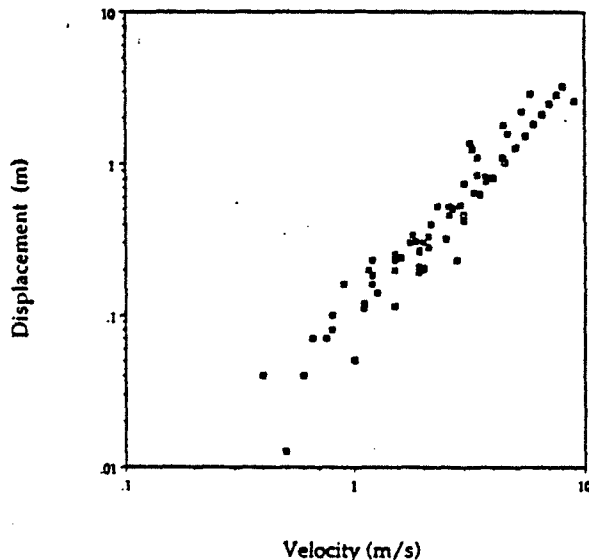


Fig. 14. Peak displacements and velocities from a number of spill zone observations of different explosions are plotted against one another. For a gravitationally controlled process peak displacement is related to velocity according to equation 6. This relation is displayed as open squares in the figure. On average for a given peak velocity the observed peak displacements are greater by a factor of two than that predicted by the gravitational model.

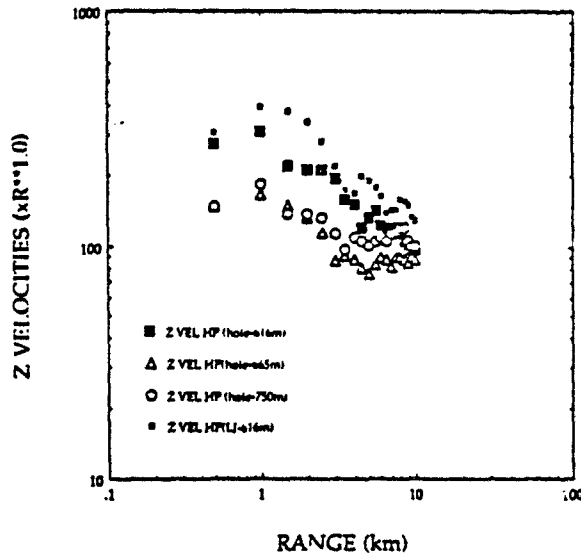


Fig. 15. Peak vertical body wave velocities ($f > 1 \text{ Hz}$) in the FSE region for extended reflectivity synthetic seismograms utilizing the HOLE velocity model (Fig. 12a) for source depths of 616 m (above a low velocity zone, LVZ), 668 m (in LVZ) and 750 m (below LVZ). Also included are peak vertical body wave velocities ($f > 1 \text{ Hz}$, LJ 616 m) generated from the average Pahute Mesa model of Leonard and Johnson (1987).

amplification (factor of 2) for body waves directly above a source when the explosion is above the LVZ. For a 150-kt shot the spill zone extends to an approximate lateral range equal to 2 DOB which includes this region of enhanced amplification. For the source in or below the LVZ little variation is observed. Differences between the three models disappear as source-receiver offset increases and downgoing energy becomes more important. Surface wave synthetics below 1 Hz show small differences between the three models.

Comparison of peak body wave amplitudes for a 616-m-Jeep explosion in the average Pahute velocity model of Leonard and Johnson [1988] are also given in Figure 15. Differences between the two models are less than those observed for sources above and below a LVZ.

Moment Tensor Inversions

Inverse modeling of observed explosion waveforms offers another method of making source estimates. Moment tensor inversions of COALORA data (Yucca Flats) are completed in an attempt to utilize the complete FSE data in a manner which gives stable source estimates in spite of demonstrated amplitude variability. The following representation is used in these inversions:

$$U_n(t) = G_{ni,j}(t) M_{ij}(t) \quad (7)$$

where $U_n(t)$ are the frequency domain representation of the observations, $G_{ni,j}(t)$ are the Green's functions or wave propagation effects accounted for with extended reflectivity solutions, and $M_{ij}(t)$ are the components of the moment tensor.

Many different stations are utilized simultaneously in these studies in an attempt to minimize the effect of data scatter. Both absolute amplitudes and wave shapes are modeled with fits completed in the frequency domain. Characteristic comparisons between observed and

modeled ground motions give correlation coefficients that range from 0.7 to 0.9 in the time domain. The moment tensor that was determined in this inversion is given in Figure 16. The source is dominated by the isotropic component. The initial pulse is symmetric and is followed by a secondary, long period contribution, largest on the M_{33} component, the vertical dipole. The size of this secondary force moment is in general agreement with the equivalent elastic force model of spall developed from data within the spall zone (Figure 7). Off-diagonal moment tensor elements are a factor of 5-10 smaller than diagonal elements supporting the small scalar deviatoric source estimates discussed earlier. Peak isotropic moment is 7.9×10^{20} which is nearly a factor of 3 smaller than scalar moments estimated from spectra at 549 m. The scalar moment interpretation of the 549 m spectra assumes a simple propagation path effect with no way to return downgoing energy to the free surface while inversions utilize Green's functions which return downgoing energy to the surface and lead to reduced moment estimates.

Constrained explosion source estimates are made in an attempt to investigate bias from single station measurements. The source is assumed isotropic and a single, three-component set of observations are inverted for the time history, $T(t)$, and strength, M_{kk} , of the source:

$$U_n(t) = G_{nk,k}(t) M_{kk} T(t) \quad (8)$$

Each instrument location around the explosion yields a source estimate much like standard scalar estimate although equation 8 allows for inclusion of more complex propagation path effects. A moment for each station was determined with this methodology for COALORA. The average of all these single station moments is 6.8×10^{20} dyne-cm, close to the value of full moment tensor inversions and significantly smaller than simple scalar moment estimates. Using equations 3 and 4 to quantify scatter in these estimates, the multiplicative error is 1.6, close to that of the scalar moments determined from displacement spectra.

Conclusions

A number of near-source data sets from explosions have been used to constrain the explosion source function. The study has included free-field data collected at shot level, free surface data from within the spall zone, and free surface data from outside the spall zone. Data from explosions at Rainier Mesa, Pahute Mesa and Yucca Flats NTS were included.

The Rainier Mesa data illustrate the increased variability of free surface observations compared to those made in the free-field (at shot depth). Little free-field data (FFW) scatter was found about the spatial decay rate predicted by Perret and Bass (1975) for wet tuff. The free surface data (FSE) from the same explosion had a factor of 6-8 scatter. This observational result illustrates the impact of weathered, near-surface layers on ground motions and indicates difficulties that might be encountered by making source estimates from limited amounts of free surface data.

Observational data from within the spall zone (FSS) transitioning to the elastic region (FSE) was analyzed for a number of Pahute Mesa explosions. These data illustrate the strong impact source geometry has on peak motions and, possibly, spall as a secondary seismic source. From ground zero, directly above the explosion, to a lateral free surface range equal to 1 DOB peak velocity data shows little decay, $r^{-0.13}$. Beyond this range the data decays much more rapidly, $r^{-1.22}$. Simple elastic, reflectivity calculations for a layered Pahute Mesa structure with appropriate Q (Table 3) replicate this decay pattern. The data and these numerical results suggest that momentum within the spall zone, which is available for a secondary seismic source, may be most affected by spall processes in the lateral range extending to 1 DOB for standard containment depths.

Observational peak acceleration and velocity data from within the FSE region for Pahute Mesa show a scatter as large as a factor of 6-8 for both a single explosion and a number of scaled explosions. These observations

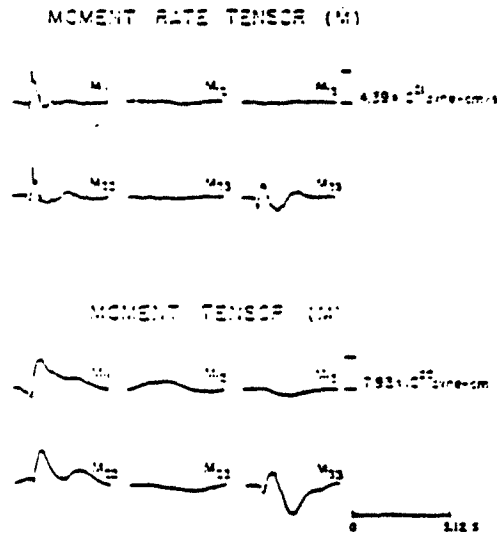


Fig. 16. Moment rate (\dot{M}) and moment (M) tensors from an inversion of the COALORA observational data. The 1 and 2 directions are in the horizontal plane while the 3 direction is vertical.

Table 3. Velocity Model for Hole^a

Depth (km)	P Vel (km/s)	S Vel (km/s)	Density (gm/cc)	Qp	Qs
0.000	1.00	0.58	1.70	50.00	22.22
0.100	2.20	1.27	2.10	50.00	22.22
0.350	3.00	1.73	2.20	50.00	22.22
0.350	1.00	0.58	1.70	50.00	22.22
0.400	1.00	0.58	1.70	50.00	22.22
0.450	1.00	0.58	1.70	50.00	22.22
0.500	3.50	2.02	2.40	50.00	22.22
0.616 ^b	3.50	2.02	2.40	50.00	22.22
0.630	3.50	2.02	2.40	50.00	22.22
0.630	2.50	1.44	2.10	50.00	22.22
0.700	2.50	1.44	2.10	50.00	22.22
0.700	3.52	1.99	2.40	100.0	44.44
1.000	3.70	2.03	2.40	100.0	44.44
2.000	4.37	2.29	2.40	100.0	44.44
4.000	5.25	3.03	2.40	100.0	44.44

^a Linear interpolation used between depth points except in case of repeated depths which signifies a discontinuity in velocity.

^b Source depth.

support the conclusion from the Rainier Mesa data that the weathered layer at the earth's surface can have significant impact on near-source observations. There is an indication in the scaled data that the one shot from below the water table has higher accelerations than the other explosions. Synthetic near-source reflectivity calculations were investigated for realistic plane-layered Pahute Mesa structures. Velocity contrasts at depth near the explosion gave body wave amplitude fluctuations as large as a factor of 2 directly above the explosion. These differences decreased with increasing source-receiver offsets. Despite strong velocity contrasts near the source the ground motion fluctuations did not approach the factor of 6-8 observed in the data. The observational

FREE-FIELD AND FREE SURFACE GROUND MOTIONS

data argues that lateral variations in the velocity structure (weathered zone), not taken into account by the synthetics, may have a strong contribution to the ground motions.

The scatter in the free surface data from Pahute Mesa is apparently frequency dependent as exemplified by the determination of long-period moment. Spectral moment estimates showed greatly reduced variation for a single explosion, a factor of 2-3. Free-surface data document the stability of the source corner frequency followed by a second higher frequency corner which decreases in frequency with increasing source-receiver offset. This second corner is attributed to attenuation and gives an average Q value for Pahute Mesa between 20 and 30. At small, near-source ranges where the source and attenuation corners separate the data indicates a f^{-2} high-frequency source model. At greater source-receiver ranges source and attenuation corners are difficult to separate and cloud the f^{-2} source interpretation.

Data from Yucca Flats were used to illustrate the relative deviatoric and isotropic source contributions. Simple spectral interpretations of observations at source-receiver distances of 2 km or less give deviatoric source estimates from transverse motions that are 5-10 times smaller than isotropic source estimates from vertical and radial motions. Transverse spectra interpreted as a Brune type model give a deviatoric source radius which is at the lower bound of the equivalent elastic source radius for the explosion. As found for the Pahute Mesa data, spectral differences between the radial, vertical and transverse spectra decrease with range. At 5 km all three components of motion give spectra that are identical in shape and strength, indicating the strong effects of scattering and attenuation.

Full wave modeling via moment tensor inversion are compared to simple spectral interpretation of free surface, near-source data. These results indicate that the scalar spectral interpretation for isotropic moment may be biased high by as much as a factor of 3. This bias is a result of the free surface interaction and the generation of surface waves not taken into account in the scalar moment estimates.

Data from the free-field and free surface have been used to constrain the explosion source function. Contributions from the isotropic explosion, tectonic stress release or driven motions and spall have been documented. Data from Rainier Mesa indicate the superiority of free-field data in making source estimates. Spall zone motions offer opportunity for constraining this secondary, seismic source and indicate a strong geometrical effect. At near-source distances strong trade-offs can develop between source estimates and the effects of attenuation and scattering. The advantage of near-source data sets is the ease at which experiments can be designed to separate these source and propagation effects as documented by this review.

Acknowledgments. This work was done under support from Defense Advanced Research Projects Agency under contract F19628-89-K-0025 to Southern Methodist University (BWS), Department of Energy Source Region Program at Los Alamos National Laboratory (BWS), and Air Force Geophysics Laboratory (RER).

References

- Archuleta, R. J., E. Cranswick, C. Mueller, and P. Spudich, Source parameters of the 1980 Mammoth Lakes, California, earthquake sequence, *J. Geophys. Res.*, **87**, 4595-4607, 1982.
- Bache, T. C., Estimating the yield of underground nuclear explosions, *Bull. Seis. Soc. Am.*, **72B**, S131-S168, 1982.
- Bernreuter, D. L., E. C. Jackson, and A. B. Miller, Control of the dynamic environment produced by underground nuclear explosions, in *Proceedings of Symposium on Underground Explosions*, 14-16 Jan 1970, Las Vegas, Nevada, Report Conf-700101, Vol 2, 979-993, 1970.
- Day, S. M., N. Rimer, and J. T. Cherry, Surface waves from underground explosions with spall: Analysis of elastic and nonlinear source models, *Bull. Seis. Soc. Am.*, **73**, 247-264, 1983.
- Fletcher, J., J. Boatwright, L. Harr, T. Hanks, and A. McGarr, Source parameters for aftershocks of the Oroville, California, Earthquake, *Bull. Seis. Soc. Am.*, **74**, 1101-1123, 1984.
- Germain, L. S., *Perret and Bass Revisited: I-Hard Rocks; II-Wet Tuff*, Defense Nuclear Agency, Washington, DC, DNA-TR-86-407, 1 October 1986.
- Haskell, N. A., Analytic approximation for the elastic radiation from a contained underground explosion, *J. Geophys. Res.*, **72**, 2583, 1967.
- Hays, W. W., *Prediction of Ground Motion Characteristics of Underground Nuclear Detonations*, Environmental Research Corporation, Las Vegas, NV, NVO-1163-239, 1974.
- Helmlinger, D. V. and D. M. Hadley, Seismic source functions and attenuation from local and teleseismic observations of NTS events JORUM and HANDLEY, *Bull. Seis. Soc. Am.*, **71**, 51-67, 1981.
- Johnson, L. R., Source characteristics of two underground nuclear explosions, *Geophys. J.*, **95**, 15-30, 1988.
- Kennedy, R. P., Mighty Epic/Diablo Hawk block motion program, in *DARPA/AFOSR Symposium on the Physics of Nonisotropic Source Effects from Underground Nuclear Explosions*, Defense Advanced Research Projects Agency, Arlington, VA, DARPA-GSD-8203/AFOSR-NP-8201, 1984.
- King, D. S., B. E. Freeman, D. D. Eilers, and J. D. Johnson, The effective yield of a nuclear explosion in a small cavity in geologic material: Enhanced coupling revisited, *J. Geophys. Res.*, **94**, 12375-12385, 1989.
- Leonard, M. A., and L. R. Johnson, Velocity structure of Silent Canyon Caldera, Nevada Test Site, *Bull. Seis. Soc. Am.*, **77**, 597, 1987.
- Müller, G., The reflectivity method: A tutorial, *J. Geophys.*, **58**, 153-174, 1985.
- Murphy, J. R., and T. J. Bennett, *A Review of Available Free-Field Seismic Data from Underground Nuclear Explosions in Alluvium, Tuff, Dolomite, Sandstone-Shale, and Interbedded Lava Flows*, System, Science, and Software, La Jolla, CA, SSS-R-80-4216, 1979.
- Murphy, J. R., Free-field observations from underground nuclear explosions, in *Proceedings of the DOE/LLNL Symposium on Explosion-Source Phenomenology*, Lake Tahoe, California, 14-16 March, Lawrence Livermore National Laboratory, Livermore, CA, CONF-890398, pp. 75-91, 1989.
- Murphy, J. R., Seismic source functions and magnitude determinations for underground nuclear detonations, *Bull. Seis. Soc. Am.*, **67**, 135-158, 1977.
- O'Brien, L. J., and J. A. Lahoud, *Analysis of Ground Motions Recorded from Underground Nuclear Explosions on Pahute Mesa*, Adaptronic, Inc., McLean, VA, DOE/NV/1005 2-1, 1982.
- Patton, H. J., Characterization of spall from observed strong ground motions on Pahute Mesa, *Bull. Seis. Soc. Am.*, **80**, 1326-1345, 1990.
- Perret, W. R. and R. C. Bass, *Free-Field Ground Motion Induced by Underground Explosions*, Sandia Laboratories, Albuquerque, NM, SAND74-0252, 1975.
- Pomeroy, P. W., W. J. Best, and T. V. McEvelly, Test ban treaty verification with regional data—A review, *Bull. Seis. Soc. Am.*, **72B**, S89-S129, 1982.
- Rodean, H. C., Inelastic processes in seismic wave generation, in *Identification of Seismic Sources—Earthquakes or Underground Explosion*, E. S. Husebye and S. Mykkeltveit, Eds., D. Reidel Publishing Co., 1981.
- Rodean, H. C., *Nuclear Explosion Seismology*, U.S. Atomic Energy Commission, 1971.
- Stump, B. W., and L. R. Johnson, Near-field source characterization of contained nuclear explosions in tuff, *Bull. Seis. Soc. Am.*, **74**, 1-26, 1984.
- Stump, B. W., and R. E. Reinke, Experimental seismology: *In Situ* source experiments, *Bull. Seis. Soc. Am.*, **77**, 1295-1311, 1987.
- Stump, B. W., Constraints on explosive sources with spall from near-source waveforms, *Bull. Seis. Soc. Am.*, **75**, 361-377, 1985.
- Taylor, S. R., and J. T. Rambo, Near-source effects on regional seismograms: An analysis of the NTS explosions PERA and QUESA, submitted to *J. Geophys. Res.*, 1990.
- U.S. Congress, Office of Technology Assessment, *Seismic Verification*

STUMP AND REINKE

- of Nuclear Testing Trials*, OTA-ISC-361 (U.S. Government Printing Office, Washington, DC, May 1988)
- Vidale, J. E., and D. V. Helmberger, Path effects in strong motion seismology, in *Seismic Strong Motion Synthetics*, Bruce A. Bolt, Ed., Academic Press, Orlando, FL, 1987.
- Walker, J. J., Analysis of TV records for ground motion characterization, in *DARPA/AFOSR Symposium on the Physics of Nonisotropic Source Effects from Underground Nuclear Explosions*, DARPA-GSD-

- 8203/AFOSR-NP-8201, Defense Advanced Research Projects Agency, Arlington, VA, 1982.
- Werth, G. C., and R. F. Herbst, Comparison of amplitudes of seismic waves from nuclear explosions in four mediums, *J. Geophys. Res.*, 68, 1463-1474, 1963.
- Wheeler, V. E., and R. G. Preston, *Scaled Free-Field Particle Motions from Underground Nuclear Explosions*, Lawrence Livermore Radiation Laboratory, Livermore, CA, UCRL-50563, 1968.

**VARIABILITY OF NEAR SOURCE WAVEFORMS
FROM CONTAINED EXPLOSIONS**

Pahute Mesa: A Case Example

Brian W Stump
Department of Geological Sciences
Southern Methodist University
Dallas, Texas 75275-0395

ABSTRACT

The importance of simple elastic (with attenuation) wave propagation effects on near source observations (0.5-10 km) of seismic waves generated by underground explosions is considered. Specifically, the study is designed through a numerical exercise to answer the question of how well the geological/geophysical structure of a test site must be known in order to make good estimates of the explosion source function. This study has ultimate implications on the energy radiated to regional and teleseismic distances. Modeling of these wavefields is completed using the extended reflectivity method for plane layered geologies. This method is utilized because of the necessity to include both body and surface wave effects. Full wave velocity synthetics are generated and quantified by peak amplitude and a new energy measure which is defined as the integral of the squared velocity. Four specific effects are quantified in the study: (1)Source-receiver offset effects; (2)Source depth of burial effects; (3)Near source interface effects; and (4) 'Average' vs 'site specific' velocity model effects. The offset effects were found to be quite strong in these models with spatial decays of both body and surface waves exceeding spherical and cylindrical decay respectively. Body waves are found to decay between $r^{-1.5}$ and $r^{-1.9}$ and surface waves between $r^{-1.3}$ and $r^{-1.4}$. Body waves with frequencies greater than 1 Hz showed strong variations which did not fit these power laws in the 0-2 km range. Spatial changes in energy over the 0.5 to 10 km range were 1000-2000 for the body waves and 75-160 for the surface waves. Sources above and below interfaces were found to have the second strongest effect on amplitudes. High frequency body waves exhibited factors of 4 change in amplitude as sources moved into and below a low velocity zone. These differences disappeared as source to receiver offsets increased. Depth of burial effects were large for sources at 200 and 616m. These differences decreased with source to receiver offset also. For reasonable source depth estimates it was determined that this effect was small as long as the source remained in a smoothly varying media. The comparison between an average and site specific velocity model with a constant source depth showed small variations in peak amplitude and total energy. The amplitude and energy variations quantified in these calculations are smaller than the variations seen in near source

data sets. Lateral variations in the geological structure or source coupling effects may account for additional scatter.

MOTIVATION

Near source ground motions from underground nuclear explosions offer a diagnostic that can be utilized in the constraint of physical processes in the seismic source region. These source processes include but are not limited to the nonlinear response of the material in which the explosion is detonated, the release of stored tectonic stress in and around the explosion, and the interaction of the explosive wavefield with the free surface and other interfaces. Waveforms are affected by all of these processes as well as the geological media through which the seismic waves propagate. In any study attempting to either resolve the explosive source function, discriminate the resulting wavefield from that developed by a naturally occurring earthquake, or constrain the yield or size of the explosion one must be able to separate the wave propagation effects from the source itself.

The purpose of this study is to begin to quantify the role simple near source wave propagation effects play in the observed wavefields separate from source issues such as coupling. We shall focus upon wave propagation at Pahute Mesa in the 0-10 km range and quantify the variability of amplitudes that might be experienced within the constraints of current geological and geophysical models of this area of the Nevada Test Site. Through this numerical exercise we would like to answer the question of how well the geological structure must be known in order to make good estimates of the explosion source function. A secondary but longer term goal of this study is to investigate the effects that this near source structure has on energy observed at regional and teleseismic distances. This second goal is beyond the scope of the current study.

We will first address effects of source-receiver offset in the radiated wavefield. The purpose of this part of the study will be to identify distance ranges in which the wavefield exhibits substantial changes and those in which it does not. Strong gradients in the radiated energy will translate into large variations of amplitudes and possible sources of error in analysis.

The effect of source depth of burial will be addressed. Relative coupling of energy into body and surface waves must be quantified

before the adequacy of either or both phases as diagnostics for source strength or character can be judged.

Pahute Mesa is characterized by rhyolitic lava, bedded tuffs, and ash flow tuffs ranging from partially to densely welded. This general structure leads to interfaces which can in some cases be represented by relatively steep increases or decreases in velocity. In view of this geological model we will investigate the wave propagation effects of interfaces near explosive sources.

It is hoped that this study of the 'geometrical' effects of wave propagation at Pahute Mesa (by 'geometrical' we mean elastic wave propagation) will help in ascertaining the usefulness of near source data in constraining the source physics from explosive sources and possibly the yield of the nuclear device. In light of this last goal a comparison of an average velocity model for Pahute Mesa will be made against a site specific model developed through downhole exploration studies.

The strongest motivation for a numerical study such as this one is the observational data itself. Figure 1 is a compendium of scaled peak accelerations observed from a number of Pahute Mesa nuclear explosions plotted against scaled range. There is an approximate factor of ten scatter in peak accelerations at any given range. The physical reason for this scatter could either be the effect of different wave propagation (depth of burial, proximity to interfaces, or receiver structure) or source coupling. Sources below the water table yield the highest amplitudes at most ranges (solid squares in Figure 1) suggesting a coupling effect. This data can be contrasted to the variation of peak accelerations from a single explosion given in Figure 2. Although the data density is reduced, there is still a large amount of scatter in the data indicative of wave propagation differences from this single source. The scatter in the data decreases at longer periods. From the same data as used in Figure 2 acceleration spectra were determined and a long period spectral level chosen. This level was then converted to moment. The average moment in this case is 3.8×10^{23} dyne-cm with a multiplicative error of 1.49. Scatter in moment values is reduced from that of peak accelerations (Figure 3). Even in this data set there is an indication of local receiver effects as stations with high moments from vertical waveforms also yield high moments interpreted from the radial and transverse motions

PAHUTE MESA SCALED ACCEL

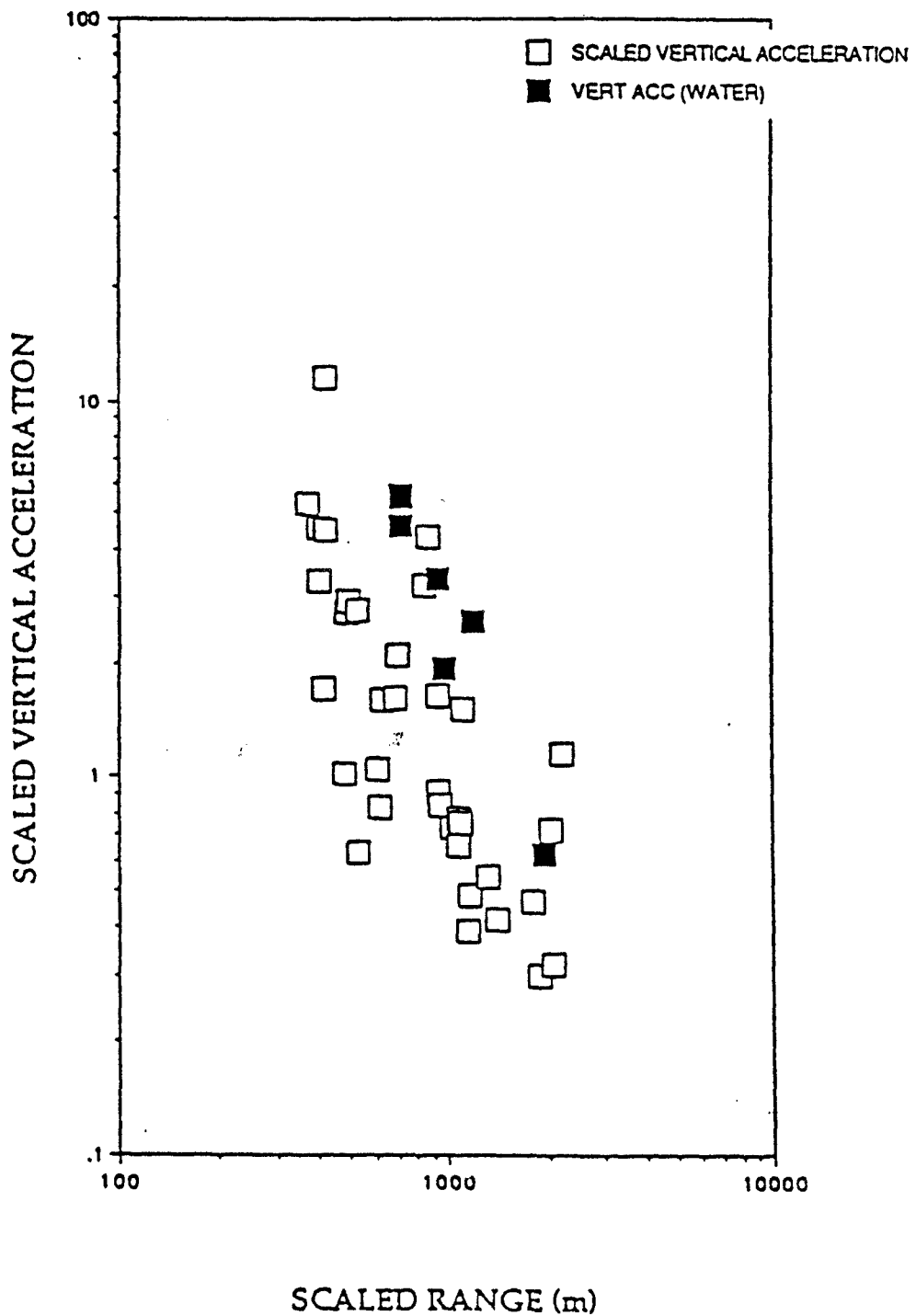


FIGURE 1

SINGLE SHOT ACCEL

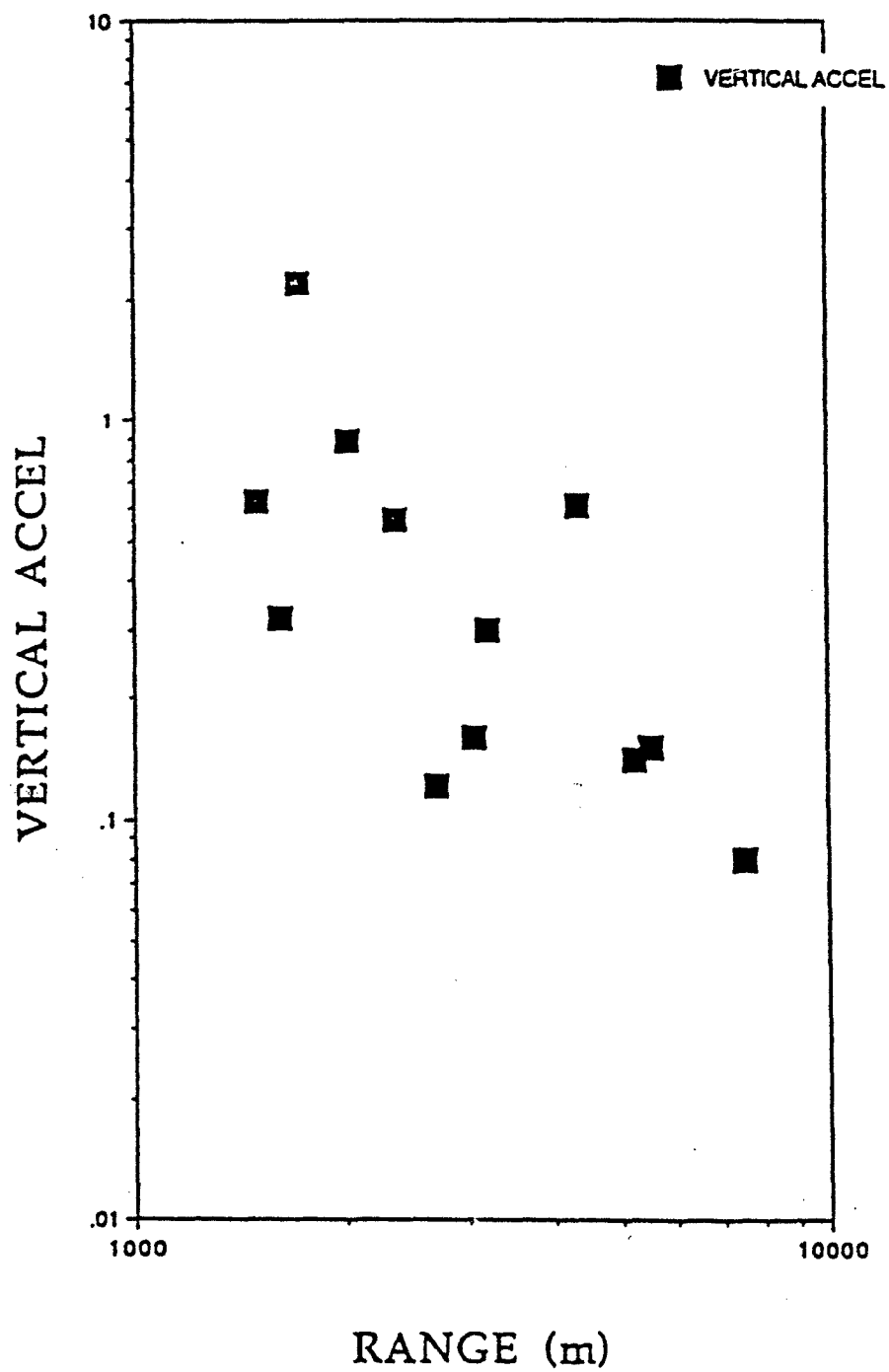


FIGURE 2

SINGLE EXPLOSION MOMENTS

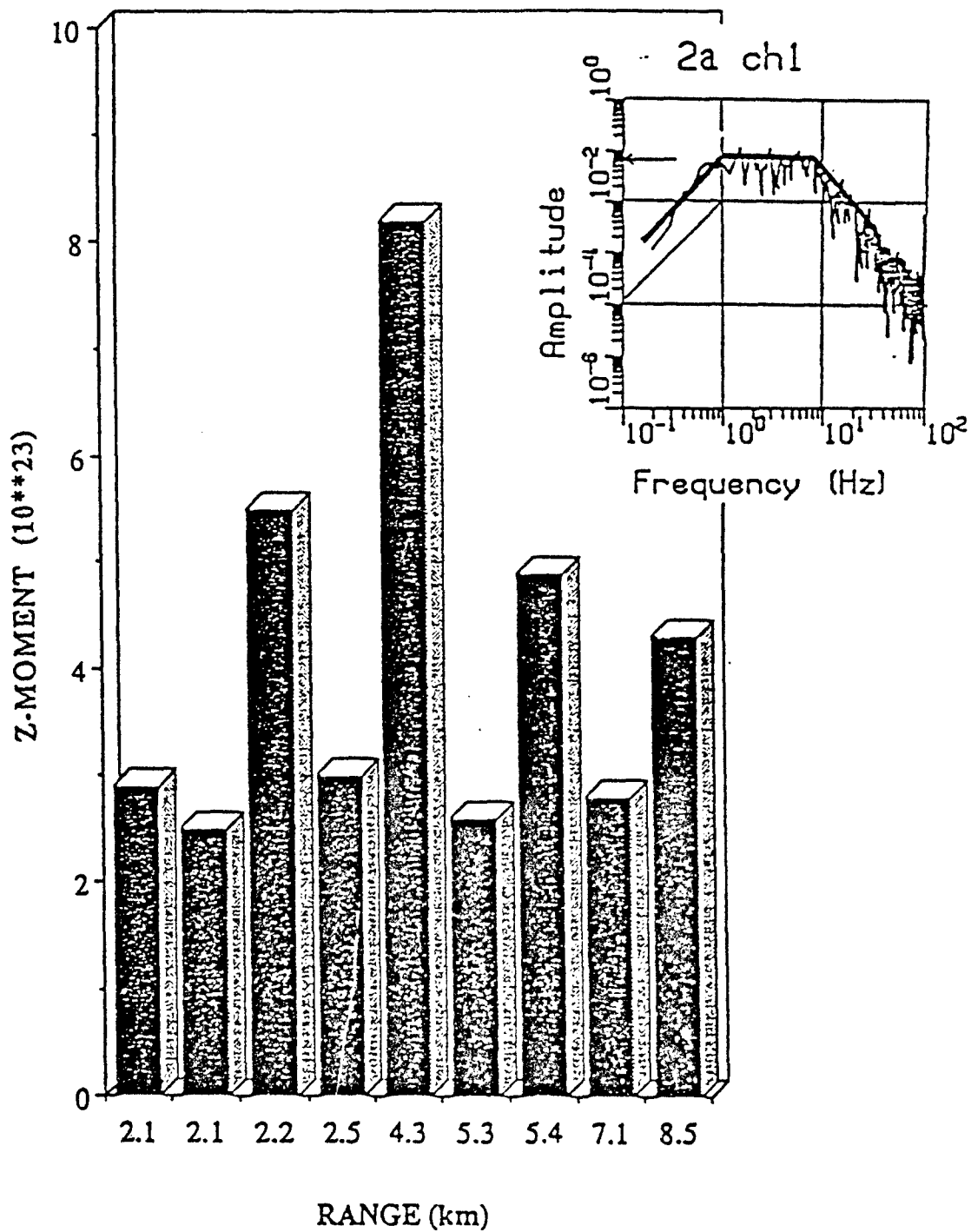


FIGURE 3

(Figure 4). The multiplicative errors from the radial and transverse data were 1.58 and 1.79 respectively.

The approach taken in this study is to bound the variability in near source waveforms expected from: (1) Offset effects; (2) Depth of burial effects; (3) Interface effects; and (4) 'Average' versus 'site specific' geological/geophysical structure.

SINGLE SHOT MOMENTS

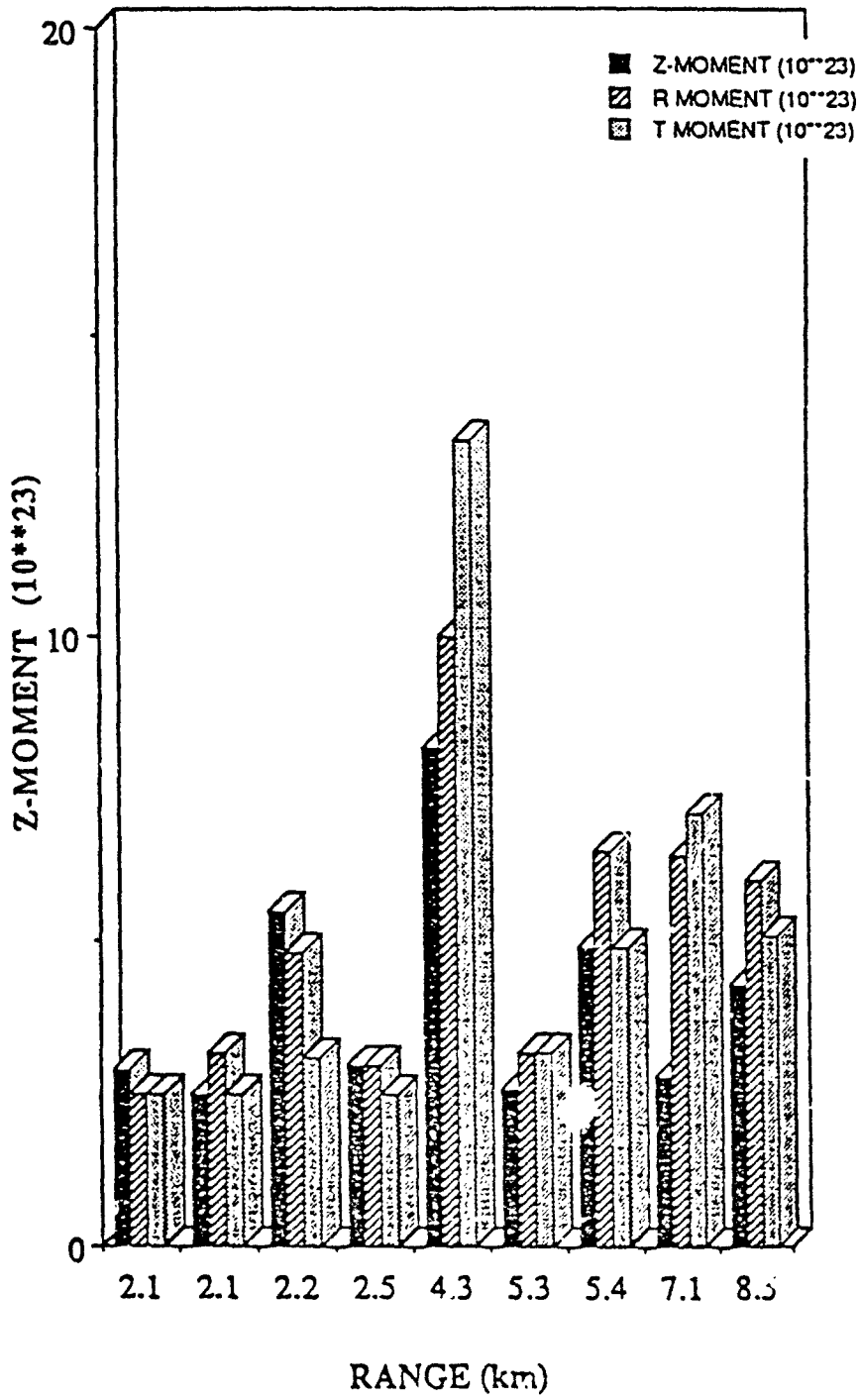


FIGURE 4

METHODOLOGY AND MODELS

A number of researchers (Vidale and Helmberger, 1988; Johnson, 1989; Stump and Johnson, 1984) have noted the importance of both body and surface waves in near source waveforms. Although the distances over which observations are made are relatively short (0-10 km, this study), the shallow source depths(200-1000m) lead to these effects. It is important to develop a computational technique that includes both body and surface waves. Focus in the initial part of this study will be on offset effects, depth effects, and interface effects all of which can be addressed with a plane layered structure.

With the listed constraints and goals the extended reflectivity method was chosen for seismogram synthesis (Muller, 1985). This methodology allows for the determination of the complete response of plane layered structures and includes effects of both body and surface waves. In some instances where waveforms are dominated by vertically propagating energy the reflectivity method can be extended to include separate source and receiver structures (Kind, 1985).

The choice of appropriate geological/geophysical model for Pahute Mesa lies at the heart of this exercise. Two different models were chosen in order to replicate variability in waveforms one might expect from the range of data types available to a seismologist as he approaches a new testing area. The first model was developed from downhole logs recovered from an emplacement hole. This model is represented by solid lines in Figures 5a and b (HOLE). Near surface velocities begin at 1.0 km/s increase to a depth of approximately 350m (3.0 km/s) where a bedded tuff is encountered and P velocities drop to 1.0 km/s. Below 500m a more competent material is encountered and velocities rise (3.5 km/s) until 630m where a nonwelded tuff is encountered and velocities drop again for approximately 70 m to 2.5 km/s. This detailed velocity model is contrasted with a relatively smooth model (dashed lines Figures 5a and b) developed from the linearized damped least-squares travel-time inversion of Leonard and Johnson, 1987. Both velocity models show a similar increase in velocity with depth but low velocity zones identified in downhole acoustic logs are missing in the Leonard and Johnson model. Differences in these models will allow us to quantify the effect of detail structure on radiated

PAHUTE MESA P VELOCITY MODELS

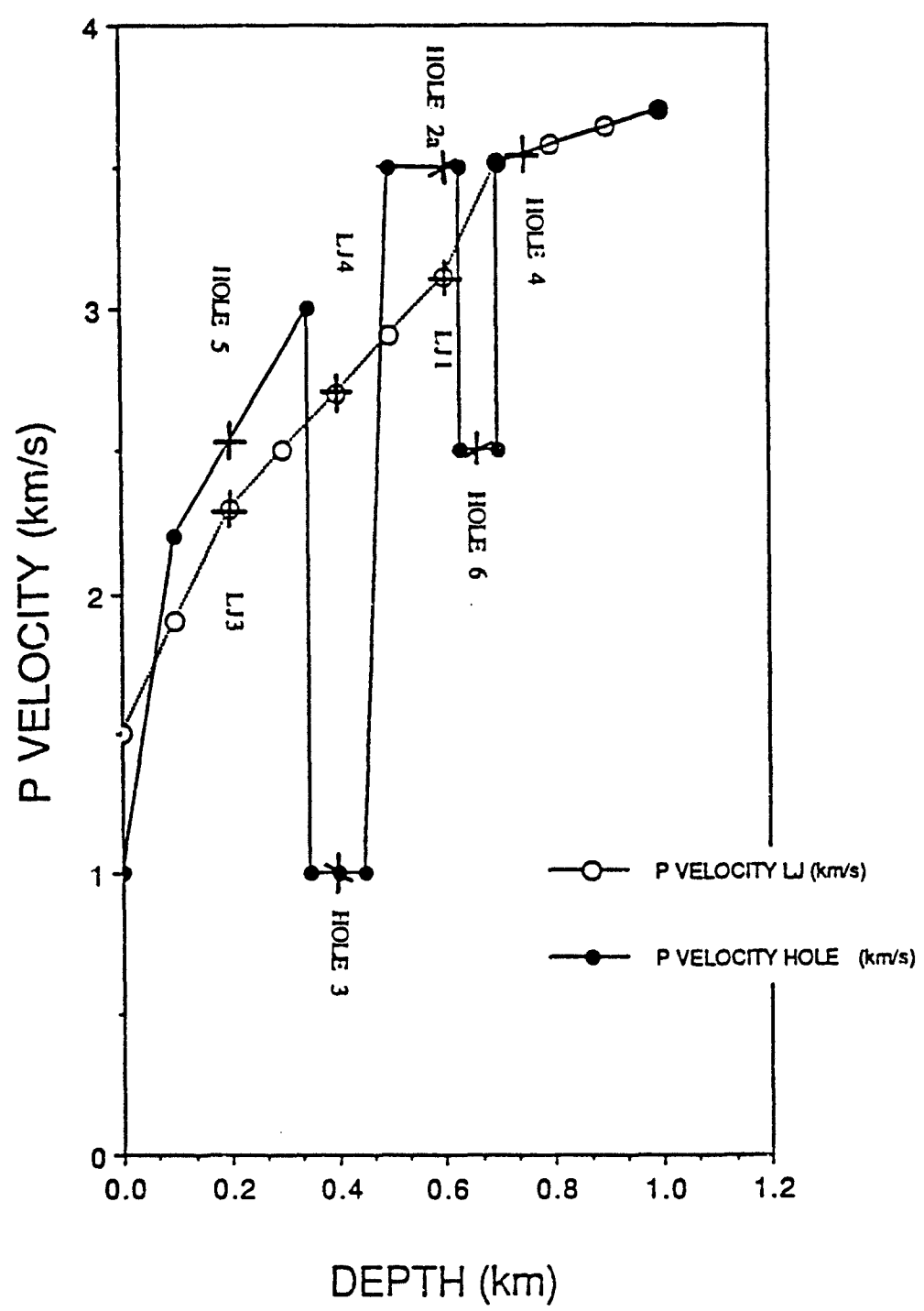


FIGURE 5a

PAHUTE MESA S VELOCITY MODELS

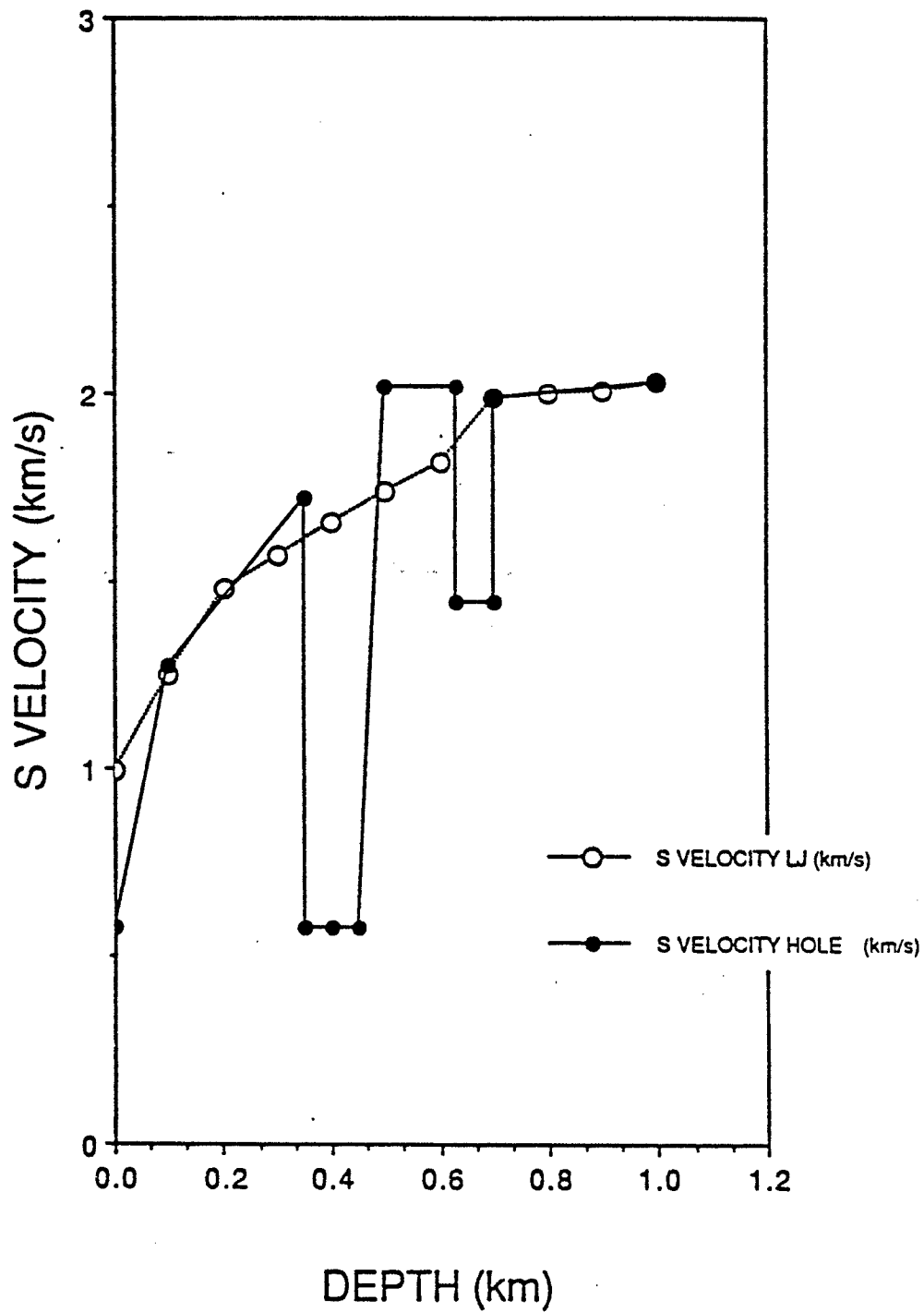


FIGURE 5b

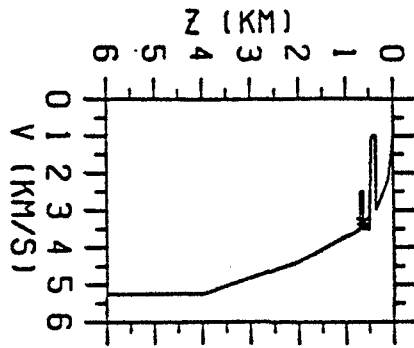
wavefields and identify the importance of interfaces close to an explosive source. At a depth scaling of $122\text{m}/\text{kt}^{1/3}$, a 150 kton explosion would be emplaced at a depth of 648 m close to the deeper velocity decrease in the HOLE model.

This investigation has several shortcomings and is intended as the start of a more exhaustive numerical exercise to quantify propagation effects. The most apparent problem is the plane layered structure with similar source and receiver effects. The separate source and receiver algorithm of Kind (1985) will allow the quantification of some of these effects. Two and three dimensional models which include the effects of scattering may be called for at a latter date. No attempt to replicate source depth effects such as those proposed by Mueller and Murphy (1973) have been included. Source coupling differences are ignored when there is obvious data (Figure 1) that supports its importance.

A characteristic set of waveforms at 0.5 km increments from the HOLE velocity model is given in Figures 6a-d. The numerical data are sampled at 32 samples/s and the waveforms are relative velocity for a source of constant moment. In Figures 6a and b one can identify the early arriving body waves followed by latter, longer period surface waves. In order to crudely separate body and surface waves for this model the data were high and low pass filtered at 1 Hz. The low pass filtered (4 pole) vertical components are given in Figure 6c while the high pass data are replicated in Figure 6d. In the amplitude analysis that follows these two representations will be used to quantify the effects of body and surface waves.

In order to contrast the effects of the various propagation models peak velocities were picked. Careful analysis of Figures 6a-d reveals rapid changes in waveshapes and amplitudes, particularly for the body waves. As a second, more stable estimate of radiated seismic energy, the integral of squared velocity was chosen as a measure of source strength. Since the waveforms involve both body and surface waves, it cannot be taken as an absolute energy estimate. The measure is defined as:

$$IV^2 = \int_0^b v^2(\vec{x}, t) dt$$



MAX 397

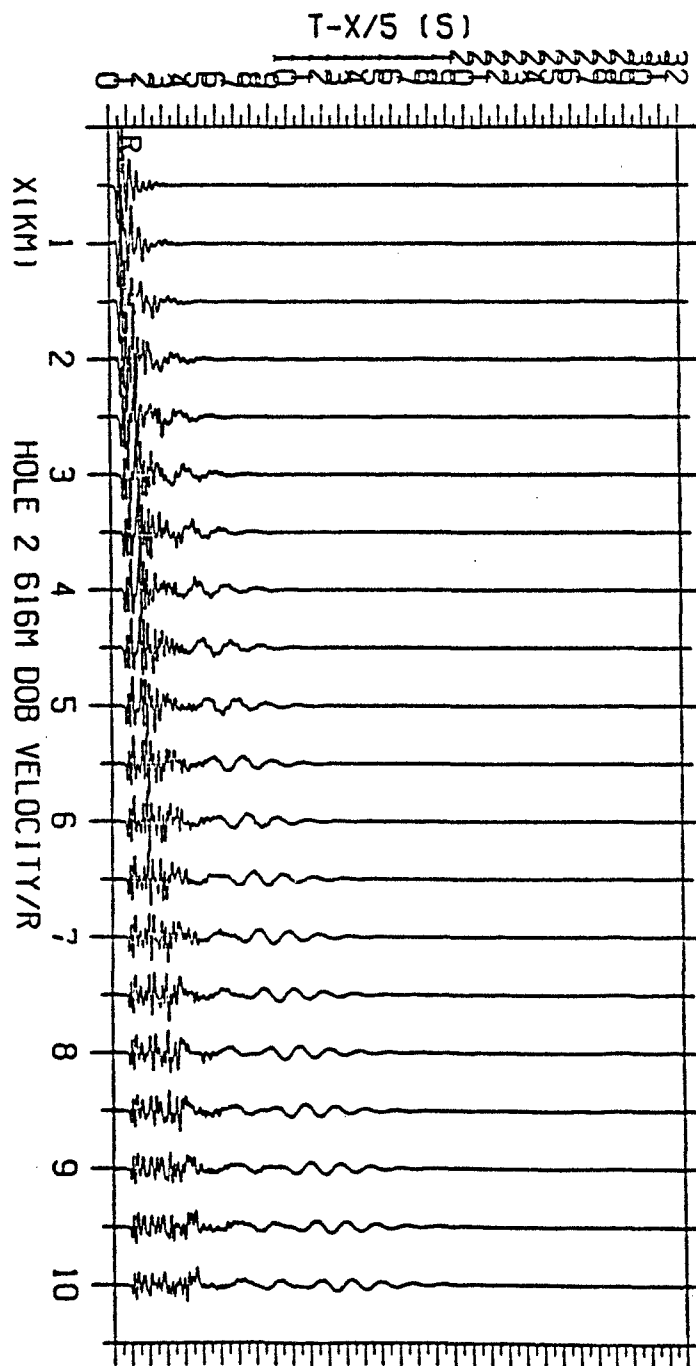
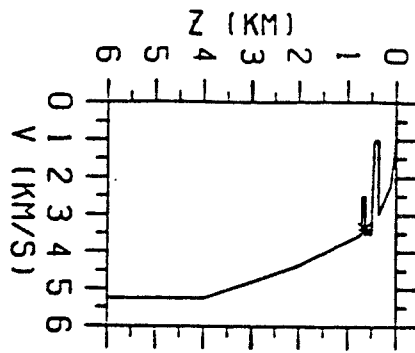


FIGURE 6a



MAX 307

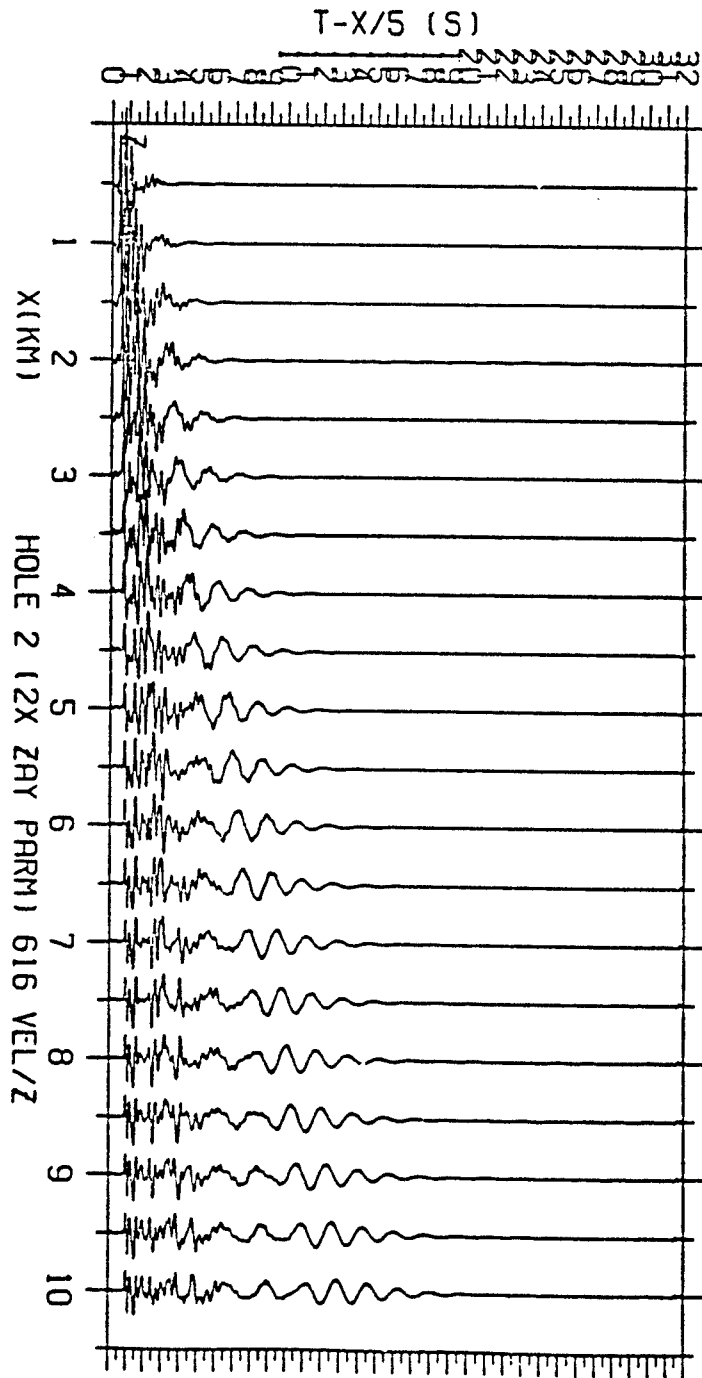
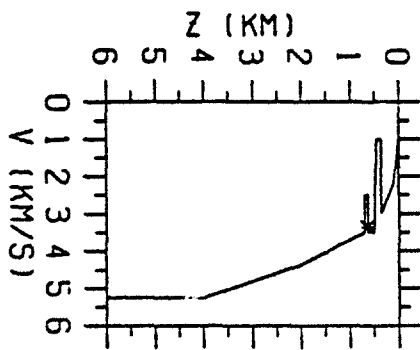


FIGURE 6b



MAX 66

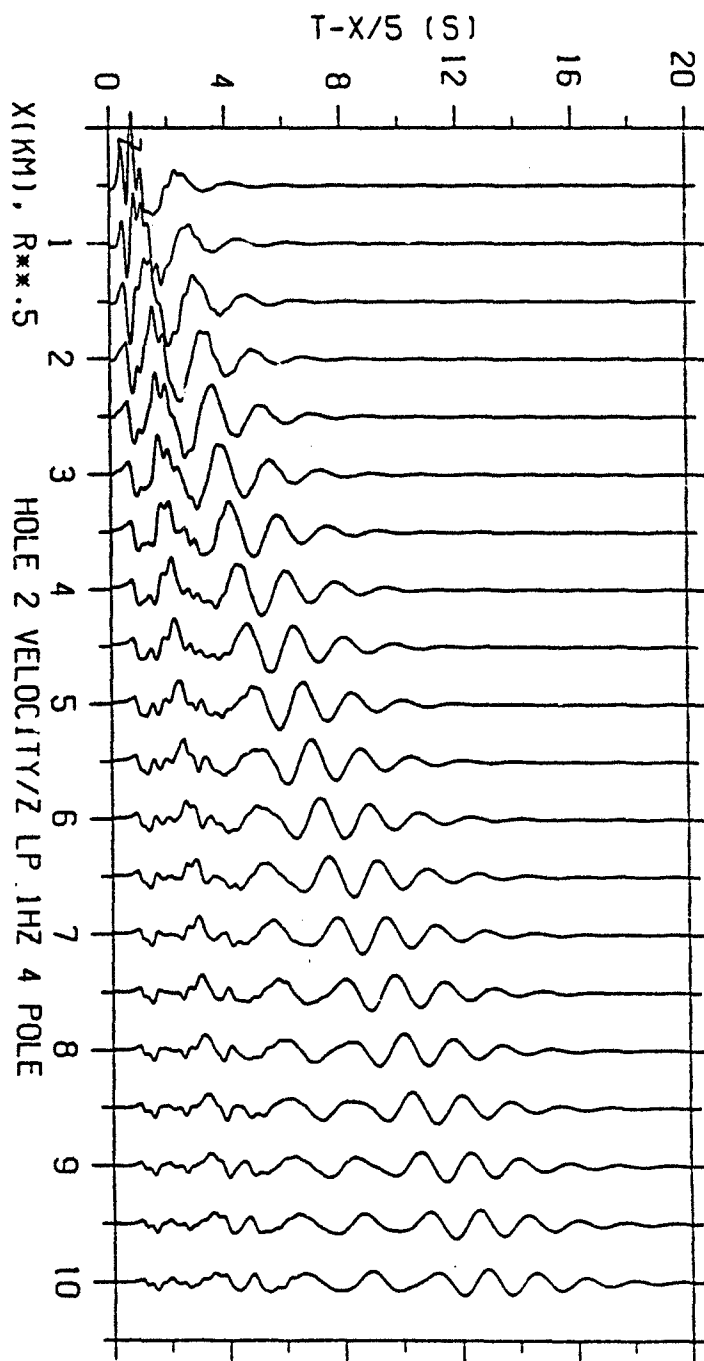
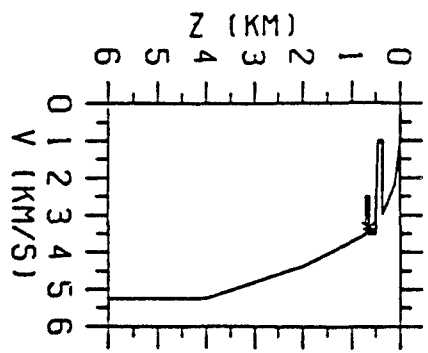
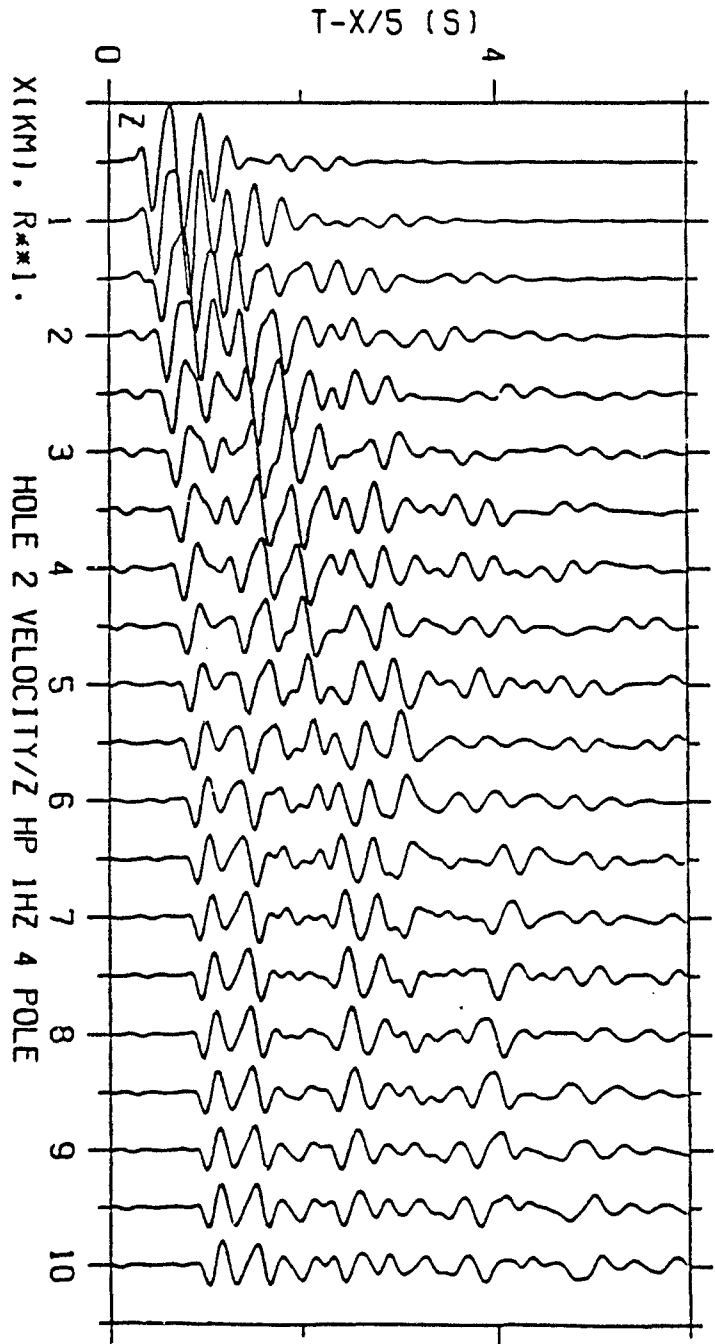


FIGURE 6c



MAX 313



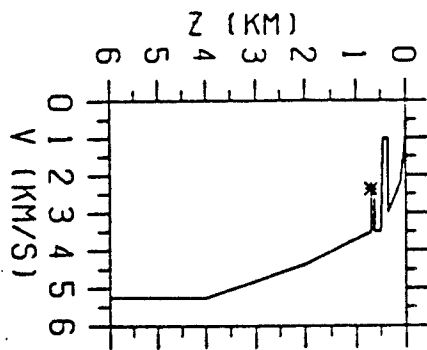
X(KM), R*1.
HOLE 2 VELOCITY/Z HP 1HZ 4 POLE

FIGURE 6d

A representative set of energy calculations as a function of time are given in Figures 7a and b. In this case the source is at a depth of 665m in the low velocity tuffs of model HOLE . The limit as t_0 approaches infinity is taken as the measure which will be applied to the observational data. The dispersion in the propagation path effects can be easily identified as at 1 km the energy plateau is reached in approximately 2 seconds while at 10 km it takes nearly 18 seconds for the final static value to be reached. These plots are for waveforms which have been low pass filtered at 1 Hz and as such they are dominated by surface waves. Plots have been scaled by r^1 to account for cylindrical divergence in surface waves. Peak values of energy in both radial and vertical plots exhibit smooth decays as a function of range. This well behaved decay is interpreted as a stable estimate of source strength with no ranges at which there are erratic variations.

Similar energy plots but now for high pass filtered waveforms which emphasize the body waves are given in Figures 8a and b. These waveforms have been scaled by r^2 to replicate spherical divergence of body waves. Dominance of body waves is illustrated by the fact that peak energy values are reached at early times at all range, at 1.5s for 1 km and 4s for the 10km range. Energy values show significant variation in the 0.5 to 2.0 km range. The radial value at the 1.0 km range is a factor of two larger than the 0.5 km value (after scaling). These wave propagation variations indicate that for short source-receiver offsets one would expect strong variations in the radiated wavefield from the HOLE velocity model. A more smoothly spatial varying wavefield is found at the greater source-receiver offsets.

Comparing the body(>1Hz) and surface(<1Hz) wave results, it is apparent that high frequencies or body waves exhibit strong variations in the 0-2 km range with surface waves or long periods showing more constant decay patterns.



MAX 1418

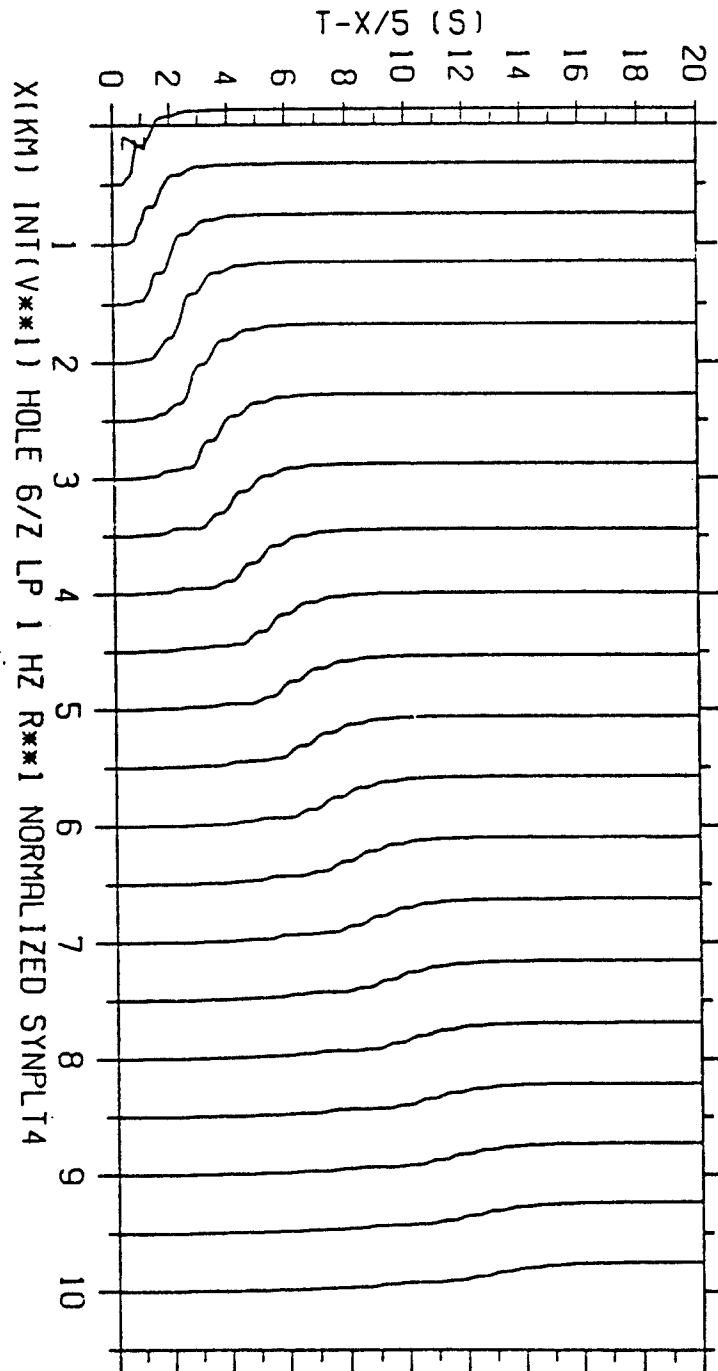
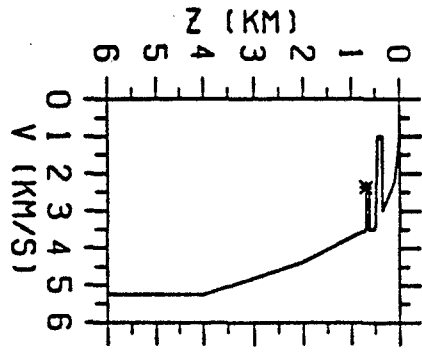


FIGURE 7a



MAX 867

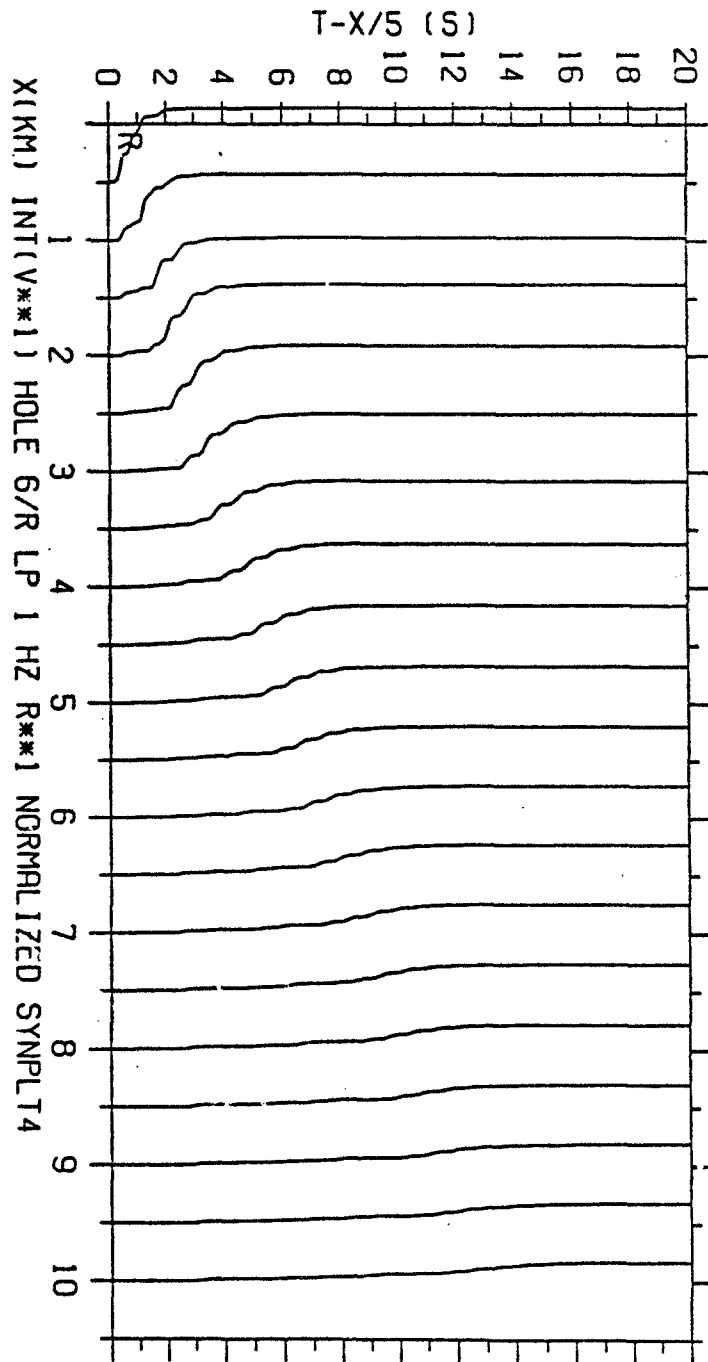
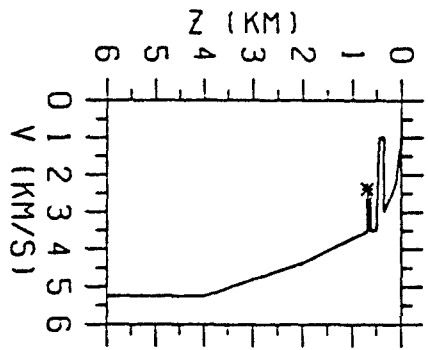


FIGURE 7b



MAX 6930

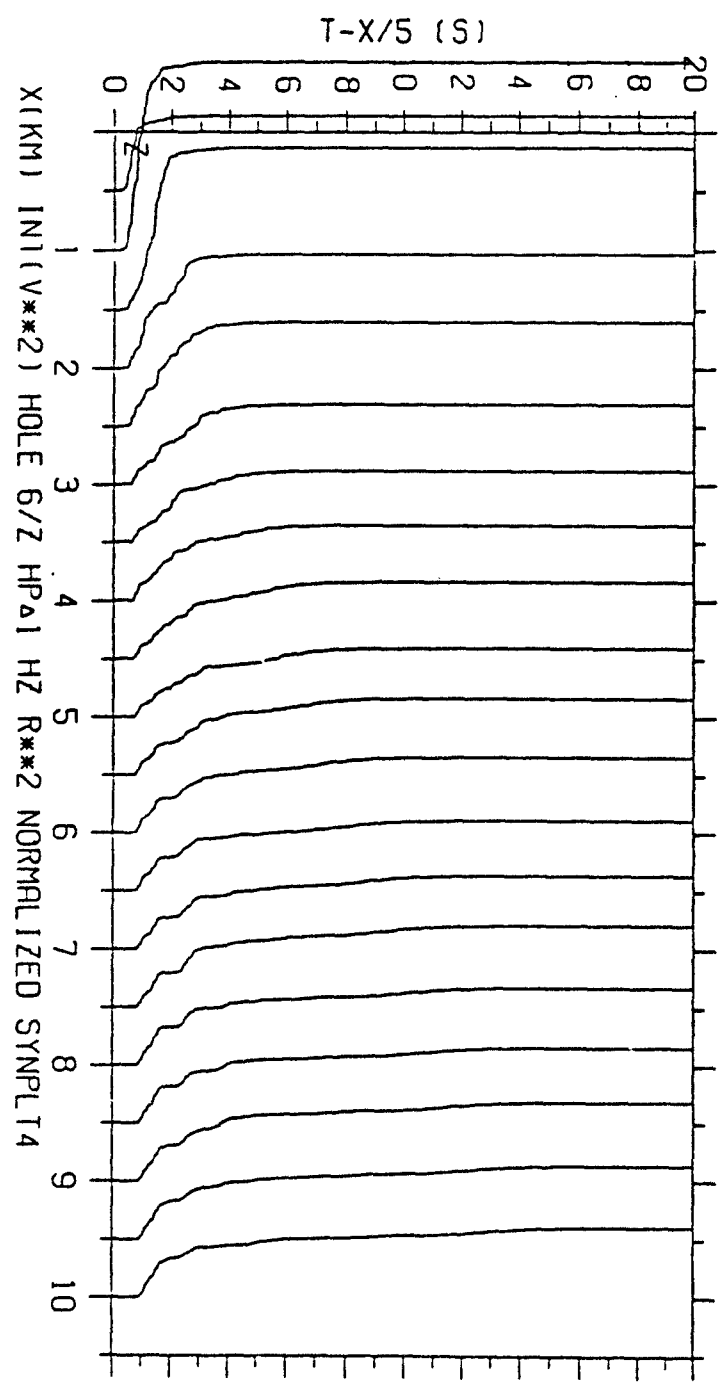


FIGURE 8a

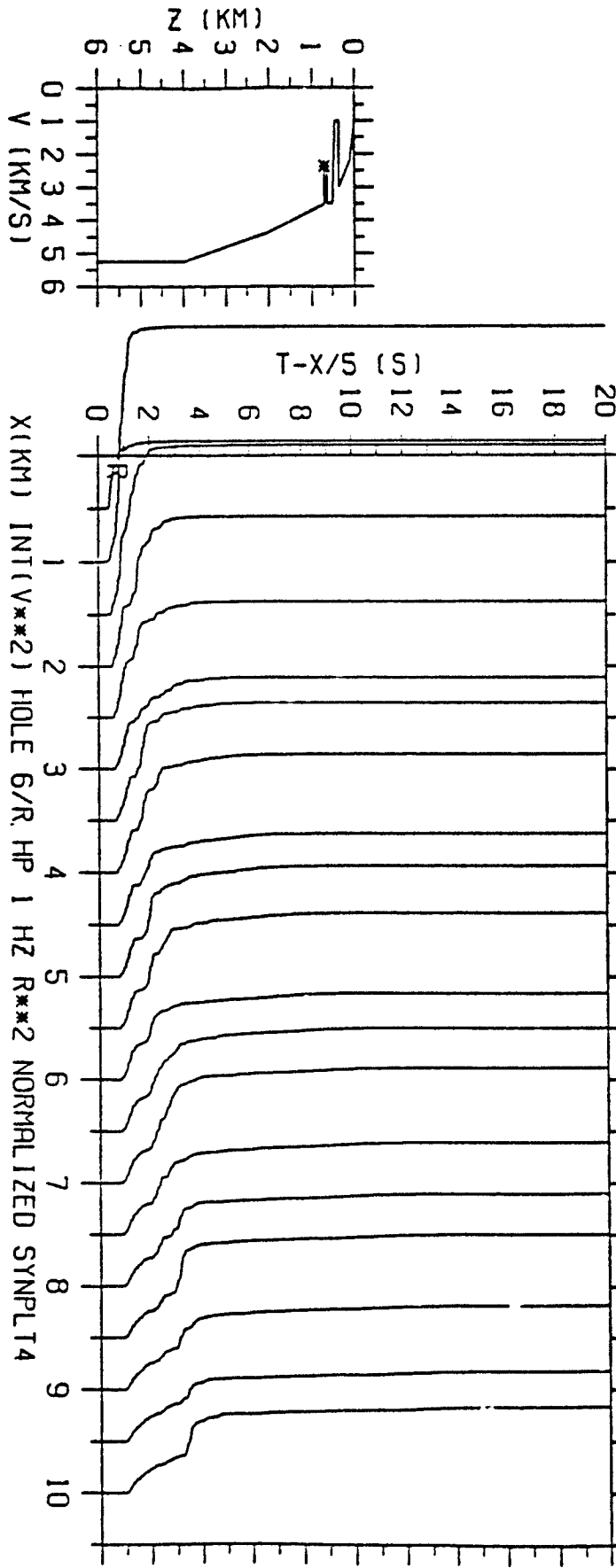
ANALYSIS

OFFSET EFFECTS: Effects of offset on amplitude and energy in a sense quantify transition from upgoing to horizontally propagating to turning rays on seismograms. Waveforms displayed in Figures 6a-d illustrate the dominance of body waves in the 0.5-2.5 km range with development of a strong surface wave contribution at more distant ranges. The body wave packet at closest ranges has a duration of 1-2s while it extends to 4s at 10 km. Surface waves in contrast extend beyond 16s at the 10 km range for the HOLE (Figure 5) velocity model. As discussed previously, energy estimates support a similar picture in terms of ground motion duration with surface waves dispersing energy over a window nearly four times the duration of that from the body waves at 10 km.

Peak velocity estimates as a function of offset for the HOLE velocity model are summarized in Figures 9a and b ($>1\text{Hz}$) and Figures 10a and b ($<1\text{Hz}$) while equivalent energy plots are given in Figures 11 and 12. These plots include data from sources at a variety of depths which will be discussed in detail latter. For purposes of quantifying offset effects numerical data for a source at 616m (solid squares in all plots) will be discussed as a characteristic data set.

High pass filtered velocity data have been scaled by r^1 to account for body wave decay while low pass filtered data have been scaled by $r^{0.5}$ to correct for surface decay. Similarly energy plots are scaled by r^2 for high pass filtered data and r^1 for low pass filtered data.

Both vertical(Z) and radial(R) high pass filtered velocities show strong geometrical effects surpassing standard r^1 elastic decay. Beyond 1 km vertical velocities decay as $r^{-1.5}$ while radial velocities decay more quickly at $r^{-1.9}$. These are elastic effects introduced by the layered velocity structure reproduced in Figure 5. The decay in amplitudes is not a smooth function as suggested by the simple decay laws but a good deal of complexity is introduced by geological structure with focusing and defocusing. Any one peak amplitude estimate can diverge from the simple decay laws by 50-100%.



MAX 5643

FIGURE 8b

SYNTHETIC PEAK VELOCITIES (4 pole HP @ 1 Hz)

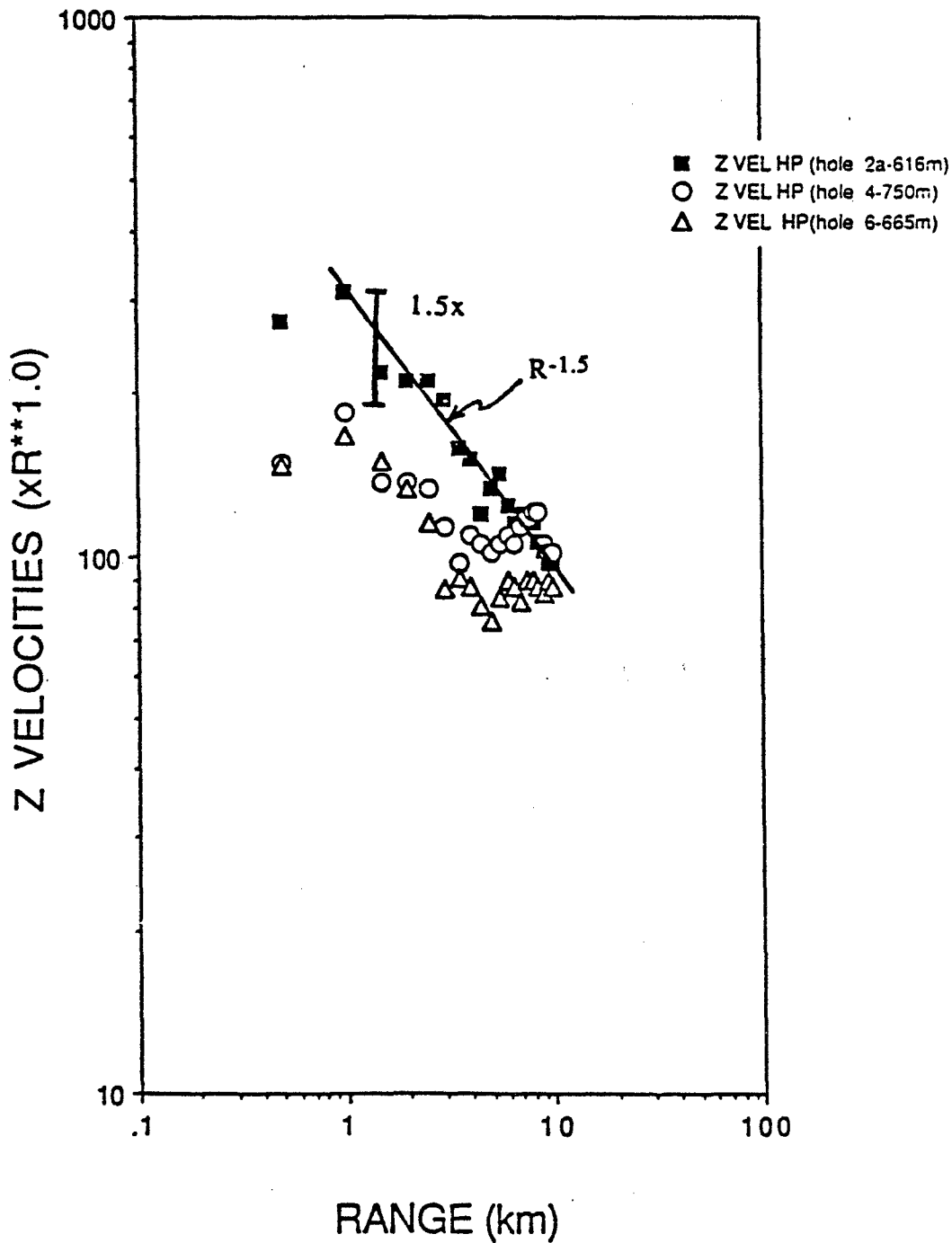


FIGURE 9a

SYNTHETIC PEAK VELOCITIES (4 pole HP @ 1 Hz)

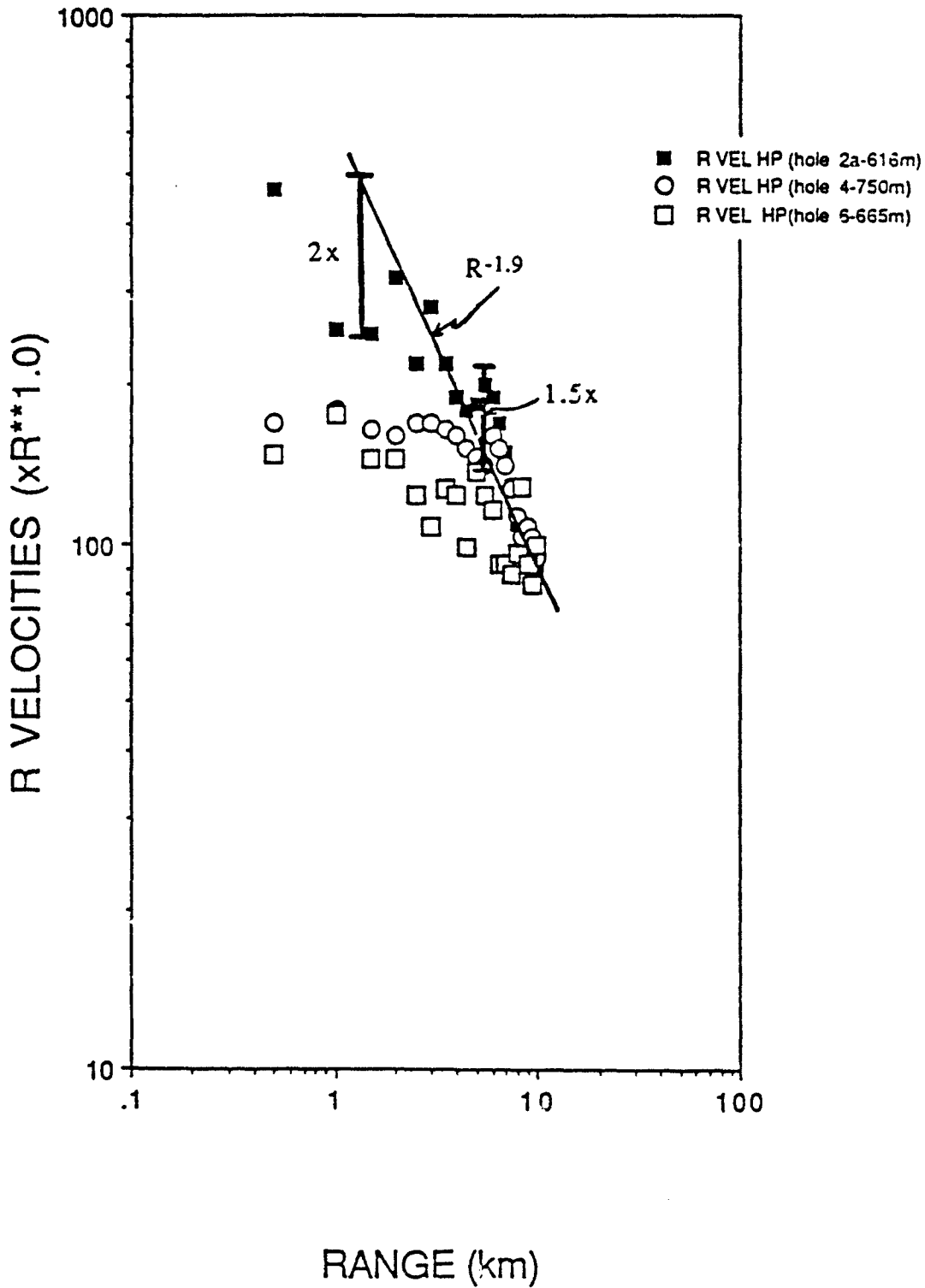


FIGURE 9b

SYNTHETIC PEAK VELOCITIES (4 pole LP @ 1 Hz)

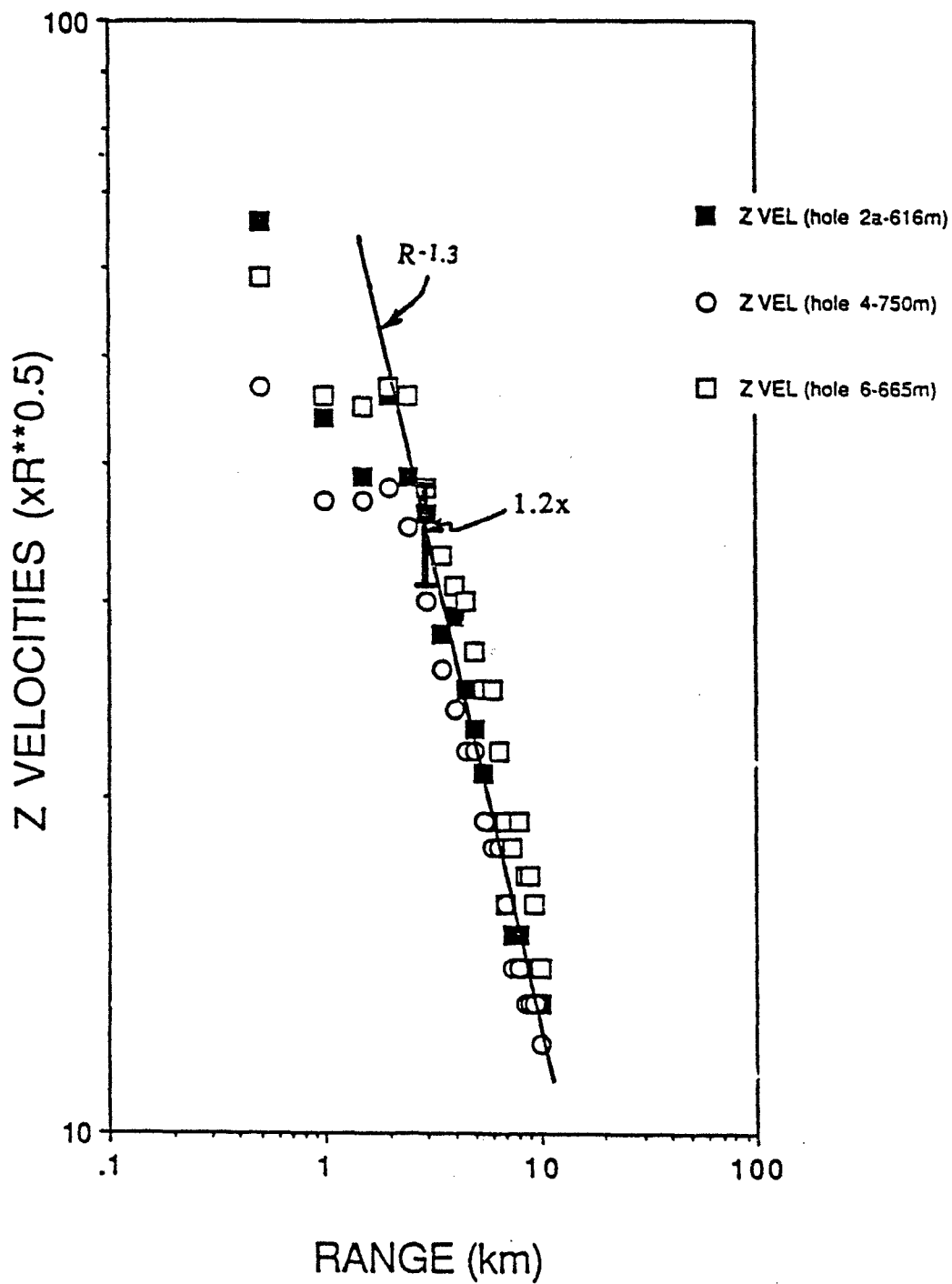


FIGURE 10a

SYNTHETIC PEAK VELOCITIES (4 pole LP @ 1 Hz)

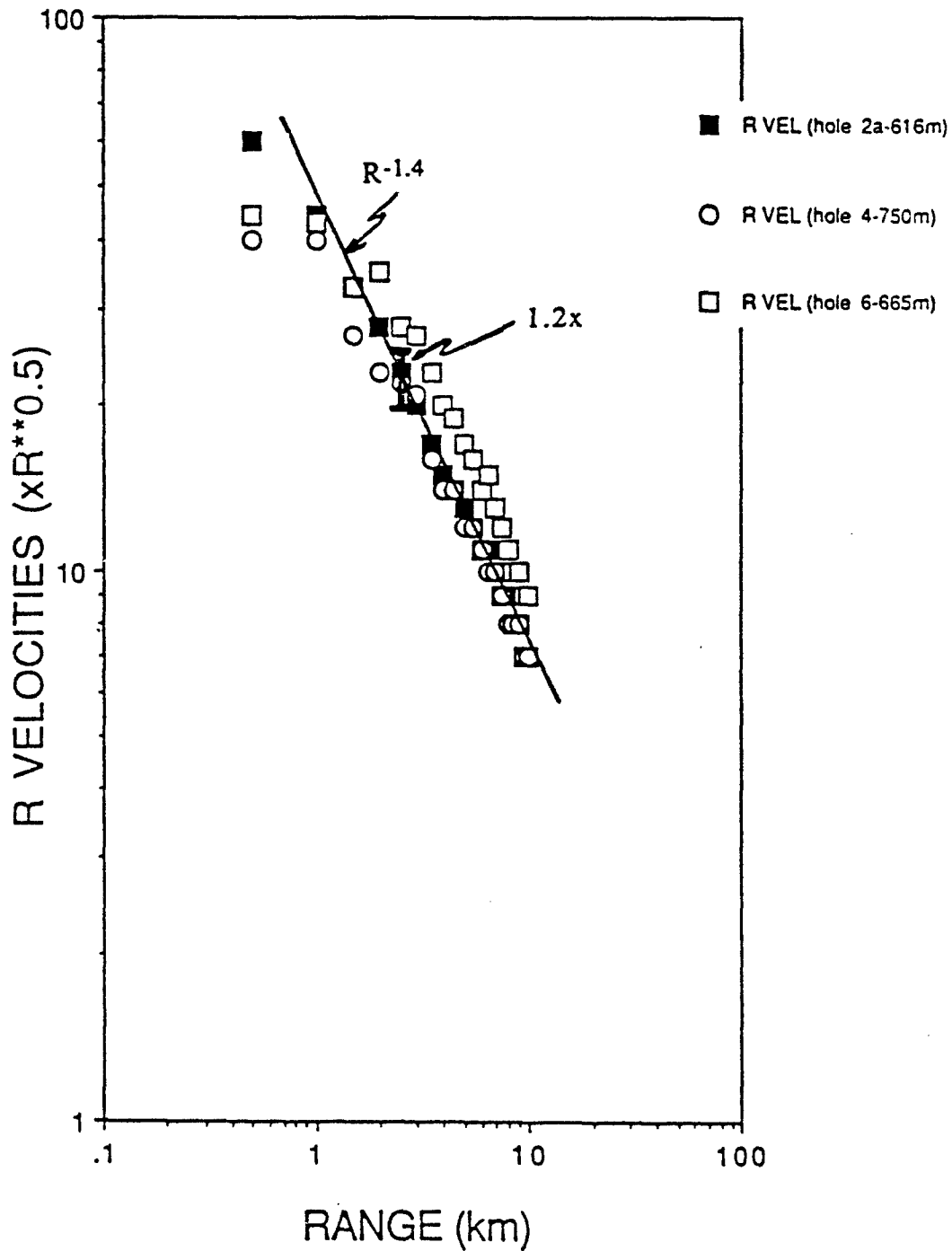


FIGURE 10b

SYNTHETIC INTEGRAL OF V^{**2} (4 pole HP @ 1 Hz)

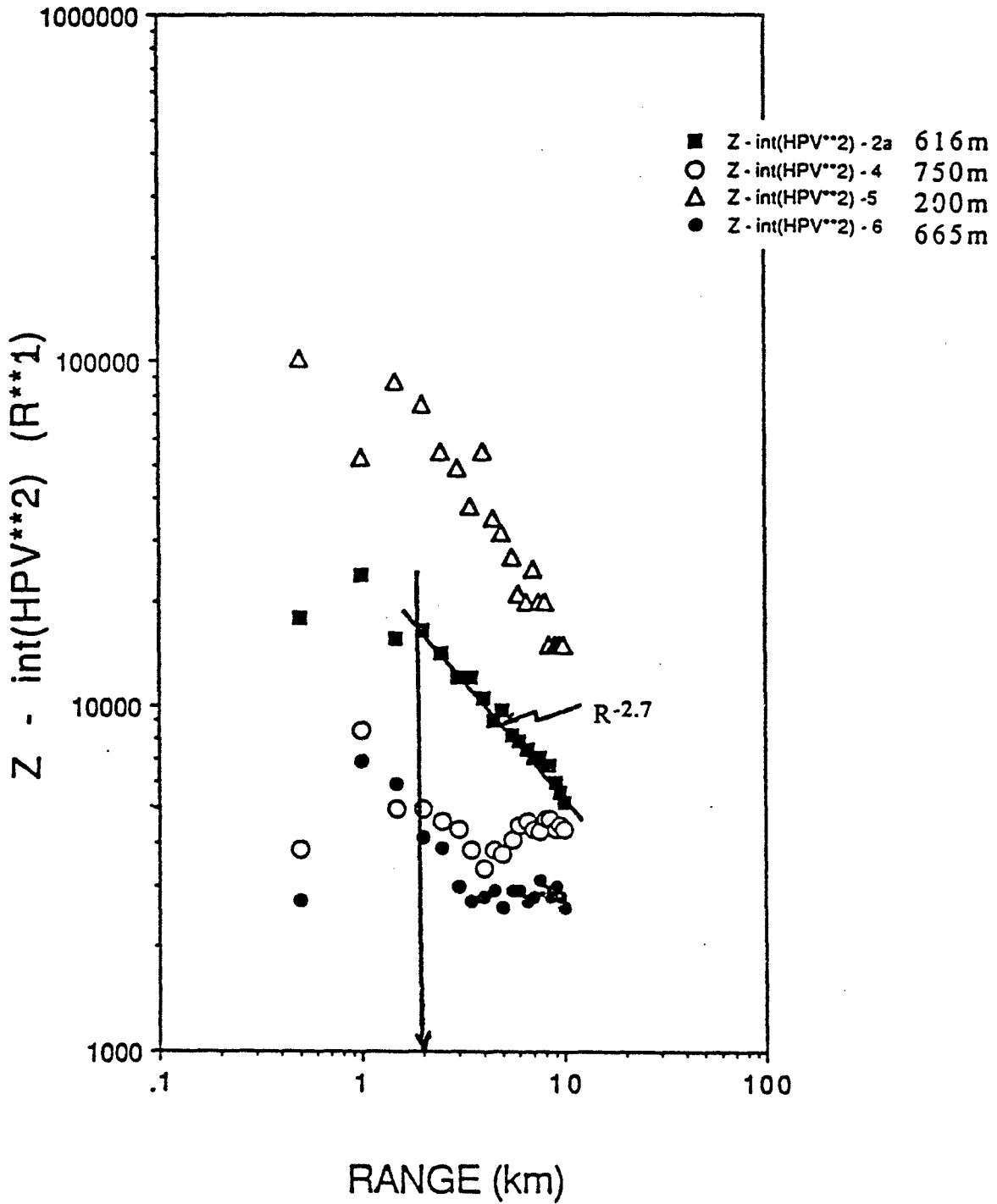


FIGURE 11a

SYNTHETIC INTEGRAL OF V^{**2} (4 pole HP @ 1 Hz)

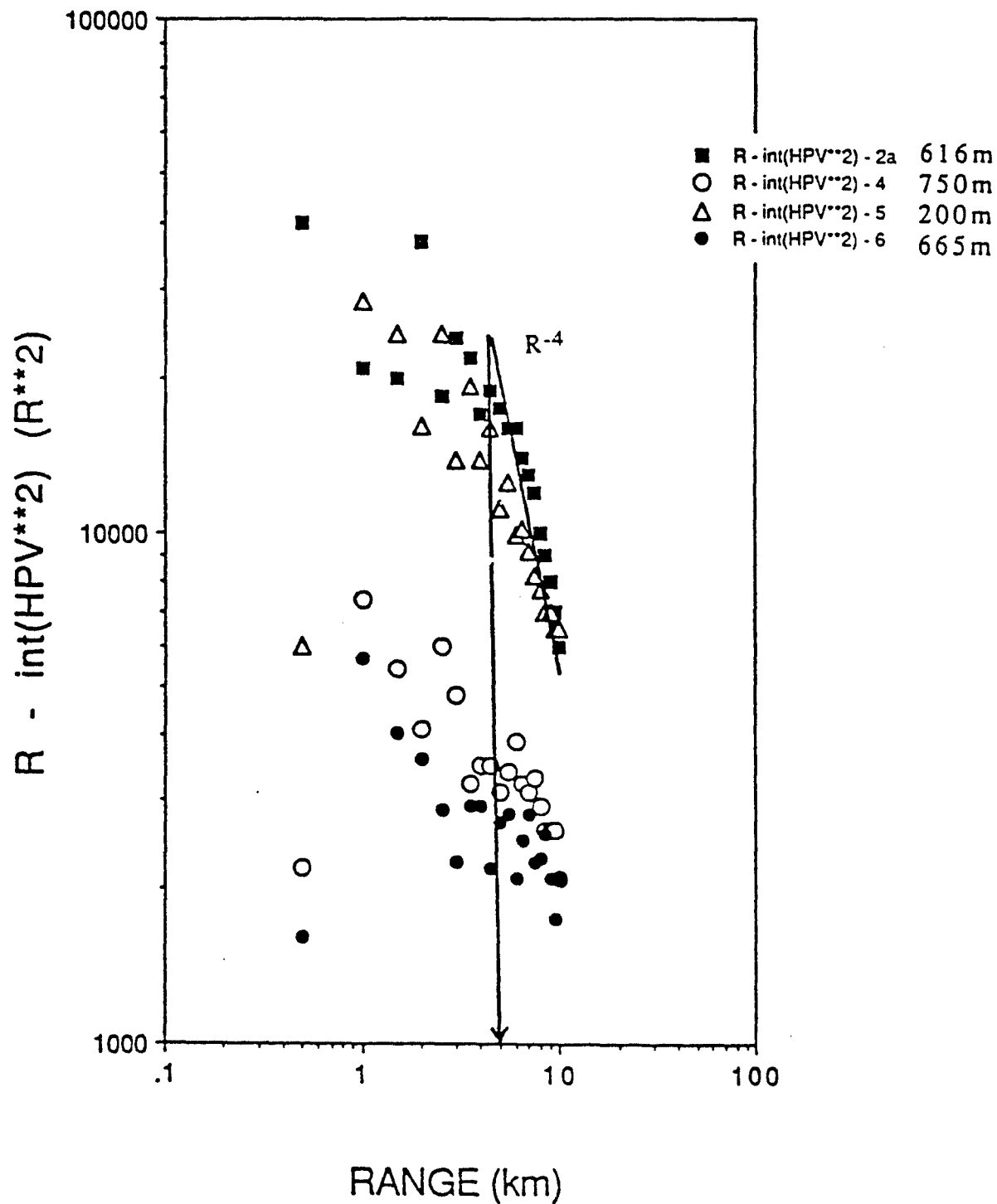


FIGURE 11b

SYNTHETIC INTEGRAL OF V^{*2} (4 pole LP @ 1 Hz)

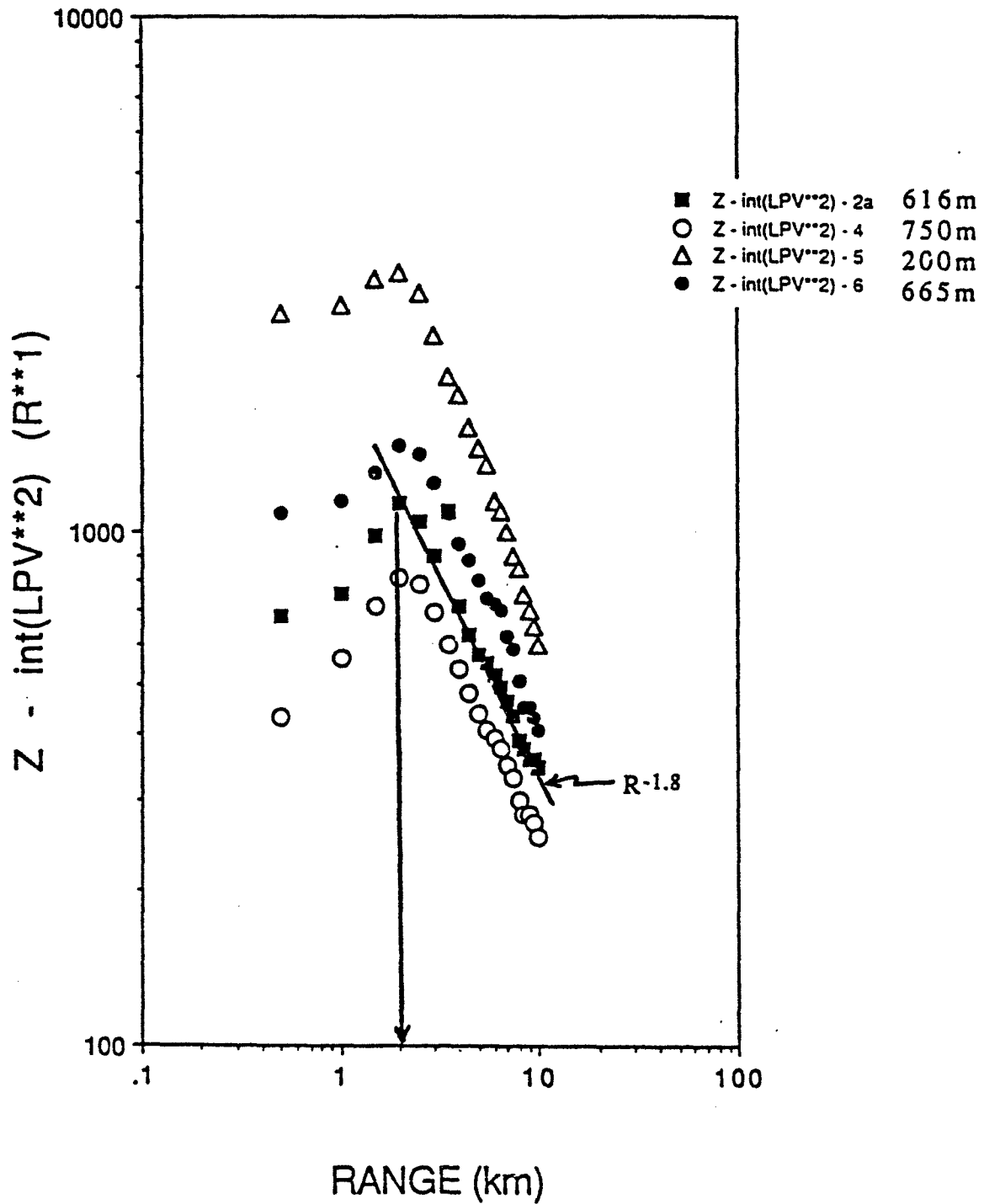


FIGURE 12a

SYNTHETIC INTEGRAL OF V^{*2} (4 pole LP @ 1 Hz)

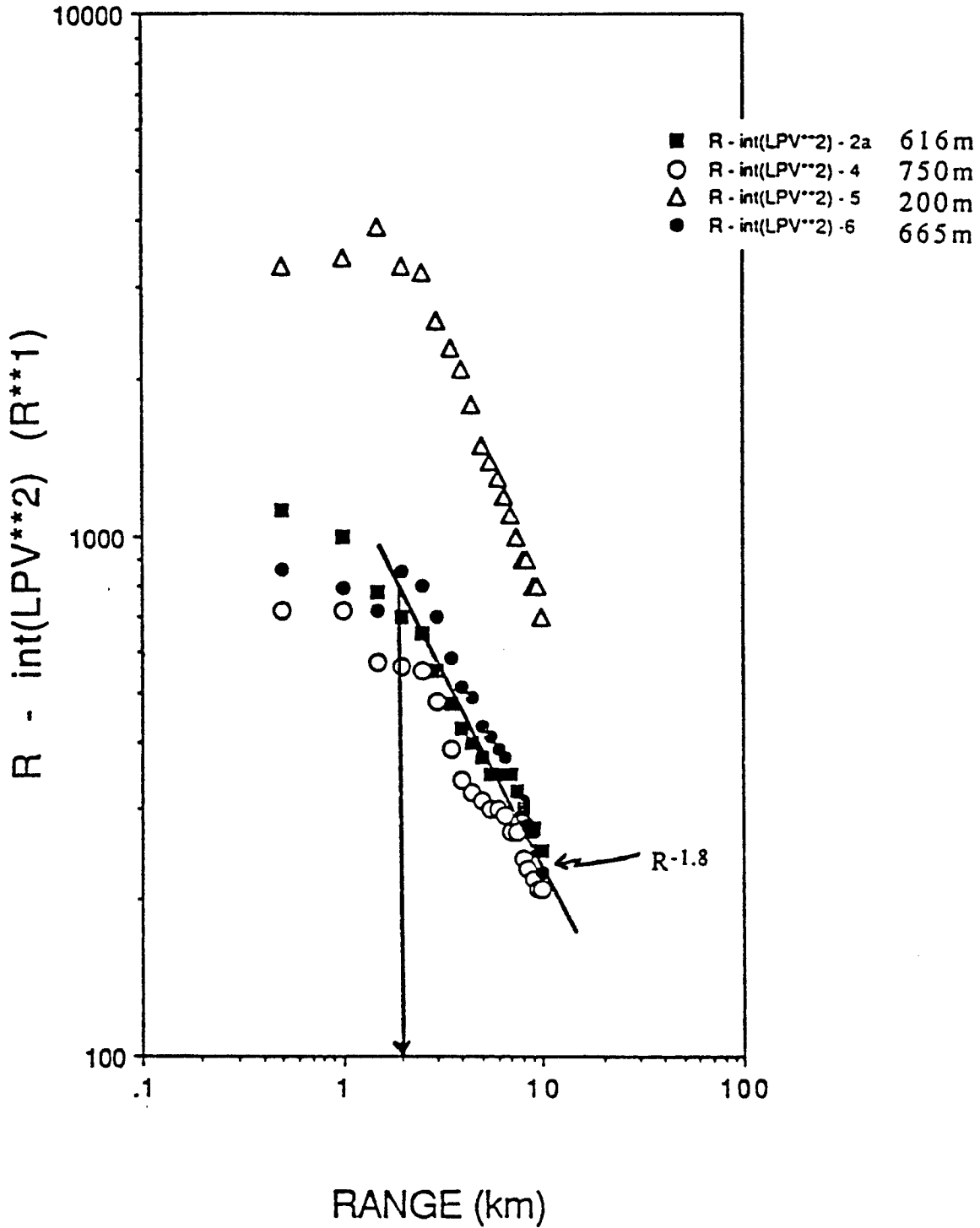


FIGURE 12b

Long period peak amplitudes (Figures 10a and b) which are dominated by surface wave contributions also show spatial decays in excess of simple $r^{-0.5}$ elastic half space results. Beyond 1-2 km decay rates are $r^{-1.3}$ for vertical surface waves and $r^{-1.4}$ for radial motions. Scatter about these decay laws is much less than that observed for body waves. As indicated in the figures, variation of any one measurement from the decay law is at most 10-20%. This result indicates the more consistent nature of long periods from the HOLE structure.

Energy estimates for both high pass (Figures 11a and b) and low pass (Figures 12a and b) filtered data are more smoothly varying as a function of offset than the peak amplitudes. This conclusion is particularly true for body wave energy above 1 Hz. For both high and low pass filtered data there is a change in decay rate at approximately 2 km. Beyond this range data decays at a constant rate. At shorter ranges data decays in some instances and increases in others. There are significant variations in energy estimates at distance ranges of less than three depths of burial. This result was found in the time series displayed in Figures 8a and b.

DEPTH OF BURIAL EFFECTS: Source depth effects are best illustrated using the smoothly varying velocity model of Leonard and Johnson (Figures 5a and b). Since peak amplitude results showed significant station to station variability and energy estimates utilizing the entire waveform are more consistent between individual stations, depth of burial results will be quantified with the integral of velocity squared. Frequency effects were determined by high and low pass filtering of the data at 1 Hz.

Major depth changes were considered with sources at 200m, 400m, and 616m. Low pass filtered vertical and radial peak energy estimates are reproduced in Figures 13a and b while high pass filtered data are given in Figures 14a and b. Shallow sources yield larger energy estimates at the free surface as determined from the time integral of ground velocity squared. As much as a factor of ten increase in energy existed for a source buried at 200m compared to the one at 616m. Differences in energy estimates decreased with offset, reaching values close to 2 at 10km. These source energy differences can be compared to the geometrical decay of energy over the observation range of 0.5 to 10 km. For high frequencies the energy differences (0.5 to 10 km) are between

SYNTHETIC INTEGRAL OF V^{**2} (4 pole LP @ 1 Hz)

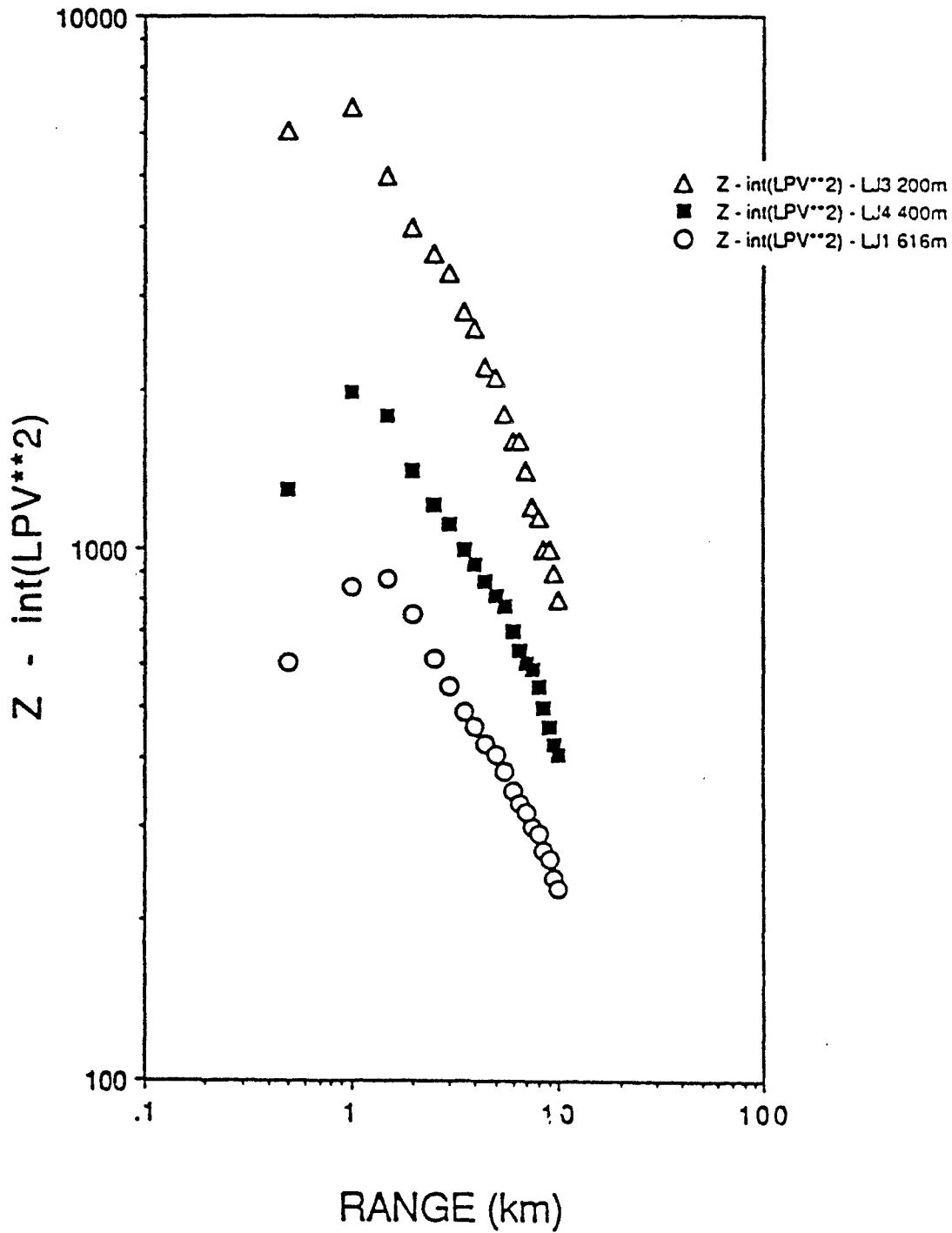


FIGURE 13a

SYNTHETIC INTEGRAL OF V^{*2} (4 pole LP @ 1 Hz)

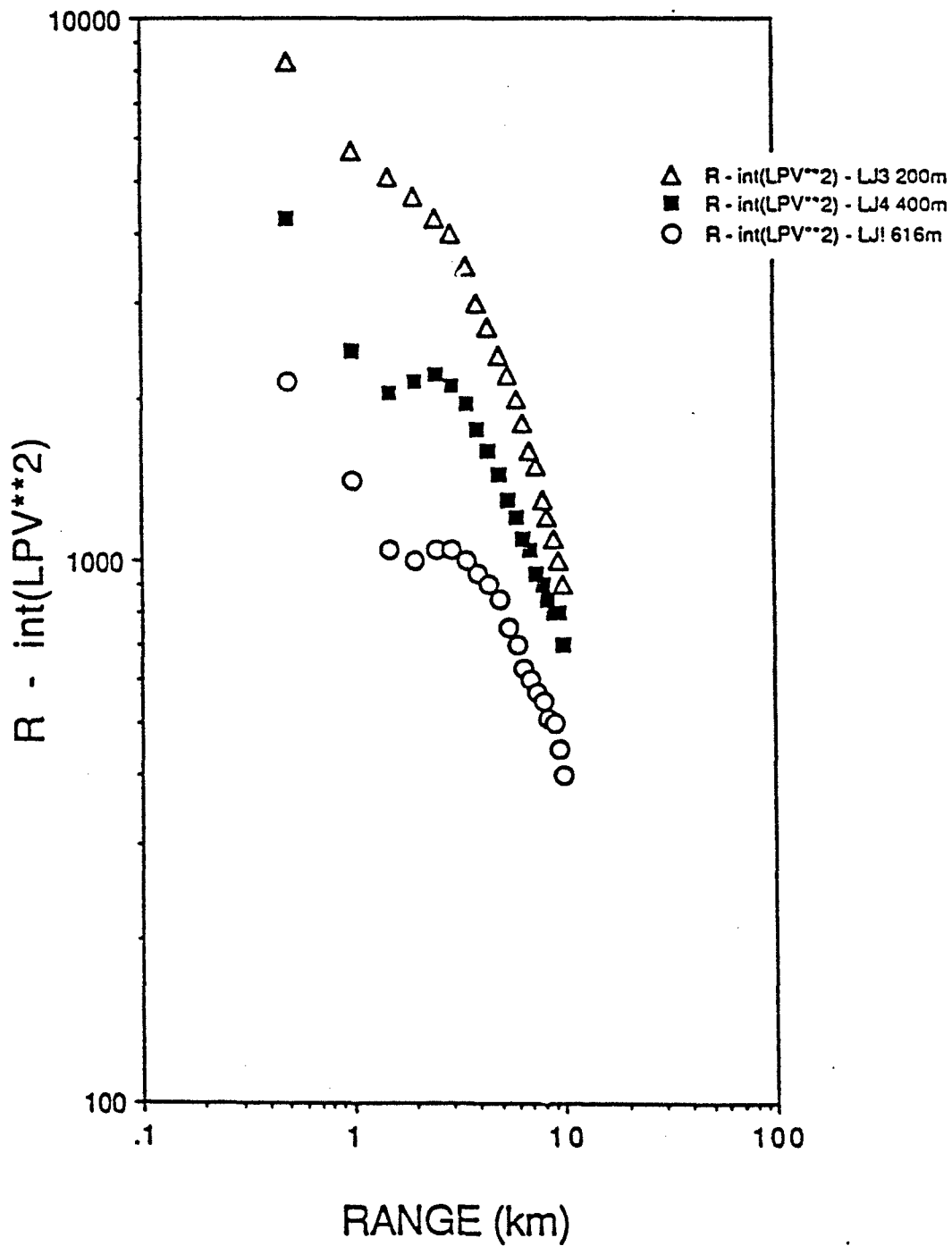


FIGURE 13b

SYNTHETIC INTEGRAL OF V^{*2} (4 pole HP@ 1 Hz)

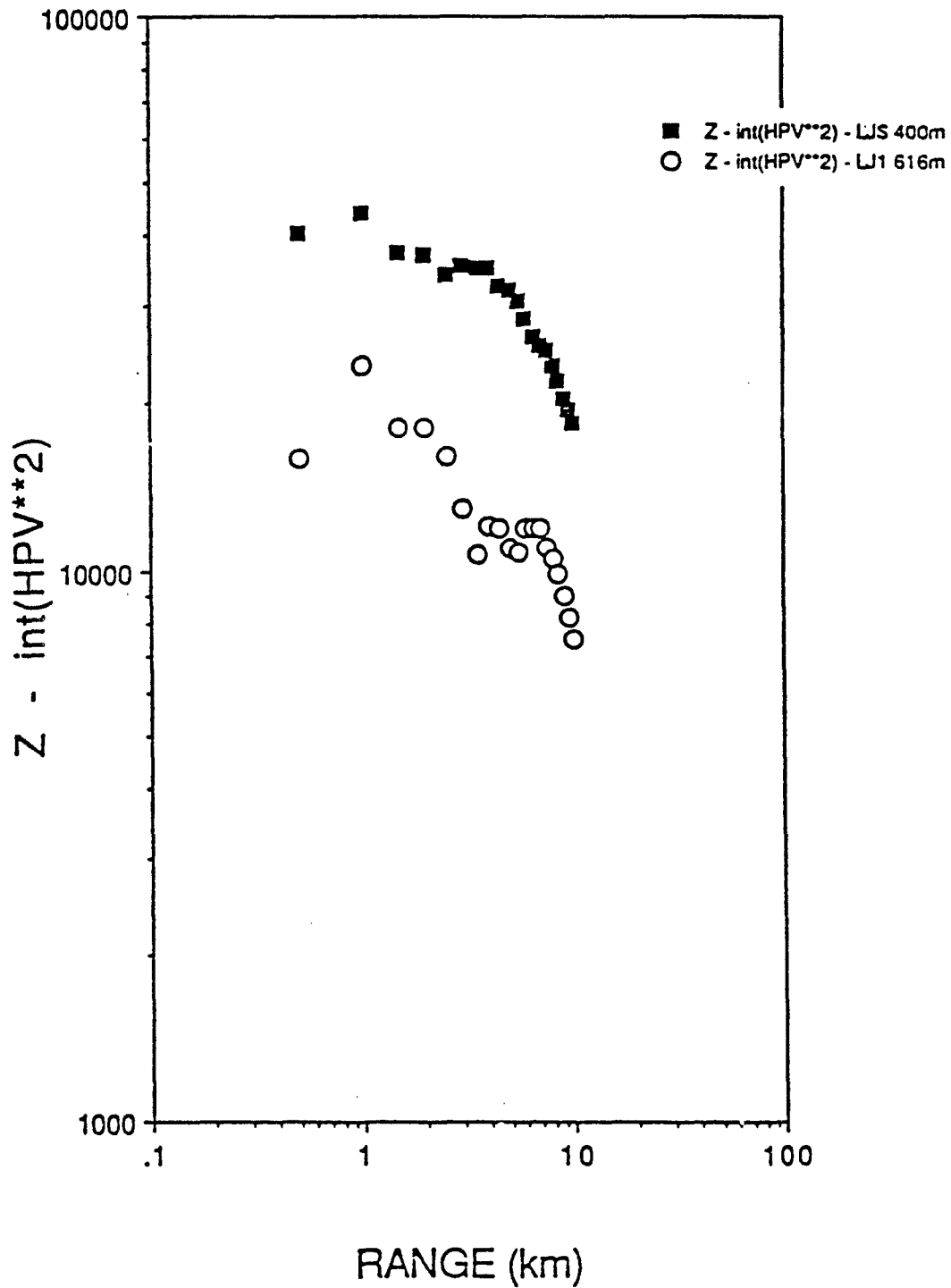


FIGURE 14a

SYNTHETIC INTEGRAL OF V^{*2} (4 pole HP @ 1 Hz)

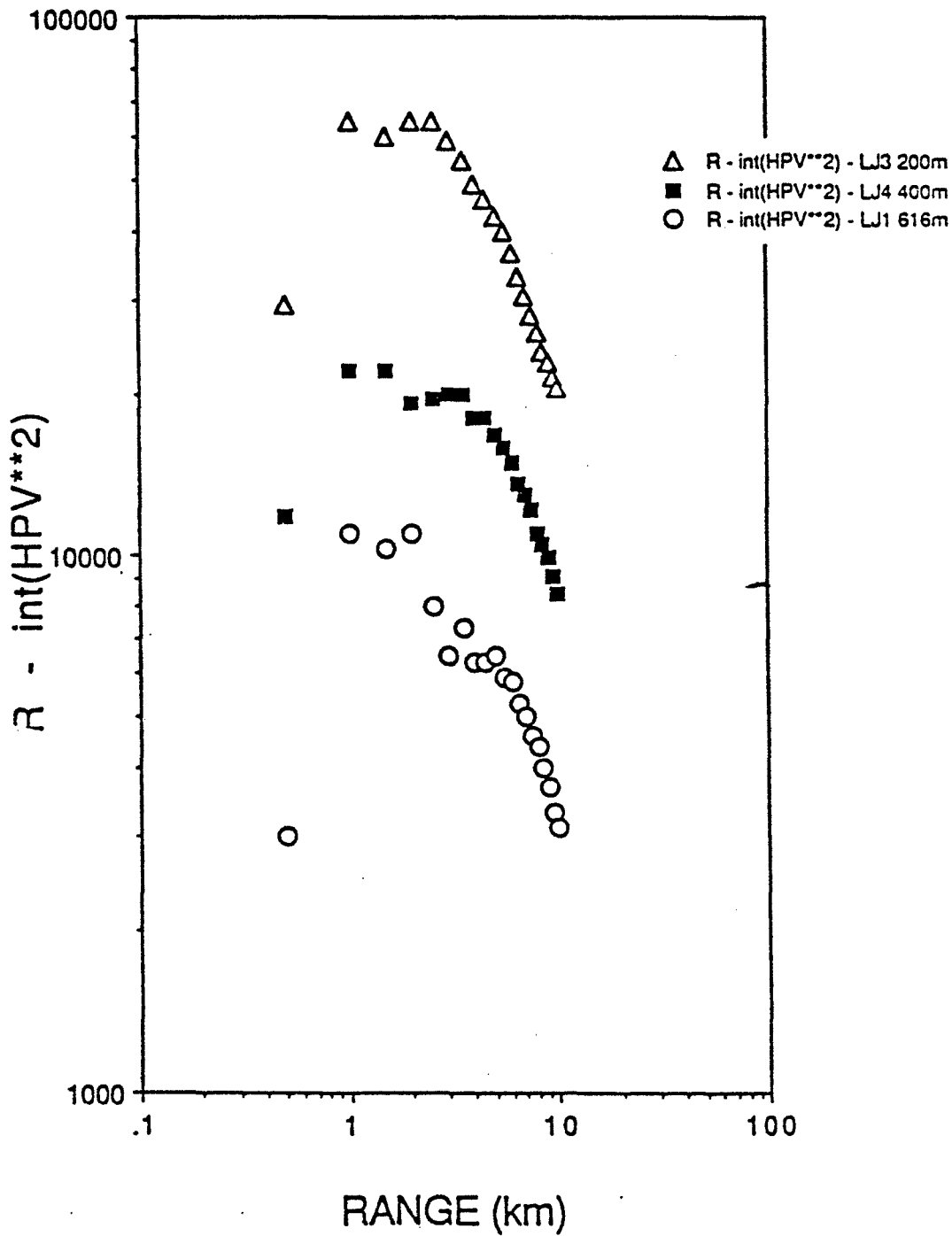


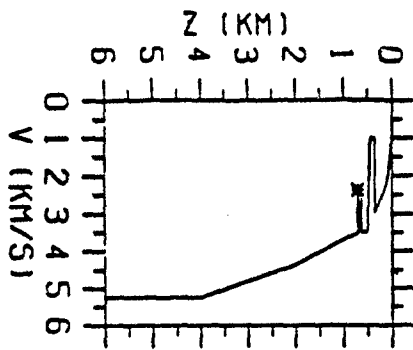
FIGURE 14b

1000-2000 while for the low frequencies they are between 75-160. In both the high and low pass data sets the spatial decay is between 1 and 2 orders of magnitude greater than the energy differences at a constant range for sources at 200,400 and 616m depths. These 'energy' values are for the integral of velocity squared. Taking the square root of results gives numbers comparable to velocity estimates given earlier. Variations between the 400 and 616m sources in the low pass data then become 1.4 at 0.5 km and 1.3 at 10 km.

Errors in depth estimation should be much smaller than variations introduced in these numerical trials. It is concluded that errors in waveforms introduced through depth errors are small. In contrast spatial decay of these effects is strong enough that accurate spatial locations of receivers is important. Data in the 5-10 km range exhibit the smallest variation with source depth. Data below 1 Hz were found to give more stable estimates.

INTERFACE EFFECTS: The third goal of this numerical exercise was to quantify effects near source interfaces have on radiated seismic energy. The HOLE velocity model was chosen to explore this variation. As indicated in Figure 5, there is an approximate 30% decrease in P velocity at 630m depth extending to 700m. This depth range is close to the scaled depth for a 150 kton explosion. The velocity decrease is representative of velocity changes found at Pahute Mesa of the the Nevada Test Site. They are representative of variations introduced by the amount of welding in the tuffs and transitions to rhyolitic lavas. In order to quantify these geological effects on seismic radiation a set of synthetic calculations were completed with sources at 616m (above low velocity zone), 665m (in low velocity zone), and 750m (below low velocity zone). Waveforms for the 616m source have been reproduced in Figures 6a and b. Radial and vertical velocity records for the 665m source are in Figures 15a and b while those for the 750m source are in Figures 16a and b. Comparison of these three sets of time series identifies a dramatic decrease in amplitudes for the 665 and 750m sources relative to that at 616m. This decrease in amplitude for the two deeper sources is greatest at closest offsets and is balanced at farther ranges by slower spatial decay rates for deeper sources.

These conclusions can be further illustrated by comparing peak velocities. Figures 9a and b reproduce the peak amplitudes from



174

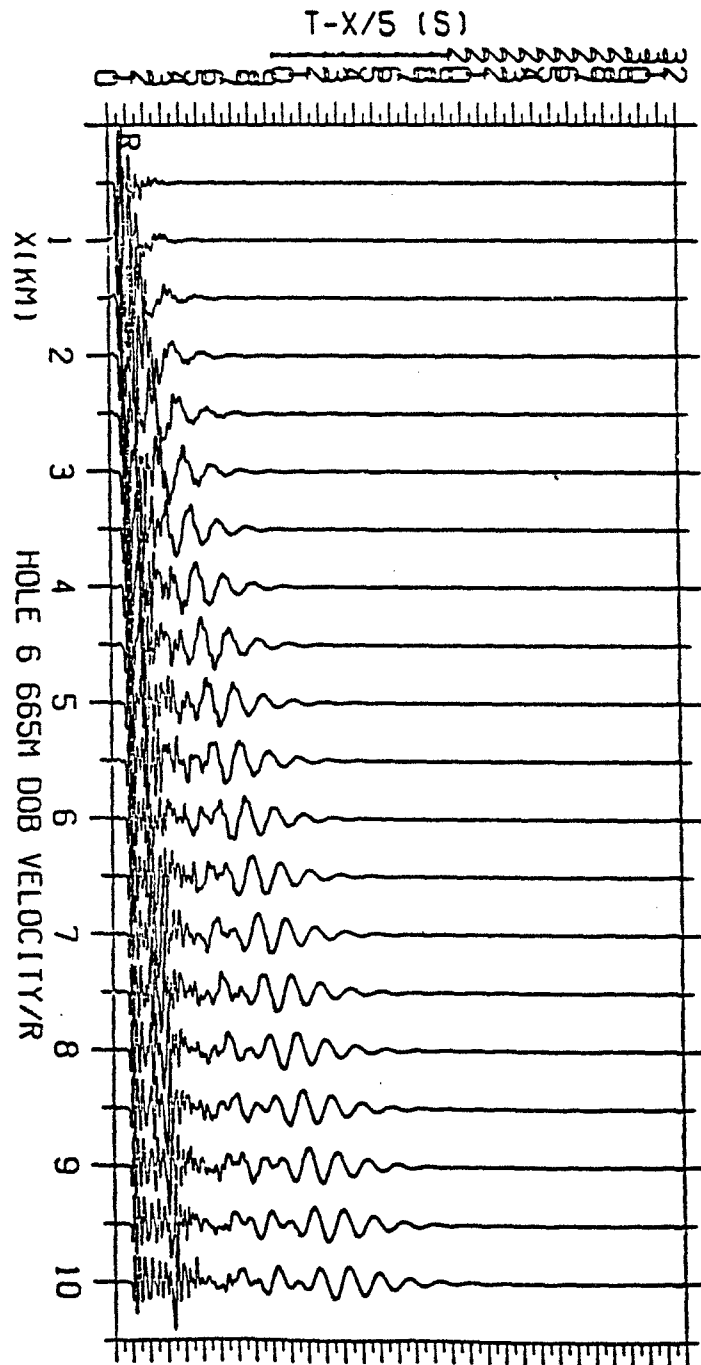
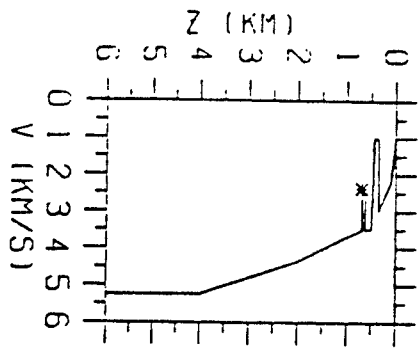


FIGURE 15a



176

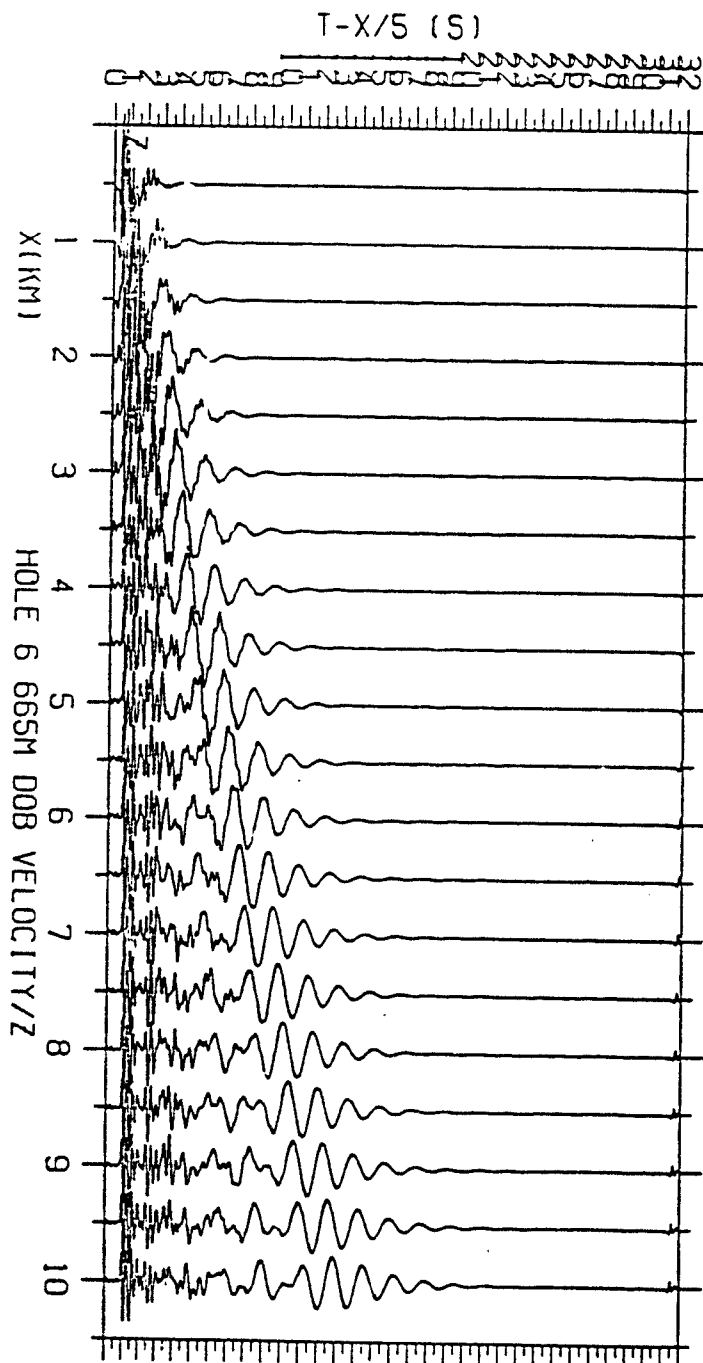
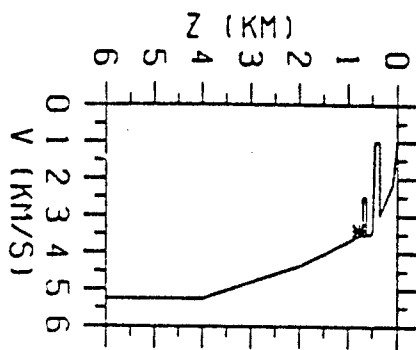


FIGURE 15b



149

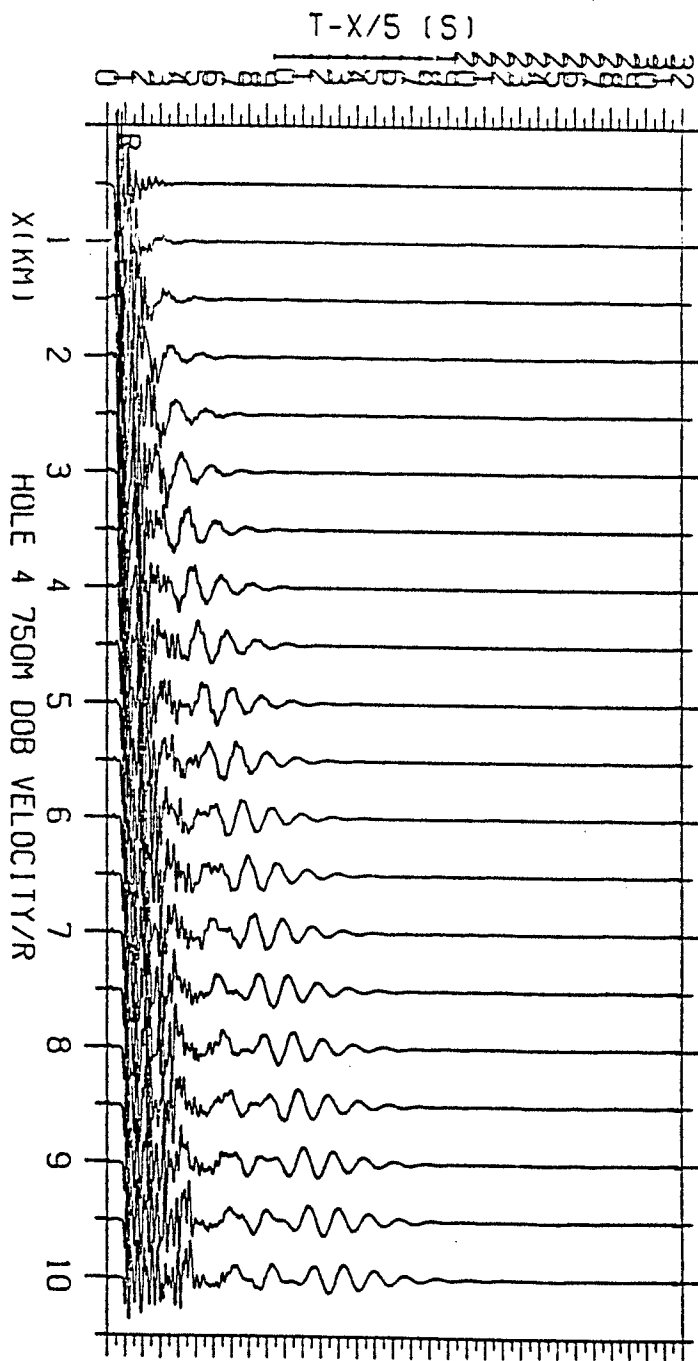
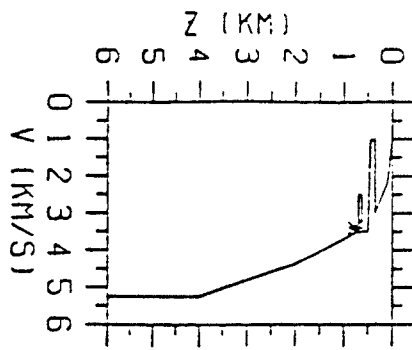


FIGURE 16a



159

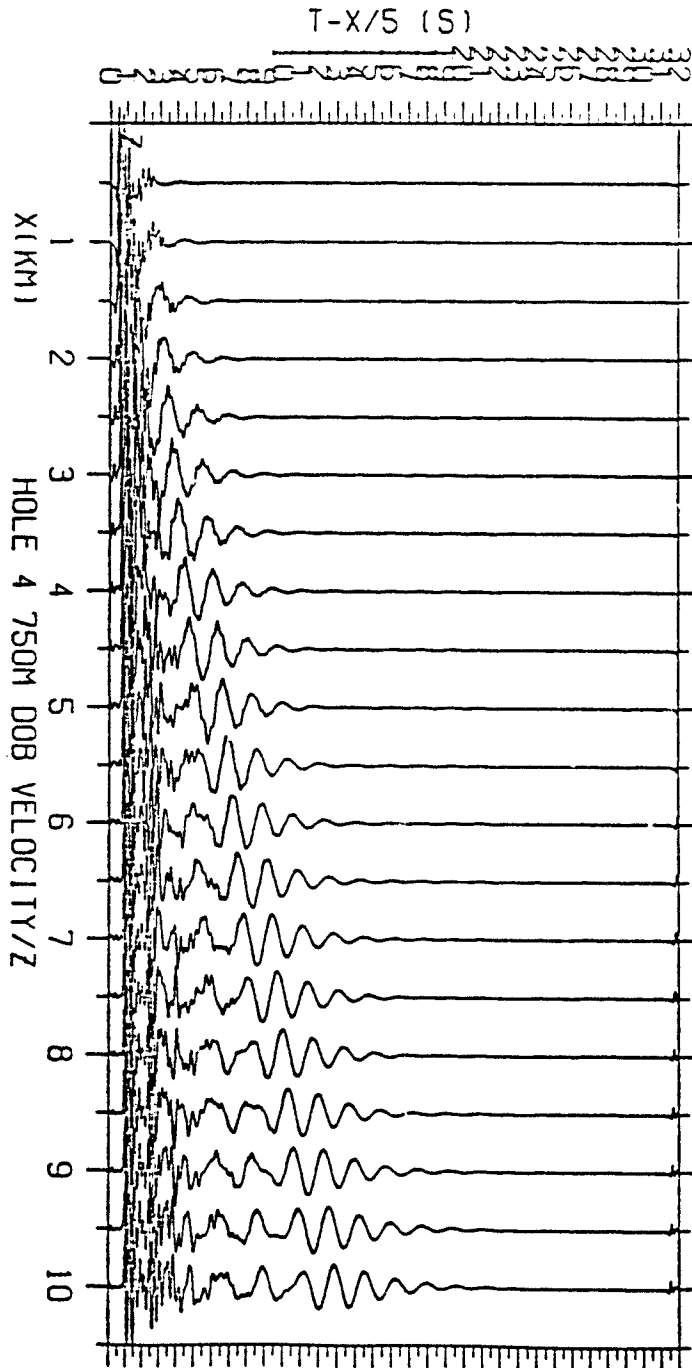


FIGURE 16b

the high pass filtered data ($>1\text{Hz}$) which are dominated by body waves. Over the 0.5-3km range, the 616m source yields peak amplitudes that are a factor of two or more greater than those for the two deeper sources. Although there is a great deal of scatter in these peak amplitude estimates, data from all three depths of burial merge near 10 km.

Energy estimates were made for the same high pass filtered data as well as for a source at 200m DOB in the HOLE velocity structure. Comparisons of these estimates are given in Figures 11a and b. As with peak velocity data, energy estimates indicate a wide difference for data from above (616 and 200m) and below (665 and 750m) the interface at the shortest offsets. This difference decreases with range. The major effect in the near source waveforms occurs as the source moves below the first interface of the low velocity zone. The 665m source which is in the low velocity zone gives results which are nearly identical to those for the source at 750m which is completely below the low velocity zone.

Long period ($>1\text{Hz}$) peak amplitude data are given in Figures 10 a and b. Differences between sources above and below the interface exhibited by the body waves are greatly reduced for near source long period ($<1\text{Hz}$) surface waves. There is a 20% difference between peak amplitudes for all three source depths. Long period energy estimates are reproduced in Figures 12a and b along with estimates for the 200 m source. There is less than a factor of 2 difference in total energy for the three source depths with this difference again decreasing with range. At 10km this energy difference is a factor of 1.8 for the vertical motions and 1.2 for the radial. In units of velocity this reduces to factors of 1.3 and 1.1 respectively. These small differences are contrasted by the large differences already discussed for the 200m DOB source.

Interface effects are strongest in high frequency body waves. In all cases the effect of moving a source above or below an interface near the scaled depth for a 150 kton explosion decreases with range. The smallest variations in surface seismic radiation are found for long period motions ($<1\text{Hz}$) which are dominated by surface waves. At 10 km range the square root of the integral of squared velocity is found to vary by a factor of 1.3-1.1 as sources are moved above and below a realistic low velocity zone near shot depth.

VELOCITY MODEL COMPARISONS: The final issue that was addressed in these synthetic tests was the importance of a site specific velocity model (such as that developed from a downhole log at the test site) in contrast to an average model for a test site. In order to quantify this discussion synthetic velocity records were developed for the 'average' Leonard and Johnson velocity model and the 'site specific' HOLE \ velocity log. Sources for this final comparison were placed at a depth of 616m. Vertical and radial synthetics were high pass filtered at 1Hz (Figures 17a and b) and low pass filtered at 1 Hz (Figures 18a and b) for comparison. Peak velocity differences in these models are remarkably small. The biggest differences occurs at the smallest offsets. Radial data in Figure 17b for the two velocity models nearly match one another beyond the 3 km range. The one difference from this general trend is in the low frequency radial data where the two velocity models lead to a diverging set of curves with increasing range.

Of the effects considered which include source-receiver offset, source depth, proximity to an interface, and average/site specific velocity model, the velocity model seems to have the least effect on peak amplitudes for the target depth of 616m.

LJ and HOLE PEAK VELOCITIES (4 pole @ 1 Hz)

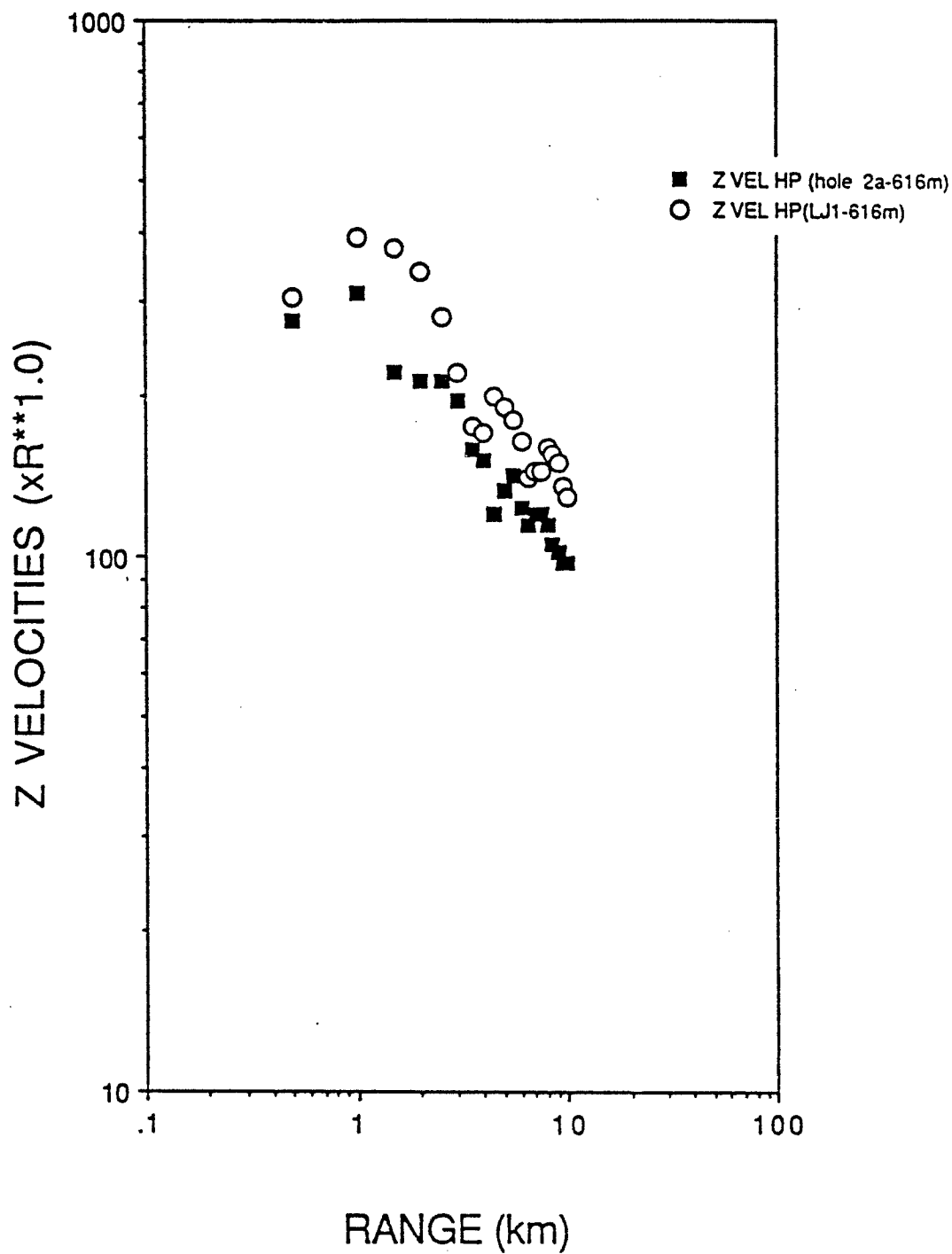


FIGURE 17a

LJ and HOLE PEAK VELOCITIES (4 pole @ 1 Hz)

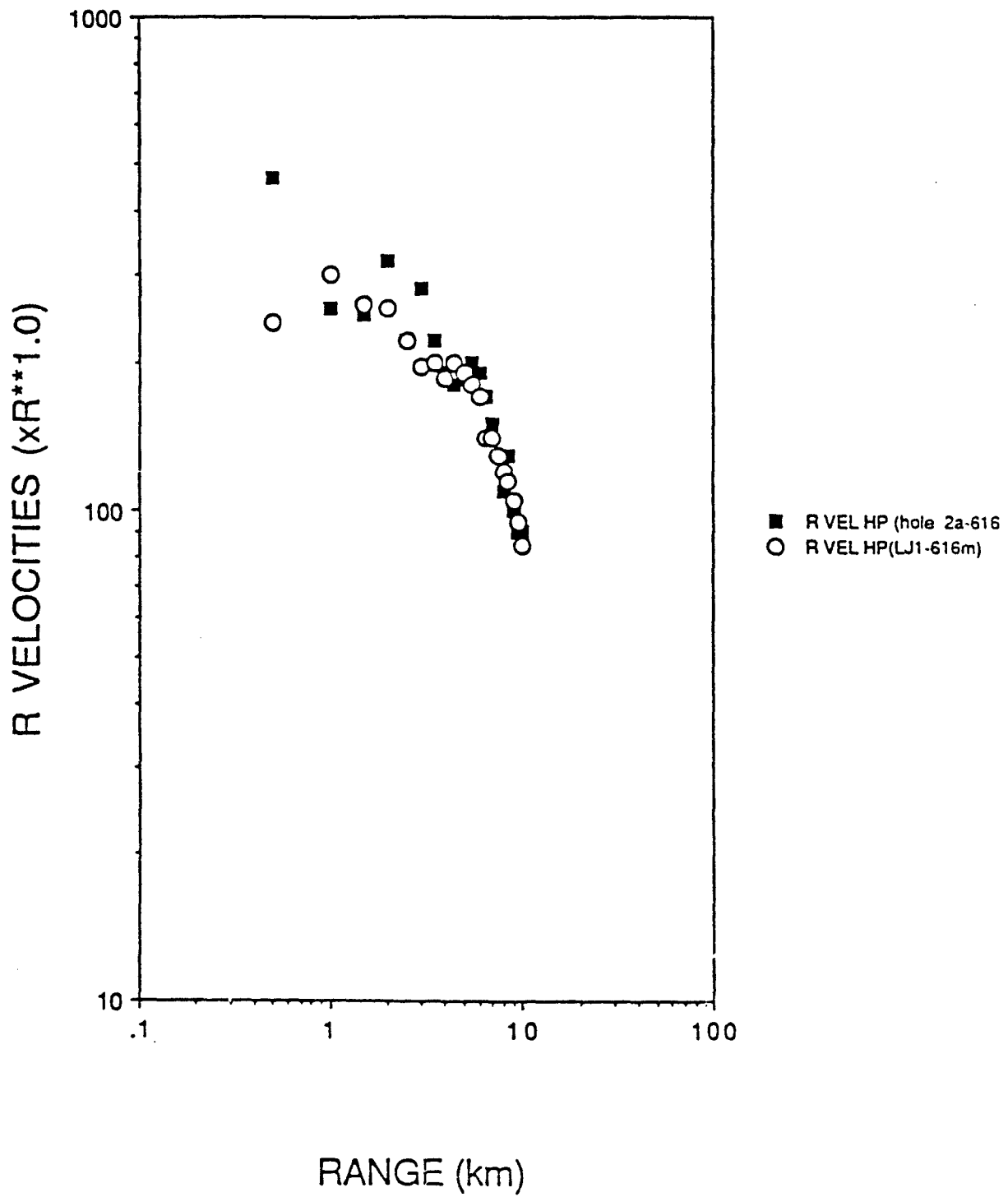


FIGURE 17b

LJ and HOLE PEAK VELOCITIES (4 pole LP @ 1 Hz)

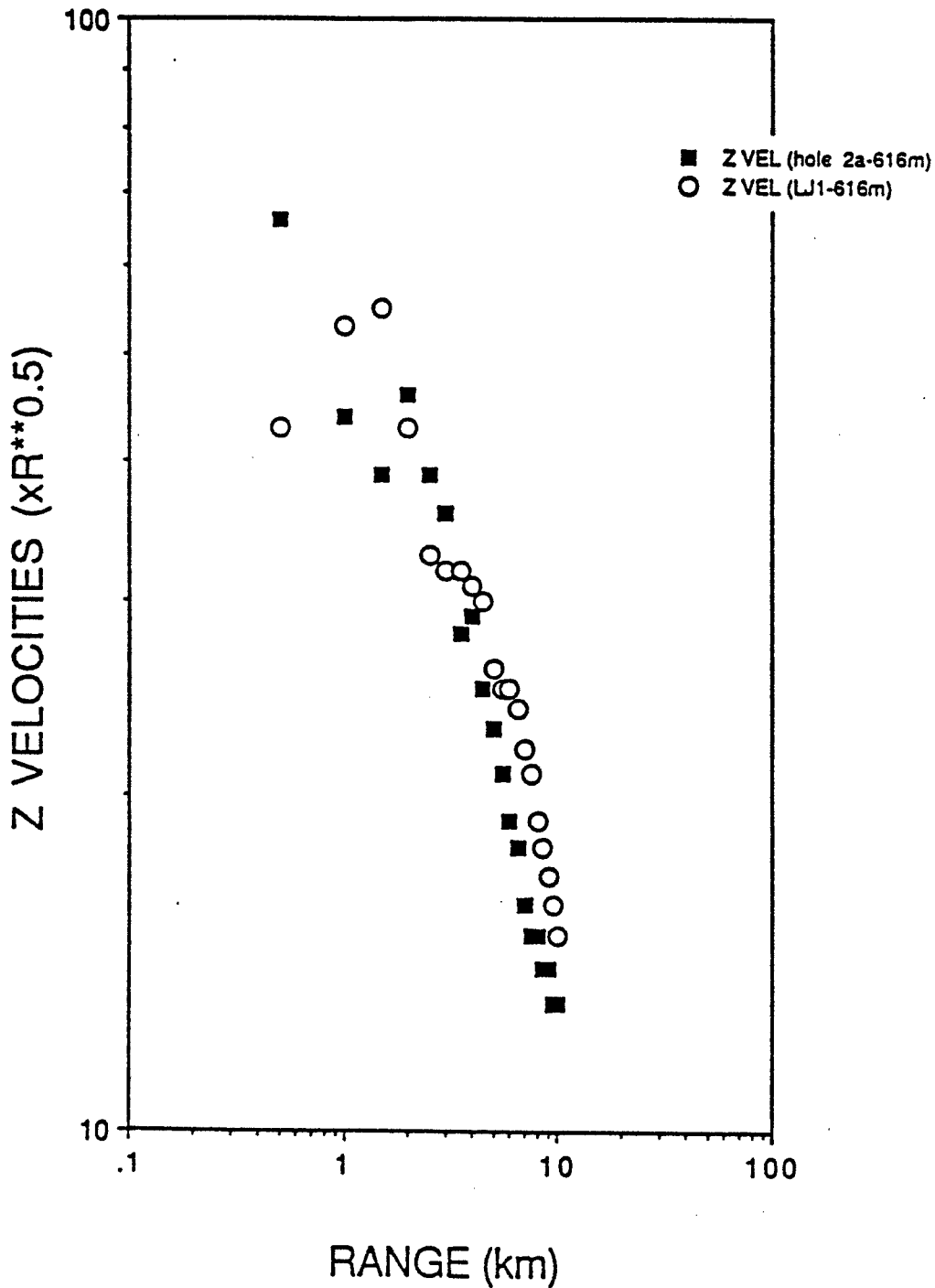


FIGURE 18a

LJ and HOLE PEAK VELOCITIES (4 pole LP @ 1 Hz)

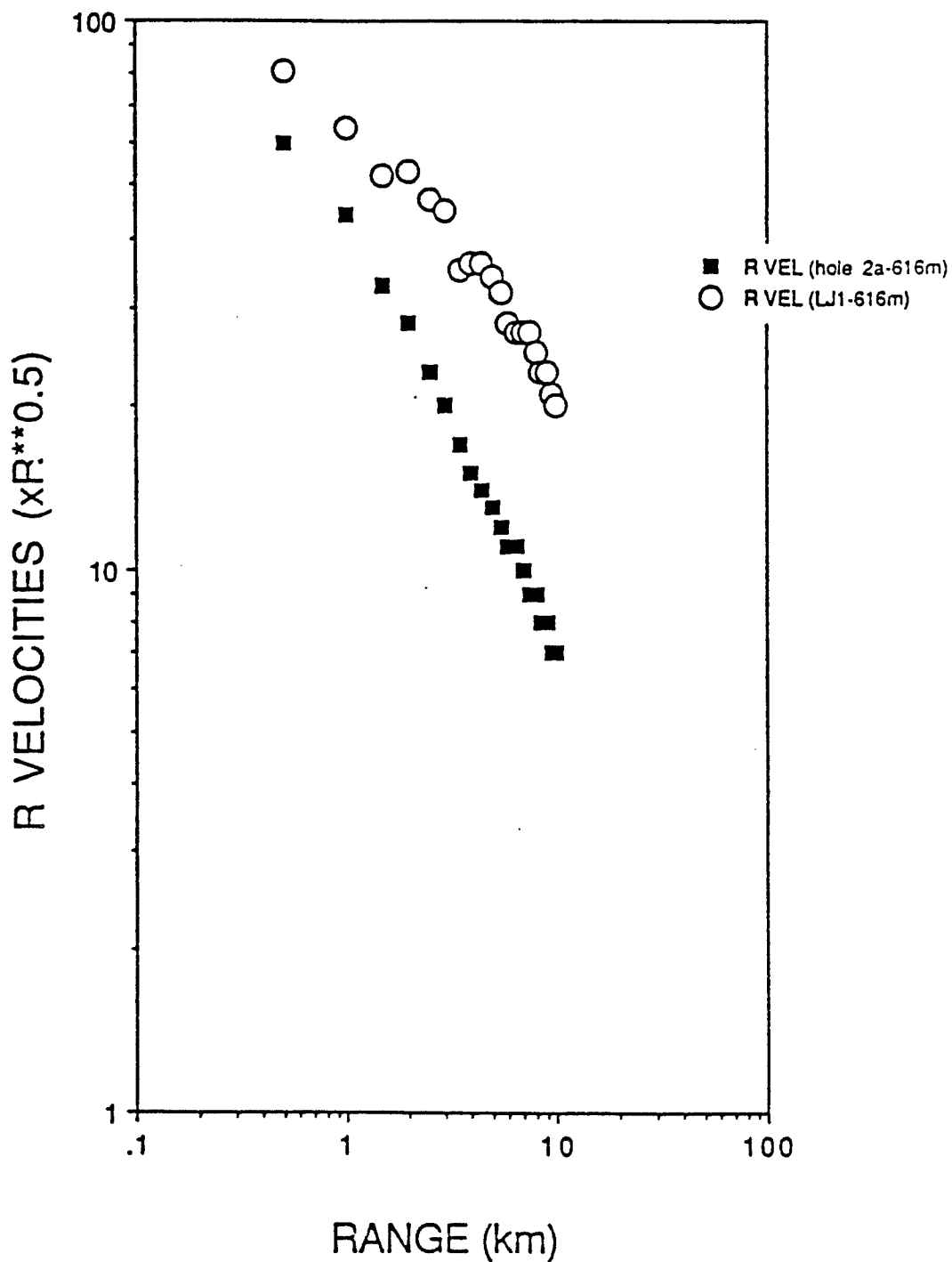


FIGURE 18b

CONCLUSIONS/RECOMMENDATIONS

A program designed to quantify geometrical effects of near source seismic wave propagation has begun. Analysis is motivated by observational data from Pahute Mesa of the Nevada Test Site and as a result velocity models developed in this study are applicable to this area. Extended reflectivity modeling is used to synthesize seismograms from plane layered structures in the 0.5 - 10.0 km range. Calculations show strong contributions from body and surface waves over this near source region. Surface waves are particularly strong because of shallow burial depths (200-750m).

Data were crudely separated into body and surface wave contributions using high and low pass filters centered at 1 Hz. A general observation is that body waves show stronger amplitude fluctuations than surface waves when peak velocities are considered. In order to develop a more stable estimate of source strength from these observations the time integral of the squared velocity was introduced as a new waveform measure. Preliminary analysis of this function(roughly called an energy measure) with the synthetic data indicates that it is a more robust estimate of source strength.

Four specific questions were addressed in this initial waveform modeling exercise using the measures discussed. These questions dealt with the quantification of the following effects: (1)Source-receiver offset; (2)Proximity of interfaces to the source; (3) Source depth of burial; and (4)'Average' vs 'Site Specific' velocity models.

The effect of offset on the radiated wavefield was found to be the strongest at horizontal distances of 0 to 3 depths of burial. The P waves (as quantified by data above 1 Hz) were most variable over this range. Adjacent stations separated by only 0.5 km were found to change in amplitude by a factor of two. These changes were seen as both velocity increases and decreases. At greater distances body waves decayed according to a power law which always exceeded simple geometrical spreading. Radial velocity decayed as $r^{-1.9}$ while vertical velocities decayed as $r^{-1.5}$. Surface wave peak amplitudes also showed some variation in amplitudes at close source to receiver offsets. At ranges greater than 1-2 km surface waves fit power law decay patterns. These

decays exceeded cylindrical spreading with values of $r^{-1.4}$ for vertical components and $r^{-1.3}$ for radial components. Variations in individual surface wave observations from this decay were 10-20%, much smaller than that observed for body waves. Energy estimates (integral of the square of velocity) exhibited dramatically reduced scatter from station to station when compared to peak amplitude estimates.

Source proximity to an interface was replicated with a series of sources at depths of 616, 665 and 750 m in the HOLE velocity model (Figure 5). The 616m source is above a low velocity zone, the 665m source is in the low velocity zone, and the 750m source is below the zone. Strong differences in the body waves generated by the source above the low velocity zone and those in and below the zone were observed. Over the 0.5 to 3.0 km range, the 616m source yielded body waves above 1 Hz that were a factor of two to four larger than those for either of the two deeper sources. Differences between the data from the three source depths decreased with increasing offset. Long period waveforms represented by surface wave contributions were much less affected by source depth with differences in the range of 20% between individual peak amplitudes for the three source depths.

Source depth effects were quantified by considering sources at 200, 400, and 616m. Energy estimates indicated that as much as a factor of ten increase in surface energy for the 200m source compared to the 616m source. These differences were greatest at short source-receiver offsets and decreased to a factor of 2 at 10 km. Source depth effects were 1 to 2 orders of magnitude less than the change in energy due solely to geometrical spreading over the 0.5 to 10 km range. Variations between the 400 and 616m sources were even less. The conclusion drawn from these trials was that for reasonable constraints on source depth variations in radiated energy will be small at large (3-10km) offsets for the velocity model considered.

The final set of trials focused on two sets of synthetics, one from an average Pahute Mesa velocity structure and the second from a specific model developed with downhole information. Sources were placed at 616m in both structures. Differences between synthetics for the two models were small compared to other effects identified in these trials. Again the biggest differences occurred at small offsets.

These trials have identified that peak velocity estimates in the near source region may exhibit strong lateral variations at close offsets and high frequencies which are dominated by body waves. These differences degrade when greater offsets or longer periods (surface waves) are considered. The integral of squared velocity is found to be a stable source estimate. These new criteria may be useful in analyzing observational data sets. Effects of interfaces and low velocity layers were found to be strongest for body waves at short offsets. Finally, with reasonable estimates of source depth this error should not be dominant in observational data as long as the source is not near an interface.

Purely geometrical wave propagation effects have been identified in these numerical exercises with no consideration of coupling effects. Strong effects, as big as a factor of 4, have been found for high frequency body waves at short offsets. Reduced effects are found for longer period surface waves at great source to receiver offsets. These factors are less than the factor of 10 found in the observational data set. Additional scatter must be introduced by lateral variations in the geological structure and coupling effects from explosion to explosion. The fact that scatter in peak amplitude data does not decay with range as suggested by these numerical trials also calls for one of these other mechanisms.

Many things have not been considered by these trials. Our next step is to complete ray tracing in the structure to come to a better understanding of the reasons for the large variations in body waves at short offsets. The stability of long period, long offset data motivates a new analysis of the observational data reproduced in Figures 1-4. The reduced scatter in long period moment estimates may be a reflection of physical effects explored in these trials. Implementation of energy estimation to the observational data set is now warranted.

Consideration of separate source and receiver structures on near source waveforms must also be completed. This modeling is the first step in investigating lateral variations in propagation path. We intend to begin this analysis with the method of Kind (1985).

REFERENCES

Kind, R., 1985. The reflectivity method for different source and receiver structures and comparison with GRF data, *J. Geophys.*, 58, 146-152.

Leonard, M. A. and L. R. Johnson, 1987. Velocity structure of Silent Canyon Caldera, Nevada Test Site, *Bull. Seis. Soc. Am.*, 77, 597.

Muller, G., 1985. The reflectivity method: A tutorial, *J. Geophys.*, 58, 153-174.

**ISOTROPIC AND DEVIATORIC
CHARACTERIZATION OF THE COALORA
NUCLEAR EXPLOSION IN YUCCA FLATS**

Brian W Stump
Department of Geological Sciences
Southern Methodist University
Dallas, TX 75275

Robert E Reinke
FCDNA/FCTP
Kirtland AFB, NM 87115

Kenneth H Olsen
P. O. Box 1273
Lynnwood, WA 98046-1273

Lane R Johnson
Department of Geology and Geophysics
University of California
Berkeley, CA 94720

Abstract

Near-source data from the nuclear explosion Coalora detonated at Yucca Flats, Nevada Test Site are utilized to constrain the seismic source function. The equivalent seismic source is interpreted in terms of physical processes in the source region with the aid of data from within the explosion's nonlinear region. The isotropic, deviatoric, and cylindrical spall contributions are separated and quantified. Standard spectral interpretations of the radiated wavefield for source resolution are contrasted against complete waveform modeling with moment tensor determination. Individual waveform spectra (source-receiver offsets < 2 km) can be interpreted in terms of an isotropic source model which is in agreement with a Mueller-Murphy model, including f^2 high frequency decay and source corner frequency of 1.8 Hz. Moment tensor inversion produces an isotropic source strength of 8×10^{20} dyne cm while scalar moments from the spectral interpretation are a factor of 2.5 larger. This difference is attributed to the application of simple propagation path corrections in the spectral interpretation. The deviatoric component of the moment tensor is a factor of 5-10 times smaller than the isotropic component. Deviatoric source radius, as estimated from the spectral data, is 124 m, smaller than the equivalent elastic source radius which is bounded between 133-202 m. Stress drop estimated with the Brune source model is 84 bars with an average slip of 33 cm. The spall source contribution is longer period and delayed in time from the initial explosion. Its contribution to the diagonal elements of the moment tensor is dominant on the M_{zz} component at least a factor of 3 larger than the M_{yy} and M_{xx} components. Spall source strength from waveform inversion is within a factor of 2 of forward spall models developed from acceleration data within the spall zone but is longer in duration than the forward model, reflecting the effect of a quasi-point source assumption in the forward models. Complex propagation effects dominate the data beyond 2 km. This complexity is exemplified by wavetrains at 5.1 km that extend to beyond 20 s in duration and similarity of radial, vertical, and transverse acceleration spectra in contrast to short waveform durations and strong spectral differences between transverse and radial-vertical spectra at distances less than 2 km. These propagation path effects suggest that source biases can develop at ranges as close as 2-5 km.

Introduction

Seismic source studies of underground explosions are motivated by the need to separate physical processes that generate seismic waves at near-source, regional, and teleseismic distances. These physical processes include but are not limited to direct coupling of the spherical explosion, repartitioning of energy near the free surface by tensile failure and driven motions along planes of weakness, and tectonic stress release. Application of such physically based models to seismic data is necessary for a complete understanding of discrimination issues and yield determination for the purposes of nuclear test ban treaty verification. A physically based model of the source provides the methodology to extrapolate from one geological environment to another and therefore can be tested against new data sets.

The simplest characterization of the seismic source consists of a spherically symmetric or isotropic equivalent elastic source function. A variety of such models have been developed with different parameterizations and constrained by not only near-source but regional and teleseismic data (Haskell, 1967; Mueller and Murphy, 1971; von Seggern and Blandford, 1972; Wallace and Burger, 1987). These characterizations have been extended to chemical explosions (Stump and Reinke, 1987; Stump, 1987).

Additional phenomena accompany the detonation of an underground explosion. One of these secondary processes is near-surface-layer tensile failure, spall (Eisler and Chilton, 1964; Eisler et al, 1966). As the initial spherical compressive wave from the explosion encounters the free surface, it reflects as a tensile wave propagating away from the free surface. This tensile wave may fail near-surface layers. Momentum trapped in the layer results in the failed material following a ballistic trajectory. This nonlinear process may be responsible for repartitioning part of the explosion energy as seen in the radiated seismic wavefield. The importance of this process as a source of seismic waves was addressed by Viocchi (1973). He argued that spall had a significant contribution to surface waves at 10-20 km. Day et al (1983) presented a spall model which conserved momentum and found that the process had no contribution to 20 s surface waves at teleseismic distances.

Stump (1985) argued from data within the spall zone that the process made a significant contribution to near-source surface waves from chemical explosions although at a much shorter period (.1-1 s) than Day's surface wave analysis. Patton (1990) has analyzed near-source observations in the spall zone at Pahute Mesa, NTS in order to develop scaling relations for spall mass and momentum. Day and McLaughlin (1991) show the equivalence of point force and moment tensor representations of the equivalent spall source model which could be developed from such measurements. Other authors have argued that the spall secondary source can have important contributions to regional waves (Patton, 1988; Taylor and Randall, 1989) and teleseismic P waves (Schlittenhardt, 1991).

Transverse shear motions and Love waves have been observed from all types of explosions (Kisslinger et al, 1961; Ohta, Y. and A. Kubotera, 1968; Aki and Tsai, 1972; Wallace et al, 1985; Burger et al, 1986). Transverse motions have been attributed to mode conversions and scattering (Gupta and Blandford, 1983), tectonic strain release (Aki and Tsai, 1972; Wallace et al, 1985; Burger et al, 1986), or driven motion along planes of weakness (Bache et al, 1979). Quantification of these complex propagation effects and deviatoric source contributions are important for verification applications as they make the explosions look more earthquake-like and may bias seismic yield estimates.

Trade-offs between the seismic source (it's strength and physical characterization) and propagation path effects are possible in any study of the equivalent linear source representation. The focus of this study is on near-source data (< 6 km) where propagation path effects can be minimized. Even at these close ranges a number of authors have presented evidence for propagation path complications. McLaughlin et al (1983) utilizing closely spaced arrays found a degradation in coherence above 5 Hz for observations at 6 km from nuclear explosions. Vidale and Helmberger(1987) give evidence for two dimensional structural effects on near-source waveforms from nuclear explosions at the Nevada Test Site (NTS).

The seismic experiment on the Coalora event (Yucca Flats, NTS) which we report was designed to quantify both the deviatoric and isotropic parts of the equivalent elastic nuclear source in partially saturated tuffs and alluvium,

primary materials in which the United States tests nuclear devices (US, Dept of Energy, 1987). Several investigators have studied near-source ground motion from explosions in these materials (Werth and Herbst, 1962; Perret and Bass, 1976). The Yucca Flats test site was chosen because of the vast quantity of geological and geophysical site characterization information. Ferguson et al (1988) studied the basin structure under Yucca Flats with high resolution seismic reflection and gravity data. The geologic structure close to the experiment is well constrained by many downhole geological and geophysical measurements (Figure 2). As a result, structural effects can be taken into account close to the source (< 2 km).

Experimental Design

The Coalora experiment had an announced yield of "less than 20 kilotons (kt)" (US Dept of Energy, 1987). The working point (WP) depth of the explosion was 274 m in Yucca Flats (Figure 1). A great variety of geological and geophysical information was available to constrain the wave propagation model. Figure 2 summarizes these data which include the surface expression of Yucca Fault, location of a seismic reflection survey, downhole acoustic logs, and locations of available geologic cross sections such as that developed around the Coalora emplacement hole (Figure 1).

The Yucca Flats structure summarized in the inset of Figure 1 is based upon the seismic reflection survey and inversion of available gravity data (Ferguson et al, 1988). The model consists of layers of alluvium, tuff, wet tuff, and Paleozoic sedimentary rocks. Paleozoics are near the surface on either side of the 10 km wide valley. At the center of the valley, where the shot was detonated, depth to the Paleozoics is 1 km. The Coalora cross section in Figure 1 gives more shot region detail. Major geologic characteristics include Yucca fault with a maximum 150 m of displacement within 300 m of the working point, interbedded tuffs, and 500 m water table. Large velocity and density contrasts exist within the interbedded tuffs. A downhole acoustic log 333 m NW of Coalora (Figure 3a) indicates near-surface velocity of 1.5 km/s with a positive gradient to 2.0 km/s at 400 m. Below 400m, the vitrified Rainier Mesa tuff reaches a velocity of 3.0-3.5 km/s. This particular log does not penetrate below this material. A second log, U31a, (Figure 3b), 1.5 km N of Coalora, shows similar effects. At this location, two vitrified tuff units, the Ammonia Tanks between 210-275 m and the Rainier Mesa between 335-400 m, are apparent.

The instrumentation array within two depths of burial of the Coalora ground zero is illustrated in Figure 4. These gages are used to constrain the depth and range of spall and improve resolution of spall contributions to near-source waveforms. Included in this array are two downhole packages in the emplacement hole for the purposes of constraining the depth of spall. The

WEST-EAST CROSS SECTION THROUGH U310

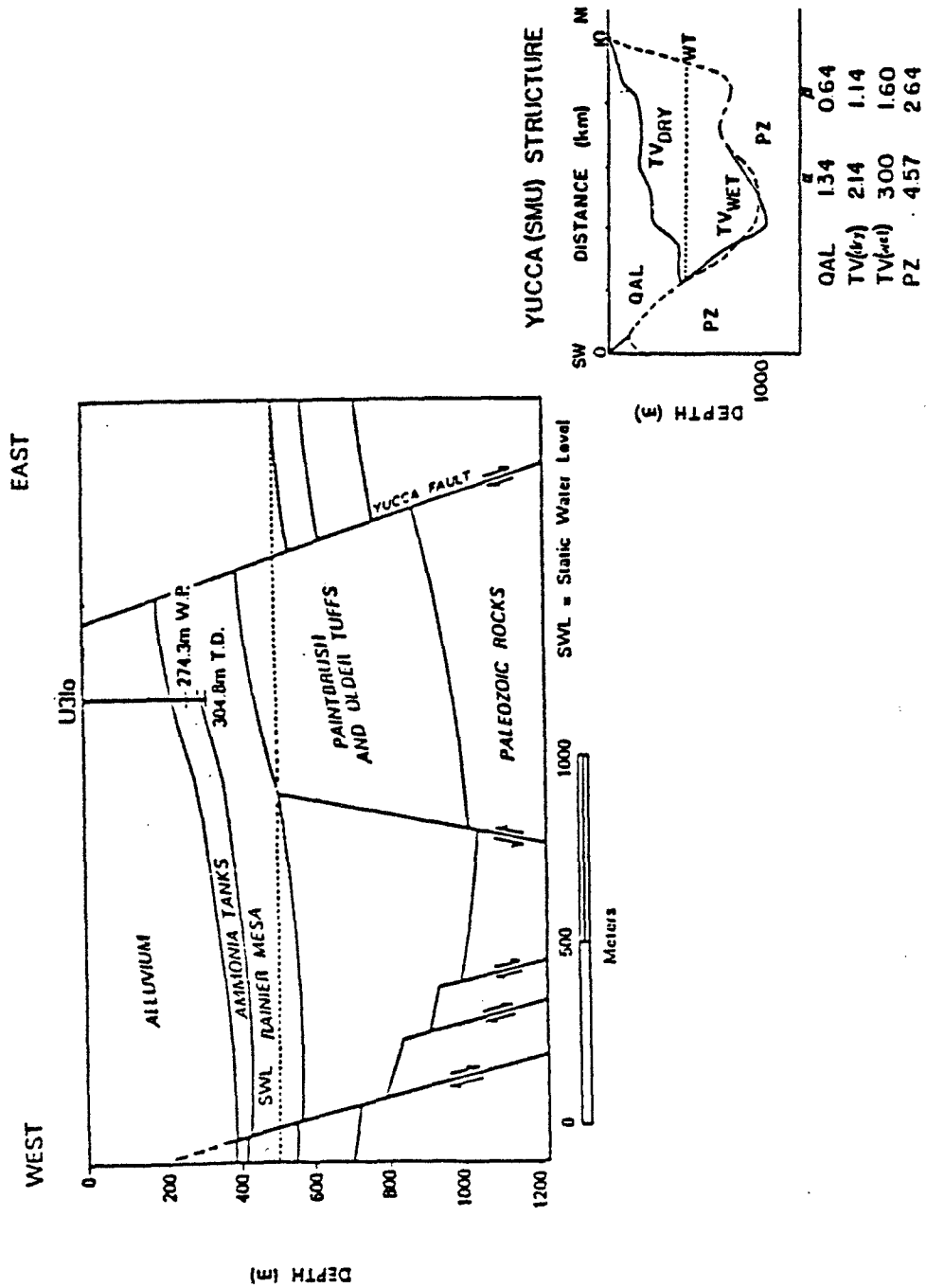


Figure 1: Geological cross section passing through the emplacement hole for the Coalora explosion. The general Yucca Flats velocity model as determined by Ferguson et al, 1988 is given in figures lower left hand corner.

COALORA SITE INFORMATION

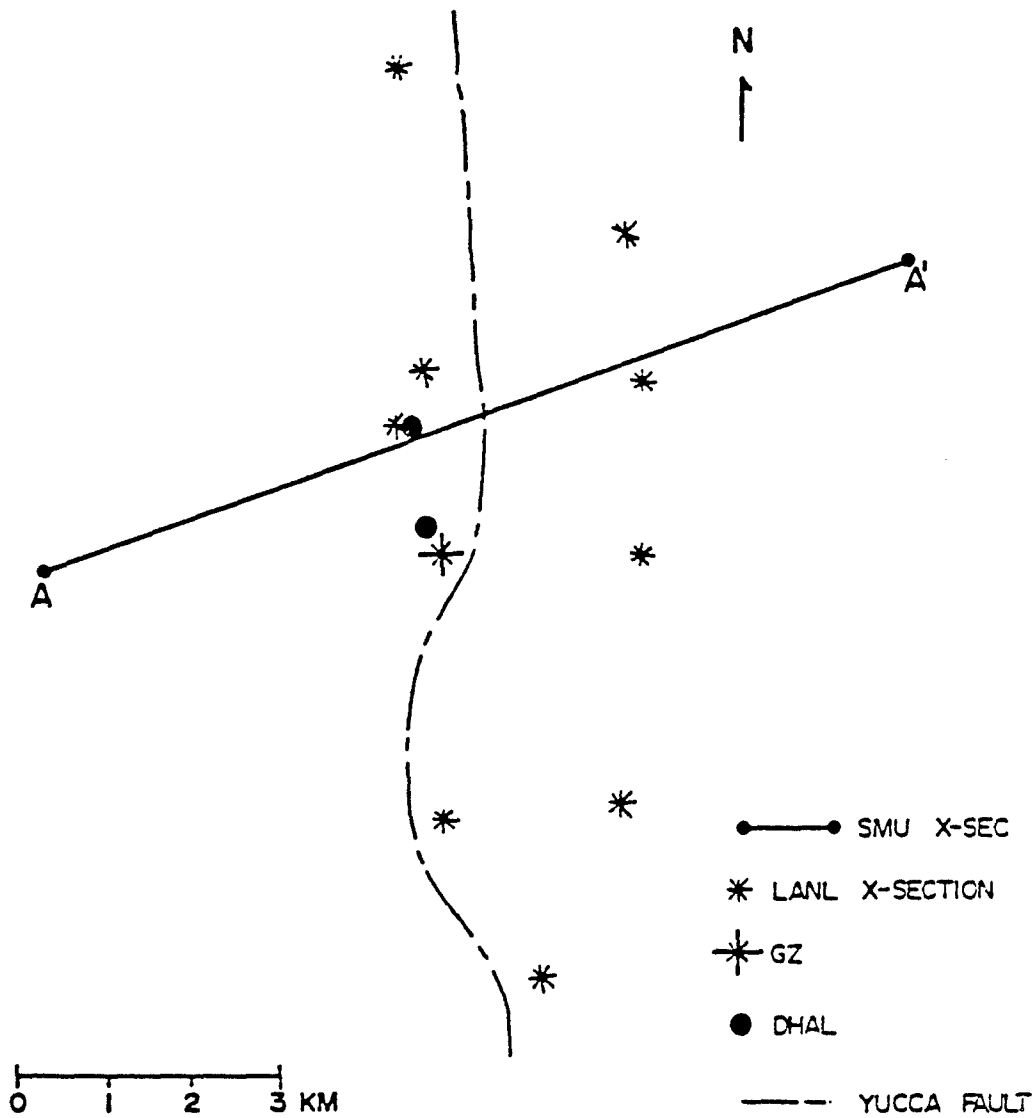


Figure 2: Map summarizing geological information available for constraining structure in and around the Coalora test site. The SMU cross section is based upon a reflection survey, stars represent geologic cross sections based upon emplacement or exploratory holes, and DHAL are dry hole acoustic logs.

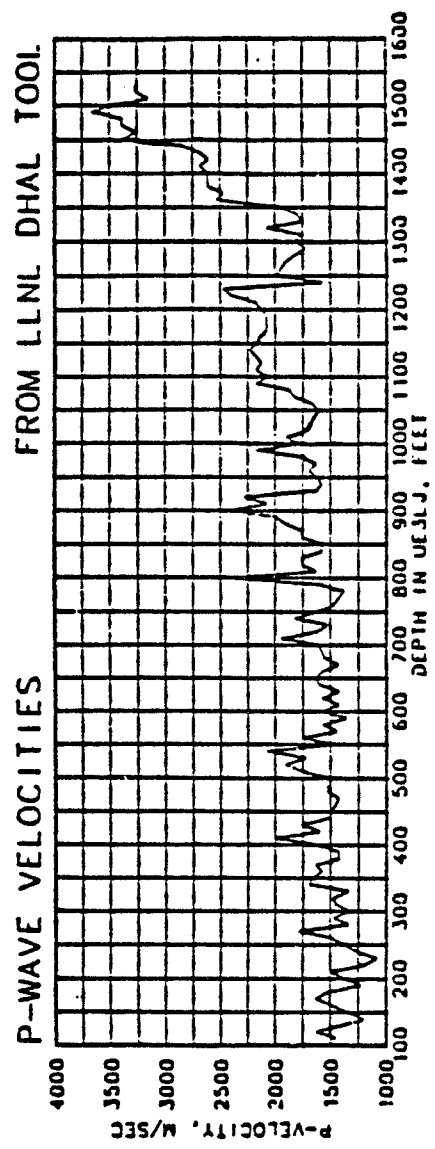


Figure 3a: Dry hole acoustic log located 350m NW of Coalora.

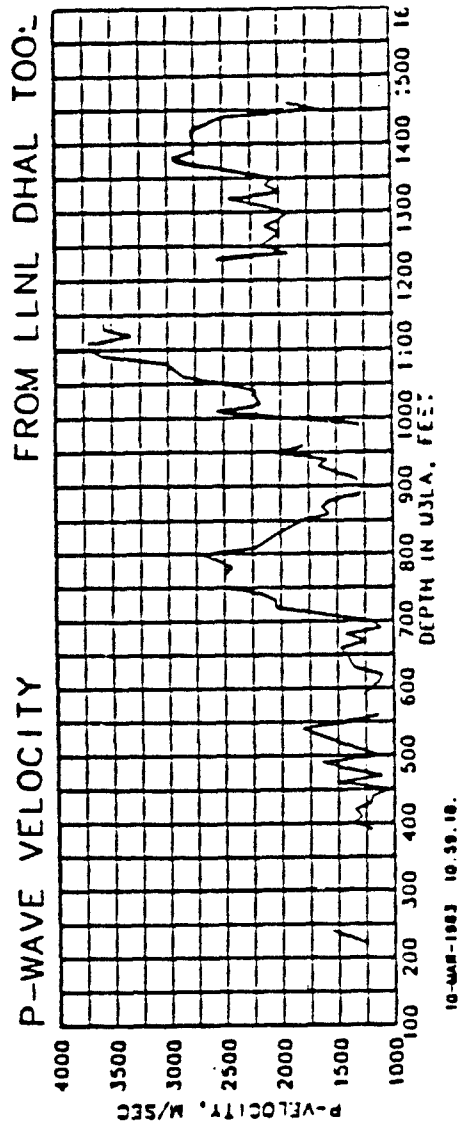


Figure 3b: Dry hole acoustic log

located 1500m N of Coalora.

COALORA CLOSE-IN ARRAY

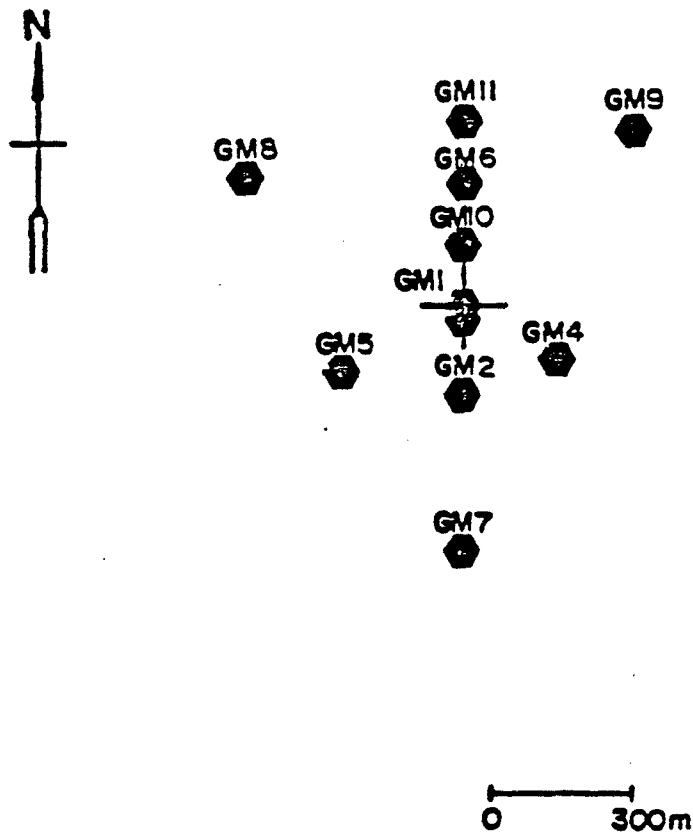


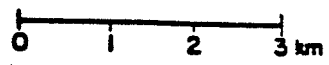
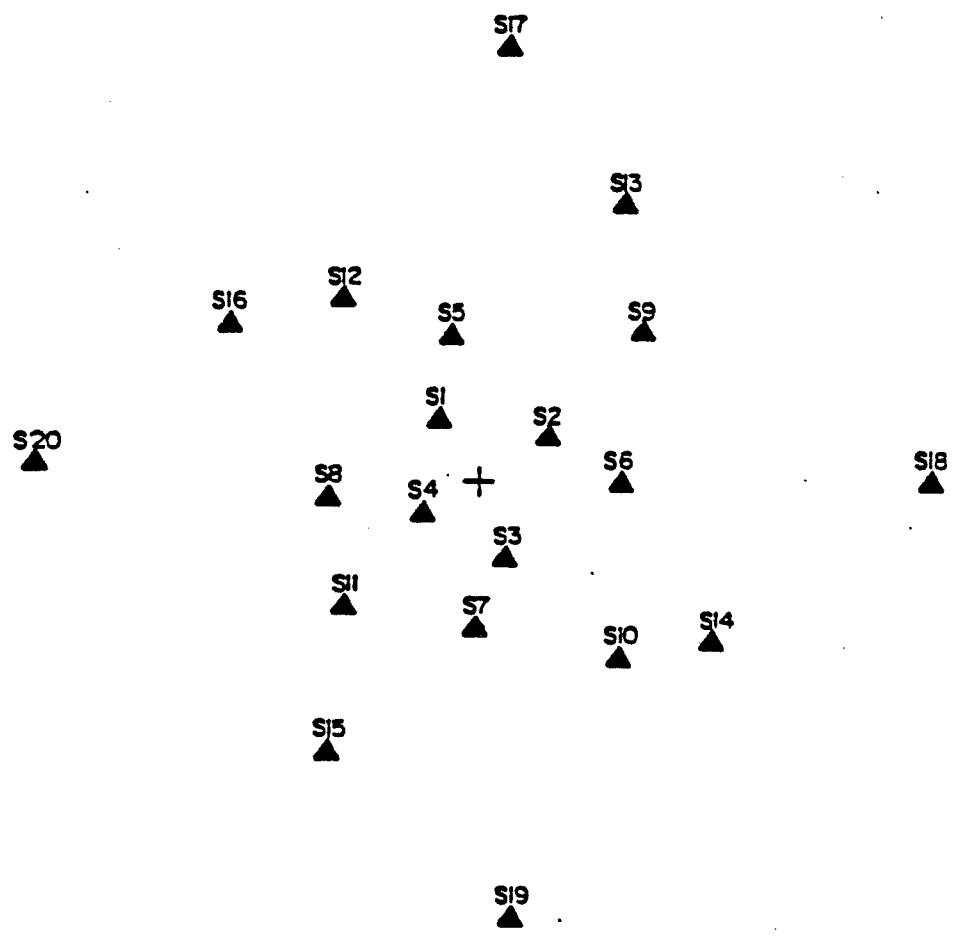
Figure 4: Plan view of accelerometer array within two source depths of burial. Cross bar in the center of figure is representative of ground zero.

abundance of data at different azimuths and ranges from the source provides opportunity for improved resolution of the deviatoric source contribution. All 13 close-in accelerometers were hardwired to a central recording site. Data were recorded on high speed analog tape recorders and digitized post-test.

The second part of the instrumentation array consisted of three-component force-balance accelerometers with digital event recorders placed between 0.86 and 5.10 km (Figure 5). A total of 20, three-component stations were installed. The data were sampled at 200 samples per second. Data words were each 12 bits.

The two accelerometer arrays were designed to provide data over a range of azimuths and distances such that contributions from the spherical explosion, the cylindrical spall, and the deviatoric source components could be separately resolved.

COALORA SEISMIC ARRAY



EACH STATION 3COMP
ACCELERATION

Figure 5: Three-component force-balance accelerometers recorded with digital event recorders. Stations span the bounds of Yucca Flats with closest stations 0.86 km and most distant 5.16 km.

Observational Data

Vertical accelerograms from within the spall zone are reproduced in Figure 6. Records are characterized by arrival of the compressive wave, minus-one-g-dwell during free-fall, and impulsive rejoin. The closest downhole gauge at a depth of 114 m shows evidence of multiple spall while the most distant free-surface gauge that showed a spall signature was at a horizontal range of 274 m (a radial distance equal to one depth of burial). Spall extends to just beyond one depth of burial in the Coalora experiment. Two delineations of the total spall zone are given by the solid and dashed lines in Figure 6. Limited data existed for defining the depth of spall directing below ground zero (GZ) and no data existed for spall depth beyond GZ. The depth of spall below GZ was placed conservatively just below the deepest gage that spalled. The boundary of the spall zone at other distances was taken in its simplest form as a linear line connecting the deepest spalled gage and the first free surface range where spall was not observed. Based on more complete spall data sets from chemical explosions (Stump, 1985), spall zone shape is found to be more bowl like, thus the more extensive dashed line model. The exact shape of the spall zone is dependent upon the material properties around the explosion, source depth and size. Due to a lack of complete azimuthal coverage in the spall zone the process was assumed cylindrically symmetric. Records from geophones at a horizontal distance of 93 m and four azimuths separated by 90° yielded arrival times which were identical within 3 ms. This scatter is within measurement error and so supports at least an initially cylindrical pulse from the explosion. These gages were clipped after the first arrival and cannot be used to estimate symmetry from latter arriving phases.

Observational data within two depths of burial are summarized in Figure 7. Vertical (Z), radial (R), and transverse (T) displacement waveforms at three 549 m range stations are displayed. Displacements result from twice integrating the accelerograms. Waveshapes for the radial and vertical displacements at the different azimuths are very similar although peak amplitudes vary by 30% about the mean. Relative to the vertical and radial, transverse displacements are shorter in duration, exhibit larger variations in

COALORA DISPLACEMENT AT 549m RANGE

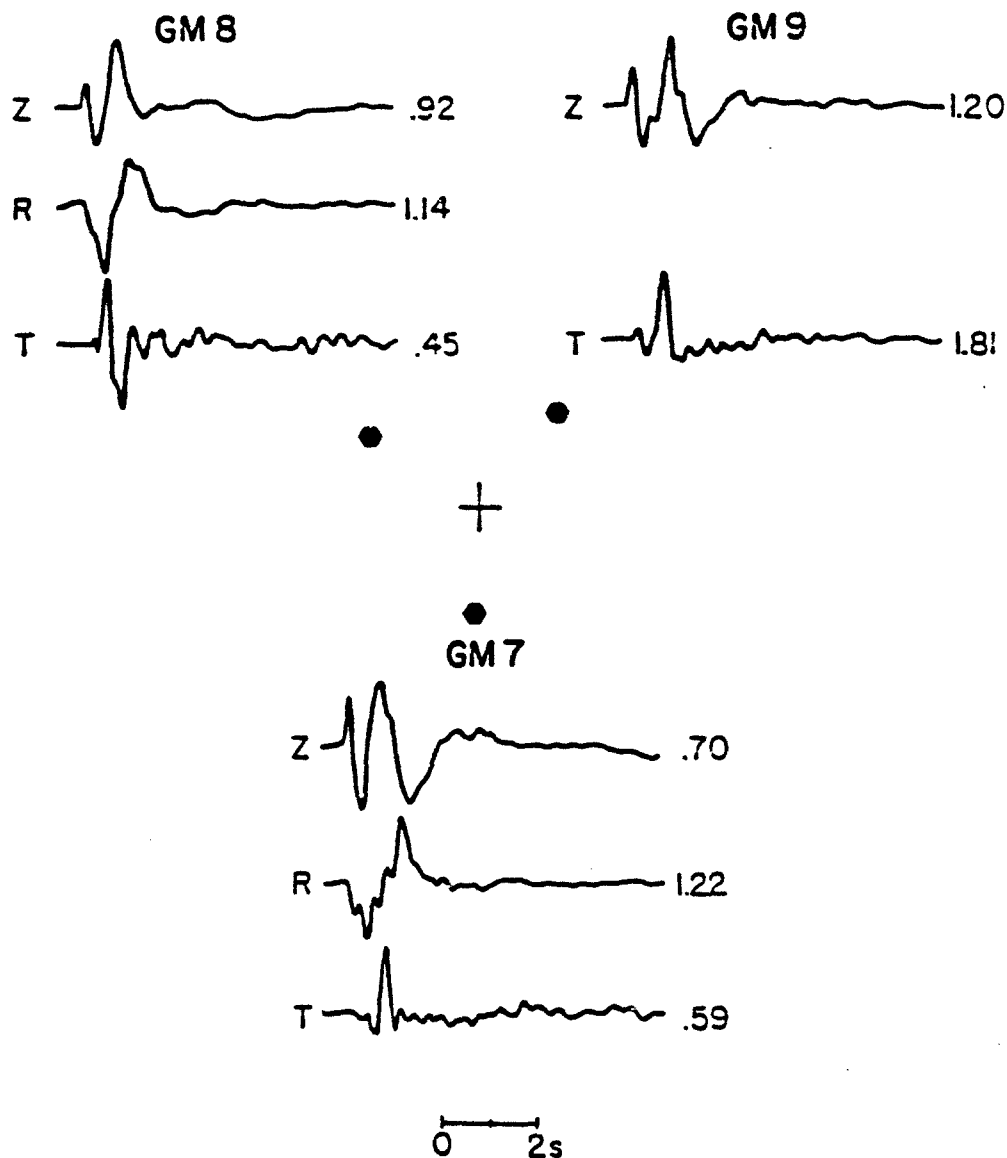


Figure 7: Displacement waveforms (accelerations integrated twice) at three azimuths from source and at a range of 549 m. Vertical(Z), radial(R), and transverse(T) displacements are given. Peak displacements in cm.

amplitude, and change first motion as a function of azimuth. Large amplitude, relatively simple transverse motions are observed at ranges equal to two depths of burial. Displacement spectra were estimated for the vertical and transverse records at the 549 m range (Figure 8). Envelope functions were fit to each spectrum with a long period level, corner frequency, and high frequency decay. Transverse spectra (549m range) exhibit higher corner frequencies, more rapid decay of high frequencies, and lower long period levels than the vertical spectra. These spectral parameters will be used as source model constraints.

Accelerograms recorded at more distant ranges (0.86-5.10 km) are summarized in Figures 9a(Z), 9b(R), 9c(Γ). Four representative ranges (0.86, 1.66, 3.38, and 5.10 km) have been chosen from the 20 instruments fielded. The effect of the two- and three-dimensional structure of Yucca Flats (Figure 1) becomes apparent in these waveforms. At 5.10 km range, near the valley edge, all three components of motion exhibit a complex wave train with duration of over 20 s. Displacement records and spectra for the 5.10 km data are given in Figure 10. Unlike the simple waveforms at 549 m with obvious spectral differences between vertical and transverse components, all three components at this range have nearly identical spectral shapes and amplitudes. The resulting source corner frequency one would interpret from the data is reduced from that observed at the closer ranges, especially on the transverse components. The 5.10 km waveforms and spectra are evidence that more distant observations are strongly influenced by complex geological structure underneath Yucca Flats. Simple spectral source interpretations would be severely biased at this more distant data.

The effect of the valley structure around Coalora was quantified with two and three dimensional finite element calculations by Wojcik and Vaughn (1984). Results of these calculations show asymmetries in the radiated wavefield beyond 1-2 km. Transverse motions in these calculations attributable to diffraction by the Yucca Fault were 20-30% the size of radial and vertical motions. Since the main purpose of this study is to constrain the physical parameters of the seismic source function, primary emphasis will be placed on observational data well away from boundaries of the valley. Modeling

COALORA DISPLACEMENT SPECTRA AT 549m RANGE.

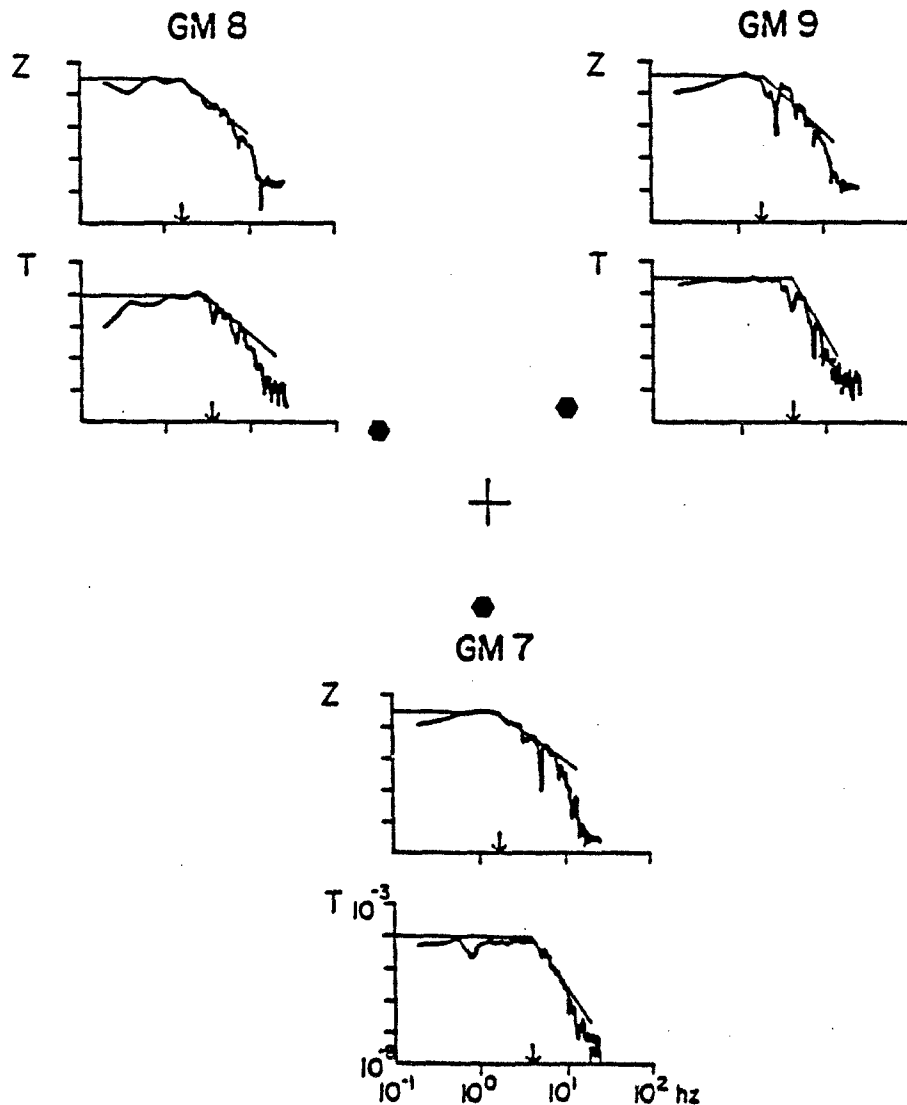


Figure 8: Spectral estimates from vertical(Z) and transverse(T) waveforms in Figure 7. Original time series were windowed with a 10% cosine taper. A simple spectral model consisting of a constant long period level, a high frequency decay (f^{-n}), and a corner frequency (f_c) was fit to the data. Light line in each spectrum is this model with arrow representative of f_c .

COALORA VERTICAL ACCELERATION

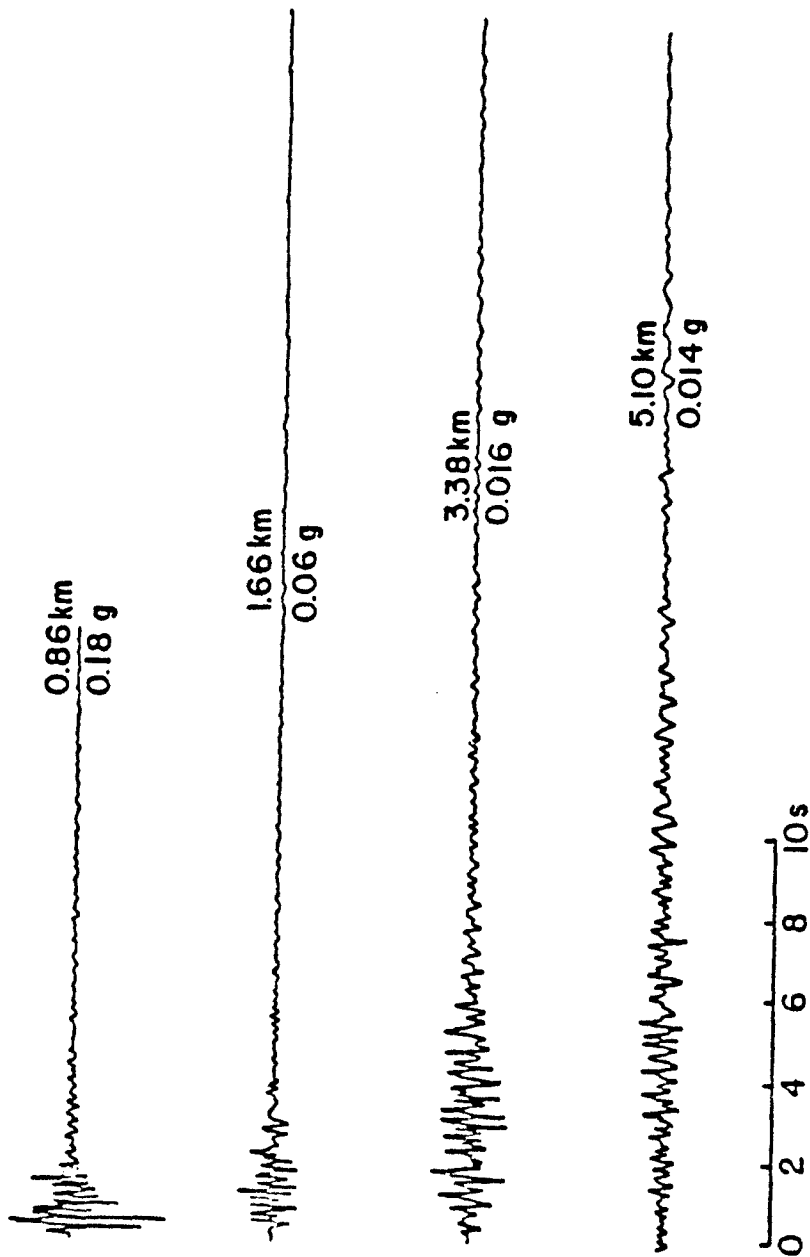
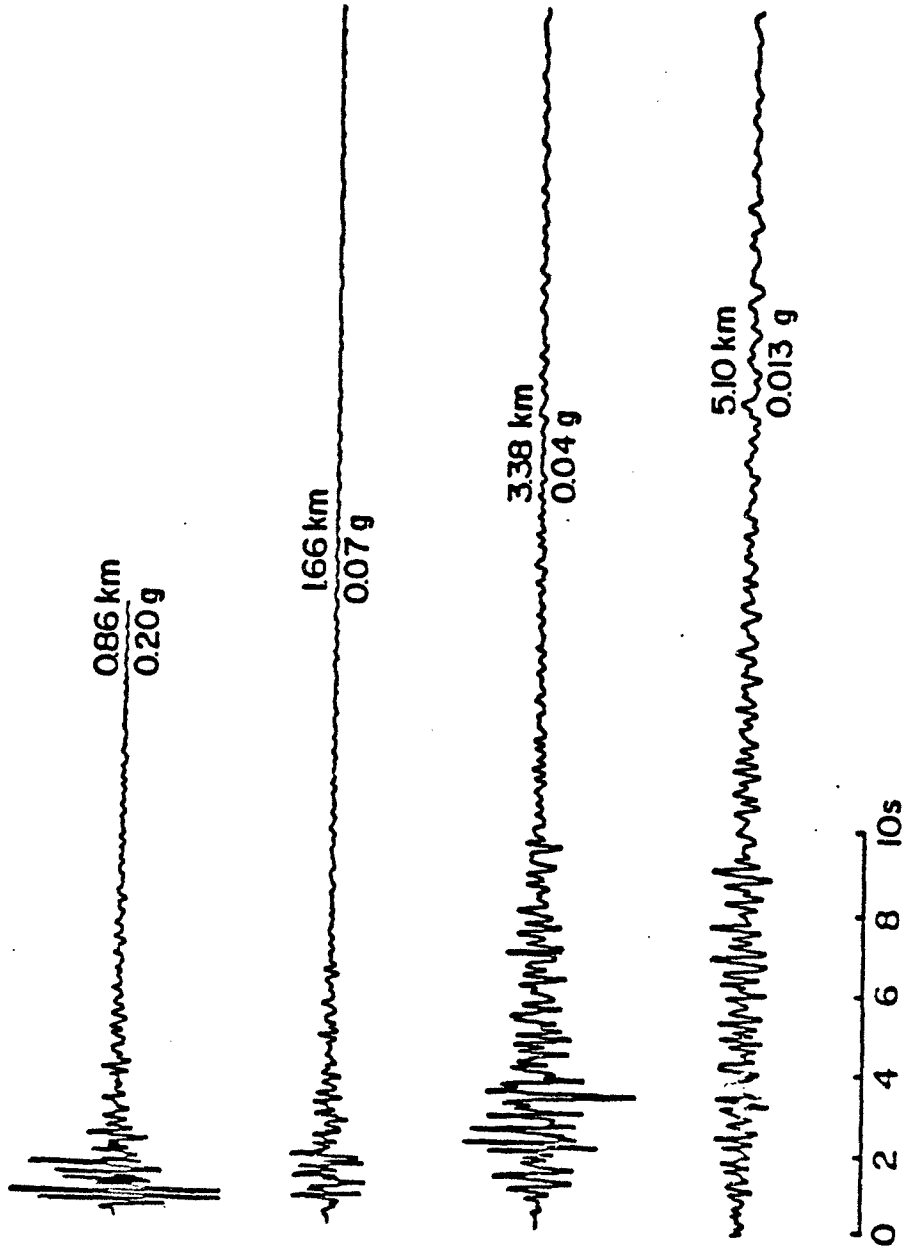
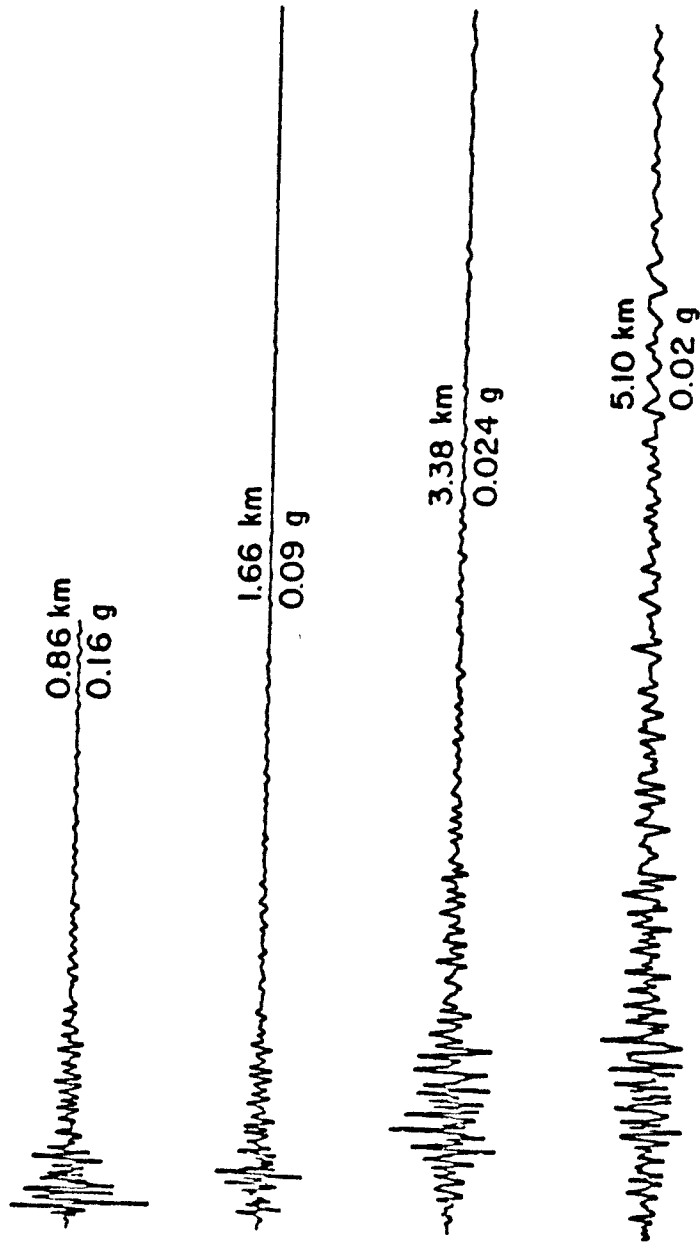


Figure 9a,b,c: Vertical(a), radial(b), and transverse(c) accelerograms spanning the 0.86-5.10 km range.

COALORA RADIAL ACCELERATION



COALORA TRANSVERSE ACCELERATION



COALORA DISPLACEMENTS AT 5.16 km

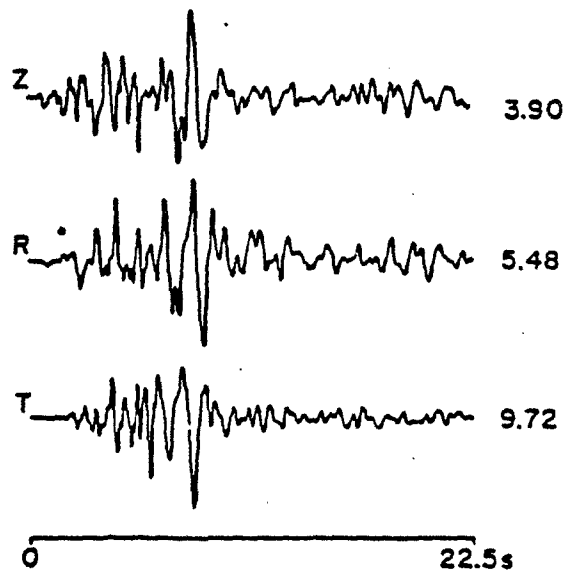
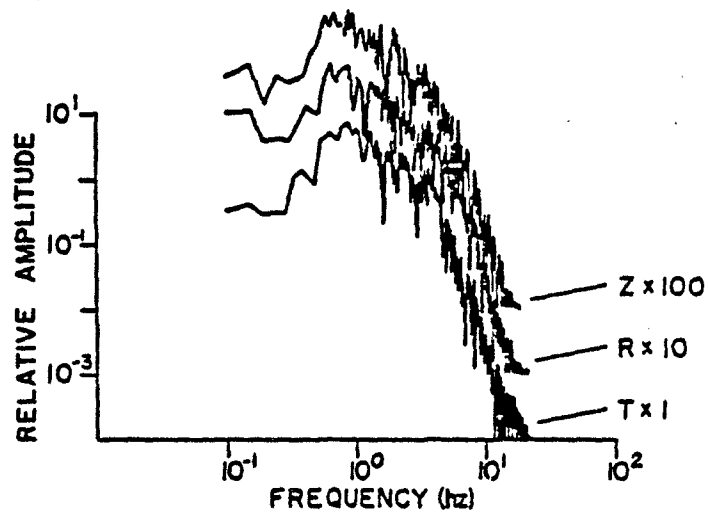


Figure 10: Vertical(Z), radial(R), and transverse(T) displacements and displacement spectra from data at 5.16 km range. Z and R spectra have been arbitrarily scaled by factors of 100 and 10 so that all three could be compared on a single plot.

and interpretation will be restricted to observations within 2 km of the explosion.

Standard Temporal and Spectral Source Interpretations

The simplest interpretation of near-source seismic data involves utilization of spectral measures such as long period level for seismic moment and corner frequency for source dimension. In order to test these measures with the Coalora data set, spectra such as those displayed in Figure 8 were used to estimate long period spectral level, corner frequency, and high frequency decay (Table 1). Radial and vertical components were assumed to be dominated by the isotropic source component. Transverse motions were assigned to the deviatoric source. Based on the valley size beneath Yucca Flats, increasing waveform complexity with range, growing homogeneity of RTZ spectra with range, and 2/3D simulations of Wojcik and Vaughn (1984) source analysis was limited to data within 2200 m of the explosion working point. Moment estimates for isotropic and deviatoric source contribution are given in Figure 11:

$$M_I = 4\pi\rho R\alpha^2\Omega_0 \quad (1a)$$

$$M_D = 4\pi\rho R\beta^2\Omega_0 \quad (1b)$$

Density (ρ) was taken from emplacement hole data at shot depth as 1.8 gm/cm³, compressional velocity (α) as 1.9 km/s, and shear velocity (β) as 1.16 km/s which implies a Poisson's ratio (ν) of 0.2. Ω_0 is long period displacement spectral level. The high shear velocity was chosen so that deviatoric moments would be an upper bound relative to isotropic moments. Following the methodology of Archuleta et al. (1987) average log moments and their standard deviations were computed according to:

$$\log \langle M_0 \rangle = [(1/ns) \sum_{i=1}^{ns} \log (M_{0i})] \quad (2a)$$

$$\text{std dev} (\log \langle M_0 \rangle) = \left[\left(\frac{1}{ns-1} \right) \sum_{i=1}^{ns} (\log M_{0i} - \log \langle M_0 \rangle)^2 \right]^{1/2} \quad (2b)$$

Table 1a: Deviatoric Estimates

Station	Range (m)	DC (cm-s)	f_c (Hz)	Slope	Moment (dyne-cm)
GM2T	274	0.37	3.4	3	3.6×10^{20}
GM4T	365	0.34	3.3	2 ⁺	4.4×10^{20}
GM6T	389	0.32	3.5	3	4.3×10^{20}
GM7T	612	0.09	4.0	4	2.0×10^{20}
GM8T	614	0.10	3.5	2 ⁺	2.1×10^{20}
GM9T	612	0.30	3.5	3 ⁺	6.4×10^{20}
GM10T	307	0.49	3.5	3 ⁻	5.3×10^{20}
GM11T	495	0.24	3.7	3 ⁺	4.3×10^{20}
S1T	893	0.10	3.5	4	3.1×10^{20}
S3T	940	0.10	2.8	3	3.3×10^{20}
S5T	1692	0.07	3.4	4	4.2×10^{20}
S7T	1663	0.06	2.6	2 ⁺	3.8×10^{20}
S8T	1722	0.10	3.0	4	6.1×10^{20}
S11T	2117	0.10	2.2	3	7.5×10^{20}

Table 1b: Isotropic Estimates

Station	Range (m)	DC (cm-s)	f_c (Hz)	Slope	Moment (dyne-cm)
GM7Z	612	0.30	1.8	2	2.8×10^{21}
GM7R	612	0.36	2.1	2 ⁺	3.4×10^{21}
GM8Z	614	0.30	1.6	2	2.8×10^{21}
GM8R	614	0.36	1.8	2	3.4×10^{21}
GM9Z	612	0.34	1.8	2 ⁺	3.2×10^{21}
GM11Z	495	0.34	2.0	2	2.6×10^{21}
GM11R	495	0.90	1.4	2	6.9×10^{21}
S1Z	893	0.20	1.9	2	2.8×10^{21}
S1R	893	0.38	1.6	2 ⁺	5.3×10^{21}
S3Z	940	0.24	2.0	3 ⁺	3.5×10^{21}
S3R	940	0.40	2.0	3	5.8×10^{21}
S5Z	1692	0.21	1.4	2	5.5×10^{21}
S5R	1692	0.20	1.7	2 ⁺	5.3×10^{21}
S7Z	1663	0.16	1.6	2 ⁺	4.1×10^{21}
S7R	1663	0.26	1.7	2 ⁺	6.7×10^{21}
S8Z	1722	0.11	1.7	2 ⁺	2.9×10^{21}
S11Z	2117	0.12	1.9	3	3.6×10^{21}
S11R	2117	0.10	2.1	3	3.3×10^{21}

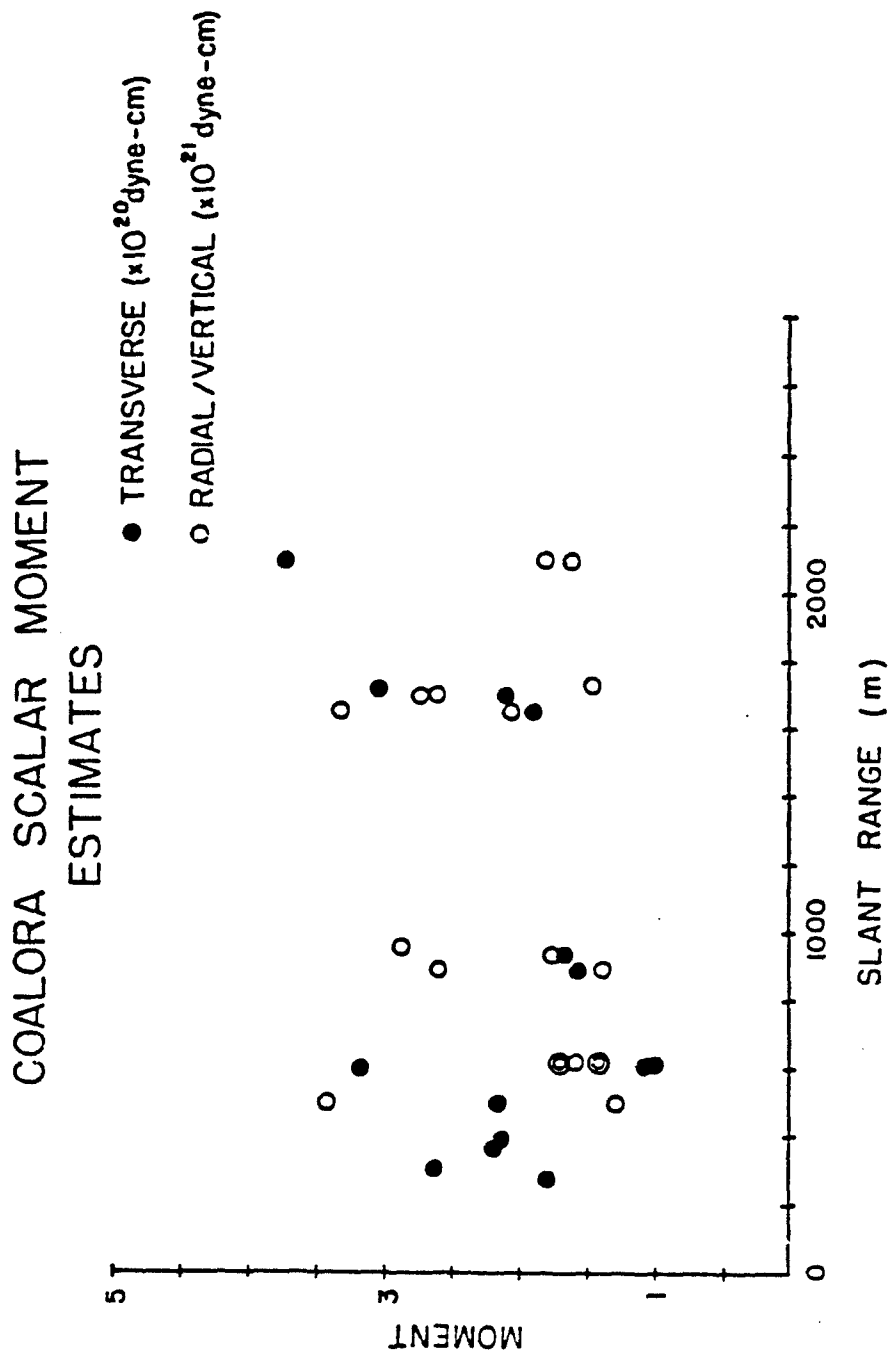


Figure 11: Isotropic(radial and vertical) and deviatoric(transverse) moment estimates for Coalora.

Mean isotropic and deviatoric logarithmic moments from observational data were 21.29 (standard deviation of mean 0.14) and 20.60 (s.d.m. 0.16) respectively. These estimates for M_I (isotropic) and M_D (deviatoric) moments are 1.95×10^{21} and 3.97×10^{20} dyne-cm. The isotropic scalar moment is a factor 4.91 larger than the deviatoric scalar moment. The multiplicative error term is defined according to:

$$EM_o = \text{antilog} [\text{std dev} (\log \langle M_o \rangle)] \quad (3)$$

The multiplicative error term for the isotropic and deviatoric moments are 1.36 and 1.44. The standard deviations (std dev) of the two means are nearly equal.

Corner frequencies were estimated by fitting an envelope function to the data (Figure 8). These corner frequencies are displayed in Figure 12 as a function of source-receiver separation. Transverse corner frequencies are significantly larger than radial or vertical estimates at close range. This difference decreases with increasing range. The slow decay of the transverse corner relative to the more constant radial/vertical values may reflect the importance of the attenuation model in interpreting high frequency source corners beyond 1200-1400 m. The lower isotropic corner frequency appears unaffected to 2200 m. Mean isotropic corner frequency is 1.82 Hz with a multiplicative error term of 1.12. Mean deviatoric corner frequency is 3.28 Hz with a multiplicative error term of 1.13.

In order to interpret the data Mueller-Murphy source models were calculated for detonations of 1, 10, and 100 kt in alluvium. A scaled depth of $122 \text{ m/kt}^{1/3}$ was used. Velocity and density structure was chosen appropriate for the Coalora site and consistent with values used to interpret the scalar moments. Envelop functions were fit to the Mueller-Murphy source spectrum to replicate analysis applied to the observations. High frequency decay in Mueller-Murphy source model is close to that found in the R/Z data, f^2 (Table 1a). The observed isotropic corner frequency of 1.82 falls between

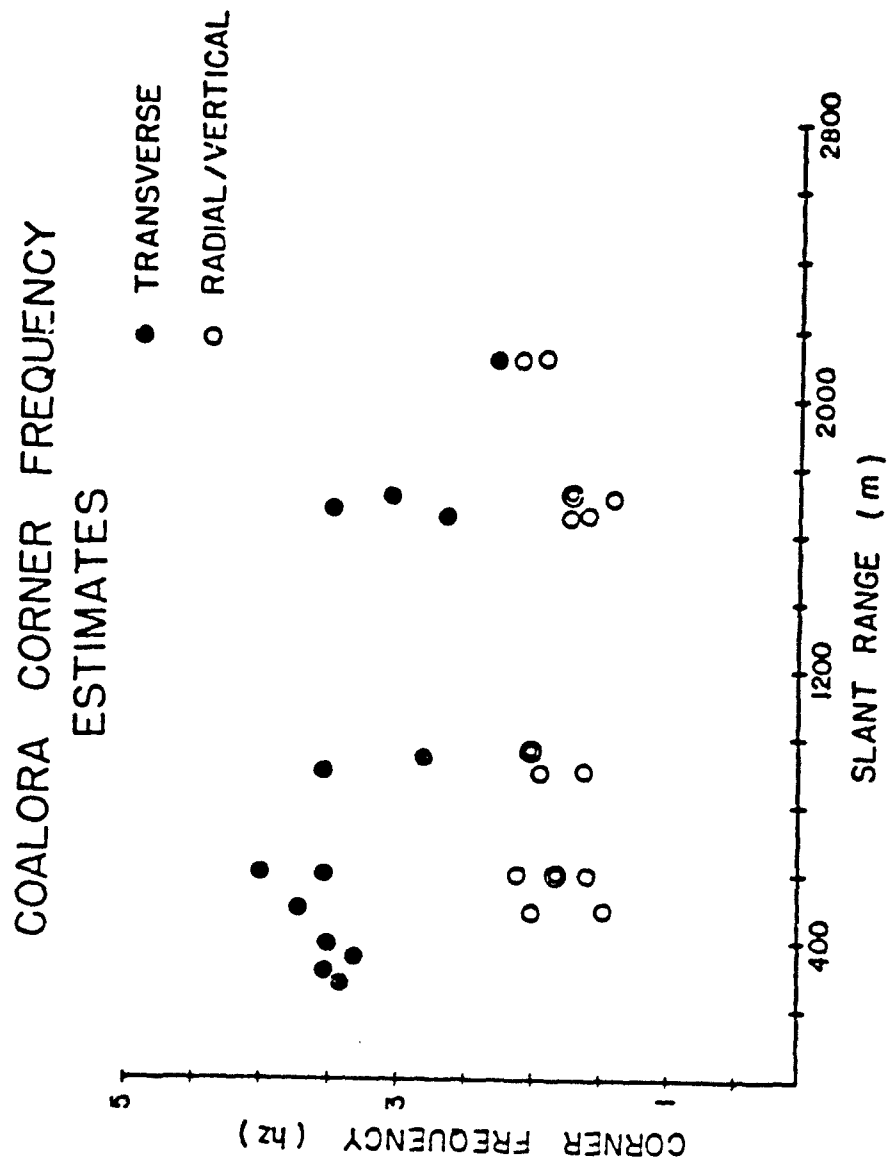


Figure 12: Corner frequency estimates from radial, vertical, and transverse displacement spectra of Coalora explosion.

model values of 2.5 Hz for 1 kt and 1.7 Hz for 10 kt, consistent with the announced yield of "less than 20 kt."

Spall is a secondary source process that occurs near the free surface. Accelerometer data from within the spall zone (Figure 6) were used to develop an equivalent body force model for this process. The model represents spall as a set of vertical point forces that conserve momentum (Day et al, 1983) which can be shown to be equivalent to the standard moment tensor representation (Day and McLaughlin, 1991). Escape velocity of near surface material is constrained by integrals of the accelerograms while total spall mass (m_T) is estimated from the data (Figure 6). Bounds placed on the spall process were discussed in the earlier *observational data* section. Spall mass estimates (solid and dashed lines, Figure 6) for this explosion were $1.2-4.4 \times 10^{10}$ kg. Following Stump (1985), temporal and spatial finiteness of the spall zone is replicated with a source rise time, T_{SR} . Initiation time of the failure process across the test bed is used as an estimate of the secondary source rise time. Physically this rise time reflects the fact that spall initiation does not occur simultaneously over the entire test bed but is dependent upon tensile strength of the material, geometry of the explosion, and propagation velocity of the media. In addition to spall rise time, an average spall dwell time, T_S , is needed in the three vertical forces that make up the total equivalent seismic source. This value is also estimated from the spall zone data. With these parameters the three vertical forces that represent (1) spall initiation, (2) material relaxation, and (3) rejoin become:

$$f_1(t) = \left[\left(\frac{30t^4}{T_{SR}^5} - \frac{60t^3}{T_{SR}^4} + \frac{30t^2}{T_{SR}^3} \right) m_T V_0 (H(t) - H(t - T_{SR})) \right] \quad (4a)$$

$$f_2(t) = -m_T g \left[\begin{aligned} & \left(\left(\frac{6t^5}{T_{SR}^5} - \frac{15t^4}{T_{SR}^4} + \frac{10t^3}{T_{SR}^3} \right) \cdot (H(t) - H(t - T_{SR})) \right) \\ & + (H(t - T_{SR}) - H(t - T_S)) \\ & + \left(\left(1 - \left(\frac{6(t - T_S)^5}{T_{SR}^5} - \frac{15(t - T_S)^4}{T_{SR}^4} + \frac{10(t - T_S)^3}{T_{SR}^3} \right) \right) \right. \\ & \left. \cdot (H(t - T_S) - H(t - T_S - T_{SR})) \right) \end{aligned} \right] \quad (4b)$$

$$f_3(t) = \left[\left(\frac{30(t-T_S)^4}{T_{SR}^5} - \frac{60(t-T_S)^3}{T_{SR}^4} + \frac{30(t-T_S)^2}{T_{SR}^3} \right) m_T V_o (H(t-T_S) - H(t-T_S-T_{SR})) \right] \quad (4c)$$

Spall rise time for Coalora was taken as 300ms. Dwell time varied across the test bed, a value of 300 ms with a consistent escape velocity of 1.47 m/s was chosen. The approximate equivalence of spall rise time and dwell time has been observed in chemical explosion tests (Stump, 1985). The smoothness of the time function decreases the high frequency spall signal. A lower bound source contribution was calculated by assuming a spall mass of 1.2×10^{10} kg. The resulting source time function and its spectrum are given in Figure 13. The time domain results emphasize the initial downward force due to material failure (1), the upward relaxation of the unspalled body (2), and the downward force associated with spall rejoin (3). The model predicts a peak force of 1.1×10^{16} dynes and a time duration of approximately 0.6 s. The peaked spectrum results in little contribution from spall at the long periods or high frequencies, but strong effects around the dominate period of 0.6 s. This 'dominant' period is below the characteristic corner frequency of the explosion model (1.7-2.5 Hz) but close enough in frequency to bias corner frequency or long period spectral levels if it is strong. The peaked nature of the secondary source could in some cases be misinterpreted in terms of explosion overshoot. The time integral of the spall force model gives a maximum value of 7.2×10^{14} dyne-cm which will be used latter to compare to the time derivative of the moment tensor determined by inversion of the near-source data.

Full use of transverse waveforms and spectra at the closest ranges (<2200m) is dependent upon a deviatoric source model. One possible representation is that attributed to Brune (1970) in which a shear stress is applied instantaneously to the fault surface and the resulting displacement field determined. Strictly speaking this model is only appropriate for earthquake sources. One could imagine that this shear stress is a result of the initial compressive waves from the source being resolved along planes of weakness

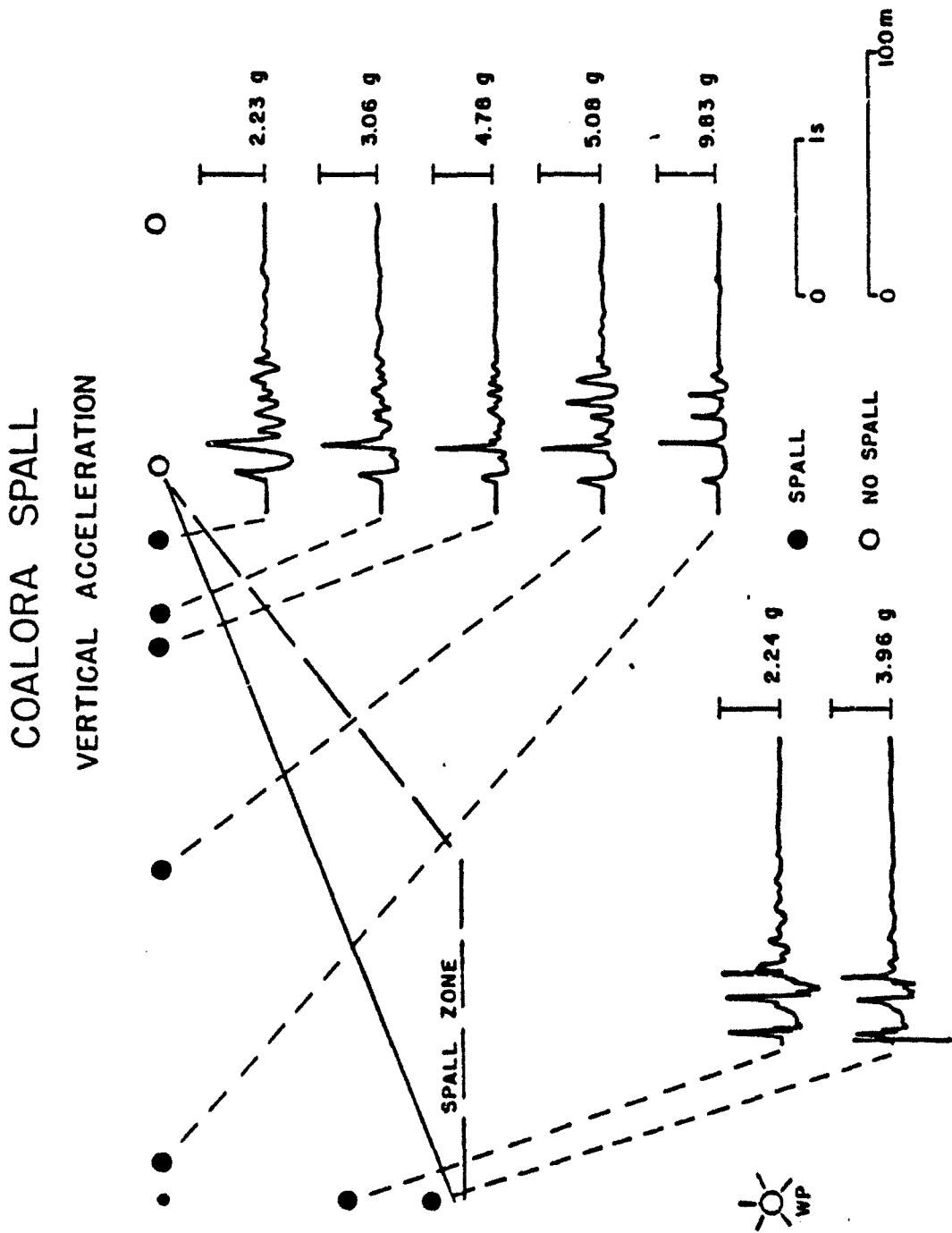


Figure 6: Vertical section displaying accelerograms from downhole and surface gages within two depths of burial which constrain the spall zone. Solid circles represent vertical accelerometer records that show characteristic -1 g dwell indicative of spall. Solid and heavy dashed lines are bounds on the depth of the spall zone.

SPALL FORWARD MODEL
COALORA

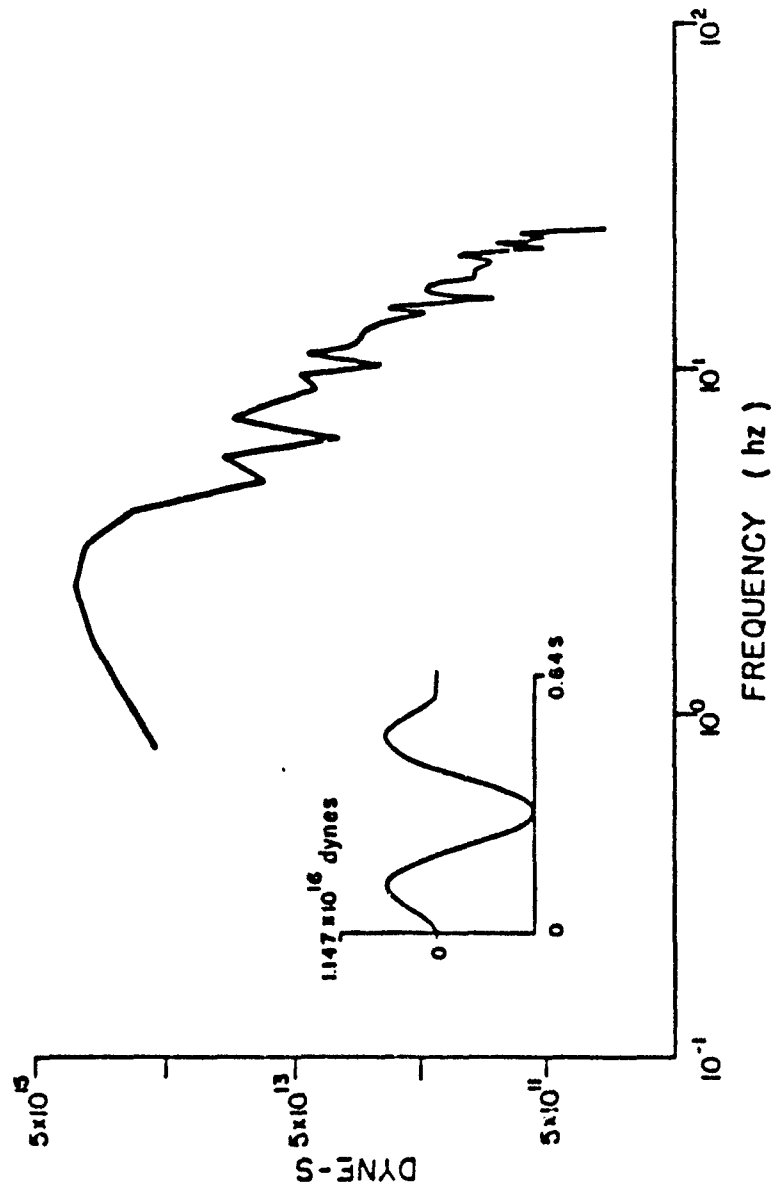


Figure 13: Spall source model developed from observational data within spall zone. Time function of vertical force along with its spectrum are given.

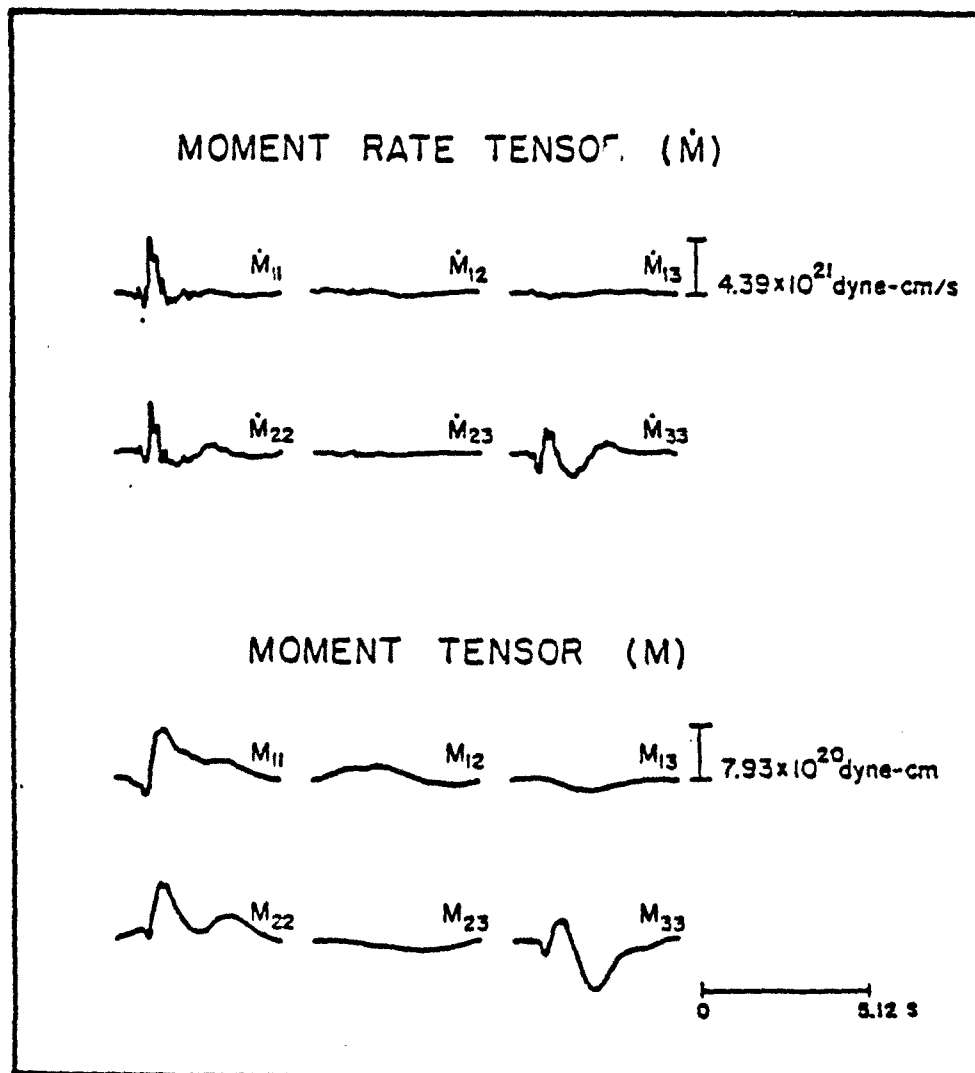


Figure 19: Moment rate (M_{ij}) and moment (M_{ij}) tensors from an inversion of the Coalora observational data.

or bedding planes in the geological material surrounding the explosion. For such a deviatoric source model the shear wave (T) spectrum can be interpreted in terms of moment, stress drop, fault radius, and average slip. Application of this model to the Coalora transverse spectral data (Figure 8 and Table 1a) results in the source properties given in Table 2. Corner frequency decreases with increasing range beyond about 1 km (Figure 12). Since the Brune model interpretation assumes the spectral corner frequency is characteristic of the source, data within 1 km of the explosion were used in the deviatoric source analysis. Source radii estimated from these data range from 110-144 m (124 m mean, 8.85 standard deviation of the mean -s.d.m). Stress drops varied from 47-149 bars (89 bars mean, 34 s.d.m). Average displacements on the fault were 18-56 cm (33 cm mean, 12 s.d.m). Source displacements calculated from the radiated wavefield are similar in size to displacements on faults and bedding planes found upon re-entering tunnels surrounding nuclear explosions at Rainier Mesa (Kennedy, 1984).

Using Coalora shot medium properties, equivalent elastic radii for a 1 and 10 kt explosion were calculated to be 133 m and 202 m respectively. The average deviatoric source radius from this study, 124 m, falls inside the equivalent elastic radii. Bache et al (1979) studied regional records (131-368 km) from the nuclear explosions Mighty Epic and Diablo Hawk at Rainier Mesa, NTS to constrain block motions. They estimated deviatoric moments for the two shots to be 1.3×10^{21} dyne-cm and 2.6×10^{21} dyne-cm respectively. Since corner frequencies could not be unambiguously determined by Bache et al. (1979), trade-offs existed for the range of possible source parameters. Source radii between 168-385 m coupled with displacements between 11-46 cm and stress drops of 20-120 bars bounded the possibilities. Equivalent elastic radii for the two events were estimated at 160 m. Deviatoric source radii in Bache's analysis appear to be larger than elastic radii although these estimates are not directly obtained from spectral data. Motions along faults and bedding planes were measured following the Mighty Epic and Diablo Hawk tests (Kennedy, 1984). Fault motions from Mighty Epic were between 0.24 m and 1.68 m at ranges of 74-124 m. The radius which encompasses these displacements is slightly less than the elastic radius as found for the Coalora experiment. These displacements represent motions on isolated planes

Table 2: Brune Model

Station	Range (m)	Radius (m)	Stress Drop (bars)	Displacement (cm)
GM2	274	127	76	29
GM4	365	131	87	34
GM6	389	123	100	37
GM7	612	110	66	21
GM8	614	123	49	18
GM9	612	123	149	56
GM10	307	123	124	46
GM11	495	117	120	42
S1	850	123	70	26
S3	900	144	47	20
S5	1670	149	62	28
S7	1640	144	51	22
S8	1700	144	87	38
S11	2100	172	54	28

which when summed would yield the Coalora near-source transverse observations.

Waveform Modeling and Inversion

Synthetic Green's functions for Yucca Flats around the Coalora explosion were developed so that waveform modeling for source determination could be completed. Geological and geophysical structure data utilized in these calculations were presented in the experimental section. The velocity-depth model is given in Figure 14. A linear velocity gradient in the top 0.3 km is followed by a jump in the P and S velocity at the vitrified tuffs. A slight jump in P velocity at the water table (500 m) is followed by a positive velocity gradient to the Paleozoics where another large step in velocity is recorded. A simple attenuation model was assumed with Q_p equal to 100 and Q_s equal to 44. Although important, little information exists for constraining shear wave velocities. Poisson's ratio was taken as 0.25. Synthetics were calculated utilizing the extended reflectivity methodology (Muller, 1985) so that the effects of both body and surface waves could be included. Green's functions for a pure explosion source are displayed in Figure 15 along with observations at 411/850 m (solid line-radial, dotted line-vertical).

Rather than attempt a trial and error waveform matching procedure, Green's functions were used in a constrained inversion of observational data. The first trial assumed that the waveforms could be modeled with just an isotropic source. In this case the only unknown is the source strength and its time/frequency function:

$$U_n = G_{nk,k} M_{kk} T(f) \quad (5)$$

where U_n are the radial and vertical motions, $G_{nk,k}$ are the Green's functions of the isotropic source, M_{kk} are the absolute source strength, and $T(f)$ is the source spectral shape. In the constrained inversions the source strength (M_{kk}) and shape ($T(f)$) are determined by matrix inversion given a set of Green's functions ($G_{nk,k}$) and observational data (U_n). This procedure can be applied to single or multiple source observations. Figure 16 is the resulting source spectrum and time functions from application of this procedure to one set of vertical and radial waveforms (transverse unfit

COALORA VELOCITY MODEL

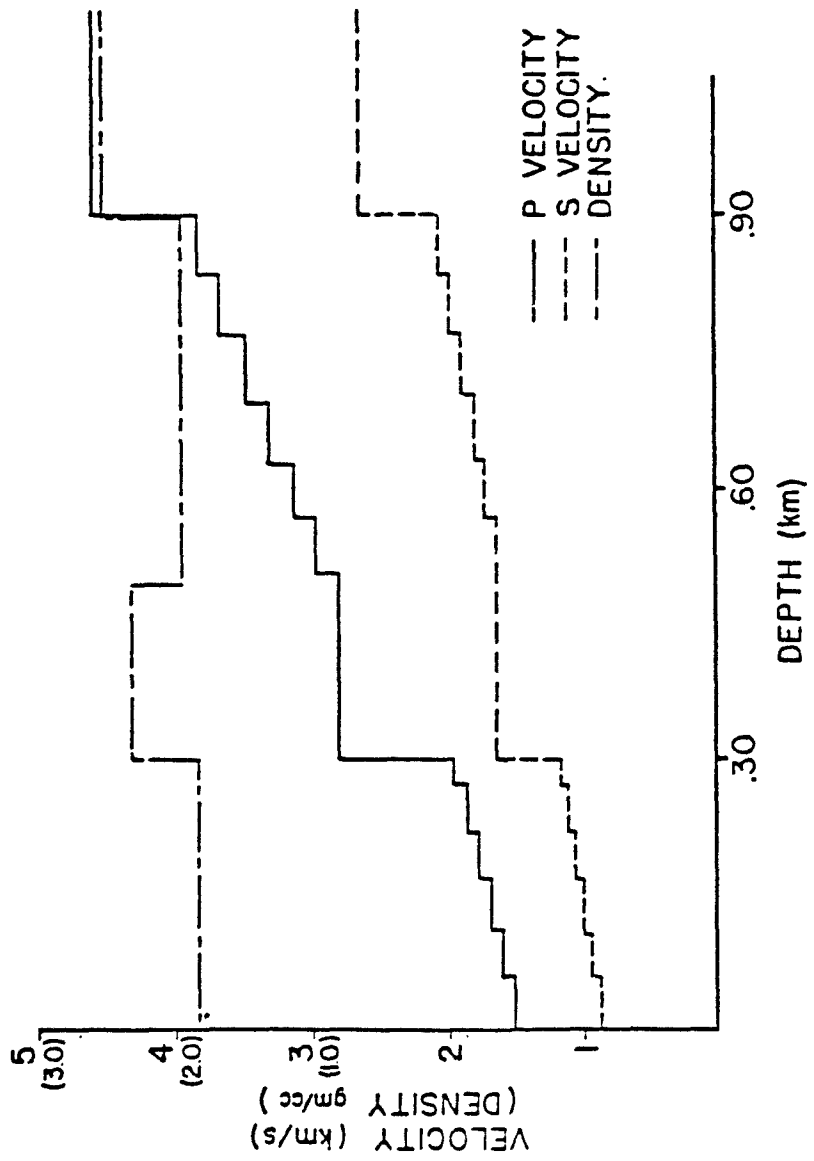


Figure 14: Velocity model developed for Coalora explosion in Yucca Flats.

COMPARISON OF ISOTROPIC SOURCE SYNTHETICS AND OBSERVED VELOCITY RECORDS

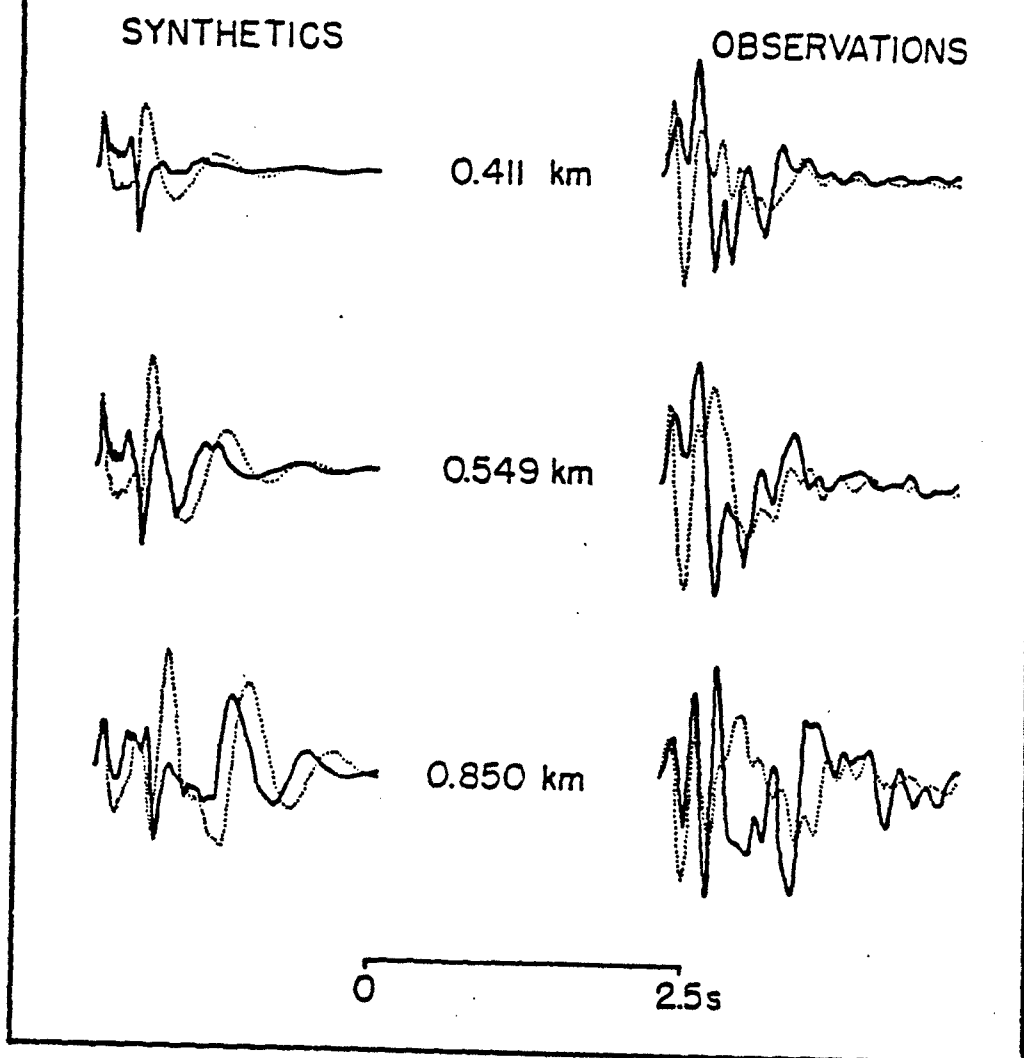


Figure 15: Isotropic Green's functions for velocity model in Figure 16 and selected observations in the 411-850 m range. Radial components are designated by solid lines while vertical components are dotted lines.

ISOTROPIC DECONVOLUTION

0.411 km

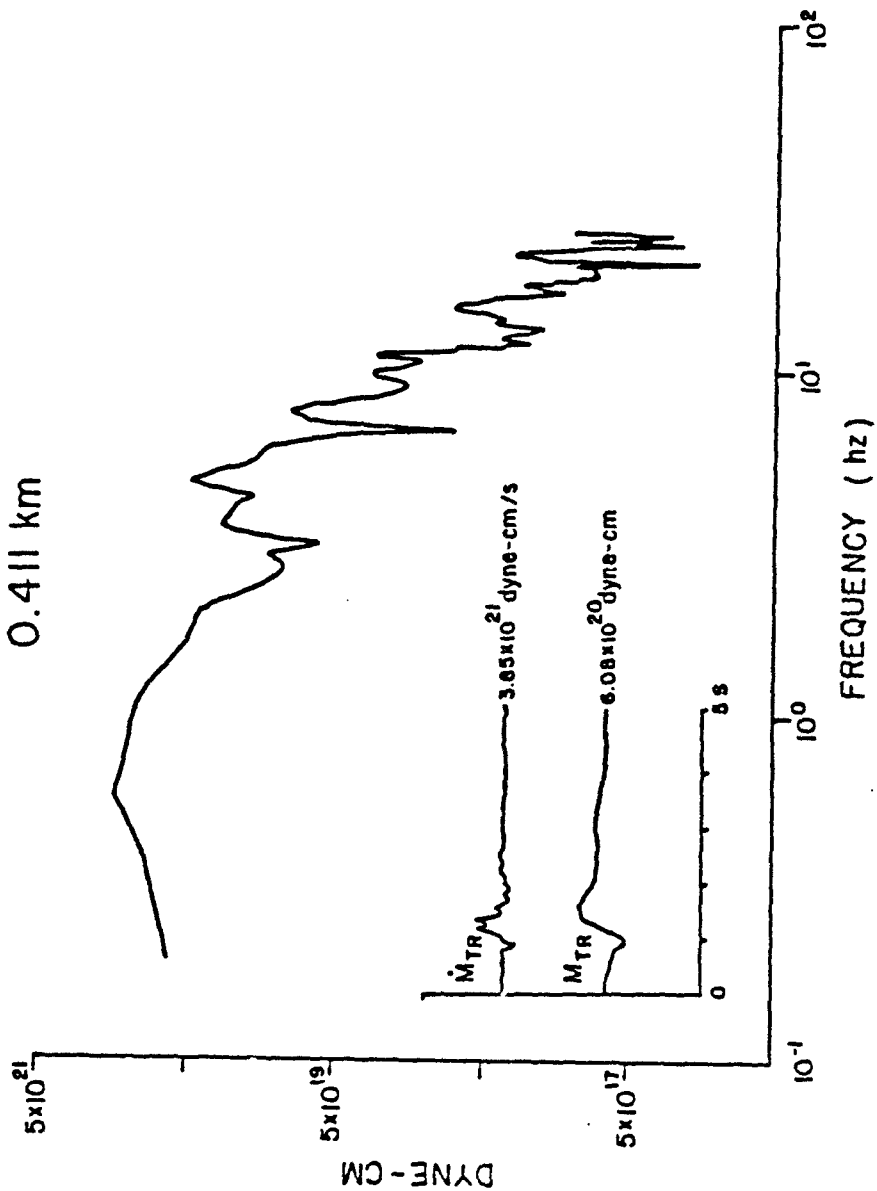


Figure 16: Result of a single station isotropic source inversion. Observation was at 411m. Source spectrum, its time history, and its time derivative are given.

because of isotropic assumption) from the Coalora explosion at a range of 411 m. Isotropic moments determined by this procedure for all single station data between 411 and 2100 m are given in Figure 17. The mean isotropic moment estimate is 6.9×10^{20} dyne-cm, smaller than the scalar source estimates since Green's functions used in the inversion focus more energy to the free surface than the simple propagation path corrections used in scalar source interpretation. Although the constrained isotropic moments have a factor of 4 scatter, they indicate no systematic increase or decrease in moment with range. This result indicates that propagation path effects within this range were properly taken into account in a relative way.

These constrained inversions may be biased if spall or deviatoric source contributions are important. Full moment tensor inversions were conducted to assess these secondary source contributions:

$$U_n(f) = G_{ni,j}(f) M_{ij}(f) \quad (6)$$

In this case all six elements of the moment tensor, M_{ij} , are determined at each frequency value given the matrix of Green's functions, $G_{ni,j}$, and the observational data, U_n , in the frequency domain. The observations within 2 km of the explosion working point were used in these inversions, a total of eleven, three-component observations. The basis for this data choice was discussed earlier.

Summary of one source inversion is given in Figure 18, where observed and calculated vertical, radial, and transverse velocity records are reproduced. One measure of the adequacy of the source inversion is how well the resulting source predicts the observations. Correlation coefficients for individual records range from 0.71 to 0.94. Transverse motions are as well modeled as vertical and radial components.

A second criteria in judging the inversions is the size of the condition number (ratio of largest to smallest eigenvalue) of the $G_{ni,j}$ matrix as a function of frequency. These values give a measure of resolution of model parameters by the data. The condition numbers are between 10 and 20 across

SINGLE STATION CONSTRAINED
ISOTROPIC MOMENT

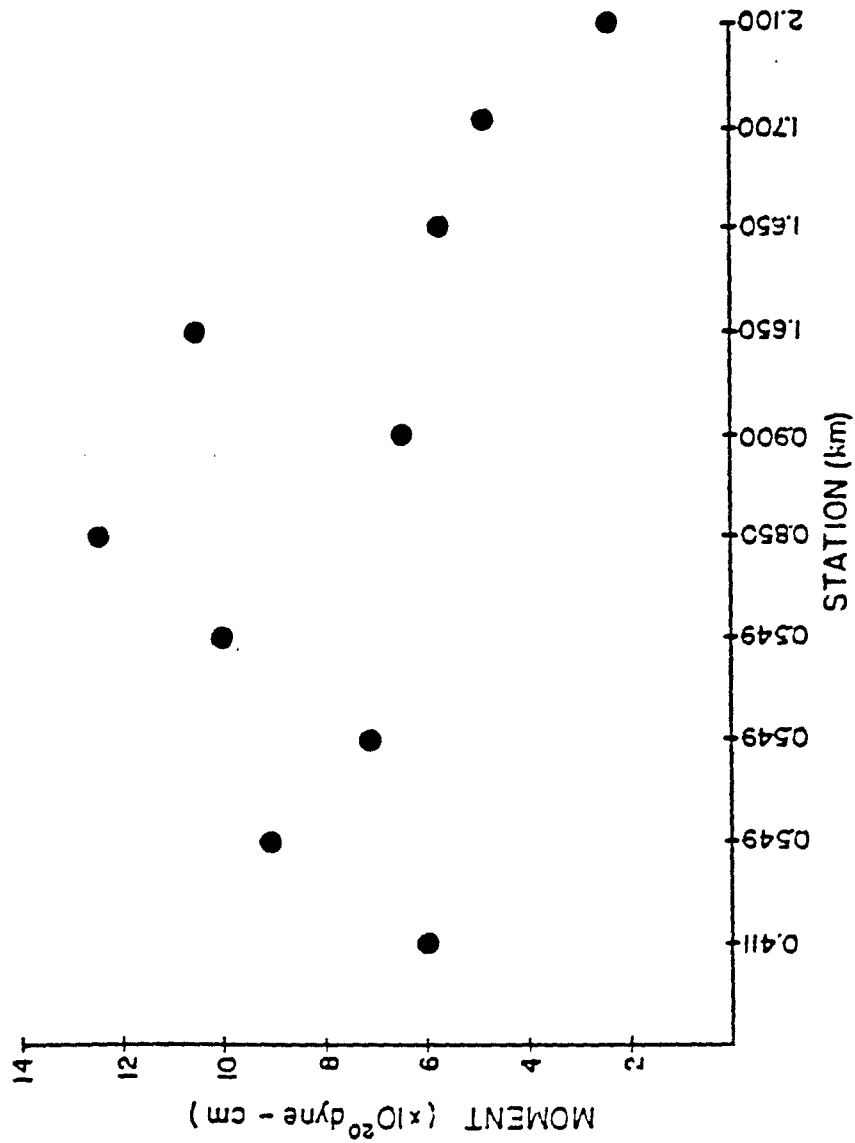


Figure 17: Summary of peak time domain moment estimates from single station isotropic source inversions such as the one in Figure 18.

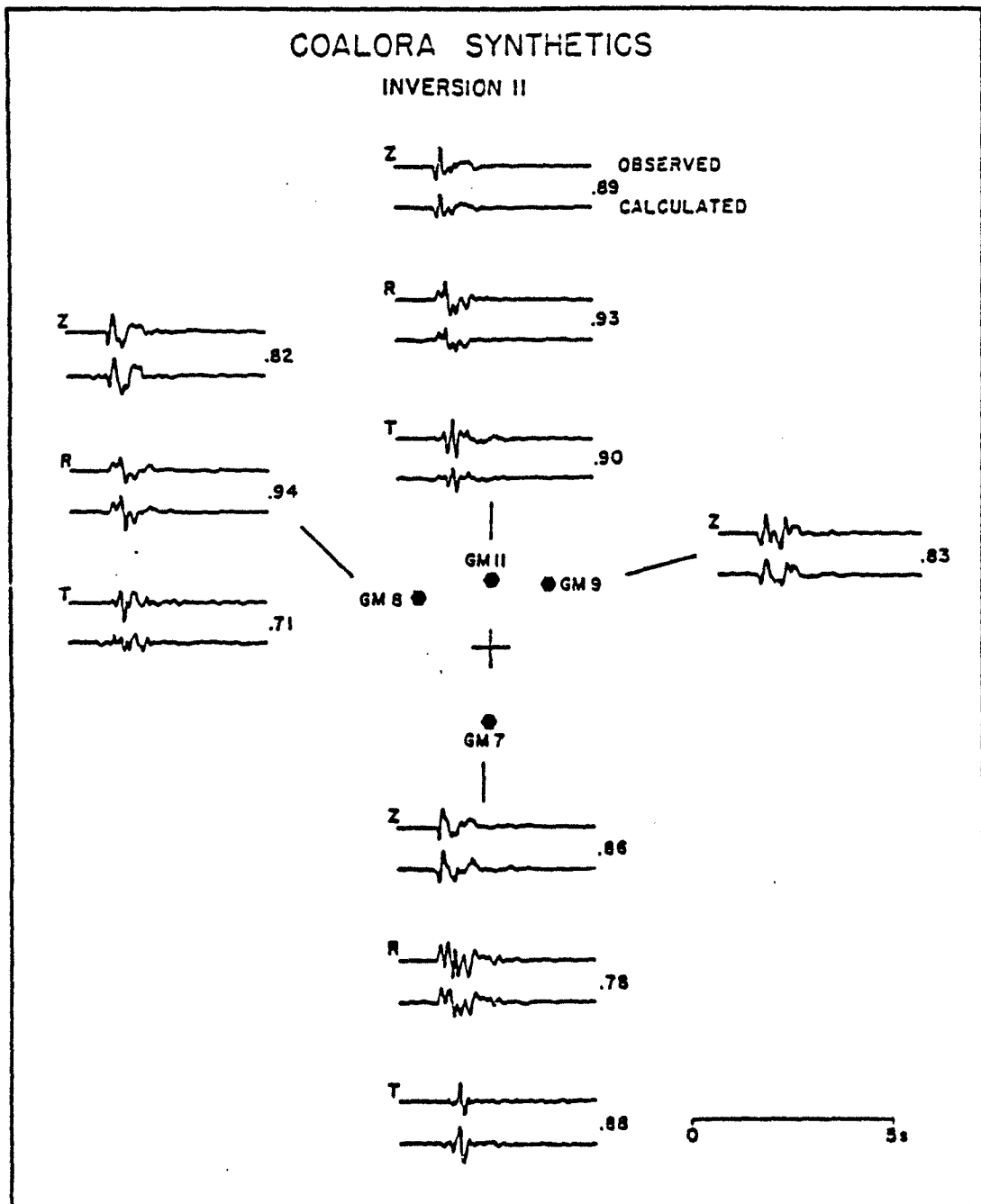


Figure 18: Observed and calculated seismograms from moment tensor inversions at four stations. Correlation coefficient for each fit is noted next to waveform pairs.

the entire frequency band for the array. Experience with synthetic inversions with realistic noise indicate that these values are more than acceptable.

The time derivative of the moment tensor and its integral for the Coalora source inversion are given in Figure 19. The source is dominated by diagonal elements of the moment tensor. The initial pulse is symmetric and is followed by a secondary long period contribution, largest on the M_{33} component, the vertical dipole. This secondary source found on the diagonal elements of the moment tensor is consistent with the spall forward model discussed earlier. As Day and McLaughlin (1991) show, the moment tensor representation of the spall source function is proportional to the doubly integrated body force representation of spall scaled by α^2/h , where α is the P velocity (1.9 km/s) and h is the source depth (274m) assumed in the moment tensor inversions. The integral of the body force spall model developed earlier (7.15×10^{14} dyne-s) can be compared to the strength of the secondary long period arrival on the M_{zz} component of the moment rate tensor in Figure 19. The source strength of this secondary pulse from the moment tensor inversion is 1.7×10^{21} dyne-cm/s which compares to the forward spall model estimate of 9.4×10^{20} dyne-cm/s. The spall forward model assumed the lower bound of spall mass (1.2 - 4.4×10^{10} kg) so with an intermediate mass estimate the forward model from the spall zone data and the inverse model from moment tensor inversion would be in very close agreement for spall source strength. The secondary spall pulse in Figure 19 is 1.5 s in duration which is a factor of two longer than the forward spall model. This increased duration may reflect the approximate way in which spall spatial finiteness is taken into account in the forward model.

Off-diagonal elements of the moment tensor are a factor of 5-10 smaller than the diagonal elements supporting the small deviatoric scalar moments determined earlier. Separation of the deviatoric components of the moment tensor is complicated by the apparent spall contribution. No attempt was made at further analysis of the deviatoric component.

The peak in the diagonal elements of the moment tensor is 7.9×10^{20} dyne-cm. This moment estimate compares with the mean scalar value of 1.95×10^{21} and the average constrained value of 6.9×10^{20} .

Implications

The Coalora experiment offered the opportunity to constrain important source processes contributing to near-source ground motion from a nuclear explosion. Data identified important contributions from the isotropic source, spall, and other deviatoric sources. The instrumental array included gages from within the spall zone out to ranges comparable to the scale of the major geological feature, Yucca Flats. Detailed site characterization data from throughout the valley were available for constraining propagation path effects. At ranges of 2 km or less the waveforms were simple with distinct differences between the radial/vertical (R/Z) and transverse (T) motions. As propagation distance increased, all three components of motion (RTZ) became similar in appearance in both the time and frequency domains. At 5.1 km range ground motions had durations in excess of 20 s with similar corner frequencies and long period levels for all (RTZ) components. Three dimensional wave propagation calculations for the site indicate that the Yucca Flats two and three dimensional structure become important at ranges beyond 2 km. Strong similarity in spectra and long duration of motion at 5.1 km are attributed to attenuation and scattering effects within the basin underlying Yucca Flats. Effects of attenuation on the deviatoric source can be seen as a decrease in apparent corner frequency for transverse spectra with range. Source studies were constrained to data within 2100 m of the source. Use of more distant data could result in a biased source estimate at Yucca Flats.

The isotropic part of the source dominates moment tensor inversions with a total source strength near 8×10^{20} dyne-cm. Observed isotropic corner frequencies (1.8 Hz) fall within the bounds of plausible values predicted by a Mueller-Murphy source model (1 kt - 2.5 Hz; 10 kt - 1.7 Hz). High frequency decay of f^{-2} is observed also in support of the Mueller-Murphy source model. Scalar source estimates from observed spectra are approximately 2.5 times

larger than complete moment tensor estimates. This difference is attributable to the different way the two estimates treat downgoing energy and surface waves with the scalar moments being biased high. The multiplicative error factor for the scalar isotropic moment was 1.36 representative of the spatial variability of the seismic energy at these near-source distances.

The deviatoric source has higher corner frequencies although the absolute moment is 5-10 times smaller than the isotropic. Simple Brune type models lead to an equivalent source radius of 124 m which is slightly smaller than the elastic radius, a moderate stress drop of 89 bars, and an average displacement of 33 cm. The source radius and average slip are comparable to observations in the tunnels of Rainier Mesa following explosions. These near-source observations when not dominated by attenuation or scattering effects give a consistent characterization of the deviatoric source contribution. In the case of data from Yucca Flats these estimates may become biased when data beyond 2 km are used because of scattering and attenuation effects.

Forward calculations of the size of the spall contribution are comparable to a late time, longer period arrival seen in the moment tensor. This source contribution is dominant on the M_{zz} component and agrees with similar results for chemical explosions (Stump, 1987). The spall source strength determined from forward models constrained by spall zone data and moment tensor inversions are consistent with one another. The duration of the spall contribution from the inversions is longer than that determined by the forward model and may reflect the approximate way in which source finiteness is taken into account. The fact that the spall source function is delayed in time and longer period in duration than the spherically symmetric explosion source time function means that it could lead to a biased estimate of the explosion source time function if not taken into account. Its close proximity in time to the explosion time function means that it could be interpreted as overshoot in the source time function. Isotropic source deconvolutions of the Coalora data (Figure 16) do indicate significant overshoot in the source time function.

Constrained isotropic source inversions offer opportunity for single station explosion source estimates. Applying this procedure to data spanning a wide

range of distances, we illustrated that there is no trend in moment (with respect to data scatter) over the range, 549 - 2200m. This observation argues that attenuation has been properly taken into account over these distances.

The Coalora experiment illustrates the importance of combining motion measurements from within the source region (spall zone) and outside it so that a complete unambiguous picture of the equivalent seismic source can be interpreted. Such studies could provide the basis for developing physically supported scaling relations for each of the individual source contributions.

References

- Aki, K. and Y. B. Tsai (1972). Mechanisms of Love-wave excitation by explosive sources, *J. Geophys. Res.* **77**, 1452-1475.
- Bache, T. C., W. E. Farrell, and D. G. Lambert (1979). Block motion estimates from seismological observations of Mighty Epic and Diablo Hawk, Defense Nuclear Agency Report 5007F, Washington, D. C. 20305, 184 pages.
- Brune, J. N. (1970). Tectonic stress and the spectra of seismic shear waves from earthquakes, *J. Geophys. Res.* **75**, 4997-5009.
- Burger, R. W., T. Lay, T. C. Wallace, and L. J. Burdick (1986). Evidence of tectonic release in long-period S waves from underground nuclear explosions at the Novaya Zemlya test sites, *Bull. Seism. Soc. Am.* **76**, 733-755.
- Day, S. D., N. Rimer, J. T. Cherry (1983). Surface waves from underground explosions with spall: analysis of elastic and nonlinear source models, *Bull. Seism. Soc. Am.* **73**, 247-264.
- Day, S. D. and K. L. McLaughlin (1991). Seismic source representations for spall, *Bull. Seism. Soc. Am.* **81**, 191-201.
- Eisler, J. and F. Chilton (1964). Spalling of the earth's surface caused by underground nuclear explosions, *J. Geophys. Res.* **69**, 5285-5293.
- Eisler, J., F. Chilton, and F. Sauer (1966). Multiple subsurface spalling by underground nuclear explosions, *J. Geophys. Res.* **71**, 3923-3927.
- Ferguson, J. F., R. N. Felch, C. L. V. Aiken, J. S. Oldow, and H. Dockery (1988). Models of the Bouguer Gravity and Geologic Structure at Yucca Flat, Nevada, *Geophysics*, **53**, 231-244.
- Gupta, I. N. and R. R. Blandford (1983). A mechanism for generation of short-period transverse motion from explosions, *Bull. Seism. Soc. Am.* **73**, 571-591.

Haskell, N. A. (1967). Analytic approximation for the elastic radiation from contained underground explosion, *J. Geophys. Res.* 72, 2583.

Kennedy, R. P. (1982). Mighty Epic/Diablo Hawk block motion program, in DARPA/AFOSR Symposium on the Physics of Nonisotropic Source Effects from Underground Nuclear Explosions, DARPA-GSD-8203/AFOSR-NP-8201, Defense Advanced Research Projects Agency, Arlington, Va 22209.

Kisslinger, C., E. J. Mateker, Jr., T. V. McEvelly (1961). SH motion from explosions in soil, *J. Geophys. Res.* 66, 3487-3496.

McLaughlin, K. L., L. R. Johnson, and T. V. McEvelly (1983). Two-dimensional array measurements of near-source ground acceleration, *Bull. Seism. Soc. Am.* 67, 349-375.

Mueller, R. A. and J. R. Murphy (1971). Seismic characteristics of underground nuclear detonations. Part I. Seismic scaling law of underground detonations, *Bull. Seism. Soc. Am.* 61, 1675-1692.

Ohta, Y. and A. Kubotera (1968). An example of Love waves generated by small explosions, *Zisin (J. Seismol. Soc. Japan)*, Ser. 2, 21, 109-120.

Patton, H. J. (1988). Source models of the Harzer explosion from regional observations of fundamental-mode and higher order mode surface waves, *Bull. Seism. Soc. Am.* 78, 1133-1157.

Patton, H. J. (1990). Characterization of spall from observed strong ground motions on Pahute Mesa, *Bull. Seism. Soc. Am.* 80, 1326-1345

Perret, W. R. and R. C. Bass (1974). Free field ground motion induced by underground explosions, SAND74-0252, Sandia National Laboratories, Albuquerque, New Mexico.

- Schlittenhardt, J. (1991). The effects of spall on teleseismic P-waves: an investigation with theoretical seismograms, AGU Monograph on Explosion Source Phenomenology (in press).
- Sobel, P. A. (1978). The effect of spall on m_b and M_s , Teledyne Geotech report SDAC-TR-77-12, Dallas, Texas.
- Stump, B. W. (1985). Constraints on explosive sources with spall from near-source waveforms, *Bull. Seism. Soc. Am.* 75, 361-377.
- Stump, B. W. and R. E. Reinke (1987). Experimental seismology: *In Situ* source experiments, *Bull. Seism. Soc. Am.* 77, 1295-1311.
- Stump, B. W. (1987). Mathematical representation and physical interpretation of a contained chemical explosion in alluvium, *Bull. Seism. Soc. Am.* 77, 1312-1325.
- Taylor, S. R. and G. E. Randall (1989). The effects of spall on regional seismograms, *Geophys. Res. Lett.* 16, 211-214.
- Vidale, J. E. and D. V. Helmberger (1987). Path effects in strong motion seismology, in *Seismic Strong Motion Synthetics* edited by Bruce A. Bolt, Academic Press, Orlando, Fl.
- Viecelli, J. A. (1973). Spallation and the generation of surface waves by an underground explosion, *J. Geophys. Res.* 78, 2475-2487.
- von Seggern, D. H. and R. R. Blandford (1972). Source time functions and spectra for underground nuclear explosions, *Geophys. J.* 31, 83-97.
- Wallace, T. C., D. V. Helmberger, and G. R. Engen (1985). Evidence of tectonic release from underground nuclear explosions in long-period S waves, *Bull. Seism. Soc. Am.* 75, 157-174.

Wallace, T. C. and J. F. Barker (1985). Modeling near-field observations from nuclear explosions in dry tuff and alluvium, AFGL-TR-85-0321, Air Force Geophysics Laboratory, Hanscom AFB, Ma 01731. ADA165227

Werth, G. C. and R. F. Herbst (1963). Comparison of amplitudes of seismic waves from nuclear explosions in four mediums, J. Geophys. Res. 68, 1463-1474.

Wojcik, G. L. and D. K. Vaughn (1984). Large-scale analysis of three-dimensional seismic waves, WA-CA R 8403, Weidlinger Associates, Menlo Park, California, 94025.

Near-Source Characterization of the Seismic Wavefield Radiated from Quarry Blasts

Sharon K. Reamer*
Klaus-G. Hinzen**
Brian W. Stump*

March 1992

*both at Department of Geological Sciences, Southern Methodist
University, Dallas Texas 75275

**Bundesanstalt für Geowissenschaften und Rohstoffe, Stilleweg 2,
3000 Hannover 51, Federal Republic of Germany

keywords: temporal finiteness, spatial finiteness, chemical explosion,
quarry blast, cylindrical seismic source, linear superpositioning
techniques

SUMMARY

A series of controlled seismic experiments performed in a limestone quarry demonstrate the utility of high precision electronic detonators in studying source characteristics of multiple explosive arrays. At near-source ranges (80–130 m), where source dimensions are on the same order as source–receiver distances, the influence of the difference in travel path length among individual explosions on the seismograms is significant. Focusing of the seismic energy is observed as a function of station location with respect to the source array and is attributed to the extended source length (68–94 m) and firing time of the source (380–544 ms).

We examine two methods for modeling ripple-fired explosions at near-source ranges using the principles of superpositioning. The first method is based primarily on acquisition of an adequate single shot signal and requires well-constrained shot times. Amplitude variations which result from travel path differences are not modeled, which restricts use of this technique for purposes of blast vibration reduction to larger distances (>2 – 3 source dimensions) where the spatial finiteness effects of the source begin to diminish. For near-source distances (< 2 source dimensions), we successfully model multiple-source seismograms by convolving a synthetic seismic source signal for a single explosion with individual half-space Green's functions calculated for each explosion in the array. Our single-source model for a cylindrically-shaped single charge (borehole length of 17.5 m and diameter of 90 mm) of 68 kg consists of a modified Mueller–Murphy approximation which utilizes source parameter estimates taken from chemical explosion study results. Model parameters include a final cavity radius of 0.25 m and an elastic radius of 18 m. The final model is obtained by convolving the simulated single-source time series

with half-space Green's functions calculated for several source depths and superposed to approximate the spatial extent of the borehole. The relative amplitude and phase characteristics of the observed single-source signal at the same distance (80.6 m) are reproduced by this model.

Multiple-source synthetic seismograms contain individual Green's functions for each source-receiver distance but utilize identical sources for the explosive array. Focusing effects are shown to be due to the effect of propagation path differences between individual explosions in agreement with the results of Anderson and Stump (1989) in simulating multiple-source seismograms. Good fits to the measured production shot amplitude spectra are obtained with the synthetic spectra. Spectral peaks are well matched due to precision of the firing times which were controlled by electronic detonators. Our example of delay time variances for 32 ms production shot (Appendix) argues for better constraint of firing times for controlled seismic experiments. Such constraint requires a 1% error or less in cap firing times which can be realized by the use of firing systems with an order of magnitude increase in precision compared to pyrotechnic detonators.

INTRODUCTION

The present study focuses on the generation and propagation of seismic waves from multiple explosion arrays. We analyze seismic data collected from three production blasts and a single explosion in a limestone quarry to assess the influence of an explosive source extended in space and time on the seismic wavefield. We also explore the efficacy of linear superpositioning techniques and equivalent source models for chemical explosions.

Previously, seismological studies of ripple-fired explosions were limited and dispersed somewhat unevenly in the literature. Interest in recent years has increased mainly due to the necessity of discriminating large commercial blasts from small nuclear explosions. Several recent studies have addressed the discrimination problem at regional distances (Baumgardt and Ziegler, 1988; Hedlin et al, 1989; and Su et al, 1991), although in most cases with limited knowledge of or constraints on the seismic source used in deriving the proposed discriminants. Smith (1989) examined spectral characteristics of multiple-delay, multiple-row explosions and identified a significant tradeoff between attenuation due to scattering and source characteristics at regional distances.

Anderson and Stump (1989) present results of modeling near-source seismograms recorded from multiple-row, multiple-delay production shots in a granite quarry in Massachusetts. Individual Green's functions for each source-receiver distance in the array were calculated and convolved with a simulated single-source. Extended source time duration (temporal finiteness) and propagation path differences due to extended source spatial dimensions (spatial finiteness) were well reproduced despite a limited knowledge of the actual firing times or constraints for the single-source model. Hinzen (1988) used superpositioning with weighted amplitudes to model a series of five explosions fired in a single row. The recorded seismograms from a single explosion fired separately from the row shot but located next to the multiple array were used for the superpositioning. By using an in situ single shot, the seismic response of the individual sources and extended time duration of the multiple explosions were well modeled, although amplitude differences due propagation path differences from the extended source dimensions were not reproduced. It was thought that amplitude variations could be attributed to

coupling differences between individual charges. Some studies have indicated that nonlinear, dynamic source effects may be observable in the elastic region (Minster and Day, 1986). However, experimental confirmation of superpositioning for two charges fired simultaneously with spatial separations of different lengths (Stump and Reinke, 1988) argues against dynamic interaction of the sources being observable in far-field seismic data.

As noted by Hinzen (1988), knowledge of the exact firing times is essential to any study of ripple-fired explosions. The data in the present study are unique in that firing times are controlled with electronic detonators. The electronic firing system reduces scatter in firing times and allows precise measurement of actual detonation times. This provides us the opportunity to test and compare observed production shot seismograms to time series calculated from two superpositioning methods: (1) empirical superpositioning with an in situ single shot, and (2) linear superpositioning with calculated source and travel path functions.

Additionally, the single shot data provides constraints on our single-source model. As discussed by Herrmann et al (1989), there is a need for refinement of source models for small-yield chemical explosions. We examine the Mueller-Murphy (Mueller and Murphy, 1971) source model with parameter estimation adjusted for our quarry explosions. Scaling of source parameters for small chemical explosions at depth using the Mueller-Murphy model is explored in detail by Grant (1988) using both a forward modeling approach and moment tensor inversions. We pay particular attention in the synthetic calculations to modeling the single explosion in the forward case and thereby extend the work of Anderson and Stump (1989) in modeling the temporal and spatial finiteness of the multiple explosion seismograms.

DESCRIPTION OF EXPERIMENTS

Blast Design

The experiments consisted of three multiple explosions (production shots) and one in situ single shot fired in a limestone quarry in northern Italy. Figure 1 shows the plan of the quarry bench and shot locations for three production shots (SVI3, SVI5 and SVI6) and the single shot (SVI4) examined in the present study. Each production shot was fired in a single row at neighboring parts of the 15 m highwall. The firing direction for each production shot is indicated by the arrows in front of the highwall in Figure 1. The single shot, SVI4 was also located on the quarry bench and recorded at similar distances to the production shot experiments. Shot SVI3 produced 14.4 kilotons (kt) of material with a total charge weight of 1.26 tons (t) of explosives, SVI5 produced 16.0 kt with 1.35 t, and SVI6 produced 20.7 kt with 1.75 t.

The single shot, SVI4, consisted of 68 kg of explosives including 11 kg of high energy explosives in the bottom of the hole and 57 kg of ammonium nitrate fuel oil (ANFO). The explosives were initiated from the top of the hole. The charges were stemmed with 3 m of drill cuttings. The borehole was drilled at an inclination of 30° to the vertical with a borehole length of 17.5 m, diameter of 90 mm, and burden of 5 m. Loading of the boreholes for the production shots was identical to the single shot for most but not all cases. For example, 16 out of 20 holes for SVI5 were loaded as described for SVI4. The other four holes contained high energy mixtures in the middle of the charge column instead of at the bottom. However, total charge weights per hole were kept constant at 68 kg for all production shots considered here. A crosscut view of the typical borehole is shown in Figure 2 in addition to a plan view of SVI5 and SVI6. The 20

boreholes for SVI5 had spacing and burden of 4 m and 5 m, respectively, for a total array length of 76 m. A constant delay time of 20 ms was used which gives a total desired firing time of 380 ms. Actual shot times for SVI5 were not recorded. For the 26-hole array, SVI6, borehole spacing and burden were the same as for SVI5 except for holes 22-26 where the quarry wall turns. Delay intervals for SVI6 alternated between 18 and 27 ms for a total desired firing time of 540 ms (Figure 2). Actual shot times recorded for SVI6 (Table 1) vary from desired firing times by values ranging from 0.02% to 1.5%. Shot times for SVI3 (not shown in Figure 2), with 18 holes (burden and spacing at 4 and 5 m, respectively) and a constant 32 ms delay (544 ms total desired firing time), were also recorded with a maximum deviation from desired times of 1.4%. This small variation between desired and actual firing times was achieved by the use of electronic detonators.

Seismic Station Locations and Data Acquisition

Station locations for each production shot formed a stretched semicircle around the row of explosions. The distance between each of these stations and the closest borehole was 80 m. Stations A through E, as shown in Figure 1, are considered in this study. Station A was located 80 m behind the last borehole (hole 18) of SVI3 (measured perpendicular to the explosive array), while stations B and C were positioned 80 m behind the first and last boreholes of SVI5, respectively. Station D was located 80 m behind the first borehole of SVI6, and station E was positioned 80.6 m distance from the single shot, SVI4. Each station consisted of a three-component 4.5 Hz geophone with 62% critical damping. All stations were calibrated with a shaking table. Signals were digitally recorded with a central recording system utilizing 64 channels. The data were sampled at the rate of 15.625K samples per second with a dynamic range

of 12 bits including polarity. Length of the recorded signal was 1 s for the production shot and s for the single shot experiment. The recording system is described in detail by Hinzen (1988).

Firing System

The production shots were initiated by a computer driven electronic firing system. This system offers a maximum of 60 time steps of which 18, 20, and 26 have been used in SVI3, SVI5, and SVI6. The detonators contain an integrated circuit which interacts with the blast computer. Each detonator is programmed at the factory for one of the possible time steps. In the field, the time length of the delay step is preset at the blast computer to values between 1 and 100 ms. This preset delay time multiplied by the time step of the detonator gives the absolute firing time. By dropping time steps in the row of the detonators, unequal delay time intervals, as were used for SVI6, can be realized. A detailed description of the firing system is given by Hinzen et al (1987).

EXPERIMENTAL DATA

Figure 3 shows velocity seismograms from stations A-D for the SVI3, SVI5, and SVI6. The x and y components are the two perpendicular horizontal components where the x direction is parallel to the explosive array (Figure 1). The z component is vertical. All seismograms are normalized to maximum trace amplitudes, indicated in mm/s at the end of each seismogram. The firing direction for SVI5 and SVI6 recedes from stations B and D and for SVI3 and SVI5 comes closer to stations A and C (Figure 1).

The time duration of the seismic record is proportional to the total duration of the sources. Duration of the seismograms is approximately 1.2-1.3 times the total firing time at stations B and D and 1.3-1.4 for stations A and C. Except for the initial compressive wave pulse, individual

signal characteristics of a single source are obscured in the multiple source seismograms. The most notable feature is the constructive and destructive interference of seismic energy as seen in the seismograms due to the multiple explosions. Seismic energy peaks in the beginning of the seismogram for stations B and D and at the end for stations A and C. This is clear from the cumulative seismic trace energy, shown below each set of station seismograms (Figure 3). The dashed lines connect the first arrival of seismic energy with the point where 98% of the total energy per trace is reached. Cumulative trace energy at time $I-\Delta t$ is measured by the quantity

E_{cum} :

$$E_{cum}(I) = \sum_{i=1}^I \sum_{j=1}^3 V_{ij}^2, \quad (1)$$

where V_{ij} is ground velocity in mm/s. The index i runs from 1 to the total number of samples and j represents the two horizontal and one vertical components of the recording. If a constant amount of seismic energy arrives as a function of time, the cumulative energy would follow the dashed lines. The convex curvature of the cumulative energy for stations B and D illustrates that the energy arriving from SVI5 and SVI6, respectively, is greater at the beginning and decreases gradually as the shot detonation moves farther away from the station with time. The energy curve forms a concave shape for stations A and C, where the arriving energy increases with time as the detonating charges progress closer to the stations.

SUPERPOSITIONING

Empirical Model Calculations

Our first approach is to reproduce the production shot seismograms in the time domain using the hybrid modeling technique of Hinzen (1988). This empirical modeling method consists

of linear superpositioning of an observed single-source seismogram with appropriate delay times to reproduce a multiple shot seismogram. This method is frequently utilized to reduce ground vibrations due to blasting (Crenwelege, 1991; Hinzen and Reamer, 1991). Propagation effects and source properties are contained in the recorded signal from a single explosion used to synthesize production blasts at the same or a nearby location. The optimal synthetic production blast signal is calculated by varying firing time sequences until seismic vibrations are adequately reduced (usually in the frequency range between 5 and 20 Hz). The method requires precise knowledge of the firing times. Linear interaction of seismic waves from neighboring explosions and identical seismic source functions are assumed. Since the single shot contains only the propagation effects along a single source-receiver path, differences in propagation due to the actual path are not modeled directly; however, differences in path length are included by the addition of an assumed compressional wave travel time. In the time domain, this can be expressed as a series of convolutions given by:

$$V(x,t) = S(x',t') \otimes G(x,t; x',t') \otimes \sum_{i=1}^n a_i \delta(t - t_i) \quad (2)$$

where,

$V(x,t)$	=	particle velocity
$G(x,t; x',t') \otimes S(x',t')$	=	representation of measured seismic signal
x	=	spatial coordinates of station
x'	=	spatial coordinates of source
a_i	=	weighted amplitudes
t_i	=	delay and travel times, and
n	=	total number of explosions.

For this experiment, the measured single-source seismogram at station E (inset in Figure 4) is convolved with a time-delayed sequence of unit impulses. Each time delay includes firing time of the shot and travel time (with an assumed P-wave velocity of 4.5 km/s) from source to receiver.

The impulse series simulates the temporal extent of the multiple-source array. Results of the linear superpositioning for station B of SVI5 and station A of SVI3 (Figure 4) show that total source duration is well matched by the linearly superposed seismograms. However, simple linear superpositioning, as shown in the upper traces in Figure 4, does not adequately reproduce the amplitudes observed in the measured data. Variations in amplitude can be modeled directly only if the firing times are well known, as is the case for this experiment. Individual amplitude values from the observations are modeled by weighting the amplitudes of the linearly-superposed seismograms at the appropriate delay times to agree with the amplitudes of the observed multiple source event (weighting factors are determined directly from the measured production shot seismograms). The resulting velocity seismograms (bottom traces in Figure 4) match the observational data quite well demonstrating the effectiveness of this superpositioning technique if shot times are well constrained. This technique can be a useful tool for blast vibration reductions; however, the method does not provide us with any physical understanding of the mechanism for interference effects observed in the production shot seismograms. As noted by others (Smith, 1989; Anderson and Stump, 1989), spatial finiteness of the production shot array and temporal finiteness due to time delay blasting combine to produce a seismogram extended in time (proportional to total source firing time) and exhibiting characteristics of destructive and constructive wave interference. The rest of this paper will be devoted to understanding the nature of these interference effects, as observed at near-source distances.

Theoretical Model Calculations

We attribute the observed amplitude variations in the production shot seismograms to differences in propagation path among individual explosions in the array. Our primary

motivation is to quantify the contributions to the multiple shot seismograms from the seismic source and propagation path. We therefore simulate the production shot signals using a forward modeling approach. We calculate individual Green's functions for each shot of the array following the method of Anderson and Stump (1989). Each Green's function is convolved with a single-source time function and linearly superposed with the appropriate delay times to reproduce the multiple shot seismograms. This modeling approach is represented by:

$$V(x,t) = \sum_{i=1}^n S(x_i,t') \otimes G(x,t; x_i,t') \otimes \delta(t - t_i) \quad (3)$$

- where, $V(x,t)$ = seismic particle velocity
 $G_i(x,t;x_i,t')$ = individual Green's functions
 $S(x_i,t')$ = single-source model
 x = spatial coordinates of station
 x_i = spatial coordinates of sources
 t_i = delay times, and
 n = the total number of explosions.

As in the empirical modeling approach, each individual shot of the multiple array is assumed to have an identical source function. An elastic half-space with a compressional wave velocity of 4.5 km/s is assumed for the Green's function as a first-order approximation to the quarry structure estimated from average P-wave arrival times for the measured data. Density is assumed to be 2600 kg/m³, a reasonable value for the competent limestone in this area. Individual Green's functions are calculated using the method of Johnson (1974) for each source-receiver distance in the array configuration. Figure 5 shows radial and vertical component Green's functions convolved with the single-source model calculated for station D. The details of the single source model calculations will be fully discussed in the next section. Here we only wish to illustrate that the change in Green's function from the first to last explosion is not dramatic

(Figure 5), but is significant when considered in addition to the delay times between shots. The source-receiver distance increases from 80 to 126.7 m between the first and last explosion in the SVI6 array (26 holes). P and SV-Rayleigh waves are clearly separated at these distances. The amplitude ratio of P to SV-Rayleigh peaks is 0.22 and 0.18 for the vertical and 0.78 and 0.72 for the radial component at the shortest and largest distance, respectively.

The single source is estimated from a parametric seismic model for explosions originally derived for simulating the seismic response of contained nuclear explosions (Mueller and Murphy, 1971). The model proceeds at the "boundary" between elastic and non-elastic response in a continuum to the application of a spherically-symmetric pressure function. The utility of the model, whose basic principles were first derived by Sharpe (1942), resides in the parameterization of the solution in terms of "measurable characteristics" and including the effect of source depth (Mueller and Murphy, 1971). Stump (1985) and Grant (1988) have successfully used this method to model small chemical explosions (114.6 and 2.3 kg) at depth in alluvium. Details of the mathematical derivations of the semi-analytical model will not be reproduced here as they are well documented in the literature (Mueller and Murphy, 1971; Stump, 1985; Grant, 1988). Calculation of the model in the frequency domain is given by the following equation,

$$\psi(\omega) = \frac{r_{el} c^2 p(\omega)}{4\mu (\omega_0^2 - \beta\omega^2 + i\omega_0\omega)} \quad (4)$$

where, $\psi(\omega)$ = far-field displacement potential (units of volume)

r_{el} = elastic radius

c = compressional wave velocity

- μ = shear modulus
- ω = angular frequency
- ω_0 = theoretical corner frequency
- β = $(\lambda+2\mu)/4\mu$ (λ, μ are Lamé's constants)
- $p(\omega)$ = frequency domain pressure function.

The pressure function as specified as in Stump (1985) and in Mueller and Murphy (1971) represents a step pulse in time with an exponential decay and is parameterized by peak pressure, static pressure, and a decay constant (proportional to ω_0). Estimation of the model parameters elastic radius, peak pressure and static pressure bears further discussion. Grant (1988) narrows the acceptable parameter range by imposing constraints on the material properties, particularly the shear wave velocity. However, in the present study, we have a limited knowledge of the material properties in our area, and we must constrain the range of reasonable values for the pressure function and elastic radius parameters using a different approach.

Static pressures are calculated according to the proportionality relation from Mueller and Murphy (1971) for competent rock,

$$P_s = 4/3 \mu \left(\frac{r_c}{r_{el}} \right)^3 \quad (5)$$

- where, P_s = static pressure
- μ = shear modulus
- r_c = final cavity radius
- r_{el} = elastic radius.

Explicit in this calculation are the parameters for final cavity radius and elastic radius. We attempt to determine reasonable constraints for these values in our model calculations by using results from other chemical explosion studies.

First we consider that cavity radius for chemical explosions scales differently than for nuclear explosions. Grant (1988) scaled cavity radius for 2.27 kg explosions by altering the medium-dependent proportionality constant (k) relating cavity radius (r_c) in meters to yield (Y) in kilotons and depth of burial (h) in meters given by :

$$r_c = k \cdot \frac{Y^{0.29}}{h^{0.11}} \quad (6)$$

Using reasonable values for compressional velocity (4.5 km/s), density (2600 kg/m³), and shear modulus (7.8 x 10¹⁰ N/m²) for the limestone in the quarry, and a proportionality constant, k, of 25 derived using a relation for nuclear explosions (Mueller and Murphy, 1971), equation (4) predicts cavity radius values for the 68 kg single explosion in our study of between 1.4 to 1.2 m (between 3 and 17.5 m depth). However, based on both theoretical and experimental studies of chemical explosions in various media, most predictions for cavity radius are from 2 to 12 times the original borehole radius (Chiappetta et al, 1987) producing a range of values between 0.1 and 0.6 meters for an initial cavity radius of 0.05 m.

Elastic radius is often but not always defined as the "boundary" around the explosion beyond which the material behaves elastically (Mueller and Murphy, 1971; Sharpe, 1942). For chemical explosions, it can also be related to the region of fracture growth and damage to the material surrounding the borehole (Kutter and Fairhurst, 1971) and is a more transitional measure. There exist many published relationships between explosive yield and elastic radius/damage zones (e.g., Atchison and Tournay, 1959; D'Andrea et al, 1970; Siskind and Fumanti, 1974) for chemical explosions in hard rock from studies which sample small explosive yields (0.002 to 4 kg). The range of elastic radii predicted by these relations falls between 0.5 and

5.3 m for the single 68 kg charge in this study. Another frequently used estimator for elastic radius is the transition zone observed in amplitude decay rates as a function of scaled range. Using the decay rate curves for nuclear explosions in hard rock, the range of scaled elastic radius predicted for 68 kg is between 4 and 8 m (Perret and Bass, 1975). Based on peak velocity amplitude decay rates for chemical explosions (mainly production blasts) in hard rock, an initial estimate for the elastic radius is between 16–18 m (Ambraseys and Hendron, 1968). Interestingly, this measure coincides with the length of the borehole (17.5 m).

One possible interpretation of the variability in predicted elastic radius values is that a cylindrically-shaped charge scales differently than a charge of spherical shape, elastic radius being constrained by the length of the borehole in the cylindrical case. This is supported experimentally by the different scaling relationships for spherical and cylindrical charges necessary for determining the radius of damage for explosions in plexiglass and hard rock (Kutter and Fairhurst, 1971). Many Bureau of Mines studies were also carried out with cylindrical charges. Nicholls and Duvall (1966) present results which support a volumetric rather than charge weight relationship to the damage zone. Siskind and Fumanti (1974) also allude to a "rule of thumb" relation of between 1 and 2 times the length of the charge column.

When values for cavity radius obtained from the nuclear explosion relations are substituted in equation (5), static pressures are 1–2 orders of magnitude greater than peak pressures calculated from the overburden relation given by Mueller and Murphy (1971),

$$P_p = 1.5 \rho gh. \quad (7)$$

where, P_p = peak pressure
 ρ = density
 g = acceleration due to gravity
 h = overburden depth.

Reasonable static pressure values are obtained from equation (5) using cavity radius values (0.1–0.6 m) based on the chemical explosion study results. We depend on the results of the model calculations to better constrain the elastic radius values.

A suite of theoretical sources in the frequency domain are first calculated using equation (4), differentiated, Fourier synthesized, and finally convolved with the calculated Green's function at 80 m to produce velocity seismograms. Reasonable approximations to the observed single source seismogram at station E are obtained by varying cavity radius from 0.05 to 0.3 m (1–6 times the borehole radius) and elastic radius from 10–20 m. As a first approximation, the source functions are calculated assuming an overburden depth of 8 m and a Green's function depth of 8 m (near the middle of the borehole).

Two criteria used in adjusting the model parameters are peak amplitude, as measured in the time domain, and corner frequency, as measured from the velocity spectra. While not the only criteria used in the model selection, these two measures are important because they can be directly estimated from and compared between the observed and calculated seismograms. Corner frequency is inversely proportional to elastic radius (Mueller and Murphy, 1971) and is used as a constraint on this model parameter. We estimate corner frequency directly from the data by finding the change in slope at the peak spectral amplitude level. This is consistent with a parametric spectral model for explosions which postulates a static long-period displacement amplitude below the corner frequency and a high frequency spectral decay above the corner

(Reamer and Stump, 1992). We feel that the corner frequencies estimated in this way are consistent to within ± 2 Hz.

The second criterium, peak amplitude, is a more delicate parameter to adjust. As shown in equation 5, as cavity radius increases and elastic radius remains constant, static pressure increases (and overshoot decreases). Peak amplitude also increases as the source time function receives a bigger contribution from the static pressure while peak pressure remains the same. In the frequency domain, the effect is an increased long-period amplitude level (proportional to the increase in static pressure). Returning again to equation 5, if elastic radius increases and cavity radius remains constant, static pressure decreases (and overshoot increases). In this case, the source time function peak amplitudes are increased due to the increased overshoot. In our first series of tests, we experiment with combinations of elastic and cavity radius values to determine their effect on peak amplitude and corner frequency in the resulting time series (Table 2). We conclude that differences between calculated and observed peak amplitudes and corner frequencies are too large, even though synthetic waveforms and spectral shapes are in fair agreement with the observations.

For the second series of tests, refinement of model parameters is necessary. If elastic radius and cavity radius are kept constant (constant static pressure), peak amplitude can still be adjusted by varying the overburden depth, thereby adjusting the peak pressure (equation 7). Since the boreholes were stemmed with drill cuttings from the surface to 3 m depth and the charges were initiated from the top of the charge column, an overburden of 3 m seems a logical choice. However, after some experimentation, we found that an overburden depth of 5 m produced better

peak amplitude results. A physical justification for this result may be found by reviewing the explosive process. A detonation or shock front forms behind the explosive reaction as it propagates through the borehole, and a (measurable) detonation pressure builds directly behind the detonation front. For cylindrical explosions, peak borehole pressure can be expressed as a percentage of the explosive detonation pressure although variations can be quite high for ANFO (30–70%) (Chiappetta et al, 1987). A partial explanation for the difference in explosive versus borehole pressure may be that some of the explosive (shock) energy is channeled into fracturing the quarry face, thereby decreasing the effective source strength.

The cylindrical shape of the charge column (14.5 m length) also creates a dilemma for the Green's function calculations which require a single source depth. After testing several source depths, we obtain the best results for the single-shot seismograms by linearly superposing the Green's functions at different depths. Individual Green's functions are calculated at depths of 3, 5, 7, 9, 11, 13, 15 and 17 m. A downhole detonation velocity of 4800 m/s is assumed, giving a total detonation time of 3 ms from the top to the bottom of the hole. In our second set of tests, selected source models are convolved with the Green's functions and linearly superposed with the appropriate downhole detonation time. The seismic moment of the synthetic source is "distributed" over the source depths by normalizing the linearly-superposed seismogram by the number of source depths (8) used in the superpositioning. Table 3 gives parameters and results of the second set of models using the superposed Green's functions. Variations in peak amplitude and corner frequency are small compared to the first model tests. Based on comparison to the peak amplitude and corner frequency estimated from the observed seismogram at station E (top traces in Figure 6), as well as some other criteria (discussion follows), we chose a "best fit" model

from this series of tests (indicated in bold in Table 3) with a final cavity radius of 0.25 m (5.0 times the original borehole radius of 0.05 m) and an elastic radius of 18 m (Figure 6).

The radial and vertical component observed seismograms at station E (Figure 6) consist mainly of a compressional wave pulse (15 ms period) followed by the SV-Rayleigh wave (20–25 ms dominant period). The major phases and relative peak amplitudes between radial and vertical components are well modeled by the synthetics (bottom traces in Figure 6). Ratio of vertical to radial peak amplitudes is 1.05 for the observed seismograms and 1.09 for the synthetics. For the radial observed seismograms, the peak amplitude of the Rayleigh wave is slightly larger than the P-wave pulse due to the extended source depth. We are able to match this relative amplitude only by using the superposed (downhole) Green's functions.

Misfit between the calculated and observed vertical seismograms is seen in the first downward swing of the P wave cycle followed by a phase slightly smaller in amplitude. On the hodogram plots (shown at right in Figure 6), it is clear that this phase is oriented at approximately 90° to the primary P wave pulse and probably represents the initial SV pulse arriving from the source. The phase can be seen on the particle motion plot of the observed data to be slightly open, possibly due to the arrival of the free face tensile reflection (at approximately 2 ms) which would have the effect of deepening the first downward swing of the P wave phase on the radial component. In a true cylindrical source model, both P and SV energy are generated at the source (Heelan, 1953); however, we are only approximating a cylindrical source with the superposed, half space Green's functions and so are unable to adequately reproduce either the relative amplitudes between the P and SV phases or the quarry face reflection.

Choice of our final model is also constrained by the spectral response of the measured data. However, the low frequency spectral response (below the corner frequency) is primarily controlled by the cavity radius (Grant, 1988), and our final parameter adjustments were made to match both the low frequency response and the corner frequency (controlled by elastic radius) of the observations. High frequency response is automatically controlled by our choice of source function and is the same for all model calculations. Figure 7 compares amplitude spectra of the observed and synthetic seismograms. The spectral shape and amplitudes are in good agreement from the corner frequencies at 40 Hz (vertical) and 45 Hz (radial) to the high frequency limit at 400 Hz. The synthetic seismograms from our final model give the best fit to the observations at and below the corner frequency for both components. The radial component of the synthetic data contains less low frequency energy between 6 and 35 Hz than the observed data (maximum factor of four amplitude difference at 28 Hz). Between 10 and 30 Hz, the vertical observed amplitudes are almost a factor of two times higher than the synthetics.

Multiple-Source Synthetic Seismogram Calculations

For the explosion source model utilized in the present study, we calculate only two components of motion, radial and vertical. The observed data were recorded as three-component seismograms and contain a considerable amount of transverse energy. In addition, the production shot seismograms, which are oriented as shown in Figure 2, cannot be rotated into a true "radial" or "transverse" direction due to the spatial extent of the source array. Therefore, it should be noted for the superpositioning results that follow, a basic difference exists in that for each Green's function+source convolution, the orientation is radial with respect to the source whereas in the observations, only the borehole closest to the station is recorded in the radial sense. We refer to

the y component of the observed production shot seismograms as the "equivalent" of the radial component.

For shot SVI6, we calculated eight Green's functions at the different depths (the same as for the single shot model) for each source-receiver distance in the array (a total of 208 Green's functions). For each component at each distance, the Green's functions are first convolved with our source model (parameters given in Table 2) and then linearly superposed with the assumed downhole detonation time. Then the synthetic seismograms for each source-receiver location are superposed with the actual delay times recorded for SVI6. The results for the radial and vertical components of station D are shown in Figure 10. Seismograms are all plotted relative to the same scale. The first 0.16 s of the observed radial seismogram contains 18 ms delay intervals complicated by the fact that the firing order for the first four shots was not linear sequential (Figure 2). This first 0.16 s wave packet is distinct in both the observed and synthetic seismograms from the next 0.32 s where the delay intervals alternate between 18 and 27 ms. The last five shots (on the seismograms from 0.50–0.64 s) also alternate between 18 and 27 ms delays, but the holes were located 5 m perpendicular distance (y direction) farther from the station in addition to the increasing horizontal separation. The additional distance manifests in the observed and synthetic seismograms as a reduced-amplitude wave packet.

For comparison, at the top of Figure 8 we show the superposed, measured single shot (SMSS) signal for SVI6 using the seismogram from SVI4 measured at station E. Note that although the first 0.16 s wave packet can be observed in the SMSS, the focusing effect seen in the observed and synthetic seismograms is not reproduced here. For the vertical component, the

attenuation of amplitudes in the observed seismogram is more pronounced than in the synthetic although the interference effects of all three wave packets are qualitatively reproduced. Again, focusing effects are not reproduced by the SMSS. The ratio of peak radial to peak vertical amplitudes for the measured data is 1.1, for the synthetics 1.4, and 1.4 for the SMSS signal.

Superpositioning results are shown for the vertical component of stations B and C for shot SVI5 in Figure 9. Since we did not have a single shot signal located on the same quarry wall as SVI5, we used the SVI4 single shot source model for the synthetics and the SMSS. We obtained the best results for the synthetics by convolving the single-source model with the Green's functions at 11 m depth for each source-receiver distance, rather than using the Green's functions at all depths. This result may be attributable to propagation path differences at the different benches; it can be seen from Figure 1 that the two shots are located on benches perpendicular to each other. Slight differences in the source model due to inhomogeneities in the source region differences in source coupling also cannot be ruled out. Amplitudes are plotted to the same scale for all seismograms except the station C measured seismogram. Due to higher noise levels, this signal was low-pass filtered to 200 Hz. Also, we utilize only desired firing times with constant delay intervals of 20 ms for the superpositioning, since actual firing times were not recorded. Firing direction is away from station B and towards station C; the focusing effect of firing direction is seen in both the measured and synthetic seismograms. Peak amplitudes for station B agree well for the vertical component although, as for station D of SVI6, relative amplitudes are not accurately reproduced. At station C, the seismogram shape of the synthetic signal compares well to the measured data even though absolute amplitudes do not agree.

Better results could be obtained with a more detailed propagation path model; however, for a first-order approximation, the half-space assumption works surprisingly well. Reasonable comparisons are obtained for SVI5 and SVI6 for two main reasons: (1) good similarity of the seismic source function between the measured single shot and the individual explosions of the multiple array, and (2) accuracy of the delay times which, in the case of SVI5, allows us to use the desired firing times in our superpositioning model. We illustrate this last point by examining a spectral domain equivalent representation of our multiple-source seismograms given by (after Blair, 1988):

$$A(f) = S(f) \left\{ \left[\sum_{i=1}^n a_i \cos(2\pi t_i f) \right]^2 + \left[\sum_{i=1}^n a_i \sin(2\pi t_i f) \right]^2 \right\}^{1/2} \quad (8)$$

- where, $A(f)$ = amplitude spectral values
 $S(f)$ = source function (constant for each shot)
 a_i = amplitude weighting term (different for each shot)
 t_i = delay time
 n = the total number of explosions
 f = frequency.

We introduce this representation to illustrate the temporal variations as observed in the velocity spectra due to time delay blasing. Peaks in the spectra correspond to the harmonic frequencies associated with each delay and occur in multiples up to the Nyquist frequency. Spectral smearing occurs due to slight changes in the source-receiver distances (propagation path effect) which also enhances high-frequency damping of the amplitudes (Smith, 1989). Measured and superposed spectra of the vertical component of station B (SVI5) and the radial component of station D (SVI6) (Figure 10) exhibit the scalloping pattern associated with the delay time firing pattern. For SVI5, the first peak at 50 Hz corresponding to the constant 20 ms

delay interval is quite clear for the measured, synthetic and SMSS spectra. Peaks at 100, 150, 200, 250 and 300 Hz are all observable in the measured data although the peak at 150 Hz is split. The harmonics due to ripple-firing dominate the production shot spectra so that source spectral characteristics of the individual explosions cannot be easily discerned.

For SVI6, the firing pattern is complicated because of alternating 18 and 27 ms delays. In addition, the first four shots were not fired in the row order causing slight shifts in the source-receiver offsets in addition to the 18 ms delays. What is seen in both the measured and superposed spectra is a small first peak at 22 Hz corresponding to a 45 ms delay time, which is just the sum of the two alternating delays. A second smaller peak at 34 Hz corresponds to the first 27 ms harmonic. The second harmonic of the combined delay times is at 44 Hz followed by the first harmonic of the 18 ms delay at 56 Hz. The higher order harmonics of the combined delay can be picked to about 200 Hz in the synthetic and SMSS although the peaks are smeared in the measured data. Higher order harmonics of the 18 and 27 ms delays, although present, cannot be discerned in the measured spectra.

DISCUSSION

We have successfully modeled the temporal and spatial variations due to ripple-fired explosions as measured in seismic data acquired at near-source ranges. The single-source model was calculated using the analytic Mueller-Murphy (1971) explosion model with parameters constrained by results from chemical explosion studies. We tested models for a single cylindrical charge of 68 kg ANFO in limestone with borehole length of 17.5 m and diameter of 90 mm measured at 80 m distance by varying cavity radius between 0.05 and 0.3 m and elastic radius

between 10 and 20 m. The best-fit model is obtained with a final cavity radius of 0.25 m, an elastic radius of 18 m, and an overburden depth for the peak pressure function of 5 m. In order to match relative amplitudes between the P and Rayleigh wave phases of the observed data, it is necessary to linearly superpose the seismic response of Green's functions calculated at different depths to simulate the spatial extent (14.5 m) of the cylindrical source.

As shown here, temporal and spatial finiteness effects of ripple-fired blasting at 80 m distance are well modeled with linear superpositioning using a calculated source and Green's functions when constraints can be imposed on both the propagation medium and the seismic source models. However, even in the near-source region (80 m), the method requires accurate firing times (1% or less error). It has yet to be conclusively shown that ripple-fire effects of blasts with small delay times (< 40 ms) can provide a consistent, singular discrimination criterium for quarry blasts at regional distances, especially when one considers that the effects of blasting cap firing time inaccuracies (see Appendix) are convolved with attenuation and local site effects. More work is needed with explosions employing both large and small delay times in controlled experimental settings to gain a better understanding of the interaction of propagation effects and delay time variations at near-regional and regional distances.

APPENDIX

CAP SCATTER AND SEISMIC SPECTRAL RESPONSE

The combination of attenuation mechanisms and firing-time scatter can obscure the spectral harmonics associated with ripple firing. Smith (1989) observed no spectral signature at regional distances for small-delay (17 ms) overburden blasts. Spectral harmonics at regional distances can also originate due to propagation effects, either at the source or the receiver (Suteau-Henson and Bache, 1988; Hedlin et al, 1989). We want to isolate one element affecting the spectral modulation, cap scatter effects. Cap scatter is here defined as a percentage of the desired firing time and represents the deviation between desired and actual firing time. Firing time deviation has the same effect as spatial finiteness of the explosive array, namely, smearing of the spectral modulation pattern. Modification of equation (8) to include a random variation in delay times results in:

$$A(f) = S(f) \left\{ \left[\sum_{i=1}^n a_i \cos(2\pi(t_i + r_i) f) \right]^2 + \left[\sum_{i=1}^n a_i \sin(2\pi(t_i + r_i) f) \right]^2 \right\}^{1/2} \quad (A1)$$

where, r_i = noise value for each delay time.

Scatter in the delay times is not a simple noise term added to the seismic data but is inherent to the time series and corresponding amplitude spectra. Pattern recognition methods such as homomorphic deconvolution cannot, therefore, "see" the regular scalloping pattern produced by ripple-fired blasting if the delay time variations become too large.

To quantify the influence of cap scatter on the seismic spectra, we have calculated a unit amplitude impulse series representing the desired firing sequence observed at station B for SVI3

(32 ms delay). Geological structure in this case is assumed to be homogeneous and isotropic with travel times between individual charges and the seismic station added to the delay times with an assumed compressional wave speed of 4.5 km/s. The impulse response series and corresponding amplitude spectra for SV13 is shown in the bottom trace of Figure A1. The spectra of the impulse series for the exact times show the first peak at 31.25 Hz, corresponding to the inverse of the delay times (32 ms) and higher harmonics occurring at multiples of the fundamental frequency.

Cap scatter is added to the desired firing times using normally distributed random values with maximum variance levels of 1%, 2%, 4% and 6% of the desired firing times (Figure A1). The increasing amount of cap scatter disturbs the scalloping pattern of the spectra. With 1% delay time variations, the maximum possible deviation between desired and actual firing time is ± 0.32 ms for time step 1 and ± 5.44 ms for time step 17. Even at this low noise level, the regular scalloping structure of the spectra is smeared for frequencies higher than 100 Hz. With 2% maximum cap scatter, only the first peak at 31.25 can be clearly correlated with the spectrum for exact firing times. For noise levels of 4% and 6%, the ripple structure is completely destroyed. Troughs appear at frequencies where peaks are observed in the spectra for exact firing times. For example, a large spectral peak appears at the 1%, 2%, and 4% noise level at about 20 Hz. As these results indicate, even a small value of 1% noise added to the firing times disturbs the spectral modulation from the single-row production shots. Usually cap manufacturers do not give detailed information about the scatter of cap firing times. Some studies have shown that average cap scatter values of 4% are fairly representative (Blair, 1988) and variances as high as 20% of the desired firing times can be realized (Reamer et al, 1989).

ACKNOWLEDGMENTS

The authors wish to acknowledge Dynamit Nobel AG for providing support for the field experiment. We wish to thank the field and laboratory crew at the Federal Institute for Geosciences in Hannover. We also thank J. Schlittenhardt and an anonymous reviewer for helpful comments which improved the content of the written work. The research was supported by the Defense Advanced Research Projects Agency under Contract No. F19628-89-K-0025, the Institute for the Study of Earth and Man in Dallas under Seed Grant No. 899-0515, and Federal Institute for Geosciences in Hannover.

REFERENCES

- Ambraseys, J.R. and A.J. Hendron, 1968. Dynamic behavior of rock masses in *Rock Mechanics in Engineering Practice*, 203-227, eds. K.G. Stagg and O.C. Zienkiewicz, John Wiley and Sons, London.
- Anderson, D.A. and B. W. Stump, 1989. Seismic wave generation by mine blasts, *AFGL-TR-89-0194*, Air Force Geophysics Laboratory, Hanscom, AFB, Massachusetts, 1-75. ADA216218
- Atchison, T.C. and W.E. Toumay, 1959. Comparative studies of explosives in granite, *RI 5509*, U.S. Bureau of Mines.
- Baumgardt, D. R. and Ziegler, D. A., 1988. Spectral evidence for source multiplicity in explosions: applications to regional discrimination of earthquakes and explosions, *Bull. Seism. Soc. Am.*, 78, 1773-1795.
- Blair, D.P., 1988, The measurement, modelling and control of ground vibrations due to blasting in *Proceedings of the 14th Conference on Explosives and Blasting Technique*, Keystone, Colorado, 88-101.
- Chiappetta, R.F., D.G. Borg, V. A. Sterner, 1987. *Explosives and rock blasting*, Atlas Powder Co., Dallas.
- Crenwelge, O. E., 1991. Transient data analysis procedure for reducing blast-induced ground and house vibrations, in *Proceedings of the Seventh Annual Symposium on Explosives and Blasting Research*, Las Vegas (in press).
- D'Andrea, D.V., R.L. Fischer, A.D. Hendrickson, 1970. Crater scaling in granite for small charges, *RI 7409*, U.S. Bureau of Mines.
- Grant, L. T., 1988. Experimental determination of seismic source characteristics for small chemical explosions, *M.S. Thesis*, Southern Methodist University.
- Hedlin, M. A. H, J. B. Minster, J. A. Orcutt, 1989. The time-frequency characteristics of quarry blasts and calibrations recorded in Kazakhstan, USSR, *Geophys. J. Int.*, 99, 109-121.
- Heelan, P.A., 1953. Radiation from a cylindrical source of finite length, *Geophysics*, 18, 685-696.
- Herrmann, R., K. Hutchenson, M. Jost, 1989. Small explosion discrimination and yield estimation, *Proceedings of the 11th Annual DARPA/AFGL Seismic Research Symposium*, 11-17, San Antonio. GL-TR-90-0301, ADA229228

- Hinzen, K.-G., R. Lüdeling, F. Heinemeyer, P. RÖh, and U. Steiner, 1987, A new approach to predict and reduce blast vibration by modelling of seismograms and using a new electronic initiation system, The measurement, modelling and control of ground vibrations due to blasting in *Proceedings of the 13th Conference on Explosives and Blasting Technique*, Miami, Florida, 144-161.
- Hinzen, K.-G., 1988. Modelling of blast vibrations, *Int. J. Rock. Mech. Min. Sci. and Geomech. abstr.*, 25, 439-445.
- Hinzen, K.-G. and S. K. Reamer, 1991. Verringerung von Sprengerschütterungen durch Zündzeitoptimierung und elektronische Zünder – ein Beispiel aus der Praxis, *Nobel-Hefte* H. 2-4, 114-123.
- Johnson, L.R., 1974. Green's functions for Lamb's problem, *Geophys. J. Roy. astr. Soc.*, 37, 99-131.
- Kutter, H.K. and C. Fairhurst, 1971. On the fracture process in blasting, *Int. J. Rock Mech. Min. Sci.*, B, 181-202.
- Minster, J.B. and S. M. Day, 1986. Decay of wave fields near an explosive source due to high-strain nonlinear attenuation, *J. Geophys. Res.*, 91, 2113-2122.
- Mueller, R.A. and J.R. Murphy, 1971. Seismic characteristics of underground nuclear detonations, I. Seismic spectral scaling, *Bull. Seism. Soc. Am.*, 61, 1675-1692.
- Nicholls, H. R. and W. I. Duvall, 1966. Presplitting rock in the presence of a static stress field, *RI 6843*, U.S. Bureau of Mines.
- Perret, W.R. and R.C. Bass, 1975, Free-field ground motion induced by underground explosions, *SAND74-0252*, Sandia National Laboratory, Albuquerque, New Mexico, 121 pp.
- Reamer, S.K., and B.W. Stump, 1992. Source parameter estimation for large, bermed. surface chemical explosions, *Bull. Seism. Soc. Am.*, 82, 406-421.
- Reamer, S.K., B.W. Stump, R.E. Reinke, J.A. Leverette, 1989. Pomona quarry seismic experiment: near-source data, *AFGL-TR-89-0194*, Air Force Geophysics Laboratory, Hanscom AFB, Massachusetts. ADA216218
- Sharpe, J.A., 1942. The production of elastic waves by explosion pressures, I. Theory and empirical observations, *Geophysics*, 7, 144-154.
- Smith, A.T., 1989. High-frequency seismic observations and models of chemical explosions: implications for the discrimination of ripple-fired mining blasts, *Bull. Seism. Soc. Am.*, 79, 1089-1110.

Siskind, E.E. and R.R. Fumanti, 1974. Blast produced fractures in Lithonia granite, RI 7409, U.S. Bureau of Mines.

Stump, B. W., 1985. Constraints on explosive sources with spall from near-source waveforms, *Bull. Seism. Soc. Am.*, 75, 361-377.

Stump, B.W. and R.E. Reinke, 1988. Experimental confirmation of superposition from small-scale explosions, *Bull. Seism. Soc. Am.*, 78, 1059-1073.

Su, F., K. Aki, and N. N. Biswas, 1991. Discriminating quarry blasts from earthquakes using coda waves, *Bull. Seism. Soc. Am.*, 81, 162-178.

Suteau-Henson, A. and T. C. Bache, 1988. Spectral characteristics of regional phases recorded at NORESS, *Bull. Seism. Soc. Am.*, 78, 708-728.

Table 1. Comparison of Desired and Actual Firing Times for SVI6

Time Step	Desired Firing Time (ms)	Actual Firing Time (ms)	Percent Difference
0	0	0.0	0.0
1	18	17.73	1.5
2	36	35.84	0.4
3	54	54.02	0.0
4	72	71.87	0.2
5	90	89.98	0.0
6	117	116.93	0.0
7	135	134.85	0.1
8	162	162.30	0.2
9	180	180.45	0.2
10	207	207.55	0.3
11	225	225.73	0.3
12	252	252.86	0.3
13	270	270.91	0.3
14	297	297.79	0.3
15	315	315.58	0.2
16	342	342.78	0.2
17	360	360.62	0.2
18	387	387.90	0.2
19	405	406.40	0.3
20	432	432.90	0.2
21	450	451.20	0.3
22	477	476.91	0.0
23	495	495.08	0.0
24	522	517.50	0.9
25	540	536.05	0.7

**Table 2. Model parameters and results:
8 m overburden depth and 8 m Green's function depth**

cavity radius (m)	elastic radius (m)	overshoot (P_p/P_s)	vertical corner frequency* (Hz)	radial corner frequency* (Hz)	vertical peak amplitude (mm/s)	radial peak amplitude (mm/s)
0.05	10	100	100	60	14.0	16.0
0.05	13	229	90	60	25.3	25.9
0.1	10	13	90	60	14.4	16.8
0.1	15	44	38	45	34.2	34.5
0.15	10	4	100	52	18.8	18.2
0.15	13	9	48	52	24.6	28.6
0.15	15	13	48	52	34.3	35.8
0.15	18	23	38	50	48.4	50.6
0.15	20	31	36	45	59.7	61.1
0.2	16	7	40	52	38.5	42.7
0.2	18	10	38	48	48.9	52.2
0.2	20	13	34	48	59.6	62.4
0.25	16	3	40	50	40.5	46.4
0.25	18	5	38	46	49.7	54.9

*Corner frequencies are consistently estimated within ± 2 Hz accuracy.

Table 3. Model parameters and results:
5 m overburden depth** and superposed Green's functions

cavity radius (m)	elastic radius (m)	overshoot (P_p/P_s)	vertical corner frequency* (Hz)	radial corner frequency* (Hz)	vertical peak amplitude (mm/s)	radial peak amplitude (mm/s)
0.15	15	**13	45	50	31.7	29.4
0.15	16	**16	40	50	35.3	33.4
0.15	17	**19	40	50	38.9	37.1
0.15	18	14	38	48	29.5	27.5
0.2	17	5	40	50	26.7	25.5
0.2	20	9	38	48	35.4	31.0
0.25	16	2	40	48	25.1	23.9
0.25	18	3	40	45	29.7	27.3
0.25	20	5	36	45	35.3	30.7
0.3	18	2	36	48	31.7	28.4
0.3	20	3	34	45	36.4	31.5

*Corner frequencies are consistently estimated within ± 2 Hz accuracy.

**Where indicated, these models calculated with 8 m overburden depth.

FIGURE CAPTIONS

Figure 1. Three production shots, SVI3 and SVI5 and SVI6, were fired at neighboring parts of the 15 m highwall of the quarry. Single shot SVI4 (open circle) was located close to the 21st borehole of the SVI6 array. There were 18, 20 and 26 individual explosions for shots SVI3, SVI5 and SVI6, respectively. Seismic stations A–E as shown here were located on the quarry bench. Station A corresponds to SVI3; stations B and C correspond to SVI5; station D corresponds to SVI6; and station E corresponds to SVI4.

Figure 2. The plan views for SVI5 and SVI6 are shown in the upper part of the figure. A constant delay time of 20 ms was chosen for SVI5. Delay times for SVI6 alternated between 18 and 27 ms. Spacing and burden were 4 and 5 m, respectively for both SVI5 and SVI6 for total array lengths of 76 and 94 m. Burden and spacing for the last five boreholes of the SVI6 shots are irregular as the array turns a "corner" of the highwall. The crosscut view at the bottom of the figure shows the typical hole loading, borehole inclination of 30 degrees to the vertical, borehole length of 17.5 m, and diameter of 90 mm for the production shots and the single shot, SVI4.

Figure 3. Measured three-component velocity seismograms are plotted at the top of the figure for firing direction away from the station (Station B of SVI5 and station D of SVI6). Seismograms from stations C (SVI5) and station A (SVI3) are plotted in the lower part of the figure and represent the signal recorded from firing in a direction toward the seismic station. The two perpendicular horizontal components are x and y, where x is parallel to the explosive array; z is the vertical component. Seismograms are normalized to the maximum, given in mm/s at the end of each trace. Curves plotted below the seismograms are the normalized cumulative seismic trace energy. The straight dashed lines connect the first arrivals with the 98% energy level.

Figure 4. Vertical component velocity seismograms of shot SVI3 (right) and SVI5 (left) at station A and B, respectively. The upper traces (a) consist of the linearly superposed single-shot signal from shot SVI4 with a time-delayed series of unit amplitudes. The middle traces (b) are the recorded seismograms from the production shots. The lower traces (c) are the weighted amplitude results. Weighting factors are estimated directly from measured production shot amplitudes at the cumulative delay times. The measured single-shot signal is shown as inset (d) at the same time scale as the production shots.

Figure 5. Half space Green's functions from eight depths convolved with the single source time function and linearly superposed with a total of 3 ms downhole detonation time were calculated for travel paths from SVI6 to station D. The distance increases from 80 to 126.7 m from the first to the 26th hole. Every second time series is plotted here. The sections on the left and right are the vertical and radial components, respectively with amplitudes plotted relative to the maximum in mm/s (scale shown).

Figure 6. Measured (a) and calculated (b) seismograms of the single shot, SVI4 at 80.6 m distance (station E). The radial and vertical seismograms on the left and right side, respectively, are plotted to the same scale, given at left, and the maximum amplitudes are plotted above each trace. Hodograms in the radial/vertical plane are shown at the right of the figure.

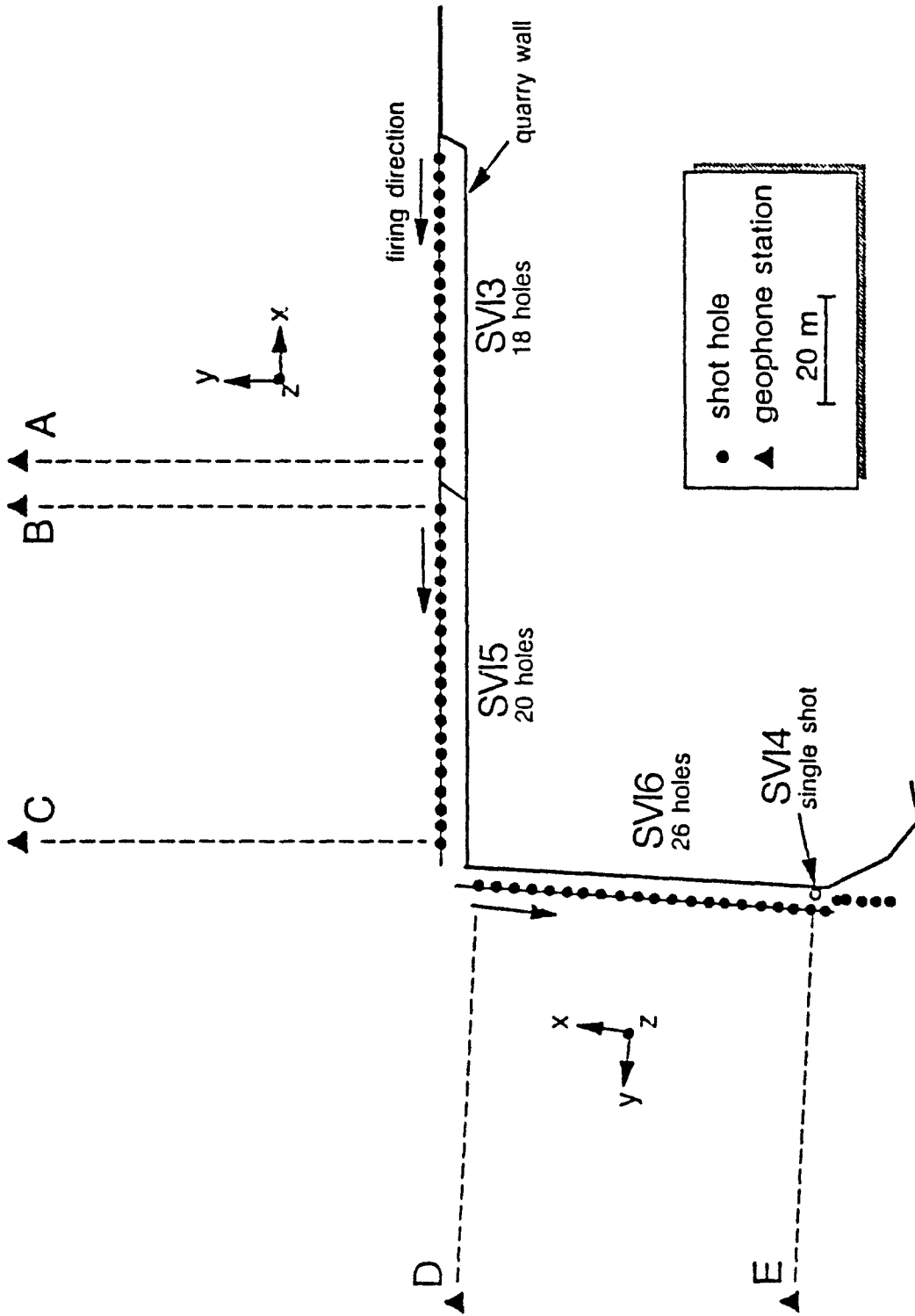
Figure 7. Velocity spectra of the measured (at station E) (thick lines) and calculated (thin lines) single shot signal, SVI4. Spectral amplitudes in mm/s/Hz are shown. Both measured and calculated signals are filtered with a low-pass, 2 pole Butterworth filter at 400 Hz.

Figure 8. Superpositioning results are shown for the vertical and radial component seismograms from SVI6 at station D. The upper traces (a) are the superposed measured single shot (SMSS) signals (SVI4). The middle traces (b) are the observed production shot seismograms. The lower traces (c) are obtained by convolving the source time function with the Green's functions calculated for each shot-receiver distance and linearly superposing the resulting seismograms with alternating 18 and 27 ms delay times.

Figure 9. Superpositioning results are shown for the vertical component seismograms from SVI5 at stations B and C. The upper traces (a) are the superposed measured single shot (SMSS) signals (SVI4). The middle traces (b) are the observed production shot seismograms. The lower traces (c) are obtained by convolving the source time function with the Green's functions calculated for each shot-receiver distance and linearly superposing the resulting seismograms with alternating 20 ms delay times.

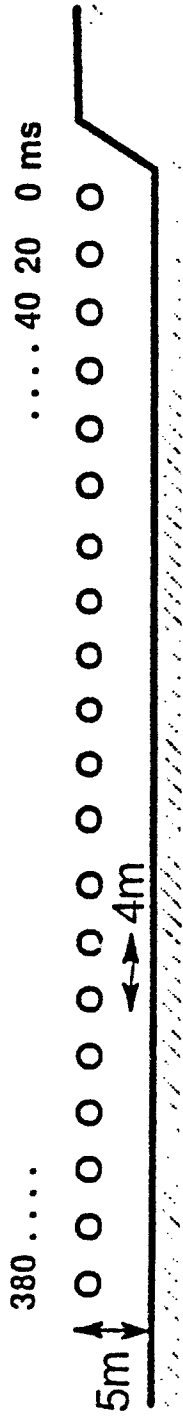
Figure 10. The spectral amplitudes of the vertical component at station B for SVI5 (left) and radial component at station D for SVI6 (right) are plotted in the middle of the figure for the measured production shot seismograms. Spectra of the corresponding calculated, superposed seismograms and the SMSS signals are given in the upper and lower traces, respectively, and are shifted upwards by two decades for easier viewing.

Figure A1. The unit impulses on the lower right of the figure are superposed and delayed in time by 32 ms including the delays for travel times for compressional waves (4.5 km/s) in a whole space. In the upper four traces, normally-distributed random numbers are added to the firing times with maximum variance levels from 1% to 6% of the desired firing times. The corresponding amplitude spectra are plotted in the left diagram on a log-log scale from 5 to 400 Hz. All amplitudes are normalized to the maximum.

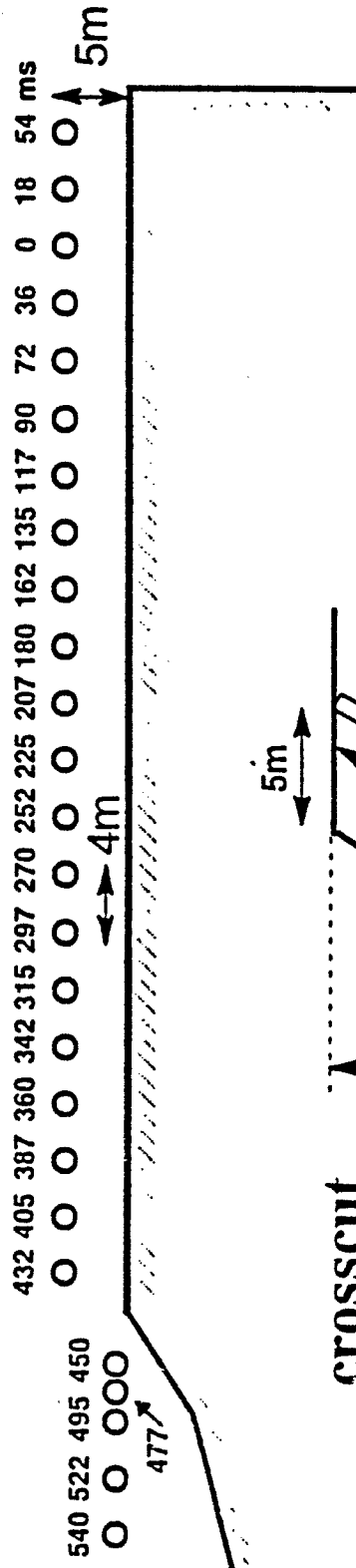


map view

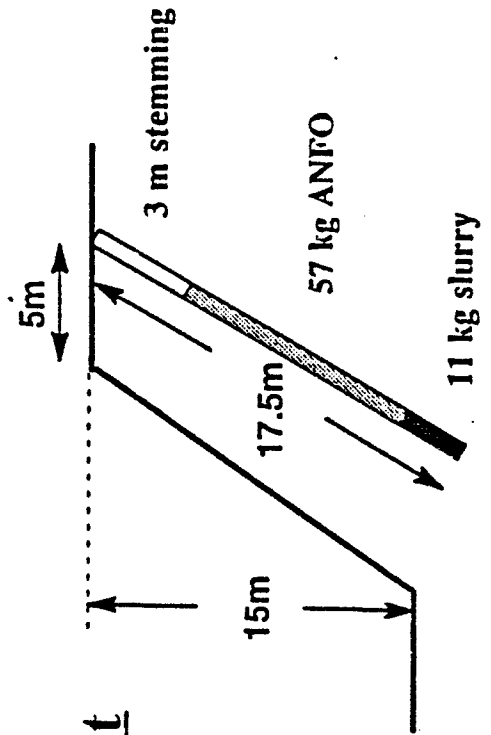
SVI5



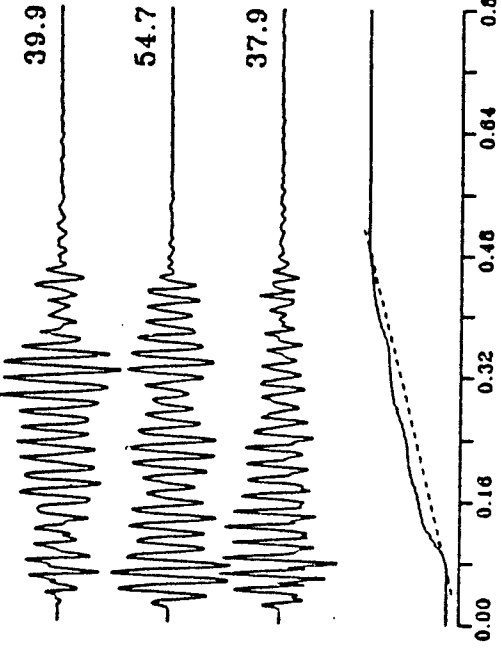
SVI6



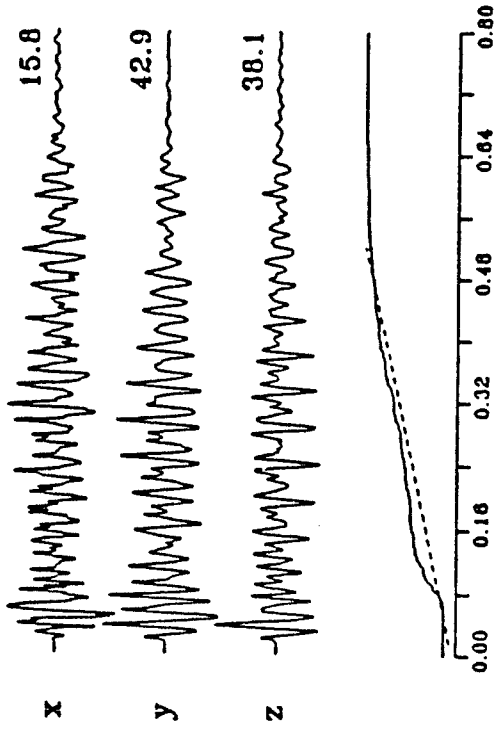
crosscut



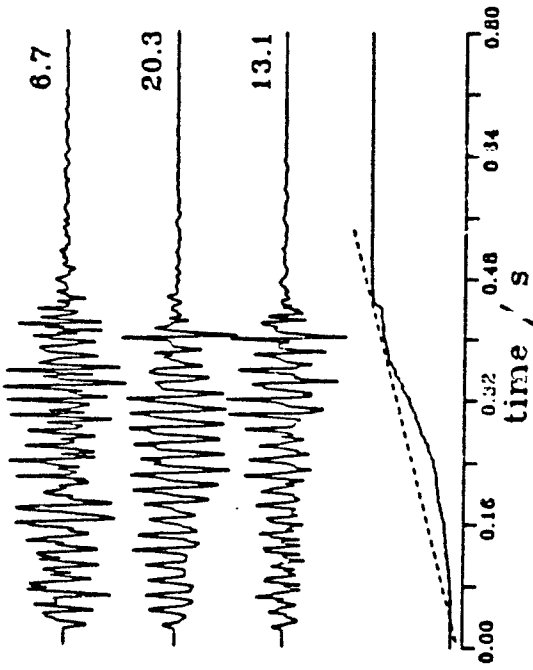
SVI5: 20 ms delay (20 holes)
station B



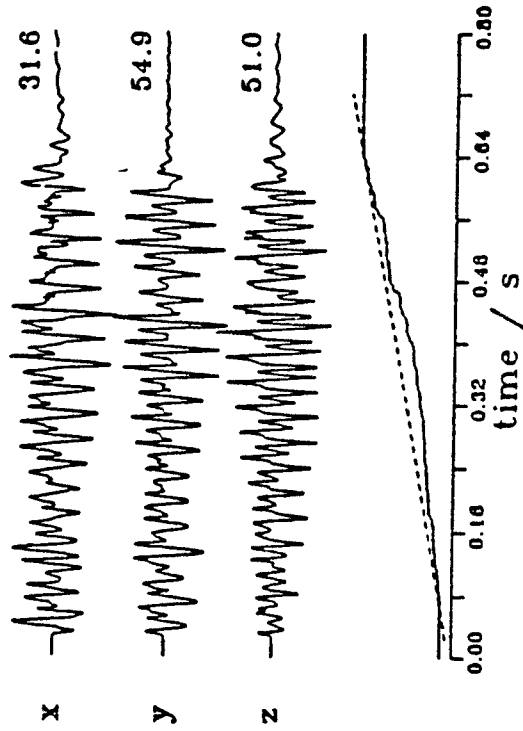
SVI6: 18/27 ms delay (26 holes)
station D



SVI5: 20 ms delay (20 holes)
station C



SVI3: 32 ms delay (18 holes)
station A

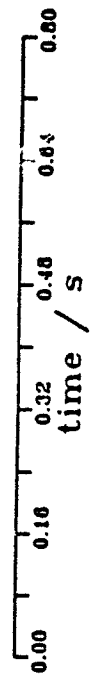
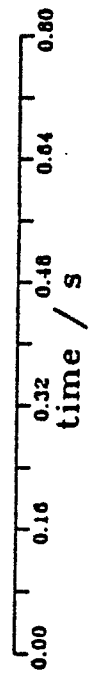
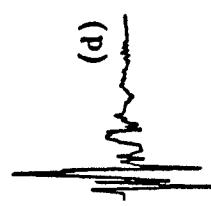
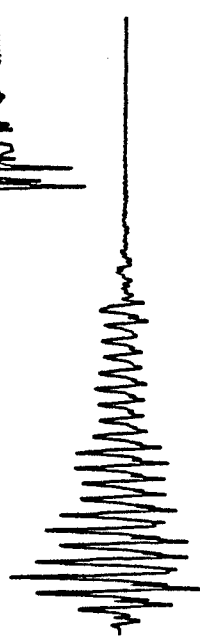
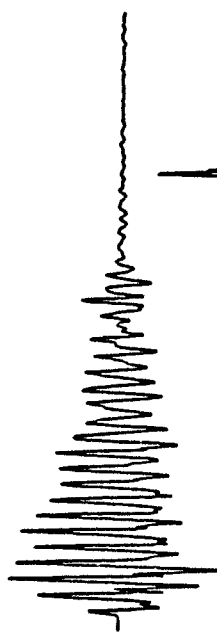
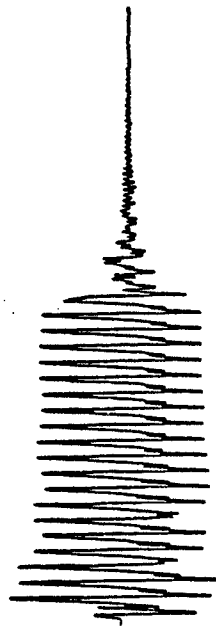


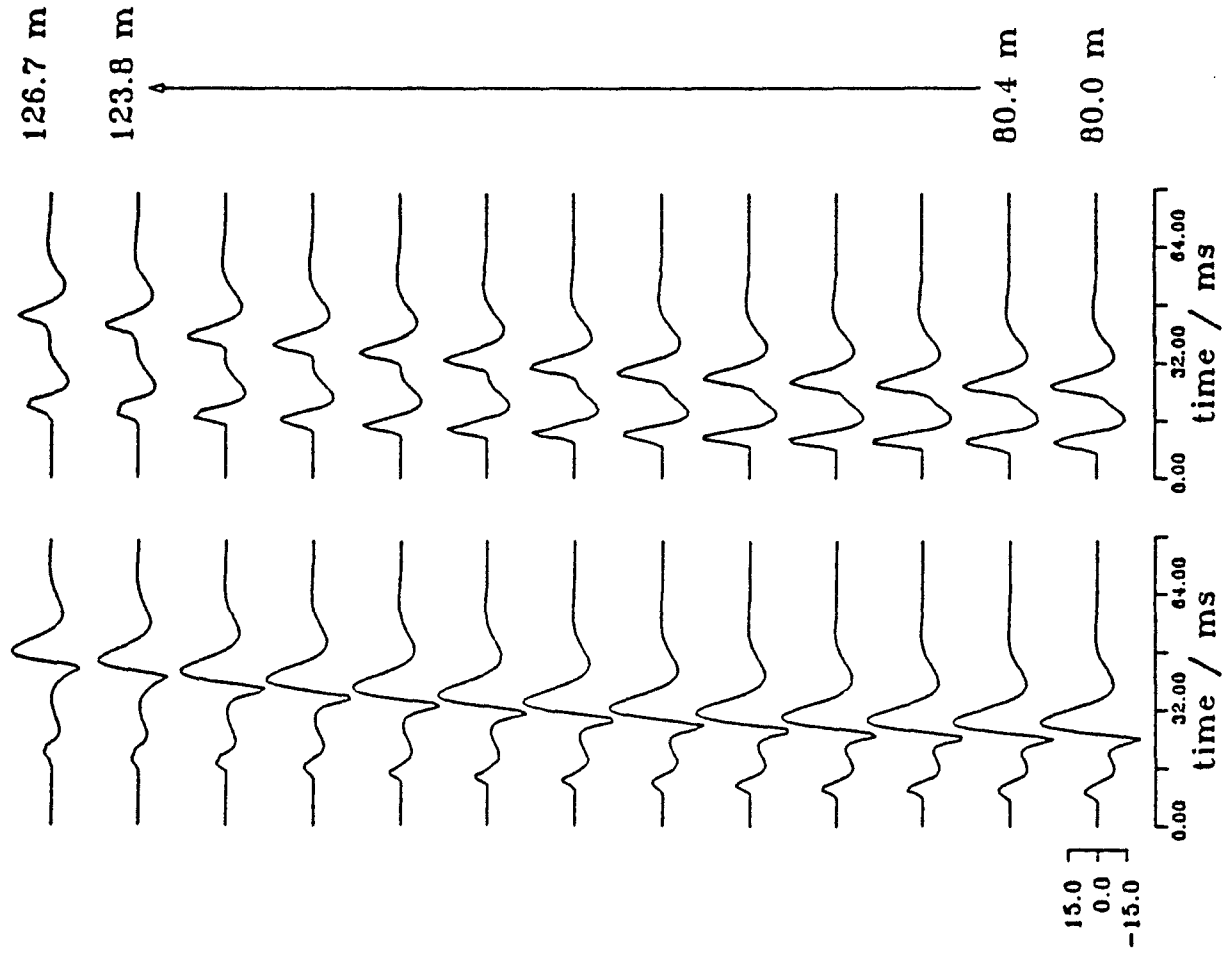
SVI5: 20 ms delay (20 holes)

SVI3: 32 ms delay (18 holes)

station B

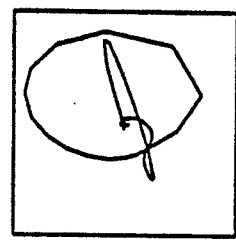
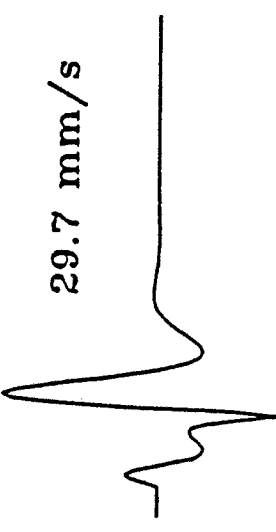
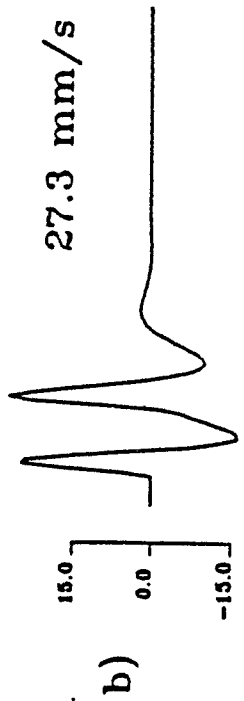
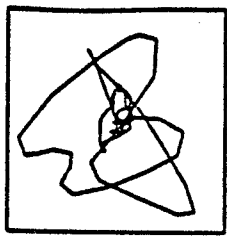
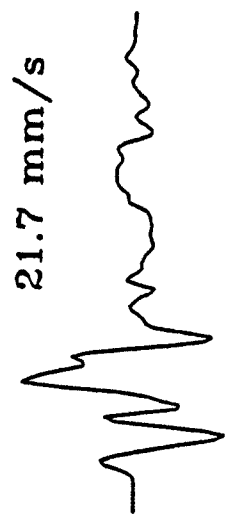
station A





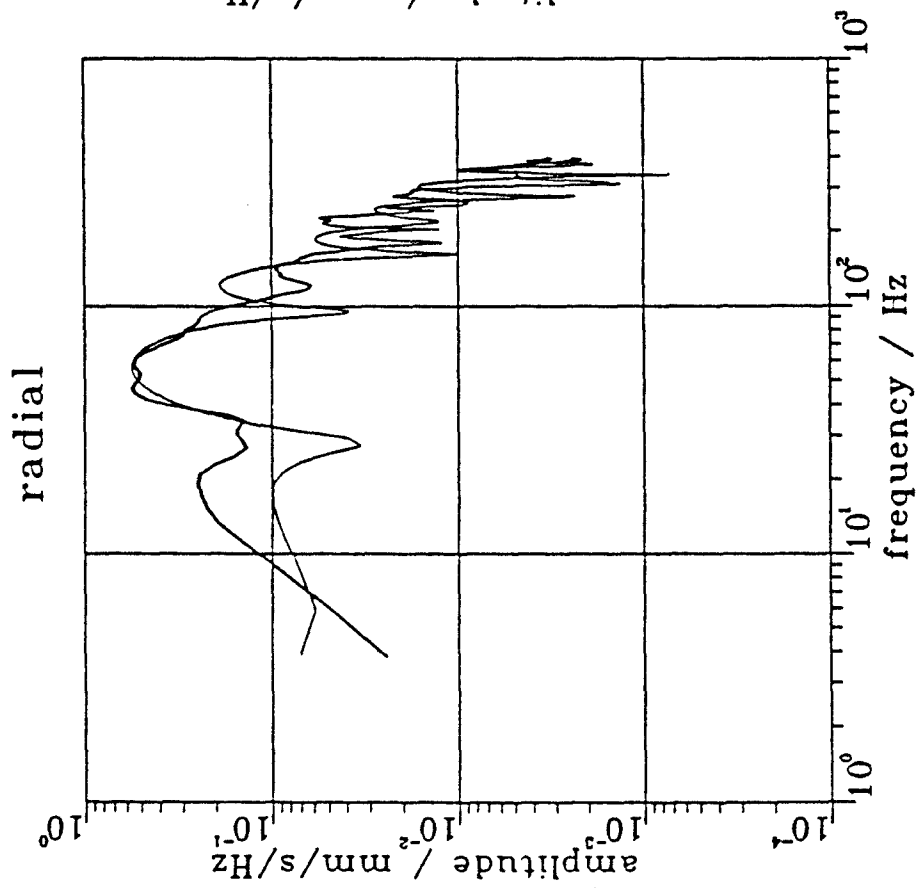
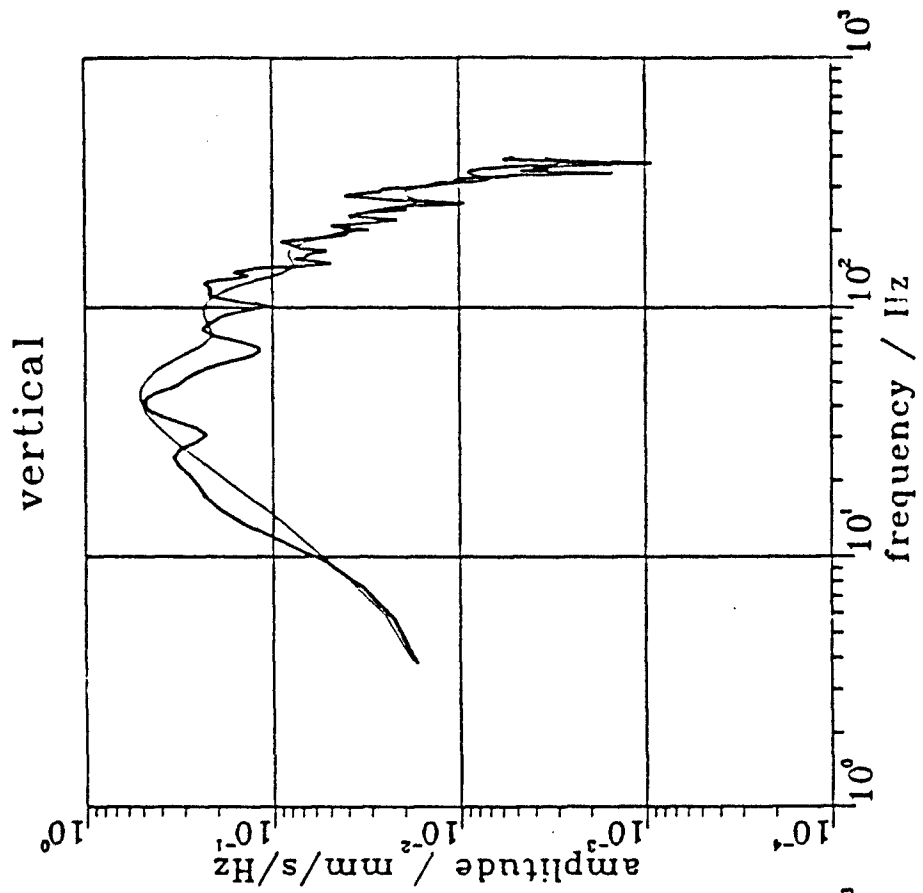
radial

vertical



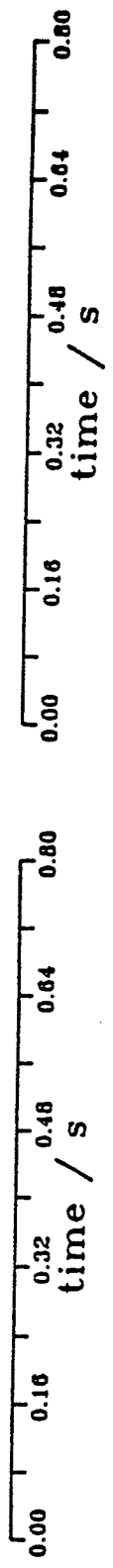
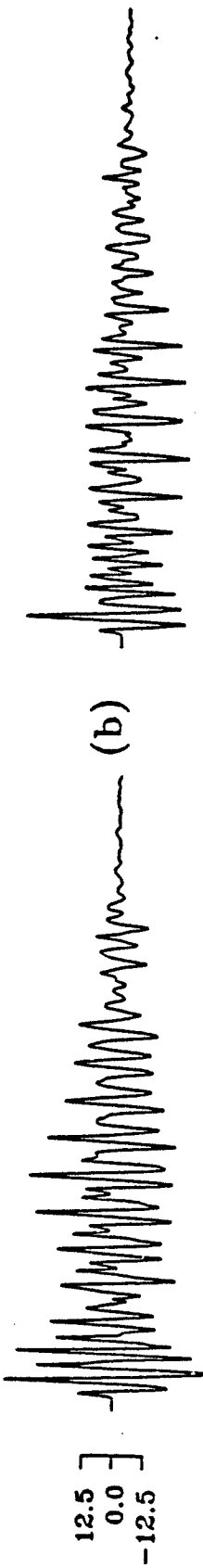
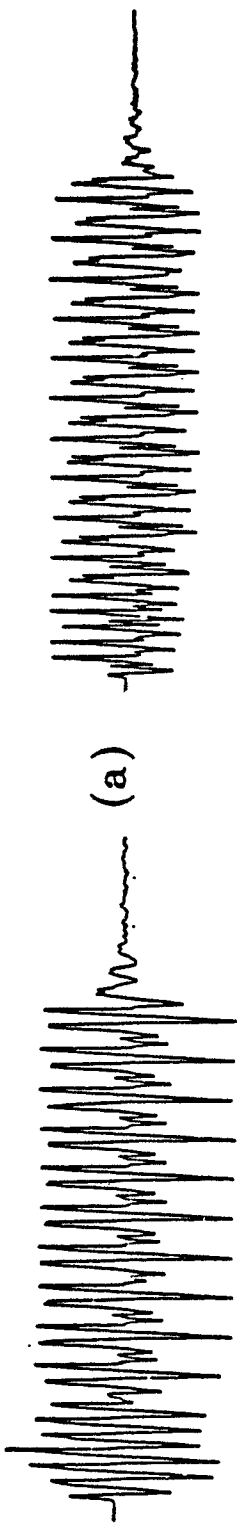
vertical

radial



SVI6: 18/27 ms delay (26 holes)

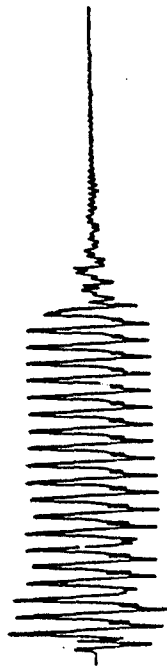
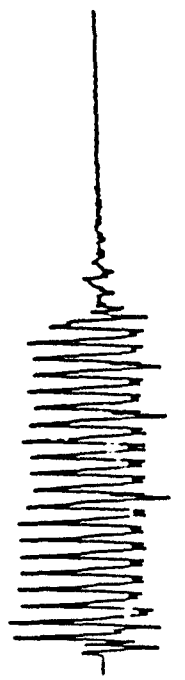
radial station D vertical



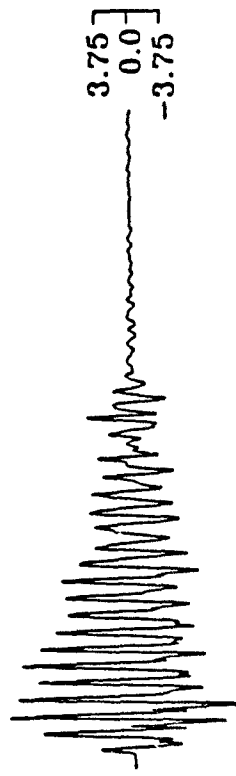
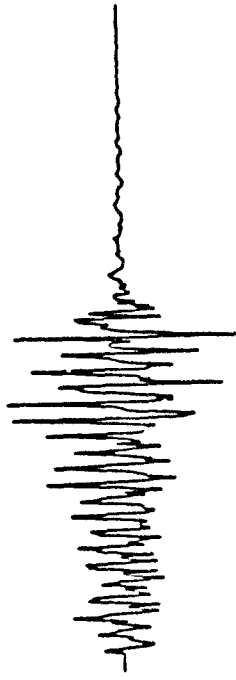
SVI5: 20 ms delay (20 holes)

station C

station B

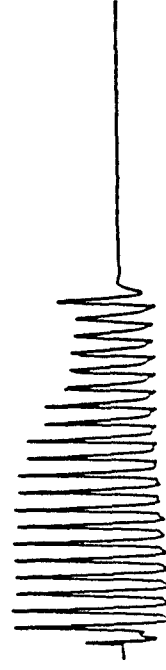


(a)

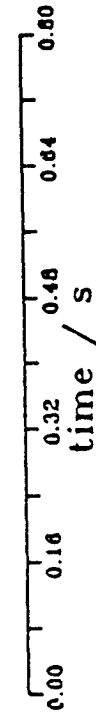
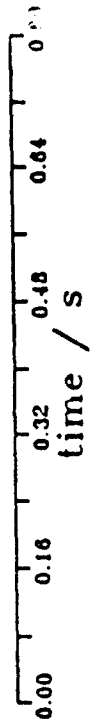


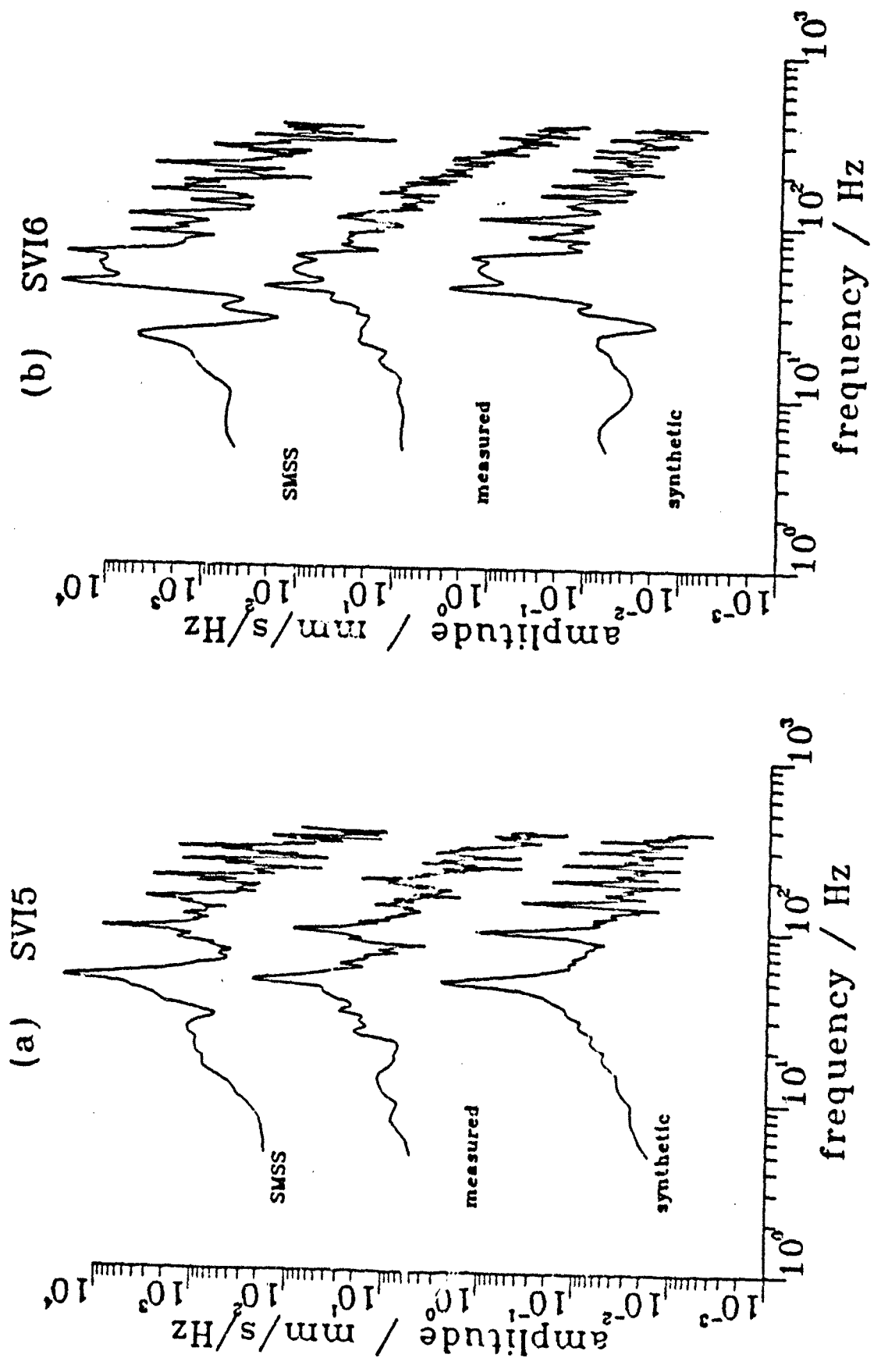
(b) 10.0
0.0
-10.0

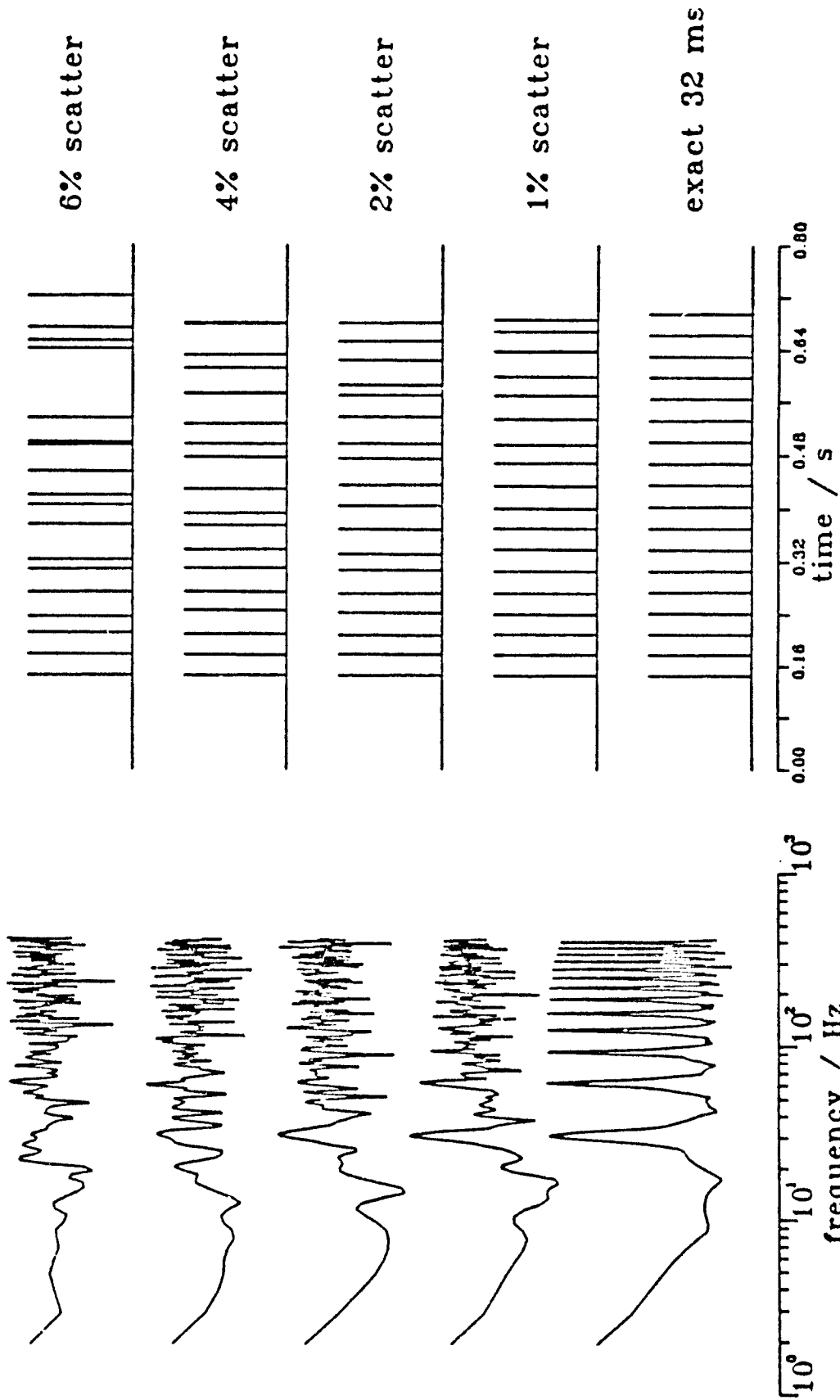
3.75
0.0
-3.75



(c)







**PHYSICAL MODELS OF SPALL ZONE GROUND
MOTIONS AND THE DETERMINATION OF SPATIAL
DECAY RATES**

Brian W Stump
Dept of Geological Sciences
Southern Methodist University
Dallas, TX 75275

and

Thomas A. Weaver
EES-3, MS-C335
Los Alamos National Laboratory
Los Alamos, NM 87545

Los Alamos

Los Alamos National Laboratory
Los Alamos, New Mexico 87545

April 10, 1992

Dear Recipient:

Enclosed is a report entitled "Physical models of spall zone ground motions and the determination of spatial decay rates" by B.W. Stump and T.A. Weaver prepared for the Source Region Program at Los Alamos National Laboratory. The report discusses results from a preliminary study designed to document relationships between physical processes in the spall zone around explosions and the radiated seismic waves. This is important for developing realistic spall models that can be used to predict effects on far-field verification signals. A simple physical model for spall is proposed that includes free-field attenuation (decay) of the wavefield coupled with free-surface interactions. The model suggests that spall data should be plotted against free-surface range and interpreted in terms of two decay rates. The decay of data at close ranges (out to about $100 \text{ m/kt}^{1/3}$) is controlled by free-surface effects while data beyond is dominated by the free-field interaction. It is illustrated that decay rates (used in quantification of spall momentum) can be biased if an improper physical model is used. The work contained in the report was funded by the Source Region Program at the Los Alamos National Laboratory for the DOE Office of Arms Control and Nonproliferation and DARPA, F19628-89-K-0025, as monitored by the Phillips Laboratory. This report is being distributed to researchers at the DOE laboratories and other government agencies and universities.

ABSTRACT

Spall, the tensile failure of near-surface layers, which is observed above contained explosions, has been identified as a possible secondary seismic source contributing to teleseismic and regional signals. The relative importance of this secondary source can be constrained if the motion field in the spall zone is characterized. Spall zone motions from nuclear explosions detonated above the water table at Pahute Mesa are analyzed to develop these models. Acceleration, velocity, displacement, and dwell time measurements are made from gauges placed directly above the explosion, most often at the free surface. Decay of peak motions are strongly affected by the free surface with little change in amplitude out to a free surface range of $100 \text{ m/kt}^{1/3}$ followed by rapid decay beyond. Free surface interactions are assessed with first-order elastic spherical wave calculations that match observed peak velocity decays. These results indicate that the spall zone motions may be strongly affected by the scaled depth of burial of the explosion. Spall zone velocities, displacements and dwell times are compared for consistency with a gravitational model. The data is in agreement with the functional form of theoretical models although observed displacements may be as much as a factor of two to four greater than the model predicts for observed velocities and dwell times. These differences may reflect the continuous nature of the spall process and/or the role of material strength in these phenomena.

DISTRIBUTION LIST

Prof. Thomas Ahrens
Seismological Lab, 252-21
Division of Geological & Planetary Sciences
California Institute of Technology
Pasadena, CA 91125

Prof. Keiiti Aki
Center for Earth Sciences
University of Southern California
University Park
Los Angeles, CA 90089-0741

Prof. Shelton Alexander
Geosciences Department
403 Deike Building
The Pennsylvania State University
University Park, PA 16802

Dr. Ralph Alewine, III
DARPA/NMRO
3701 North Fairfax Drive
Arlington, VA 22203-1714

Prof. Charles B. Archambeau
CIRES
University of Colorado
Boulder, CO 80309

Dr. Thomas C. Bache, Jr.
Science Applications Int'l Corp.
10260 Campus Point Drive
San Diego, CA 92121 (2 copies)

Prof. Muawia Barazangi
Institute for the Study of the Continent
Cornell University
Ithaca, NY 14853

Dr. Jeff Barker
Department of Geological Sciences
State University of New York
at Binghamton
Vestal, NY 13901

Dr. Douglas R. Baumgardt
ENSCO, Inc
5400 Port Royal Road
Springfield, VA 22151-2388

Dr. Susan Beck
Department of Geosciences
Building #77
University of Arizona
Tucson, AZ 85721

Dr. T.J. Bennett
S-CUBED
A Division of Maxwell Laboratories
11800 Sunrise Valley Drive, Suite 1212
Reston, VA 22091

Dr. Robert Blandford
AFTAC/TT, Center for Seismic Studies
1300 North 17th Street
Suite 1450
Arlington, VA 22209-2308

Dr. G.A. Bollinger
Department of Geological Sciences
Virginia Polytechnical Institute
21044 Derring Hall
Blacksburg, VA 24061

Dr. Stephen Bratt
Center for Seismic Studies
1300 North 17th Street
Suite 1450
Arlington, VA 22209-2308

Dr. Lawrence Burdick
Woodward-Clyde Consultants
566 El Dorado Street
Pasadena, CA 91109-3245

Dr. Robert Burrige
Schlumberger-Doll Research Center
Old Quarry Road
Ridgefield, CT 06877

Dr. Jerry Carter
Center for Seismic Studies
1300 North 17th Street
Suite 1450
Arlington, VA 22209-2308

Dr. Eric Chael
Division 9241
Sandia Laboratory
Albuquerque, NM 87185

Prof. Vernon F. Cormier
Department of Geology & Geophysics
U-45, Room 207
University of Connecticut
Storrs, CT 06268

Prof. Steven Day
Department of Geological Sciences
San Diego State University
San Diego, CA 92182

Marvin Denny
U.S. Department of Energy
Office of Arms Control
Washington, DC 20585

Dr. Zoltan Der
ENSCO, Inc.
5400 Port Royal Road
Springfield, VA 22151-2388

Prof. Adam Dziewonski
Hoffman Laboratory, Harvard University
Dept. of Earth Atmos. & Planetary Sciences
20 Oxford Street
Cambridge, MA 02138

Prof. John Ebel
Department of Geology & Geophysics
Boston College
Chestnut Hill, MA 02167

Eric Fielding
SNEE Hall
INSTOC
Cornell University
Ithaca, NY 14853

Dr. Mark D. Fisk
Mission Research Corporation
735 State Street
P.O. Drawer 719
Santa Barbara, CA 93102

Prof Stanley Flatte
Applied Sciences Building
University of California, Santa Cruz
Santa Cruz, CA 95064

Dr. John Foley
NER-Geo Sciences
1100 Crown Colony Drive
Quincy, MA 02169

Prof. Donald Forsyth
Department of Geological Sciences
Brown University
Providence, RI 02912

Dr. Art Frankel
U.S. Geological Survey
922 National Center
Reston, VA 22092

Dr. Cliff Frolich
Institute of Geophysics
8701 North Mopac
Austin, TX 78759

Dr. Holly Given
IGPP, A-025
Scripps Institute of Oceanography
University of California, San Diego
La Jolla, CA 92093

Dr. Jeffrey W. Given
SAIC
10260 Campus Point Drive
San Diego, CA 92121

Dr. Dale Glover
Defense Intelligence Agency
ATTN: ODT-1B
Washington, DC 20301

Dr. Indra Gupta
Teledyne Geotech
314 Montgomery Street
Alexandria, VA 22314

Dan N. Hagedorn
Pacific Northwest Laboratories
Battelle Boulevard
Richland, WA 99352

Dr. James Hannon
Lawrence Livermore National Laboratory
P.O. Box 808
L-205
Livermore, CA 94550

Dr. Roger Hansen
HQ AFTAC/TTR
Patrick AFB, FL 32925-6001

Prof. David G. Harkrider
Seismological Laboratory
Division of Geological & Planetary Sciences
California Institute of Technology
Pasadena, CA 91125

Prof. Danny Harvey
CIRES
University of Colorado
Boulder, CO 80309

Prof. Donald V. Helmberger
Seismological Laboratory
Division of Geological & Planetary Sciences
California Institute of Technology
Pasadena, CA 91125

Prof. Eugene Herrin
Institute for the Study of Earth and Man
Geophysical Laboratory
Southern Methodist University
Dallas, TX 75275

Prof. Robert B. Herrmann
Department of Earth & Atmospheric Sciences
St. Louis University
St. Louis, MO 63156

Prof. Lane R. Johnson
Seismographic Station
University of California
Berkeley, CA 94720

Prof. Thomas H. Jordan
Department of Earth, Atmospheric &
Planetary Sciences
Massachusetts Institute of Technology
Cambridge, MA 02139

Prof. Alan Kafka
Department of Geology & Geophysics
Boston College
Chestnut Hill, MA 02167

Robert C. Kemerait
ENSCO, Inc.
445 Pineda Court
Melbourne, FL 32940

Dr. Max Koontz
U.S. Dept. of Energy/DP 5
Forrestal Building
1000 Independence Avenue
Washington, DC 20585

Dr. Richard LaCoss
MIT Lincoln Laboratory, M-200B
P.O. Box 73
Lexington, MA 02173-0073

Dr. Fred K. Lamb
University of Illinois at Urbana-Champaign
Department of Physics
1110 West Green Street
Urbana, IL 61801

Prof. Charles A. Langston
Geosciences Department
403 Deike Building
The Pennsylvania State University
University Park, PA 16802

Jim Lawson, Chief Geophysicist
Oklahoma Geological Survey
Oklahoma Geophysical Observatory
P.O. Box 8
Leonard, OK 74043-0008

Prof. Thorne Lay
Institute of Tectonics
Earth Science Board
University of California, Santa Cruz
Santa Cruz, CA 95064

Dr. William Leith
U.S. Geological Survey
Mail Stop 928
Reston, VA 22092

Mr. James F. Lewkowicz
Phillips Laboratory/GPEH
Hanscom AFB, MA 01731-5000(2 copies)

Mr. Alfred Lieberman
ACDA/VI-OA State Department Building
Room 5726
320-21st Street, NW
Washington, DC 20451

Prof. L. Timothy Long
School of Geophysical Sciences
Georgia Institute of Technology
Atlanta, GA 30332

Dr. Randolph Martin, III
New England Research, Inc.
76 Olcott Drive
White River Junction, VT 05001

Dr. Robert Masse
Denver Federal Building
Box 25046, Mail Stop 967
Denver, CO 80225

Dr. Gary McCartor
Department of Physics
Southern Methodist University
Dallas, TX 75275

Prof. Thomas V. McEvelly
Seismographic Station
University of California
Berkeley, CA 94720

Dr. Art McGarr
U.S. Geological Survey
Mail Stop 977
U.S. Geological Survey
Menlo Park, CA 94025

Dr. Keith L. McLaughlin
S-CUBED
A Division of Maxwell Laboratory
P.O. Box 1620
La Jolla, CA 92038-1620

Stephen Miller & Dr. Alexander Florence
SRI International
333 Ravenswood Avenue
Box AF 116
Menlo Park, CA 94025-3493

Prof. Bernard Minster
IGPP, A-025
Scripps Institute of Oceanography
University of California, San Diego
La Jolla, CA 92093

Prof. Brian J. Mitchell
Department of Earth & Atmospheric Sciences
St. Louis University
St. Louis, MO 63156

Mr. Jack Murphy
S-CUBED
A Division of Maxwell Laboratory
11800 Sunrise Valley Drive, Suite 1212
Reston, VA 22091 (2 Copies)

Dr. Keith K. Nakanishi
Lawrence Livermore National Laboratory
L-025
P.O. Box 808
Livermore, CA 94550

Dr. Carl Newton
Los Alamos National Laboratory
P.O. Box 1663
Mail Stop C335, Group ESS-3
Los Alamos, NM 87545

Dr. Bao Nguyen
HQ AFTAC/TTR
Patrick AFB, FL 32925-6001

Prof. John A. Orcutt
IGPP, A-025
Scripps Institute of Oceanography
University of California, San Diego
La Jolla, CA 92093

Prof. Jeffrey Park
Kline Geology Laboratory
P.O. Box 6666
New Haven, CT 06511-8130

Dr. Howard Patton
Lawrence Livermore National Laboratory
L-025
P.O. Box 808
Livermore, CA 94550

Dr. Frank Pilotte
HQ AFTAC/TT
Patrick AFB, FL 32925-6001

Dr. Jay J. Pulli
Radix Systems, Inc.
2 Taft Court, Suite 203
Rockville, MD 20850

Dr. Robert Reinke
ATTN: FCTVTD
Field Command
Defense Nuclear Agency
Kirtland AFB, NM 87115

Prof. Paul G. Richards
Lamont-Doherty Geological Observatory
of Columbia University
Palisades, NY 10964

Mr. Wilmer Rivers
Teledyne Geotech
314 Montgomery Street
Alexandria, VA 22314

Dr. George Rothe
HQ AFTAC/TTR
Patrick AFB, FL 32925-6001

Dr. Alan S. Ryall, Jr.
DARPA/NMRO
3701 North Fairfax Drive
Arlington, VA 22209-1714

Dr. Richard Sailor
TASC, Inc.
55 Walkers Brook Drive
Reading, MA 01867

Prof. Charles G. Sammis
Center for Earth Sciences
University of Southern California
University Park
Los Angeles, CA 90089-0741

Prof. Christopher H. Scholz
Lamont-Doherty Geological Observatory
of Columbia University
Palisades, CA 10964

Dr. Susan Schwartz
Institute of Tectonics
1156 High Street
Santa Cruz, CA 95064

Secretary of the Air Force
(SAFRD)
Washington, DC 20330

Office of the Secretary of Defense
DDR&E
Washington, DC 20330

Thomas J. Sereno, Jr.
Science Application Int'l Corp.
10260 Campus Point Drive
San Diego, CA 92121

Dr. Michael Shore
Defense Nuclear Agency/SPSS
6801 Telegraph Road
Alexandria, VA 22310

Dr. Matthew Sibol
Virginia Tech
Seismological Observatory
4044 Derring Hall
Blacksburg, VA 24061-0420

Prof. David G. Simpson
IRIS, Inc.
1616 North Fort Myer Drive
Suite 1440
Arlington, VA 22209

Donald L. Springer
Lawrence Livermore National Laboratory
L-025
P.O. Box 808
Livermore, CA 94550

Dr. Jeffrey Stevens
S-CUBED
A Division of Maxwell Laboratory
P.O. Box 1620
La Jolla, CA 92038-1620

Lt. Col. Jim Stobie
ATTN: AFOSR/NL
Bolling AFB
Washington, DC 20332-6448

Prof. Brian Stump
Institute for the Study of Earth & Man
Geophysical Laboratory
Southern Methodist University
Dallas, TX 75275

Prof. Jeremiah Sullivan
University of Illinois at Urbana-Champaign
Department of Physics
1110 West Green Street
Urbana, IL 61801

Prof. L. Sykes
Lamont-Doherty Geological Observatory
of Columbia University
Palisades, NY 10964

Dr. David Taylor
ENSCO, Inc.
445 Pineda Court
Melbourne, FL 32940

Dr. Steven R. Taylor
Los Alamos National Laboratory
P.O. Box 1663
Mail Stop C335
Los Alamos, NM 87545

Prof. Clifford Thurber
University of Wisconsin-Madison
Department of Geology & Geophysics
1215 West Dayton Street
Madison, WS 53706

Prof. M. Nafi Toksoz
Earth Resources Lab
Massachusetts Institute of Technology
42 Carleton Street
Cambridge, MA 02142

Dr. Larry Turnbull
CIA-OSWR/NED
Washington, DC 20505

DARPA/RMO/SECURITY OFFICE
3701 North Fairfax Drive
Arlington, VA 22203-1714

Dr. Gregory van der Vink
IRIS, Inc.
1616 North Fort Myer Drive
Suite 1440
Arlington, VA 22209

HQ DNA
ATTN: Technical Library
Washington, DC 20305

Dr. Karl Veith
EG&G
5211 Auth Road
Suite 240
Suitland, MD 20746

Defense Intelligence Agency
Directorate for Scientific & Technical Intelligence
ATTN: DTIB
Washington, DC 20340-6158

Prof. Terry C. Wallace
Department of Geosciences
Building #77
University of Arizona
Tucson, AZ 85721

Defense Technical Information Center
Cameron Station
Alexandria, VA 22314 (2 Copies)

Dr. Thomas Weaver
Los Alamos National Laboratory
P.O. Box 1663
Mail Stop C335
Los Alamos, NM 87545

TACTEC
Batelle Memorial Institute
505 King Avenue
Columbus, OH 43201 (Final Report)

Dr. William Wortman
Mission Research Corporation
8560 Cinderbed Road
Suite 700
Newington, VA 22122

Phillips Laboratory
ATTN: XPG
Hanscom AFB, MA 01731-5000

Prof. Francis T. Wu
Department of Geological Sciences
State University of New York
at Binghamton
Vestal, NY 13901

Phillips Laboratory
ATTN: GPE
Hanscom AFB, MA 01731-5000

AFTAC/CA
(STINFO)
Patrick AFB, FL 32925-6001

Phillips Laboratory
ATTN: TSML
Hanscom AFB, MA 01731-5000

DARPA/PM
3701 North Fairfax Drive
Arlington, VA 22203-1714

Phillips Laboratory
ATTN: SUL
Kirtland, NM 87117 (2 copies)

DARPA/RMO/RETRIEVAL
3701 North Fairfax Drive
Arlington, VA 22203-1714

Dr. Michel Bouchon
I.R.I.G.M.-B.P. 68
38402 St. Martin D'Herès
Cedex, FRANCE

Dr. Michel Campillo
Observatoire de Grenoble
I.R.I.G.M.-B.P. 53
38041 Grenoble, FRANCE

Dr. Jorg Schlittenhardt
Federal Institute for Geosciences & Nat'l Res.
Postfach 510153
D-3000 Hannover 51, GERMANY

Dr. Kin Yip Chun
Geophysics Division
Physics Department
University of Toronto
Ontario, CANADA

Dr. Johannes Schweitzer
Institute of Geophysics
Ruhr University/Bochum
P.O. Box 1102148
4360 Bochum 1, GERMANY

Prof. Hans-Peter Harjes
Institute for Geophysic
Ruhr University/Bochum
P.O. Box 102148
4630 Bochum 1, GERMANY

Prof. Eystein Husebye
NTNF/NORSAR
P.O. Box 51
N-2007 Kjeller, NORWAY

David Jepsen
Acting Head, Nuclear Monitoring Section
Bureau of Mineral Resources
Geology and Geophysics
G.P.O. Box 378, Canberra, AUSTRALIA

Ms. Eva Johannisson
Senior Research Officer
National Defense Research Inst.
P.O. Box 27322
S-102 54 Stockholm, SWEDEN

Dr. Peter Marshall
Procurement Executive
Ministry of Defense
Blacknest, Brimpton
Reading FG7-FRS, UNITED KINGDOM

Dr. Bernard Massinon, Dr. Pierre Mechler
Societe Radiomana
27 rue Claude Bernard
75005 Paris, FRANCE (2 Copies)

Dr. Svein Mykkeltveit
NTNT/NORSAR
P.O. Box 51
N-2007 Kjeller, NORWAY (3 Copies)

Prof. Keith Priestley
University of Cambridge
Bullard Labs, Dept. of Earth Sciences
Madingley Rise, Madingley Road
Cambridge CB3 0EZ, ENGLAND